TELESEISMIC ARRAY ANALYSIS OF UPPER MANTLE COMPRESSIONAL VELOCITY STRUCTURE

Thesis by

Marianne Carol Walck

In Partial Fulfillment of the Requirements

for the Degree of

Doctor of Philosophy

California Institute of Technology

Pasadena, California

1984

(Submitted November 22, 1983)

This thesis is dedicated

to my parents,

Mel and Marie Walck,

and in memory of my grandfather,

Carl W. Sievert

Acknowledgments

The open, yet intense scientific atmosphere and worthwhile people I encountered here have made my sojourn at the Seismo. Lab. truly unforgettable. I appreciate the helpfulness of all the faculty members, former and present, and thank Don Anderson, Bernard Minster and Rob Clayton for advice and encouragement related to my research. Dave Harkrider was an exemplary "buddy advisor". Occasional successful receptions of footballs thrown to me by Don Helmberger brightened many of my Saturday mornings.

Two of my long-term office mates, Jeff Given and Terry Wallace, have been patient and good humored beyond the call of duty; they are also great conversationalists. Steve Cohn introduced me to the fine art of organizing ski trips, which the numerous enthusiastic skiers at the lab made memorable. The innovative ideas of many students contributed at key points in my projects. I particularly thank John Ebel and Tom Hearn for useful discussions on a number of topics. I especially appreciate Eric Chael's close friendship over the past several years. His graduation provided some additional motivation for the timely completion of this thesis.

Abstract

Large quantities of teleseismic short-period seismograms recorded at SCARLET provide travel time, apparent velocity and waveform data for study of upper mantle compressional velocity structure. Relative array analysis of arrival times from distant ($30° < \Delta < 95°$) earthquakes at all azimuths constrains lateral velocity variations beneath southern California. We compare $dT/d\Delta$, back azimuth and averaged arrival time estimates from the entire network for 154 events to the same parameters derived from small subsets of SCARLET. Patterns of mislocation vectors for over 100 overlapping subarrays delimit the spatial extent of an east-west striking, high-velocity anomaly beneath the Transverse Ranges. Thin lens analysis of the averaged arrival time differences, called 'net delay' data, requires the mean depth of the corresponding lens to be more than 100 km. Our results are consistent with the PKP-delay times of Hadley and Kanamori (1977), who first proposed the high-velocity feature, but we place the anomalous material at substantially greater depths than their 40-100 km estimate.

Detailed analysis of travel time, ray parameter and waveform data from 29 events occurring in the distance range $9°$ to $40°$ reveals the upper mantle structure beneath an oceanic ridge to depths of over 900 km. More than 1400 digital seismograms from earthquakes in Mexico and Central America yield 1753 travel times and 58 $dT/d\Delta$ measurements as well as high-quality, stable waveforms for investigation of the deep structure of the Gulf of California. The result of a travel time inversion with the tau method (Bessonova et al., 1976) is adjusted to fit the $p(\Delta)$ data, then further refined by incorporation of relative amplitude information through synthetic seismogram modeling. The application of a modified wave field continuation method

(Clayton and McMechan, 1981) to the data with the final model confirms that GCA is consistent with the entire data set and also provides an estimate of the data resolution in velocity-depth space. We discover that the upper mantle under this spreading center has anomalously slow velocities to depths of 350 km, and place new constraints on the shape of the 660 km discontinuity.

Seismograms from 22 earthquakes along the northeast Pacific rim recorded in southern California form the data set for a comparative investigation of the upper mantle beneath the Cascade Ranges-Juan de Fuca region, an ocean-continent transition. These data consist of 853 seismograms ($6° < \Delta < 42°$) which produce 1068 travel times and 40 ray parameter estimates. We use the spreading center model initially in synthetic seismogram modeling, and perturb GCA until the Cascade Ranges data are matched. Wave field continuation of both data sets with a common reference model confirms that real differences exist between the two suites of seismograms, implying lateral variation in the upper mantle. The ocean-continent transition model, CJF, features velocities from 200 and 350 km that are intermediate between GCA and T7 (Burdick and Helmberger, 1978), a model for the inland western United States. Models of continental shield regions (e.g., King and Calcagnile, 1976) have higher velocities in this depth range, but all four model types are similar below 400 km. This variation in rate of velocity increase with tectonic regime suggests an inverse relationship between velocity gradient and lithospheric age above 400 km depth.

Table of Contents

Introduction

The concept of a very dense array of seismic stations is relatively recent in earthquake seismology. First proposed in the late 1950's as a means to monitor nuclear explosions (Filson, 1975), arrays have increased in size and in scientific importance to the present day. Davies (1973) offers a definition of an array: it consists of more than three seismometers in a region (< 1000 km in diameter); the stations are similarly instrumented, and they must record at a central point to provide easy access to the data. The United States and Great Britain were the pioneers in design and implementation of seismic arrays. Britain's first networks were sponsored by the United Kingdom Atomic Energy Authority (UKAEA) and consisted of 19 seismometers in a 22.5 km cross formation. The five arrays of the United States' initial effort (Project Vela Uniform) were even smaller, with apertures of about 10 km. Research based on experiments with these small arrays led to improvements in signal processing, noise suppression and array design; larger arrays became practical and desirable in order to obtain lower detection thresholds. By 1965, the Large Aperture Seismic Array (LASA) was completed in Montana. An unprecedented 525 instruments were organized into 21 subarrays; it had a 200 km aperture and recorded digitally. Many of the medium aperture UKAEA arrays are presently in operation, but the trend is toward larger regional suites of seismometers such as NORSAR (100 km aperture near Oslo, Norway) and SCARLET (600 km aperture in southern California).

As might be expected, research conducted with arrays did not stop at nuclear test monitoring. Alert scientists realized that these densely spaced groups of stations provided several advantages. Individual signals can be combined into beams (e.g., Lacoss et al., 1969) thus suppressing noise, decreasing detection thresholds

and allowing small seismic phases to be picked out of the background. In seismically active areas, large networks facilitate increased location accuracy, and the convenience of a common data base stimulates studies of crustal structure, detailed seismicity variations, and source parameters of local events.

Arrays can also be used to study teleseismic earthquakes: their sources and the structure through which the waves propagate. Source investigations are not as prevalent as structural projects because of the narrow-band response of most array seismographs. For velocity determination, the intense spatial sampling assists analysis in three respects. First, much more detailed data are available for travel times. Given a favorable distribution of earthquakes with distance from the array, a well-constrained T(Δ) curve is constructed. Since the integral of the velocity profile from the source to the receiver controls the arrival times, they are important basic information for velocity inversion. Second, arrays are able to measure directly the apparent velocity of waves sweeping across the network. The inverse of phase velocity is related to the absolute velocity at the rays' bottoming point:

$$p = dT/d\Delta = \frac{r \sin i}{v} = \frac{r_b}{v_b}$$

where p is the ray parameter, T is travel time, Δ is distance in degrees, r is radius, v is velocity, i is the angle between the ray and a radial line from the earth's center, and b denotes the turning point of the teleseismic wave. Since p is constant for a ray, by measuring it we can determine the absolute velocity at the point where the ray is horizontal. This unique capability has prompted many structure studies using teleseisms. Third, the relative amplitudes of various phases on the same record can be tracked across a regional network. The amplitudes are very sensitive to velocity gradients near the turning point.

Over the last two decades, seismologists have taken advantage of the wealth of array data to make important advances in our knowledge of earth structure. Because most arrays have predominantly short-period vertical instruments, the research focus has been on short-period P waves. One subject of intense scrutiny is the Earth's core. Signal enhancement techniques allowed the isolation of the inner core reflections PKiKP and PKIIKP, demonstrating that the inner core boundary is sharp to 1 s P-wave energy (Engdahl et al., 1970; Buchbinder et al., 1973; Massé et al., 1974; Bolt, 1980). Array beamforming was also essential in the only observation of PKJKP (Julian et al., 1972), the inner core shear wave phase. Array determinations of $dT/d\Delta$ and ζ (azimuth of approach) for precursors to PKIKP are crucial to arguments that these precursors are caused by scattering at the core-mantle boundary (Cleary and Haddon, 1972; Haddon and Cleary, 1974; King et al., 1974), and not by arrivals from an inner-outer core transition zone, as Sacks and Saa (1971) and Bertrand and Clowes (1974) proposed.

Many investigators have measured the function $dT/d\Delta$ (Δ) for ranges appropriate for the lower mantle, 30° - 95° (see e. g., Chinnery and Toksöz, 1967; Toksöz et al., 1967; Chinnery,1969; Johnson, 1969; Corbishley, 1969; Burdick and Powell, 1980). While the velocity gradient below 800 km is relatively smooth, without large velocity discontinuities, second-order discontinuities were postulated at several depths by some of the authors listed above and also by Vinnik and Nikolayev (1970), Wright and Cleary (1972) and Wright and Lyons (1979) using arrays in Australia, Canada, the United States, the Soviet Union, Scotland and India. Unfortunately, the results are inconsistent from region to region, implying either substantial lateral heterogeneity in the lower mantle or problems involving data interpretation. Burdick and Powell (1980) point out that azimuthal bias can occur; receiver structure can

affect dT/dΔ measurements preferentially with azimuth, causing an apparent change in $p(\Delta)$ when changing source areas along the profile. Single-azimuth data sets would eliminate this bias, but such a fortunate seismicity distribution is quite unusual, and at most arrays data must be azimuthally mixed in order to achieve complete distance coverage.

Another area of interest is the local structure beneath the network. In regions of high seismicity, local events are utilized to determine crustal and uppermost mantle velocities, but for aseismic areas, teleseisms provide the only passively recorded information. Receiver structure has been investigated by block travel time inversions (Aki et al., 1976, 1977; Christoffersson and Husebye, 1979) using extensive data sets at several arrays (e. g., Husebye et al., 1976; Menke, 1977; Raikes, 1980; see Aki (1982) for a review). A different approach employs the full wave vector estimate (dT/dΔ and ζ) to characterize an event in terms of a mislocation vector on an array diagram (Manchee and Weichert, 1968; Davies and Sheppard, 1972). A suite of events produces many vectors, which often change systematically with ray parameter and azimuth (Powell, 1976). Some arrays, such as LASA and NORSAR, have very large mislocations. These arrays cannot perform more than reconnaissance teleseismic event location, as epicenter estimates are often more than 100 km in error (Davies, 1973; Filson, 1975). Powell (1976) argues for near-source locations of the perturbing velocities for LASA. Berteussen (1975, 1976), however, suggests a near-receiver origin for the observed anomalies at NORSAR. His theory received support from Haddon and Husebye (1978), who performed a joint inversion of travel time and amplitude data for the Norwegian array with a thin lens formulation. They found a significant anomaly beneath the array at a depth of 150 km.

The complexity of seismic waves which have interacted with the Earth's upper mantle (depths of between 50 and 700 km) has long fascinated seismologists, and has stimulated numerous array studies of upper mantle structure. While the general scheme of a low-velocity zone somewhere above 200 km depth and major discontinuities at 400 and 670 km may be well established, important questions remain concerning lateral variations in this depth range. A well-resolved map of the global distribution of the upper mantle velocity jumps would help put bounds on the scale of mantle convection (Hager and Raefsky, 1981) and the depth extent of differences between continents and ocean basins (Sipkin and Jordan, 1975, 1976; Okal and Anderson, 1975; Anderson, 1979). One way of determining regional structural differences is to use the same data analysis techniques on many data sets collected worldwide and compare the resultant models. In fact, P-wave apparent velocity studies of the upper mantle with arrays are very popular. Models exist for such varied regions as the western United States (Niazi and Anderson, 1965; Johnson, 1967), the Indian Ocean and Indian subcontinent (Ram and Mereu, 1977), western Canada (Dey-Sarkar and Wiggins, 1976; Ram et al., 1978), northern Australia (Simpson et al., 1974), northwest Eurasia (King and Calcagnile, 1976), southern Europe (England et al., 1977), the north Atlantic Ocean (England et al., 1978) and the Japan trench (Kanamori, 1967; Fukao, 1977). There are important differences in these models above 200 km, but relative depths of the discontinuities are not very well constrained, due to disparities in data quality, array size and analysis techniques. Also, while trenches, tectonically active continental areas and continental shields are documented, models of the deep structure of continental rifts and oceanic spreading centers, which are very important in understanding plate tectonics, are lacking.

This thesis investigates upper mantle structure by utilizing several techniques unique to seismic array analysis and applying them to data collected at the wide-aperture, 200 station California Institute of Technology - U. S. Geological Survey southern California Seismic Network (SCARLET). In Chapter 1, we tackle the receiver structure problem beneath southern California with an extensive teleseismic data set ($30° < \Delta < 95°$). Raikes (1980) collected most of these data for her P-residual study; she inverted for relative velocity anomalies using both block inversion (Aki et al., 1976, 1977) and ray tracing. We try a different approach: relative array analysis. The wave vectors at small subarrays are compared to those of the whole Caltech network through relative array diagrams and net subarray delays. This method eliminates near-source and lower mantle propagation effects, and spatially averages the data over small areas. The observations confirm the existence of a high-velocity anomaly beneath the Transverse Ranges (Hadley and Kanamori, 1977; Raikes and Hadley, 1979; Raikes, 1980). Projection of the net delays onto a thin lens yields a mean depth of about 150 km for the anomaly, which is deeper than previously suggested.

Chapter 2 is a brief review of available array techniques for analysis of upper mantle data profiles ($10° < \Delta < 30°$). Some methods are based on travel times alone, such as the classic Wiechert-Herglotz and more recent tau inversions (Bessonova et al., 1974). Others depend on detailed measurements of wave power and $dT/d\Delta$ as a function of time: the Vespa process (Davies et al., 1971) and adaptive processing (King et al., 1973) are examples. Travel time, slowness and relative phase amplitudes are all important in both forward synthetic modeling (Helmberger and Burdick, 1979) and wave field continuation. We have adapted the wave field continuation method (Clayton and McMechan, 1981), previously used with refraction

and reflection data, to teleseismic analysis.

Applications of these methods appear in Chapters 3 and 4. For these experiments, we take advantage of the convenient location of SCARLET along the east rim of the Pacific Ocean. Zones of high seismicity lie both to the north and the south at distances appropriate for upper mantle study. In Chapter 3, 29 events from Mexico are gathered and analyzed to elucidate the deep structure (to 900 km) beneath an active spreading center, the Gulf of California. We derive a model, GCA, consistent with the travel times, $dT/d\Delta$ and relative amplitude information. A major conclusion is that under this oceanic ridge, P-wave speeds are slower than for trenches (Fukao, 1977), young continental areas (Burdick and Helmberger, 1978) or continental shields (Given and Helmberger, 1980; Burdick, 1981) to depths of 350 km. Wave field continuation of the data with the proposed model, GCA, confirms that the model is consistent with the entire 1355 seismogram data set ($9° < \Delta < 40°$).

Energy from earthquakes along the northeast Pacific recorded at SCARLET is sensitive to the upper mantle beneath the Cascade Ranges and the Juan de Fuca plate, a region where young oceanic crust has undergone recent subduction. Differences between this 853 record data set ($6° < \Delta < 42°$) and that from the southern events is discussed in Chapter 4. Significant travel time differences and waveform discrepancies for distances of less than $23°$ correspond to structural changes at depth. Both the synthetic seismogram modeling and wave field continuation support resolvability of the changes between the Cascade model, CJF, which is similar to Burdick and Helmberger's (1978) model for the western United States, and GCA. The two dense data sets, after identical data processing, suggest that there is significant lateral heterogeneity in the mantle to depths of 350 km.

Chapter 1

Relative array analysis of upper mantle lateral velocity variations in southern California

Introduction

The boundary between the North American and Pacific plates in California is a classical example of a right-lateral transform in a continental environment. While the surface expression of this contact, the San Andreas fault system, is relatively simple in central California, the geologic and tectonic relationships become much more complex farther south. Local north-south compressional features are conspicuous in the Transverse Ranges near the 'Big Bend' of the San Andreas. This tectonic province is characterized by a topographic high and an area of complicated geology. South of the Transverse Ranges the multiple subparallel traces of the San Jacinto, Elsinore, and southern San Andreas faults add still more complexity to the tectonic picture.

Surface deviations from a simple boundary are associated at depth with lateral velocity variations in the crust and upper mantle. Studies of southern California crustal velocity structure using local sources reveal lateral changes in the lower crust on a regional scale (Kanamori and Hadley, 1975; Hadley and Kanamori, 1977; Cara et al., 1981; Lamanuzzi, 1981; Hearn, 1983). The large magnitude and marked azimuthal dependence of an extensive suite of teleseismic P-wave residuals led Raikes (1976, 1980) to suggest substantial lateral heterogeneity within the upper mantle at depths of 50-150 km. Based on these anomalies, Raikes and Hadley (1979) proposed a high-velocity zone beneath the Transverse Ranges at 40-100 km depth, consistent with the earlier model of Hadley and Kanamori (1977). Because this feature is not offset by the San Andreas fault, it requires significant eastward

displacement of the subcrustal plate boundary toward the Helendale-Lenwood-Camprock fault system (Figure 1.1). Alternatively, relative plate motion could be accommodated through a broad horizontal zone of simple shear below the crust, as suggested by Lachenbruch and Sass (1980). Recent observations of Pn anisotropy beneath the central Transverse Ranges (Vetter and Minster, 1981) tend to favor the latter hypothesis. Recently, Humphreys (in preparation) inverted an augmented travel time data set with a tomographic technique. The same anomaly emerged beneath southern California, but with a greater mean depth of 150 km.

The present study exploits the large aperture and dense station coverage of the Caltech-U.S. Geological Survey (USGS) Southern California Seismic Network (SCARLET), investigating these anomalies in greater detail by spatially averaging teleseismic P-wave arrival times over small groups of stations. Previous studies using seismic networks (e.g., Okal and Kuster, 1975; Vermeulen and Doornbos, 1977) provide evidence for the dominance of near-receiver effects in mislocations determined by small groups of stations. This averaging, repeated for many subarrays across the network, provides information about local perturbations of ray parameter and azimuth of approach as well as averaged arrival times. The 'relative array diagrams' (Powell et al., 1979) and plots of 'net subarray delays', which represent these data, are insensitive to near-source and lower mantle propagation effects and thus yield a picture of near-receiver anomalies relative to an average structure for southern California. SCARLET's many subarray combinations allow this analysis to provide increased resolution of upper mantle features both laterally and in depth.

Figure 1.1 Index map of southern California. S.B. denotes San Bernardino.

Analysis technique

Seismic arrays are routinely used to determine directly the ray parameter, $dT/d\Delta$, and back azimuth, φ, of distant events. This is accomplished by fitting a least squares plane to the teleseismic wave front (e.g., Otsuka, 1966)

$$T(x,y) = A(x - x_o) + B(y - y_o) + \Delta T(x_o,y_o) \qquad (1.1)$$

where $T(x,y)$ is an arrival time at the observation point (x,y), (x_o,y_o) are the array center coordinates, A and B are the components of the apparent slowness vector, and ΔT is time at the array center. Then $dT/d\Delta$ and φ are

$$dT/d\Delta = (A^2 + B^2)^{\frac{1}{2}} \qquad (1.2)$$

$$\varphi = \tan^{-1}(A/B)$$

The $dT/d\Delta$ and azimuth estimates obtained through this procedure are compared to theoretical values from a radially symmetric earth model (e.g., Jeffreys-Bullen (JB)) and USGS hypocentral parameters. This is most conveniently accomplished using an array diagram (Manchee and Weichert, 1968; Davies and Sheppard, 1972). In a polar plot of $dT/d\Delta$ versus φ, the theoretical and array values are drawn as the heads and tails, respectively, of a set of 'mislocation vectors' (Davies and Sheppard, 1972; Powell, 1976) which represent the cumulative effects of near-source, lower mantle, and near-receiver departures from the earth model as well as errors in the data.

The array diagram for SCARLET (Burdick and Powell, 1980) is striking because of the extremely small magnitude of the mislocation vectors (Figure 1.2). The average or mean vector of the diagram provides a first-order correction for slowly varying
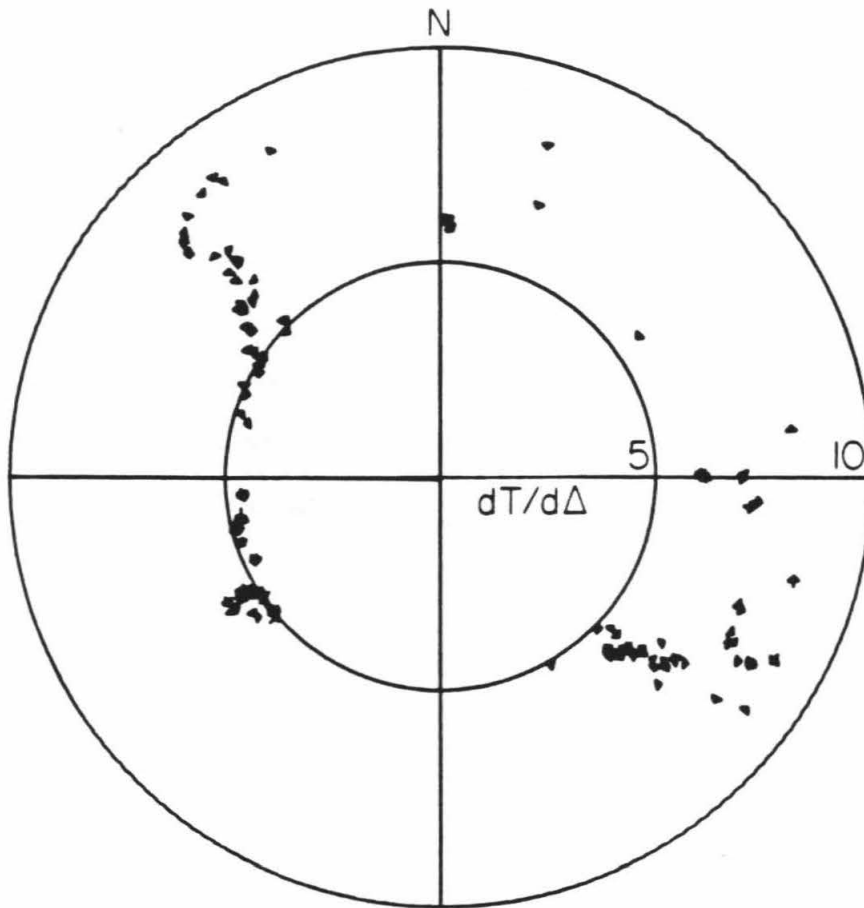
Figure 1.2 The array diagram for SCARLET. All other array diagrams shown are at the same scale; the inner circle is at 5 s/deg., the outer circle is at 10 s/deg..

receiver structure (Davies and Sheppard, 1972; Powell, 1976). The magnitude of the Caltech mean mislocation vector is only 0.06 s/deg., as compared to 0.21 s/deg. for LASA (Powell, 1976). A small mean vector is most easily explained by invoking a very simple, 'transparent', near-receiver structure, with only minimal lateral variations. However, in view of the complex local geology and large azimuthal variations of P residuals, this observation may also be interpreted as diagnostic of lateral inhomogeneities with a spatial scale small compared with the network aperture (C. Powell, personal communication, 1981). As a result, the associated perturbations to the wave front are effectively averaged by equation (1.1). If this is the case, least squares plane fits to small subsets of SCARLET located over coherent local structure should yield coefficients which differ significantly from the whole array estimates. For a subarray we have

$$T(x,y) = a(x - x_1) + b(y - y_1) + \Delta t(x_1,y_1) \tag{1.3}$$

where Δt is now the reference arrival time at the subarray center (x_1,y_1). Then the subarray dT/dΔ and φ estimates are

$$dT/d\Delta_s = (a^2 + b^2)^{\frac{1}{2}} \tag{1.4}$$

$$\varphi_s = \tan^{-1}(a/b)$$

To compare these dT/dΔ and azimuth values obtained from a subarray with those for SCARLET, we use relative array diagrams. Again mislocation vectors represent the anomalies: The head of the arrow represents the SCARLET wave vector estimate and the tail the subarray value. P waves arriving at a network from a single event have all traversed similar paths in the near-source and lower mantle regions, diverging only in the crust and upper mantle beneath the array. Thus, comparison of whole array

values with those of small subarrays allows us to isolate near-receiver velocity anomalies. The subarray mislocation vectors then represent relative lateral velocity variations beneath the network. Since mislocation vectors on the SCARLET array diagram are so small, the whole array $dT/d\Delta$ and φ estimates are very similar to those for a JB earth. Relative array diagrams for southern California subnetworks therefore characterize velocity variations relative to an average array structure which closely approximates a JB earth model.

The simplest interpretive structural models for mislocation vectors are in terms of horizontal velocity gradients or dipping interfaces. Arrows point in the down dip direction of the interface (unless it is the top of a low-velocity zone) or, more generally, in the direction of slower velocity. An example of a synthetic array diagram generated by three-dimensional ray tracing for a dipping interface is shown in Figure 1.3. The mislocation vector magnitude depends on the dip angle, the velocity contrast across the interface, and the depth to the structure. Since these parameters trade off and since we cannot distinguish between dipping interfaces and lateral gradients, relative array diagram interpretation is not unique. However, under certain assumptions it is possible to make a first-order estimate of the anomalous structure's depth from the character of the azimuthal variation of mislocation vectors. For an array of aperture S, structures of dimension $\approx$S shallower than about S/2 tend to affect rays from all azimuths. This generally results in a smooth and coherent evolution of mislocation vectors with φ and $dT/d\Delta$. Smaller-scale shallow heterogeneities are related to spatial aliasing and are discussed in a later section. A very large wavelength deeper structure could also produce a slowly varying pattern. We tested this possibility for SCARLET by dividing the network into two pairs of large (250-300 km) subarrays. In all four cases the relative vectors were of small magnitude and
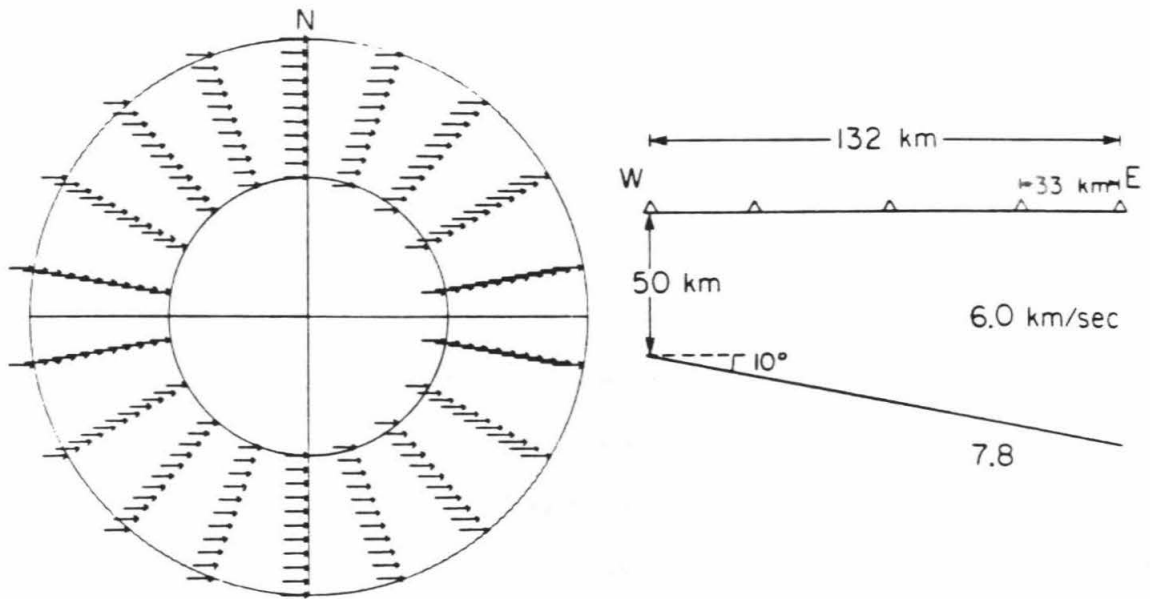
Figure 1.3 A synthetic array diagram for a planar interface dipping 10° at 50 km depth. The synthetic array contains 25 stations, is square and has a 132 km aperture. The mislocation vectors point in the direction of dip.

changed rapidly with azimuth, implying that deep heterogeneities must be of a scale smaller than these subarrays. In contrast, a smaller deep anomaly will affect only certain sectors of azimuth (Figure 1.4). When both shallow and deeper lateral variations are present beneath the same subarray, the diagram will contain signals from both anomalies. Since the shallow structure's signature is azimuthally invariant, removal of the mean vector will reveal the deeper anomaly. In addition, the portion of the diagram affected by the deep structure changes systematically with changing position of the subarray over it. Thus a large suite of overlapping subarrays can help map anomalies both laterally and in depth.

Another piece of information retrievable from spatially averaged travel times concerns the intercept (ΔT) term of equation (1.1). While A and B define the attitude of the wave front, ΔT prescribes its arrival time at the array center (x_o, y_o). A plane fit to subarray arrival times may not only be tilted by some local structure (visible on relative array diagrams) but also delayed or advanced relative to the array average wave front (Figure 1.5). We define a subarray 'net delay', η, as the difference between the subarray and whole array arrival time estimates at the subarray midpoint. The η is calculated for each event and each subarray. The whole array estimate of arrival time at the subarray center (x_1, y_1) is given by

$$\Delta T'(x_1, y_1) = A(x_1 - x_o) + B(y_1 - y_o) + \Delta T(x_o, y_o) \qquad (1.5)$$

Then

$$\eta = \Delta t(x_1, y_1) - \Delta T'(x_1, y_1) \qquad (1.6)$$

The net delays for a given subarray can then be plotted at the event's mislocation vector tail in the $(dT/d\Delta, \varphi)$ polar diagram (e.g., Figure 1.21). A positive net delay
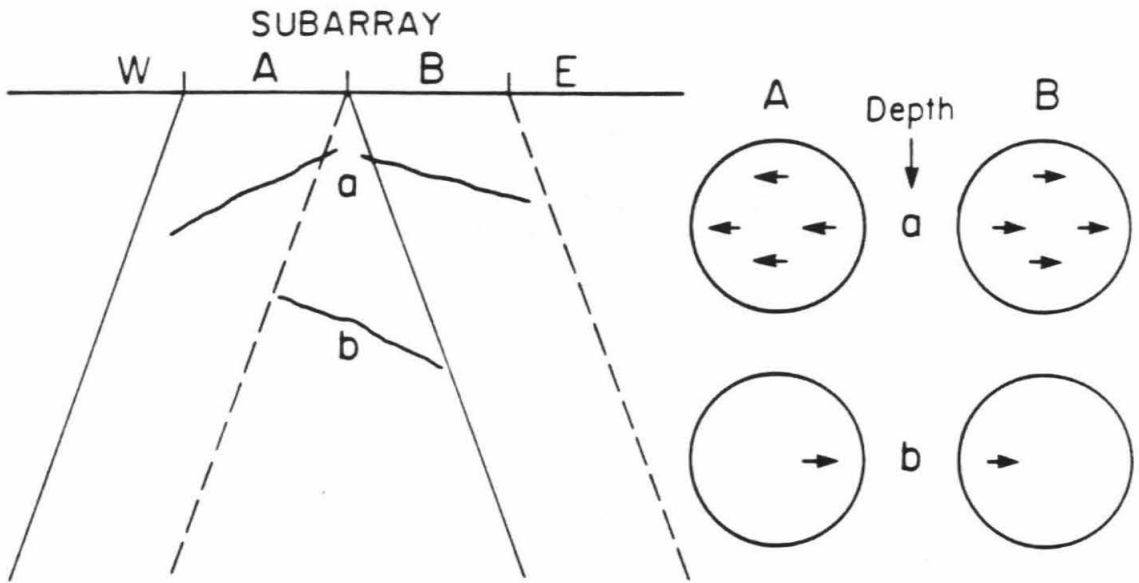
Figure 1.4 Depth determination using array diagrams. At depth level (a), the shallow structures affect all incoming rays to each respective subarray. The deeper structure (b) affects only easterly incident waves for subarray A and westerly rays for B.
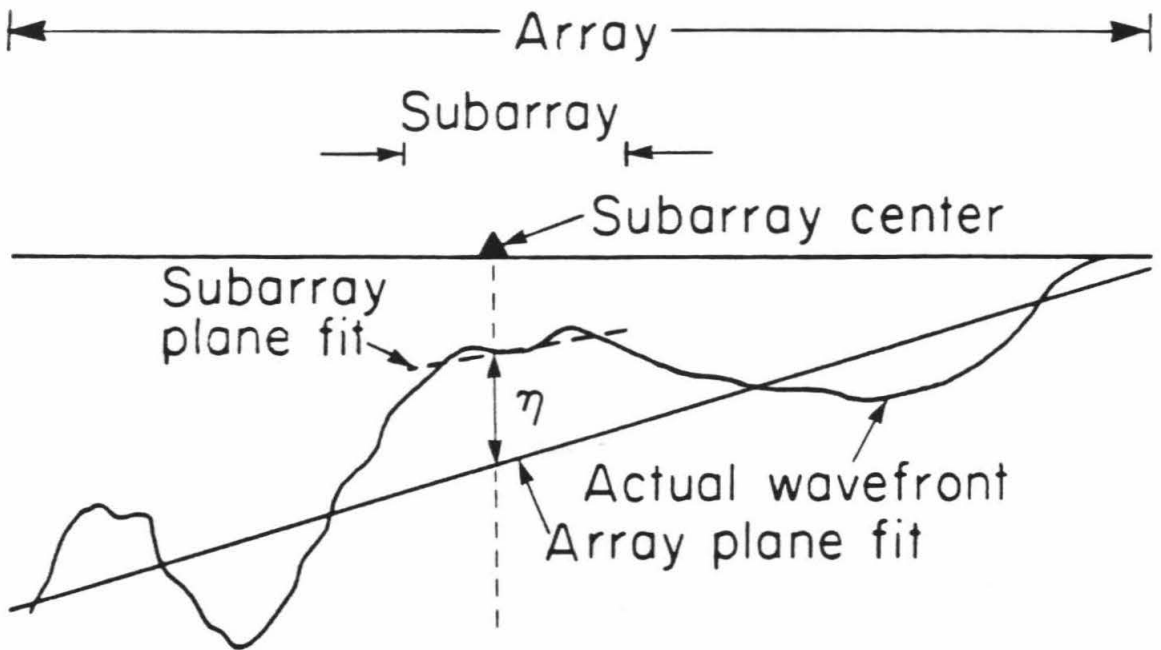
Figure 1.5 Two-dimensional sketch of local deviations of a teleseismic wave front and the effect of local structure on the subarray plane fit slope (dT/dΔ and φ anomalies) and arrival time at the subarray center (η, the 'net delay') with respect to the whole-array average wave front.

represents locally slow velocity, while a negative value implies that high velocity material was encountered along the ray path beneath the array.

Error estimates

Powell (1976) estimated the uncertainties in mislocation vectors induced by random errors in travel time picks, δt. These uncertainties depend also on the array aperture S and the horizontal phase velocity v through the relations

$$\delta(dT / d\Delta) \approx \delta t / S \tag{1.7}$$

with S in degrees, and

$$\delta\varphi \approx \tan^{-1}(v\,\delta t / S)$$

where S is in km and v is in km/s. The maximum error will occur for largest phase velocity v. Assuming v_{max} = 24 km/s ($\Delta \geq 95°$) and assigning δt = 0.1 s, the average aperture of 480 km (4.3°) for SCARLET leads to a maximum error for an arrow head of

$$\delta(dT / d\Delta) \approx 0.02 \; s / deg.$$

$$\delta\varphi \approx 0.29°$$

Each subarray used in the analysis has $S \geq 100$ km, so that the greatest error for a mislocation vector tail is

$$\delta(dT / d\Delta)_s \approx 0.11 s / deg.$$

$$\delta\varphi_s \approx 1.37°$$

Ellipses representing these errors on a relative array diagram are almost invisible on any of the plots shown here. More importantly, the error values are insignificant in comparison to the data anomalies, which reach 1 s/deg.

Because of the large aperture of SCARLET, we need to account for the curvature of the earth's surface and for the curvature of the wave front as well as the usual ellipticity and elevation corrections. Since the JB travel times contain both sphericity and wave front curvature information, a method was devised which fits a plane to the JB residuals of an event, thereby including first-order curvature corrections in the calculated $dT/d\Delta$ and φ values. The Appendix contains a detailed outline of this scheme.

The data set

SCARLET covers a large (400 x 600 km) area of southern California with about 200 short-period vertical seismometers telemetered to Pasadena. Station spacing is irregular; intervals range between 25 and 50 km, with stations concentrated in the Transverse Ranges and Imperial Valley regions (Figure 1.6). The triggered, digital Caltech Earthquake Detection and Recording system (CEDAR; Johnson (1979)) has been in operation since 1977, offering convenient data retrieval and timing accuracy capability (±0.05 s) superior to the ongoing (to 1982) 16-mm Develocorder recording system. While SCARLET is designed primarily to monitor local earthquake activity, teleseisms of magnitude ≥5.5 are often well recorded. The data base comprises 9095 P arrival times from 154 earthquakes recorded at SCARLET during 1974-1979. About 80% of these data were gathered by Raikes (1978), and 10% added by Burdick and Powell (1980) (Table 1.1). The events range in distance from $30°$ to $95°$;

Figure 1.6 Map of SCARLET in 1980. Underlined stations are used in computing the relative array diagram for the equal-aperture, more sparsely spaced array discussed in the text. Circles define subarrays referred to in Figure 1.11.

Table 1.1

Event Data

Region	Date			Origin Time			Depth	Lat.	Lon.	Magnitude
Fiji	3	8	77	3	2	32.80	571.	-17.725	-178.710	5.3
S Honshu	2	18	77	20	51	29.80	42.	32.893	140.817	6.0
Volcano Is	12	22	76	1	1	41.00	49.	23.155	143.721	5.8
N Korea	3	9	77	14	27	53.60	528.	41.413	130.878	5.9
Tonga	6	22	77	12	8	28.30	33.	-23.049	-175.920	7.2
Chile-Bol.	11	30	76	0	40	57.80	82.	-20.392	-68.919	6.5
Kamchatka	2	13	77	5	51	45.30	167.	53.875	158.634	5.0
Tonga	12	15	76	7	10	27.80	79.	-17.208	-173.994	5.5
Chile-Bol.	12	17	76	20	23	6.20	57.	-20.782	-68.456	5.6
Fiji	5	15	77	23	12	53.60	499.	-19.011	-177.672	5.5
Peru	10	8	77	3	3	38.30	100.	-10.549	-73.650	5.6
Fiji	4	14	77	4	5	31.20	535.	-17.552	-178.652	5.2
Kuril Is	4	10	77	8	31	33.40	84.	44.275	147.549	5.4
Fiji	6	3	77	14	33	7.00	573.	-18.820	-177.633	5.3
Peru-Brazil	4	9	77	4	4	12.50	564.	-9.948	-71.181	5.9
E Russia	9	9	77	2	35	12.10	550.	43.365	133.260	5.2
New Heb	5	18	77	6	43	21.10	217.	-18.875	169.194	5.2
Marianas	6	9	77	13	27	12.30	97.	13.067	144.458	5.2
Nov Zemlya	9	1	77	2	59	57.50	0.	73.270	54.581	5.7
Fiji	10	18	77	23	24	39.60	600.	-17.567	-178.800	5.9
Santiago	10	22	77	17	57	17.20	630.	-27.998	-63.010	6.2
S Honshu	7	8	75	22	46	19.20	49.	32.622	142.200	6.0
Marianas	1	1	75	14	16	1.00	313.	21.467	142.900	5.6
Honshu	5	4	75	9	31	59.20	23.	36.946	142.083	5.8
S Honshu	11	29	74	22	5	22.40	419.	30.529	138.300	6.1
Bonin Is	2	14	76	10	50	22.20	548.	26.402	140.275	5.5
Kamchatka	11	19	75	11	6	27.50	62.	54.175	161.302	6.2
Japan Sea	6	29	75	10	37	41.40	560.	38.568	129.990	6.2
Hokkaido	10	2	75	11	6	46.50	75.	43.004	145.886	5.8
Okhotsk	11	11	75	4	25	32.30	355.	46.479	145.482	5.5
Komandorsky	8	15	75	7	28	18.90	4.	54.693	167.845	6.0
S Alaska	8	2	75	10	18	17.90	33.	53.200	-161.485	6.2
Okhotsk	12	21	75	10	54	17.70	554.	51.751	151.577	6.0
Andreanof	2	22	75	8	36	7.40	48.	51.210	-179.100	6.3
S Alaska	12	29	74	18	25	0.70	67.	61.437	-150.500	5.6
Andreanof	11	11	74	5	17	51.00	68.	51.410	-178.100	5.8
Fox Aleut	1	13	75	9	19	10.30	42.	52.011	-171.100	5.7
Japan	6	4	76	4	23	32.40	21.	38.125	142.667	5.7
Solomon Is	2	22	76	18	28	58.30	56.	-6.271	154.778	5.9
Colombia	5	19	76	4	7	15.80	157.	4.433	-75.783	5.9
Okhotsk	7	10	76	11	37	12.80	387.	47.664	145.718	5.8

S Japan	6	25	76	7	47	46.30	433.	29.745	138.582	5.5
Tonga	6	18	76	1	45	37.30	33.	-24.665	-175.356	5.6
Solomon Is	6	5	76	8	20	7.20	61.	-10.019	161.012	6.2
N Chile	6	4	76	23	39	36.00	101.	-22.961	-68.542	5.4
Peru	5	23	76	16	32	33.00	73.	-10.414	-78.322	5.9
Tonga	5	20	76	4	59	47.10	292.	-15.834	-175.093	5.5
Solomon Is	5	9	76	20	44	44.70	34.	-7.403	154.630	5.8
Chile-Arg	4	18	76	19	40	20.50	113.	-25.684	-68.774	5.6
Marianas	4	7	76	7	10	15.80	217.	17.507	145.547	5.5
Kermadec	3	27	76	19	42	0.80	59.	-30.406	-178.198	5.8
South Fiji	2	3	76	12	27	30.10	477.	-24.987	179.693	5.8
Solomon Is	9	4	76	11	41	59.70	83.	-10.178	161.093	5.6
N Chile Cst	8	20	76	6	54	11.30	81.	-20.284	-69.993	5.6
Kuril Is	11	24	76	16	9	15.40	33.	51.831	160.650	5.8
N Atlantic	5	14	76	6	25	34.40	33.	10.710	-43.498	5.6
Santa Cruz	11	8	75	11	0	24.50	74.	-10.886	166.093	5.7
S Honshu	1	27	76	23	28	20.90	394.	31.213	138.053	5.0
Fiji	4	10	76	17	12	9.00	557.	-17.488	-178.500	6.0
Fiji Is	8	10	74	11	22	26.40	602.	-21.268	-179.200	5.5
Fiji	11	27	76	4	0	9.70	576.	17.736	-178.800	5.5
Peru-Brazil	12	5	74	11	57	31.30	162.	-7.648	-74.500	6.0
Jujuy Arg.	9	16	74	0	38	15.30	280.	-23.756	-65.500	5.6
Kamchatka	8	23	75	13	51	24.10	141.	54.558	160.052	5.9
San. Cruz	5	19	76	19	7	17.20	647.	-12.709	169.235	5.2
S Chile	5	30	76	3	8	54.20	28.	-41.443	-75.412	6.0
New Heb	3	4	76	2	50	0.50	90.	-14.647	167.104	6.4
Solomon Is	2	22	76	18	28	58.30	56.	-6.270	154.778	5.5
Nov Zemlya	9	29	76	2	59	57.40	0.	73.296	54.817	5.5
Kuril	3	3	76	19	48	39.80	162.	45.820	149.506	5.0
Tonga	2	3	76	18	3	52.00	212.	-17.993	-175.032	5.5
Nov Zemlya	11	1	74	4	59	56.70	0.	70.679	54.100	6.7
Nov Zemlya	8	23	75	8	59	57.90	0.	73.261	54.641	6.4
Nov Zemlya	10	18	75	8	59	56.30	0.	70.722	53.690	6.7
Nov Zemlya	10	21	75	11	59	57.30	0.	73.245	55.087	6.5
Jan Mayen	4	16	75	1	27	18.70	13.	71.383	-10.400	6.1
N Atlantic	5	26	75	9	11	51.50	33.	35.811	-17.649	6.7
Leeward Is	9	7	74	19	40	52.20	58.	15.002	-60.600	5.7
Leeward Is	3	10	76	9	4	58.80	54.	16.692	-61.100	6.0
N Colombia	3	13	76	21	44	41.30	165.	6.762	-72.966	5.4
Colombia	8	24	74	2	47	30.10	84.	4.271	-76.900	5.9
North Peru	8	16	75	0	53	53.70	123.	-5.340	-76.076	5.7
Peru-Brazil	8	9	74	4	53	30.90	159.	-8.244	-74.300	5.6
South Peru	4	27	74	6	1	47.30	113.	-14.902	-72.200	5.8
Peru-Bol.	7	12	75	6	47	37.50	156.	-17.057	-69.350	5.5
N Chile	2	26	75	20	14	59.60	82.	-19.676	-69.300	5.7
Peru	12	11	75	20	17	8.10	98.	-11.478	-74.552	6.0
Peru-Bol.	1	6	76	23	54	22.20	76.	-17.803	-69.482	5.6
Peru	1	5	76	2	31	36.30	95.	-13.201	-74.898	6.0

Chile-Bol.	2	5	76	9	53	11.70	98.	-21.568	-68.222	5.8
Chile-Arg	10	10	75	13	13	9.40	96.	-24.942	-68.073	5.5
N Chile	2	18	76	18	3	22.70	111.	-22.375	-68.613	5.4
Catamarca	3	25	75	6	41	33.00	178.	-27.838	-66.700	5.9
N Chile	12	6	75	22	47	30.40	82.	-23.679	-68.823	5.4
South Fiji	11	19	75	6	18	33.90	555.	-23.905	179.080	5.8
Kermadec	1	24	76	21	48	25.90	78.	-28.471	-177.593	6.2
South Fiji	7	24	75	19	1	42.60	579.	-23.334	-179.775	5.6
South Fiji	2	22	75	22	4	37.70	375.	-24.751	-179.100	6.2
Kermadec	5	5	76	4	52	51.20	33.	-29.582	-177.800	6.4
Fiji	6	6	75	1	8	41.10	658.	-20.472	-179.200	6.0
Fiji	8	20	75	20	18	50.90	559.	-20.273	-178.383	5.7
South Fiji	5	29	75	6	42	12.80	616.	-22.301	179.527	5.6
Fiji	2	27	75	18	42	53.70	586.	-17.786	-178.600	5.9
Solomon Is	3	8	76	4	39	55.90	47.	-10.629	165.000	6.1
Fiji	10	21	74	4	12	29.40	602.	-17.786	-178.600	6.0
Tonga	1	17	75	9	30	42.30	153.	-17.786	-174.500	5.8
Tonga	6	4	74	4	14	15.90	276.	-15.698	-175.100	6.0
Fiji Is	11	1	75	6	14	55.50	424.	-18.349	-177.858	5.8
Solomon Is	7	21	75	2	39	1.20	95.	-6.862	155.333	6.1
Solomon Is	3	2	76	10	51	9.60	61.	-6.239	154.797	5.7
Santa Cruz	12	19	75	2	14	29.60	33.	-11.676	164.804	6.0
N Chile	2	27	76	3	36	13.60	103.	-19.359	-69.065	5.5
New Heb	8	2	76	10	55	25.90	52.	-20.480	169.274	6.1
Solomon Is	10	12	76	0	40	52.90	106.	-10.383	161.295	6.0
Chile-Bol.	12	4	76	12	32	29.60	72.	-20.255	-68.531	5.6
Chile-Bol.	2	31	76	5	27	31.70	71.	-20.410	-68.632	5.4
Nov Zemlya	8	29	74	9	59	55.50	0.	73.293	55.100	6.4
Peru-Bol.	6	5	75	20	29	37.60	196.	-16.394	-69.200	5.5
Peru	5	15	76	21	55	56.20	33.	-11.523	-74.500	6.3
Solomon Is	7	20	75	23	5	18.80	50.	-6.536	154.651	6.2
Fiji	11	25	76	14	6	35.40	442.	-19.377	-177.583	6.0
Fiji	1	21	77	6	11	5.60	604.	-17.898	-178.379	5.8
Kuril Is	9	22	76	0	16	8.20	64.	44.685	149.225	6.1
Bonin Is	12	12	79	1	8	50.10	490.	28.267	139.575	6.0
Colombia	3	23	77	2	11	22.70	250.	6.685	-73.020	6.0
Argentina	2	4	77	7	46	36.60	600.	-24.512	-63.050	6.1
Kamchatka	11	17	76	5	33	34.60	112.	50.809	156.220	5.5
Panama	11	11	76	3	16	15.30	33.	4.966	-78.152	5.5
Mexico	2	2	76	14	20	42.20	32.	13.587	-92.263	5.5
Fox Is	3	28	76	6	55	15.20	36.	52.514	-167.153	5.2
Costa Rica	2	25	76	16	29	0.50	66.	10.362	-85.142	5.2
Honduras	2	8	76	8	13	46.70	5.	15.471	-88.467	5.2
Panama	2	4	76	9	1	43.40	5.	15.224	-89.102	6.2
Cent Amer	3	29	76	5	39	35.50	33.	3.902	-85.880	5.9
Fox Is	4	12	76	4	41	51.40	38.	52.216	-170.203	5.2
Kodiak	6	6	76	2	44	58.90	50.	57.255	-154.332	5.2
Cuba	9	29	76	9	52	33.80	33.	18.893	-80.752	5.2

Costa Rica	10	9	76	12	31	15.80	85.	10.765	-85.757	5.3
Kodiak	11	22	76	18	35	25.90	26.	55.963	-153.273	5.5
Panama	9	19	76	12	23	30.70	5.	7.244	-82.238	5.2
Costa Rica	12	1	76	14	15	39.00	58.	9.705	-84.770	5.3
Near Is	2	19	77	22	34	4.10	33.	53.380	170.033	6.2
Baffen Bay	11	12	76	14	47	24.90	33.	72.242	-70.212	5.8
Costa Rica	11	25	76	6	45	22.20	45.	9.637	-84.735	5.2
Honshu	2	20	79	6	32	38.00	41.	40.083	143.740	5.9
S Fiji Is	1	29	79	5	43	2.10	509.	-24.488	179.981	5.6
Fiji Is	1	20	79	17	55	18.10	574.	-22.211	-179.458	5.2
Kermadec	1	25	79	4	8	19.80	47.	-29.663	-177.522	6.2
N Atl Oc	12	13	77	1	14	18.60	33.	17.248	-54.848	5.7
Alaska	2	13	79	5	34	26.10	24.	55.329	-157.131	5.8
N Atl Oc	3	24	78	0	42	36.30	20.	29.633	-67.400	6.1
N Atl Oc	12	6	78	13	28	35.50	10.	17.335	-54.786	5.5
N Atl Rdge	2	11	79	8	1	1.50	33.	10.264	-40.839	5.4
N Atl Rdge	1	28	79	19	45	21.50	22.	11.848	-43.727	5.8

Table 1.1, continued.
Locations and origin times for the 154 events used in this chapter.

the azimuthal coverage unfortunately contains several gaps between $10°-85°$, $140°-220°$, and $330°-360°$ due to uneven distribution of world seismicity. Most events were recorded by more than 50 stations and some by more than 100; a minimum of 20 stations was required for retention in the data set. Only first arrivals were picked; cross-correlation techniques were not employed in picking arrival times. All arrival times were corrected for the earth's ellipticity and, using an upper crustal velocity of 5.5 km/s, for station elevation. Teleseismic corrections for sediments and Moho depth variations are available for some network stations (Raikes, 1980) (Table 1.2), but the set is incomplete for some areas. To test the method's sensitivity to crustal structure and also to avoid any bias in spatial averaging due to incomplete corrections, the arrival times were not adjusted for any crustal structure.

A large number of overlapping subarrays are necessary to achieve optimal lateral resolution of upper mantle and crustal structure. Uniform subarray geometry is unobtainable due to the uneven station spacing. We selected subarray centers on a latitude-longitude grid and retained in each case the stations (≥ 7) located within 50 km of the designated center.

In this fashion a systematic overlapping grid of 171 subsets of the network is constructed, each containing from 7 to 23 stations in a circular area of 100-km diameter (Figure 1.7). An additional 83 subarrays with more specialized geometries were formed to refine the analysis in areas of sparse station coverage. This method of subarray selection precludes use of data from outlying stations such as ISA, GSC, and CLC that are well separated from the bulk of the network. Thus the subarray coverage does not extend to the array's extreme limits.

A significant concern pertains to the aliasing of short wavelength heterogeneities due to finite station spacing. Averaging travel times spatially over

Table 1.2

Sediment and Crustal Thickness Corrections

Station	T_{SED} s	T_{MOHO} s	Total s
CIS		-0.2	-0.2
SCI		-0.2	-0.2
ISA		-0.3	-0.3
OBB	(0.2)	-0.2	0.0
WLK	0.7	-0.2	0.5
ING	0.5	-0.2	0.3
COA	0.55	-0.2	0.35
BON	0.8	-0.2	0.6
BCK	0.65	-0.2	0.45
COK	0.65	-0.2	0.45
RUN	0.25	-0.15	0.10
SNR	0.75	-0.2	0.55
SLU	0.55	-0.2	0.35
HSP	0.75	-0.2	0.55
SGL	0.2	-0.2	0.0
PLT		-0.2	-0.2
GLA		-0.05	-0.05
SUP			-0.10
CRR			-0.05
AMS			-0.15
YMD	0.35	-0.15	0.20
LGA	0.20	-0.15	0.05
FTM		-0.10	-0.10
TCC	0.35		0.35
VPD	0.40		0.40
SJQ	0.45		0.45
SNS	0.30		0.30
TWL	0.40		0.40
CAM	0.50		0.50
SBCD	0.20		0.20
ECF	0.15		0.15
ADL	0.40		0.40

From Raikes (1980). These values are not included in the relative array analysis; they are used only in the computation of the synthetic diagrams of Figure 1.11.

SUBARRAY CENTERS
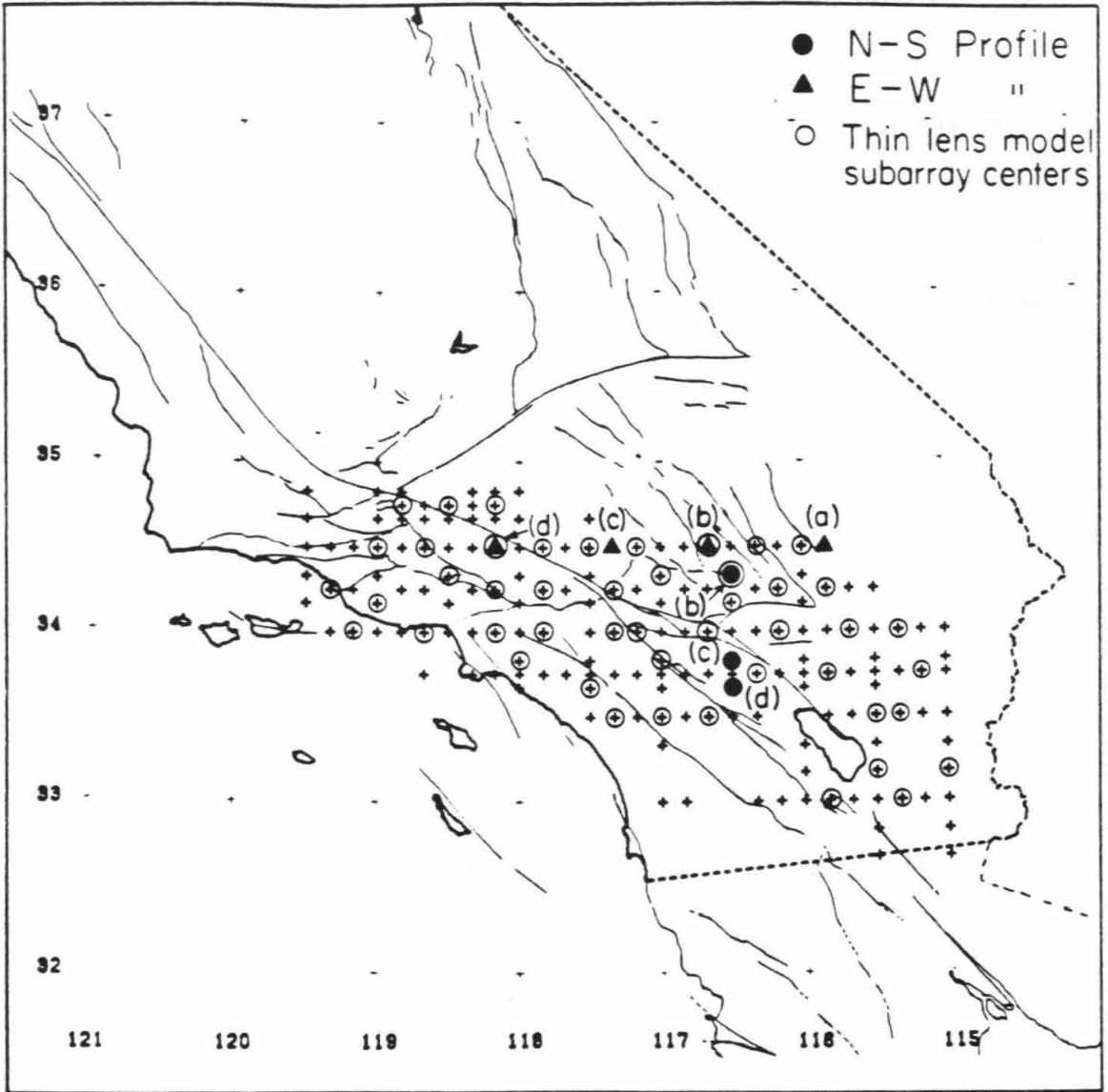
Figure 1.7 The subarray center locations for the 171 subarrays used in the analysis. Each subarray is 100 km in aperture. The circled crosses indicate subarrays used in the thin lens experiment described in the Data reduction section. Triangles and solid dots refer to diagram profiles in Figures 1.12 and 1.13.

distances of the order of 100 km does not remove aliased structural wavelengths. However, since this procedure amounts to low pass wave number filtering of lateral variations, it should minimize the difficulties associated with coarse spatial sampling. A quantitative assessment of this problem cannot be performed on the basis of our data set alone. But qualitative consistency arguments can still be proposed, based on comparisons with surface structural geology. This will be done in a later section.

Data reduction

Relative array diagrams

Inspection of relative array diagrams generated from subsets of SCARLET confirms the existence of regional lateral heterogeneities with a scale length of 200 km or less. Figure 1.8 presents two typical relative array diagrams and their subarray locations. Both the average magnitudes and the orientations of the mislocation vectors differ significantly from the whole array diagram (Figure 1.2).

Berteussen (1975, 1976) noted that mislocation vector orientations (but not necessarily magnitudes) on array diagrams for the LASA and NORSAR arrays depend critically upon array configuration and station density, even for constant aperture. He attributed dramatic shifts in arrow orientations to rapid variations in Moho depth and/or near-receiver scattering by random small-scale heterogeneities. To determine whether SCARLET is afflicted by the same problem, an array diagram was computed for the sparse 38 station network which consists of the underlined stations in Figure 1.6. The increased station separation (from ≈ 25 to ≈ 50 km) over the same aperture has little visible effect on the $dT/d\Delta$ and azimuth anomalies and the resulting array diagram is nearly identical to Figure 1.2. The station configuration changes for each

event because not all stations have useable records for every earthquake. Still, distinct coherent trends in the data are apparent for groups of events in separate source regions. We conclude that for constant aperture, SCARLET's array diagram is not dependent on specific station configuration.

We also examined the stability of selected subarrays by deleting random stations and recomputing relative array diagrams for the modified configurations. In all the tested cases the diagrams did not change significantly, indicating that the observed anomalies are probably real and not due to aliasing. Based on this remarkably stable behavior of our observations, we suggest that spatial aliasing of the kind mentioned in the previous section is not a pervasive source of difficulty.

Shallow structures. Relative array diagrams for subarrays located in the Imperial Valley, Los Angeles Basin, Ventura Basin, and San Bernardino Mountains exhibit mislocation vector patterns consistent with plane-dipping structures (see Figures 1.8a and 1.9a). Using the first-order depth classification discussed above, these areas are designated as those dominated by shallow structures. A convenient way to represent these diagrams, since the arrows do not vary with azimuth, is the mean vector. Figure 1.10 shows the mean vectors from the 34 'shallow' subarrays plotted on a map of southern California. These vectors are remarkably consistent in orientation and magnitude (many are greater than 1 s/deg.) within specific geographic areas. Striking features include the strongly north trending arrows in the Ventura Basin region, southwest pointing vectors near Los Angeles, and a synform-like orientation of vectors in the Imperial Valley. Also notable is the abrupt, nearly 180° change in arrow orientation near 33°45' -117°20' which grades into a northward trending anomaly to the east near San Bernardino.
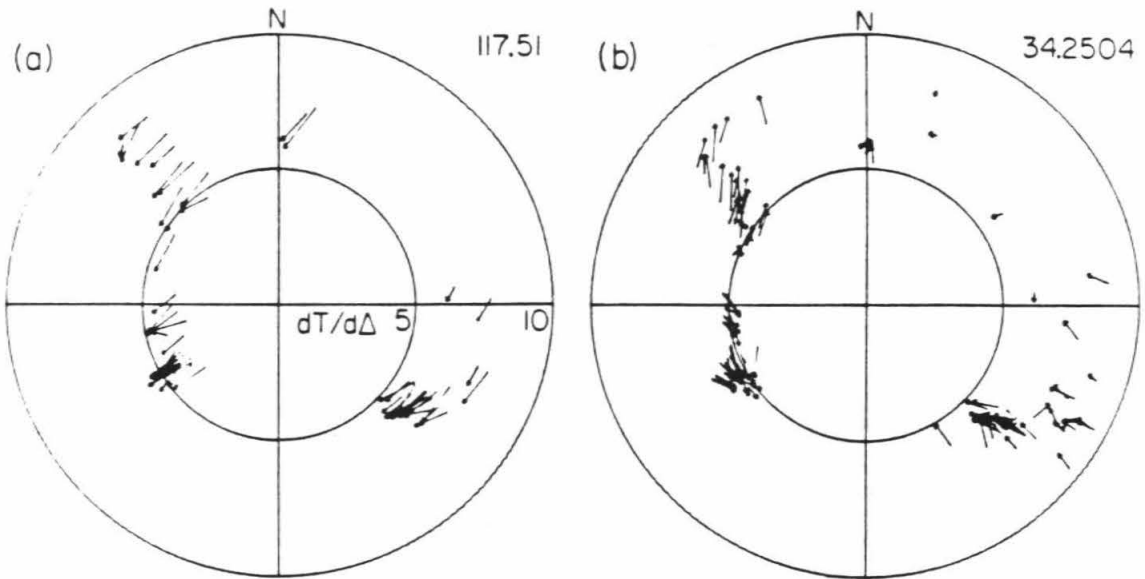
Figure 1.8 Relative array diagrams. For subarrays arranged along latitudinal lines, the label consists of the latitude in decimal degrees followed by the subarray number, counting from east to west. Subarray 34.2504, for example, is the 4th subarray from the east at 34.25°. Similarly for longitudinally arranged subarrays, the longitude is followed by the number, this time incremented from south to north. a) Subarray 117.51 is centered at (33° 40',-117° 30') and is indicative of a planar feature dipping to the southwest. b) Subarray 34.2504 (center: (34° 15',-116° 10')) shows a more complex structure. The western half senses an east-west trending antiform, while the southeast quadrant responds to a different velocity anomaly, slow to the west-northwest.
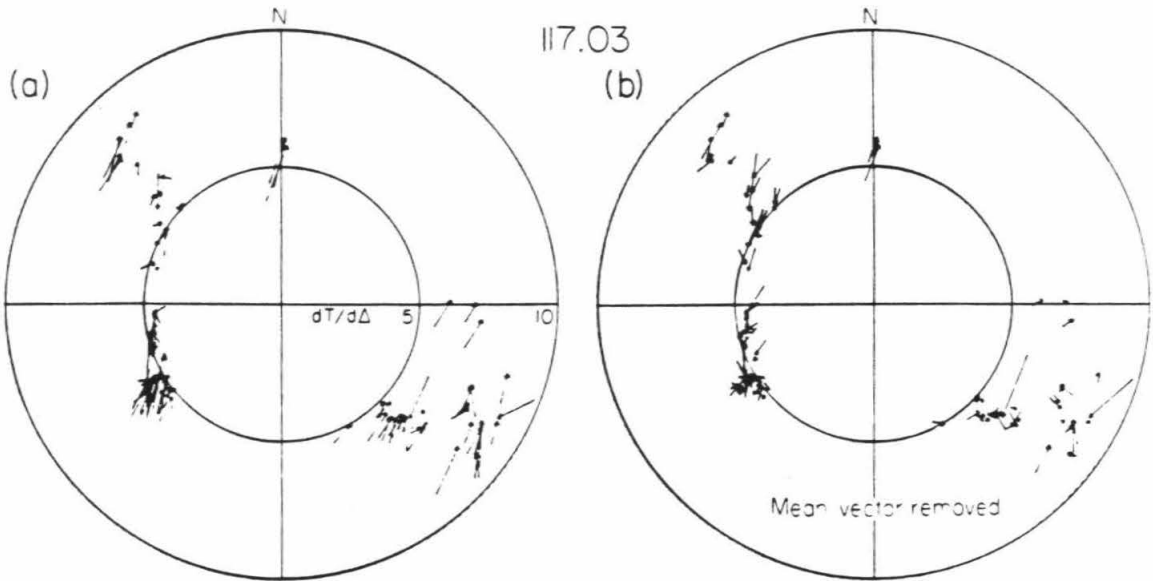
Figure 1.9 Subarray 117.03's relative array diagram. Centered at (33°50',-117°00'), this diagram is typical of the shallow San Bernardino Mountains anomaly. b) Same diagram with the mean vector removed. Note the northwest quadrant resembles a type 'B' diagram of Figure 1.12a. This is consistent with the hypothesized east-west trending antiform.

MEAN VECTORS FOR SHALLOW STRUCTURES
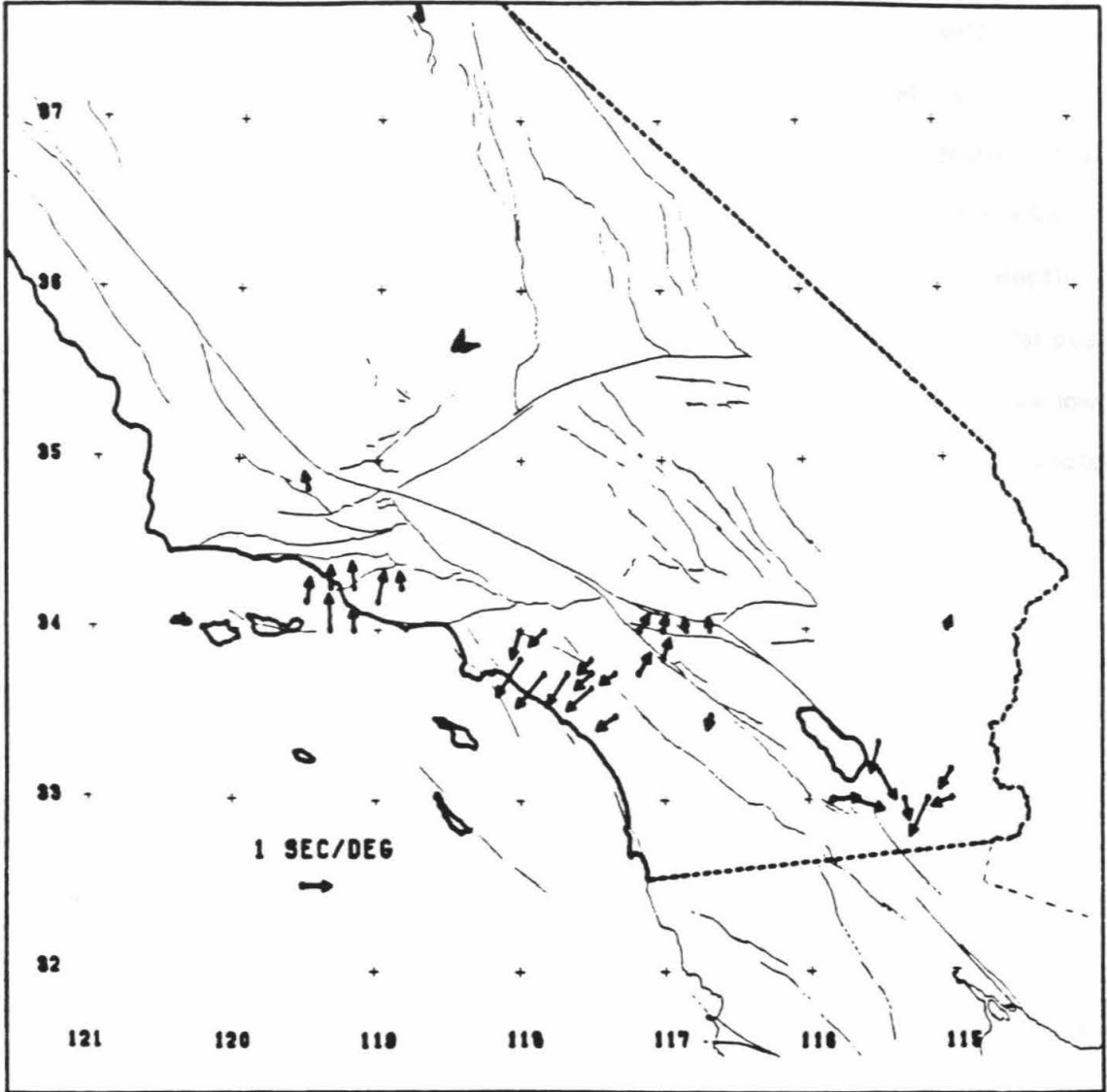
Figure 1.10 Mean vectors for the 34 'shallow' subarrays plotted on a map of southern California. The arrow tails are plotted at the subarray centers. See text for further discussion.

Except for the San Bernardino Mountains, these areas all contain young, thick piles of unconsolidated sediments in the upper crust. The Los Angeles Basin, a complex structural depression, reaches a depth of 9750 m (Yerkes et al., 1965). Bailey and Jahns (1954) estimate over 15,000 m of sediments in the axial portion of the Ventura Basin, with approximately 1500 m of Pleistocene deposits. Biehler et al. (1964) find 6400 m of unconsolidated sediments in the deepest portion of the Salton Trough; in another, more recent study, Fuis et al. (1982) determine the depth of slow-velocity sediments to be 4800 m. The P arrival data are not corrected for possible delays due to sediments; therefore it is likely that the presence of these low-velocity materials is at least partly responsible for the observed mislocation vector patterns in these three regions.

Utilizing Raikes' (1980) teleseismic P wave crustal corrections (Table 1.2) for some southern California stations, we computed synthetic diagrams for selected subarrays in the sediment-basin areas (Figure 1.11, see Figure 1.6 for location). The synthetics represent effects due solely to near-surface sediments and Moho depth variations. Figure 1.11 demonstrates that for subarrays in these three regions, observed mislocation vector orientations and, to a lesser extent, magnitudes are well matched by the synthetic diagrams. The general agreement implies that the dT/dΔ and azimuth anomalies for these areas are explicable in terms of known, shallow, sediment-related structures.

A similar explanation of the San Bernardino anomaly is unacceptable. There is little evidence for deep sediments in this area; Raikes (1978) did suggest 0.3-s delays be applied to nearby stations CKC, MLL and CFT, but synthetics generated with those corrections did not produce mislocation vector patterns even remotely similar to those observed. Three possible causes for the anomaly may be invoked.
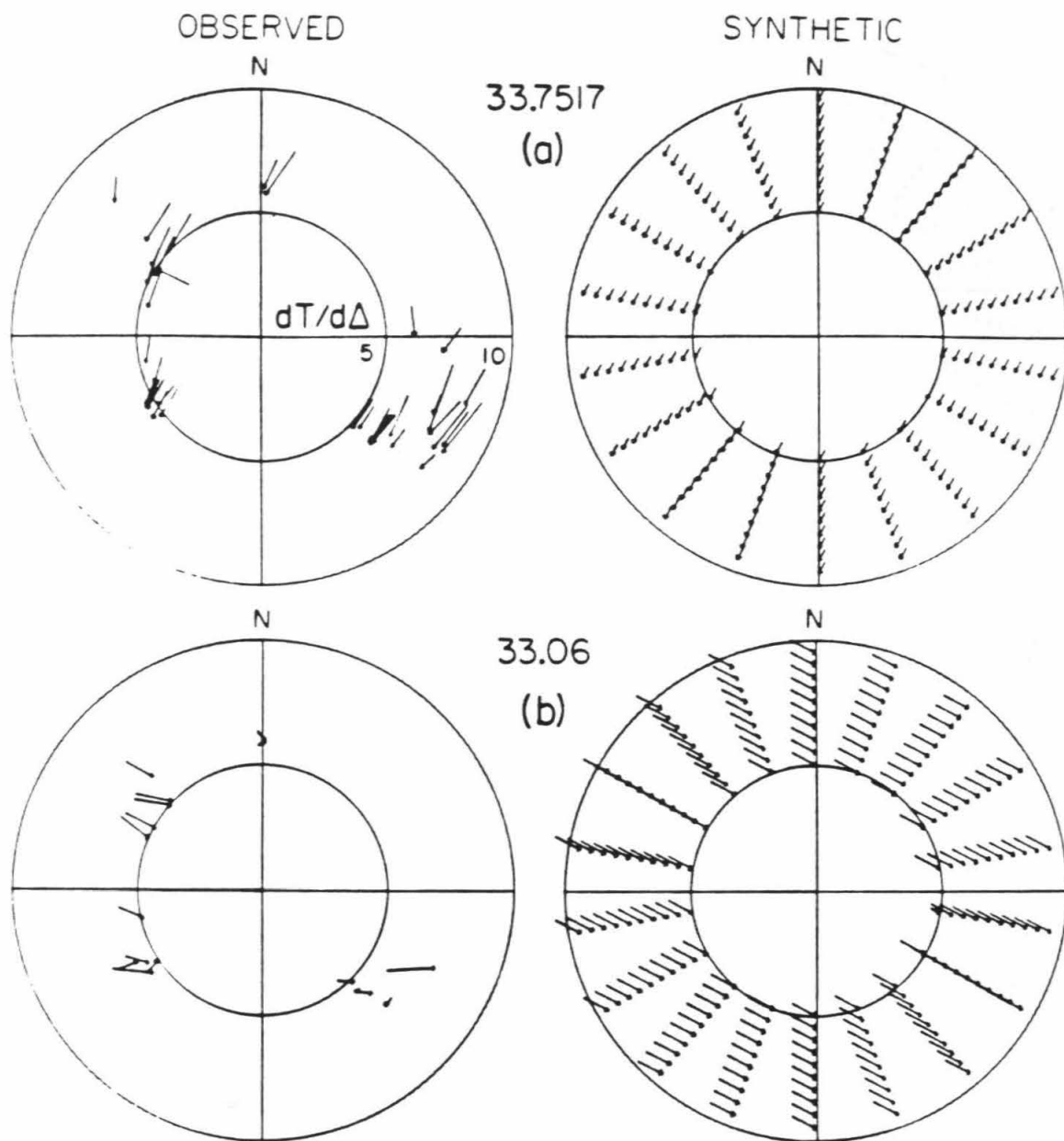
Figure 1.11 Comparison of observed relative array diagrams and synthetic array diagrams simulating sediment-related shallow structure. a) Subarray 33.7517. b) Subarray 33.06. c) Subarray 34.027. d) Subarray 115.03. These synthetic diagrams are computed by including Raikes' (1980) sediment and crustal thickness corrections. Note how in each case the orientation of the mislocation vectors is correct, while the synthetics tend to underestimate the vector magnitude.
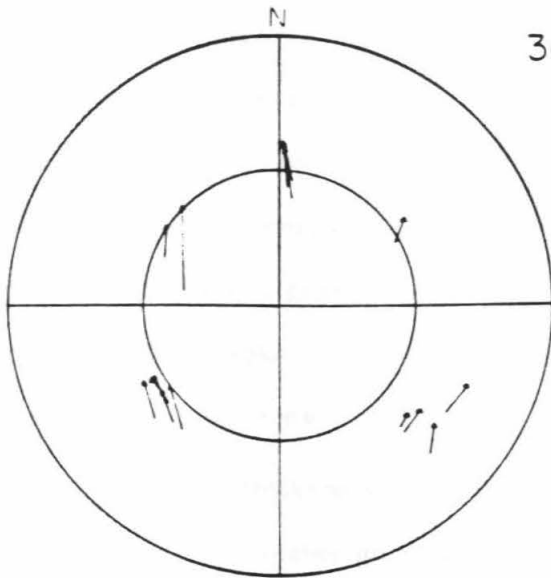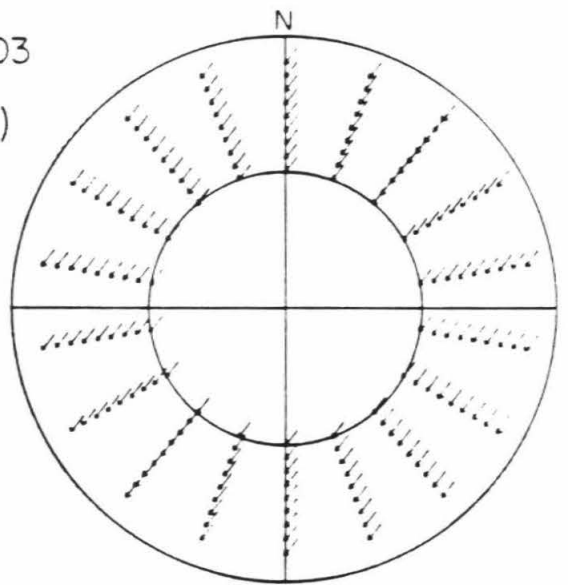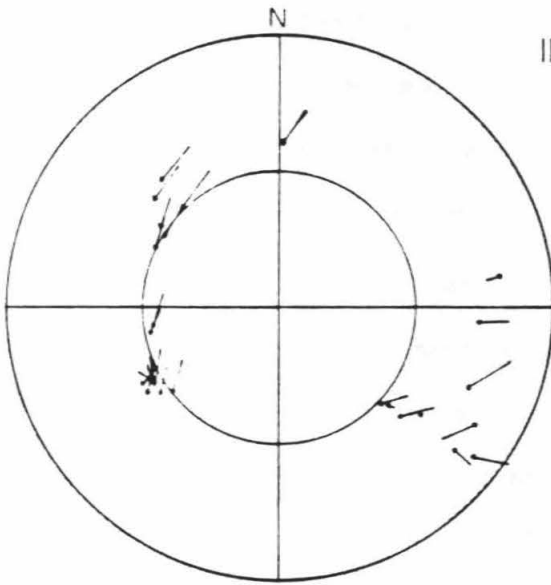
34.027

(c)
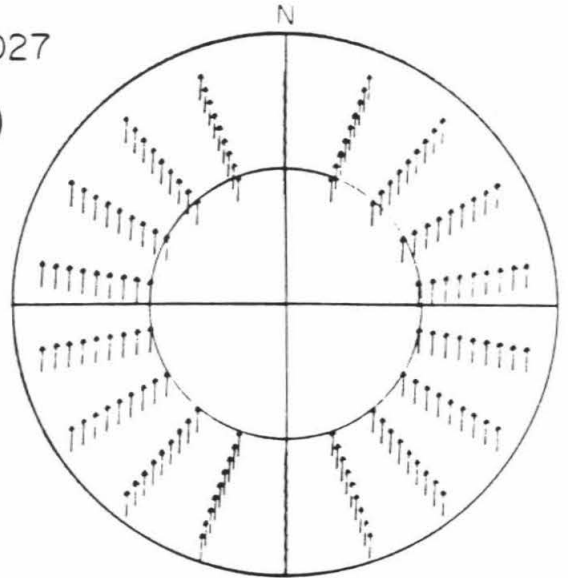
115.03

(d)

1. A sharp crustal velocity change across the San Andreas fault could occur in this region. A slower velocity in the northeastern portion of the six subarrays would generate the correct arrow orientation. However, Kanamori and Hadley (1975) find a remarkably uniform crustal velocity of 6.3 km/s for all of southern California. A transition of dominant crustal velocity from 6.2 km/s in the north to 6.7 km/s south of the Transverse Ranges postulated by Hadley and Kanamori (1977); the exact position of the transition region is not well known, but it may contribute to the observed $dT/d\Delta$ and azimuth anomalies.

2. Crustal thickening beneath the San Bernardino Mountains could also explain the data. While Hadley and Kanamori (1977) find no evidence for a crustal root in the area, recent studies by Oliver (1982) utilizing gravity data and Lamanuzzi (1981) using Pn travel time residuals both suggest a small, 3- to 8-km root beneath the eastern Transverse Ranges. It is unlikely, however, that such a small feature would cause the large observed anomalies on the relative array diagrams.

3. A local high-velocity anomaly at 40 km depth is yet another possibility. Record sections from two magnitude 4.5 earthquakes which occurred within the Transverse Ranges led Hadley and Kanamori (1977) to suggest that an area of 8.3 km/s velocity exists in this region at 40 km. Because the early arrivals associated with the feature were not observed for the August, 1978 Santa Barbara earthquake (Lamanuzzi, 1981) and because normal observations of this velocity occur in a restricted distance and azimuth range, the high-velocity body may be present at this depth only in a very small lateral area (H. Kanamori, personal communication, 1981). Additionally, Raikes' (1980) upper mantle model derived from ray tracing and teleseismic residual data determines the depth to high-velocity material in this area to be less than 50 km but only near the intersections of the San Andreas and San Jacinto

faults. Such a structure, small laterally but with a high-velocity contrast, could explain the mislocation vector data.

Deeper structures. Relative array diagrams for the remainder of the network (e.g., Figure 1.8b) have patterns which change abruptly with azimuth, implying a 'transparent' crust and uppermost mantle with substantial lateral heterogeneities located deep (50 < D < 200 km) beneath the surface. Inspection of more than 100 such diagrams reveals systematic shifts in mislocation vector patterns with position that are consistent with an east-west trending antiform located in the upper mantle under the Transverse Ranges and western Mojave Desert. Figure 1.12a illustrates the changes expected in the vectors for a sliding window of overlapping subarrays moving from north to south over such a structure (see Figure 1.7 for subarray locations). Figures 1.12b, 1.12c, and 1.12d are an example of the data in a similar profile.

Subarray 116.54 (Figure 1.12b) is located near the east end of the antiform. While waves approaching from the northwest and southwest cross the structure, rays from South American events (southeast azimuth) 'see' a different velocity anomaly; the arrows tend to point northwest, indicating low velocity at depth beneath the Salton Trough (this is better illustrated in Figure 1.8b). Moving south over the antiform, we expect the northwest quadrants' mislocation vectors to shift in orientation from north to south, as is confirmed in subarrays 116.52 and 116.51. Arrows in the southwest quadrants change to a west-northwest direction in these diagrams, more consistent with the corresponding southeast quadrants which sample velocities deep beneath the Imperial Valley. By latitude 33° 40' (subarray 116.51), rays incoming from the southwest do not intersect the antiform.
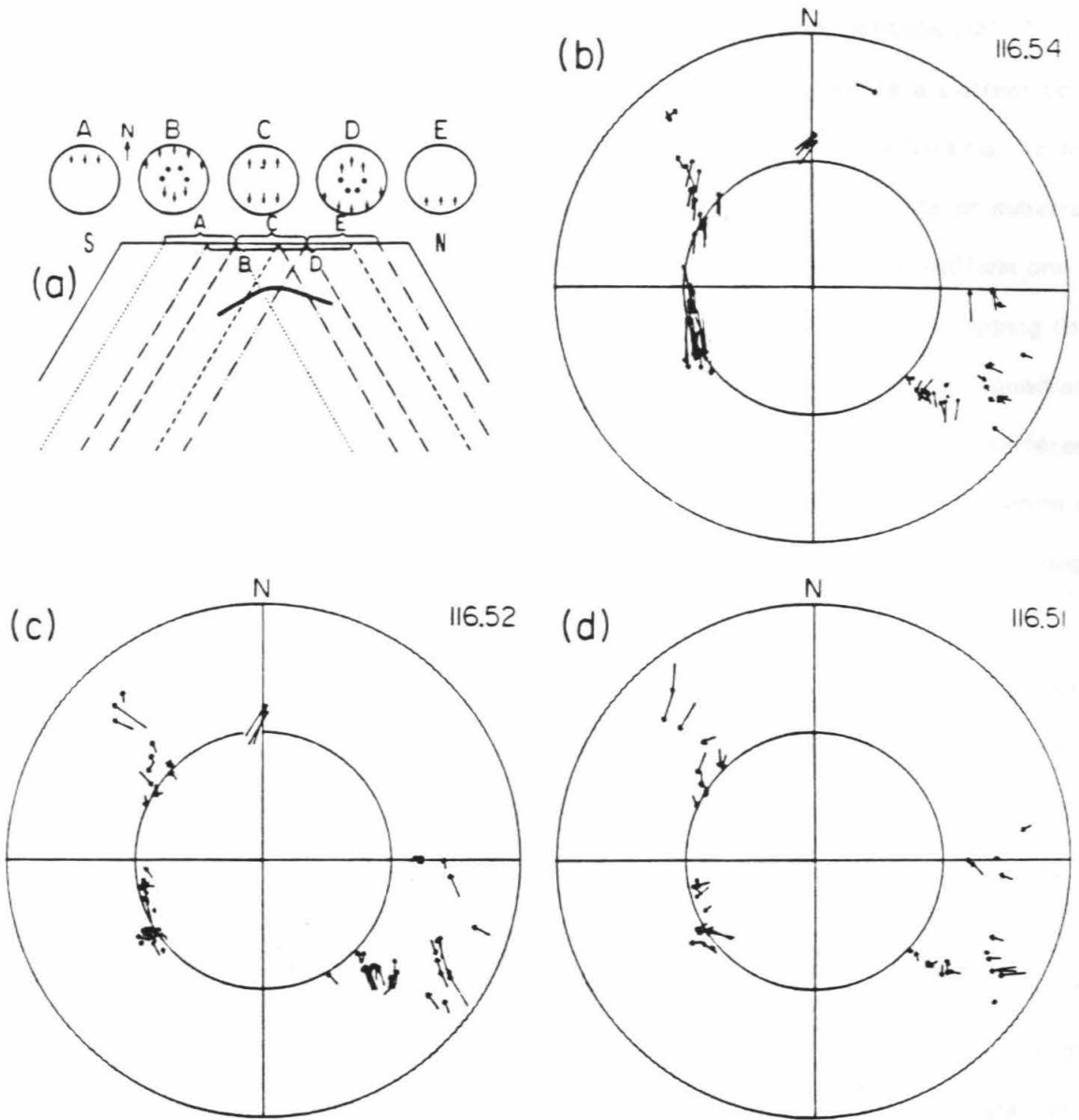
Figure 1.12 a) Schematic view of a north-south profile of relative array diagrams above an east-west trending antiform. Dots in diagrams represent small magnitude vectors. b,c,d) Data profile from north to south. See text for discussion, Figure 1.7 for location.

Diagrams from subarrays in east-west profiles place constraints on the antiform's longitudinal extent. Four of the 21 subarrays along latitude 34° 30' are illustrated in Figure 1.13. Subarray 34.506 (Figure 1.13b) exhibits a pattern consistent with subarray location entirely over the antiform and virtually on-axis. To the east, however, the vectors in the northwest and southwest quadrants of subarray 34.501 (Figure 1.13a) have rotated eastward, inconsistent with the antiform orientation pattern. Farther west, for subarray 34.515 the antiforms' south dipping limb has moved to the southeast quadrant. The northwest and southwest quadrant arrows all point to the north, indicating that arrivals from the west sense a different structure. Subarrays located even farther west than 34.515 show no evidence of the antiform pattern, implying that the western edge is probably near 119° W longitude.

By assuming a mean depth of 100 km, we estimate the antiform's longitudinal bounds to be 118° 30'-119° 00'W (west) and 115° 30'-116° 00'W (east). The latitudinal extent is more difficult to delineate due to the spatial limits of the array. A comparison of Figures 1.12a and 1.12b demonstrates that the north dipping limb of the proposed antiform extends farther north than the available densely spaced stations, so the exact northern boundary is unknown. Similarly, poor data quality in the Imperial Valley area coupled with large station spacing in the Peninsular Ranges region makes the antiform's southern range difficult to identify. But the character of the relative array diagrams at latitudes lower than 33° 45' is consistent when compared to Figure 1.12a with a southern limit of 33° 15'.

In several areas where the antiform should be visible on relative array diagrams, it is masked by shallower velocity perturbations (Figure 1.10). Removal of the mean vector from these diagrams should disclose the same anomaly. An example is given in
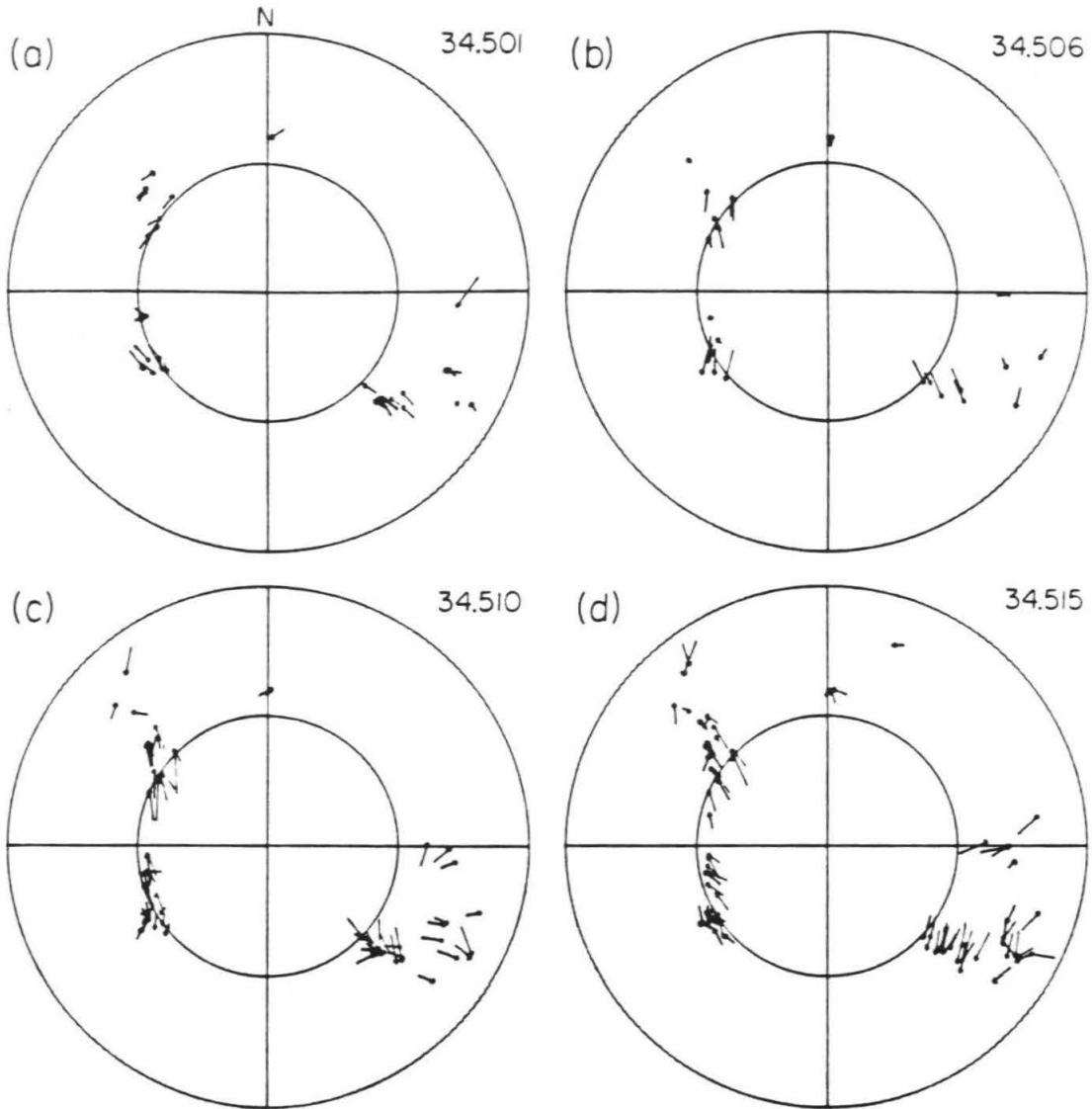
Figure 1.13 a,b,c,d) Profile from east to west (for location, see Figure 1.7). The data are discussed in the text.

Figure 1.9b for a subarray located in the San Bernardino Mountains. Upon removal of the slowly varying component, the northwest quadrant is similar to a type 'B' diagram of Figure 1.12a, while the southern quadrants appear to be random. This is consistent with a subarray position over the southern limb of the antiform; rays incident from the south do not intersect the structure and therefore show no strong trend in mislocations.

Thus nearly all of the generated relative array diagrams are useful in mapping the antiform. Figure 1.14 shows the spatial distribution of the main classes of diagrams which define the structure. We consider the consistency of the data as strong evidence for the existence of this east-west striking high-velocity anomaly. Using the Hadley and Kanamori (1977) contrast of 7.8/8.3 km/s for their high-velocity ridge, we can model the observed mislocation vector sizes, by three-dimensional ray tracing, to determine the dip of the antiform limbs. A range of $20°$ to $25°$, depending on the assumed depth, matches the arrow magnitudes and also is in general agreement with the configuration of their anomaly.

It is possible to give a crude estimate of the antiform's depth using the areal distribution of the structure-limiting subarrays (e.g., 116.51): considering each of the limbs separately as a dipping interface, we can calculate its total north-south extent for different mean depths. Constraining these limbs to join at an axis then yields a gross estimate of depth. An axial depth of 100 km at a latitude $34°15' \pm 15'$ is most consistent with our observations. An axis as shallow as 50 km is incompatible with this data set.

Time term crustal corrections. One quantitative way to correct for crustal variations in southern California is to apply the time term corrections of Hearn (1983)
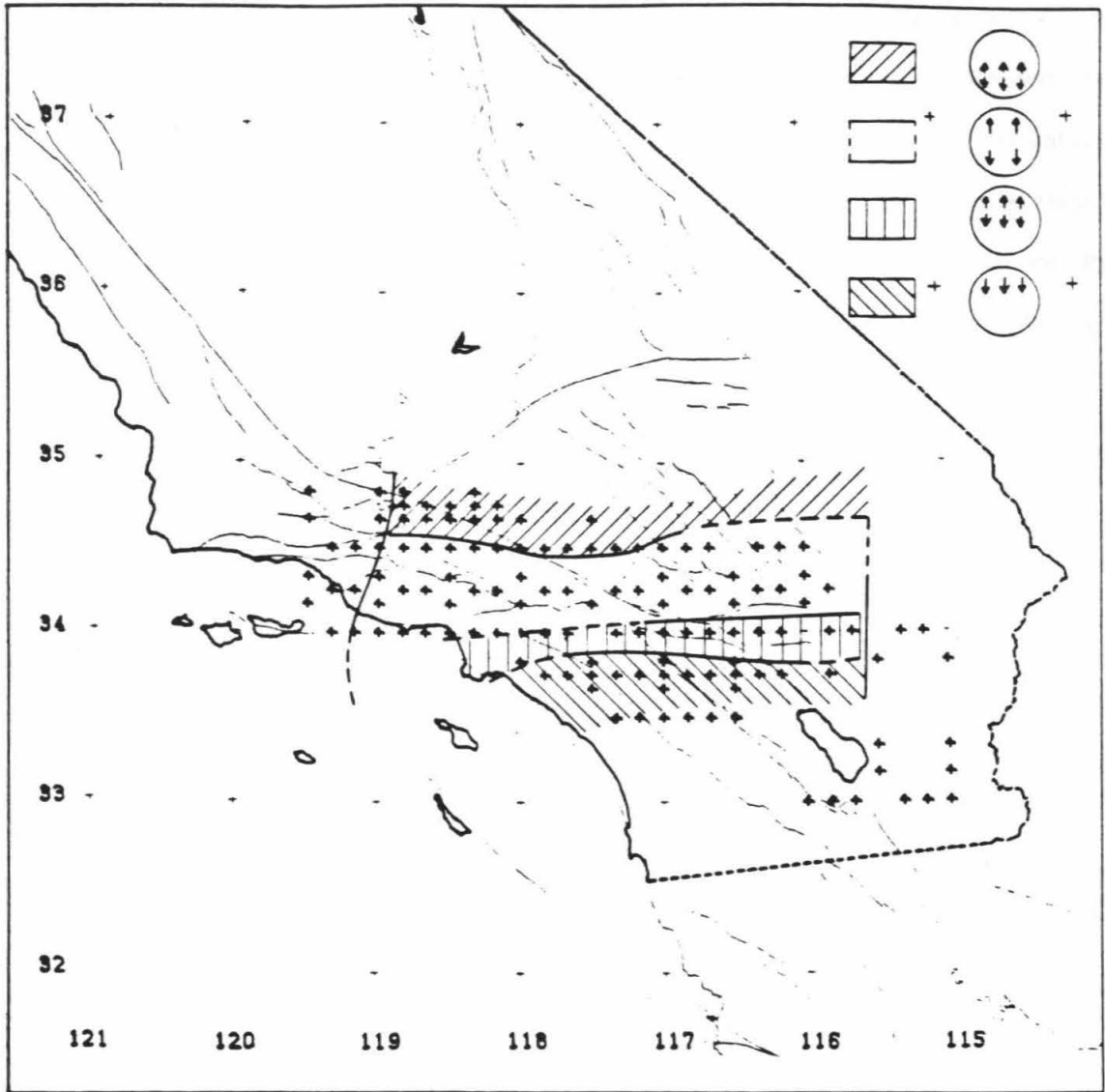
Figure 1.14 Map of the relative array diagram types observed for nearly 100 subarrays. Crosses are subarray centers. These diagrams clearly indicate a deep, east-west striking antiform in the upper mantle beneath the Transverse Ranges and Mojave Desert. Note there are subarrays at both the east and west ends that do not 'see' the structure, thus it is confined to a very limited area.

to the teleseismic travel times. He used over 2800 Pn travel times to determine variations in crustal thickness and Pn velocity on a regional scale, using a variant of the time term method (Scheidegger and Willmore, 1957; Willmore and Bancroft, 1960). Figure 1.15 is a map showing the time terms for a model with an average Pn velocity of 8.0 km/s (T. Hearn, personal communication, 1981). Table 1.3 lists the values contained in the contour map. These values are representative of both crustal thickness differences and shallow velocity variations, and are appropriate for Pn incidence angles. To apply them to teleseismic data, we must first correct the time terms for the steeper teleseismic incidence angles.

In Figure 1.16, the Pn time term represents the difference between the two illustrated Pn travel paths:

$$t_c = \frac{h \cos \theta_c}{v_c} \tag{1.8}$$

Here t_c is the Pn time term, h is the thickness of the Moho depth variation, and $\theta_c = \sin^{-1}(\frac{V_c}{V_m})$. In this treatment, the crustal velocity, V_c, is constant and only h is varied. For teleseisms, the difference in time between the path drawn and one where the crust is thinned by h is

$$t_t = h \cos \frac{\theta_{tc}}{v_c} - h \cos \frac{\theta_{tm}}{v_m} \tag{1.9}$$

Here t_t is the teleseismic time term, the teleseismic incidence angle in the crust is θ_{tc}, and θ_{tm} is the teleseismic incidence angle in the uppermost mantle. Taking the ratio of equations 1.8 and 1.9, we obtain

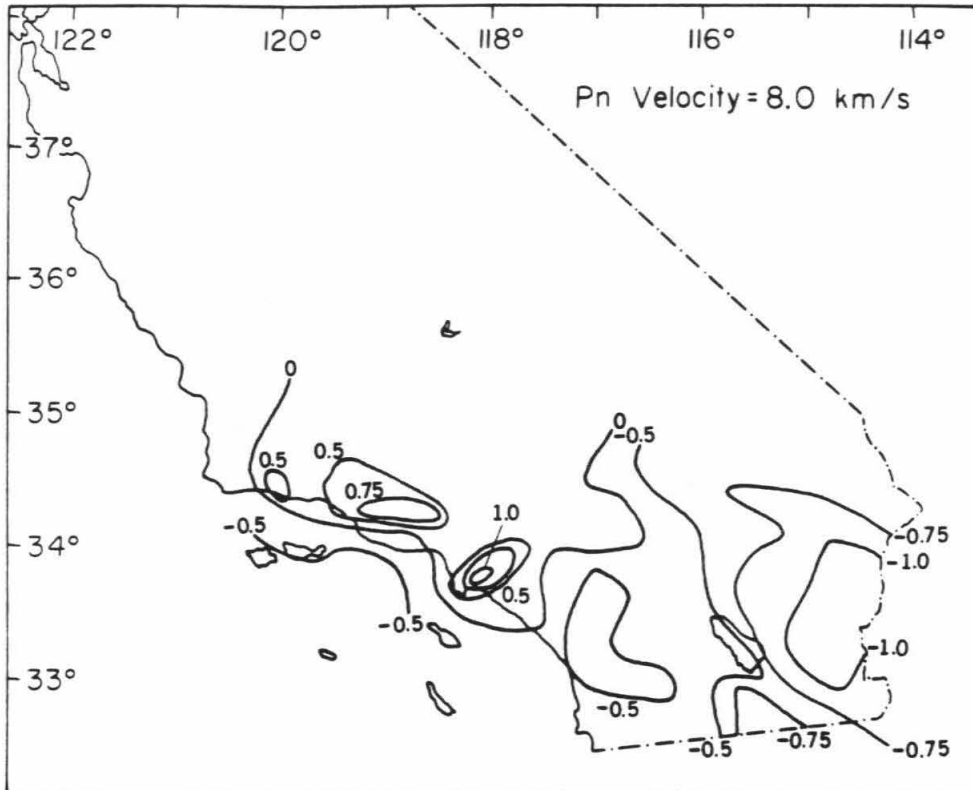$$t_t = t_c \frac{\cos \theta_{tc} - \frac{v_c}{v_m} \cos \theta_{tm}}{\cos \theta_c} \tag{1.10}$$

Figure 1.15 Contour map of time terms (T. Hearn, personal communication, 1981) used in calculating array diagrams corrected for crustal structure. The contour interval is 0.25 s.

Table 1.3

Time Term Corrections

Sta.	Lat.	Lon.	Corr., s	Sta.	Lat.	Lon.	Corr., s
ABL	34.8508	-119.2208	0.081	ADL	34.5563	-117.4170	0.587
AMS	33.1413	-115.2542	-1.037	BAR	32.6800	-116.6717	0.047
BCH	35.1850	-120.0842	-0.212	BC2	33.6570	-115.4612	-0.613
BLU	34.4067	-117.7268	0.150	BMT	35.1358	-118.5968	-0.174
BON	32.6945	-115.2685	-0.339	BSC	32.7248	-115.0440	-0.966
BTL	34.2572	-117.0048	0.456	CAM	34.2545	-119.0333	1.719
CFL	34.3328	-118.0230	-0.058	CFT	34.0352	-117.1110	0.224
CH2	33.2962	-115.3362	-1.004	CIS	33.4067	-118.4033	-0.492
CKC	34.1363	-117.1747	0.116	CLC	35.8167	-117.5967	-0.080
CLI	33.1408	-115.5273	-0.007	CMH	34.5530	-114.5720	-0.225
COA	32.8635	-115.1227	-0.865	COK	32.8492	-115.7268	-0.405
COQ	33.8605	-117.5097	0.086	COT	33.3048	-115.3533	-1.610
COY	33.3605	-116.3093	-0.609	CO2	33.8472	-115.3447	-0.612
CPE	32.8800	-117.1000	-0.143	CPM	34.1540	-116.1967	-0.203
CRG	35.2422	-119.7233	0.126	CRR	32.8863	-115.9683	-0.547
CSP	34.2978	-117.3555	0.526	CTW	33.6797	-115.8718	-0.528
DB2	33.7350	-117.0620	-0.438	DHS	33.9263	-116.3855	0.224
ECF	34.4580	-119.0907	0.965	ELR	33.1473	-115.8325	-0.291
FMA	33.7125	-118.2853	0.773	FNK	33.3830	-115.6377	-0.843
FTC	34.8708	-118.8918	0.183	GAV	34.0225	-117.5123	-0.144
GLA	33.0517	-114.8267	-0.783	GRP	34.8043	-115.6045	-0.559
GSC	35.3017	-116.8050	-0.176	HDG	34.4288	-116.3050	-0.406
HOT	33.3140	-116.5815	-0.084	IKP	32.6488	-116.1080	-0.106
ING	32.9883	-115.3102	3.030	INS	33.9357	-116.1943	-0.222
IRC	34.3900	-118.4000	0.086	IRN	34.1600	-115.1840	-0.727
ISA	35.6633	-118.4733	0.069	JNH	34.4475	-117.9545	0.019
JUL	33.0483	-116.6128	-0.208	KEE	33.6383	-116.6532	-0.265
KYP	34.1018	-118.8795	-0.120	LCL	33.8333	-118.1925	1.995
LED	34.4677	-115.9365	-0.610	LHU	34.6717	-118.4117	-0.015
LJB	34.5910	-117.8480	0.372	LRR	34.5260	-118.0277	0.367
LTC	33.4890	-115.0700	-1.103	LTM	33.9150	-114.9183	-1.211
MDA	33.9130	-116.9995	0.028	MLL	34.0913	-116.9363	0.094
MOV	34.1558	-116.5017	0.246	MWC	34.2233	-118.0583	0.188
NW2	33.0905	-115.6923	-0.388	PAS	34.1492	-118.1715	0.427
PCF	34.0532	-117.7907	0.589	PEC	33.8918	-117.1600	-0.117
PEM	34.1673	-117.8697	0.451	PKM	34.8958	-119.8188	0.153
PLM	33.3533	-116.8617	-0.152	PLT	32.7312	-114.7293	-1.010
PNM	33.9773	-115.8008	-0.540	POB	33.6867	-116.9233	-0.304
PSP	33.7938	-116.5488	-0.202	PTD	34.0042	-118.8063	0.086
PYR	34.5680	-118.7417	-0.072	RAY	34.0363	-116.8112	0.047
RDM	34.4000	-117.1850	0.180	RMR	34.2128	-116.5753	-0.009
ROD	34.6297	-116.6048	-0.466	RUN	32.9722	-114.9772	-0.903
RVM	34.1802	-114.2003	-0.689	RVR	33.9933	-117.3750	-0.206

Sta.	Lat.	Lon.	Corr., s	Sta.	Lat.	Lon.	Corr., s
RVS	34.0347	-114.5180	-0.627	RYS	34.6433	-119.3517	0.749
SAD	34.0810	-118.6650	0.097	SBAI	34.0133	-119.4372	-0.371
SBB	34.6883	-117.8250	0.120	SBCC	34.9397	-120.1720	0.184
SBCD	34.3687	-119.3438	0.852	SBLC	34.4965	-119.7135	0.293
SBLG	34.1145	-119.0642	-0.242	SBLP	34.5595	-120.4003	-0.343
SBSC	33.9947	-119.6332	-0.349	SBSM	34.0373	-120.3502	-0.707
SBSN	33.2447	-119.5063	-0.381	SCI	32.9800	-118.5467	-0.226
SCY	34.1062	-118.4542	0.060	SDW	34.6092	-117.0742	-0.197
SGL	32.6492	-115.7253	-0.788	SHH	34.1877	-115.6545	-0.397
SIL	34.3478	-116.8267	0.286	SIP	34.2040	-118.7990	0.111
SME	33.8227	-117.3553	-0.354	SMO	33.5358	-116.4617	-0.240
SNS	33.4317	-117.5483	0.141	SPM	34.4720	-115.4027	-0.705
SSK	34.2162	-117.6887	0.451	SS2	34.2077	-117.4997	0.082
SUP	32.9552	-115.8238	-0.890	SWM	34.7167	-118.5833	-0.758
SYP	34.5272	-119.9778	1.693	TCC	33.9945	-118.0128	0.332
TMB	35.0873	-119.5347	0.351	TPC	34.1058	-116.0487	-0.422
TPO	34.8788	-118.2277	-0.013	TTM	34.3353	-114.8275	-0.516
TWL	34.2783	-118.5945	1.041	VG2	33.8318	-116.8092	-0.011
VPD	33.8150	-117.7617	0.318	VST	33.1567	-117.2317	-0.535
WH2	34.3145	-114.4092	-0.372	WIS	33.2760	-115.5930	-0.915
WLK	33.0513	-115.4907	-0.501	WML	33.0152	-115.6225	-0.437
WWR	33.9918	-116.6560	0.033	YEG	35.4363	-119.9593	-0.029
YMD	32.5547	-114.5447	-0.970	RCH	34.3073	-116.3505	-0.454
FLS	34.9700	-117.0400	0.493	JFS	35.3500	-117.6700	0.551

Table 1.3, continued.
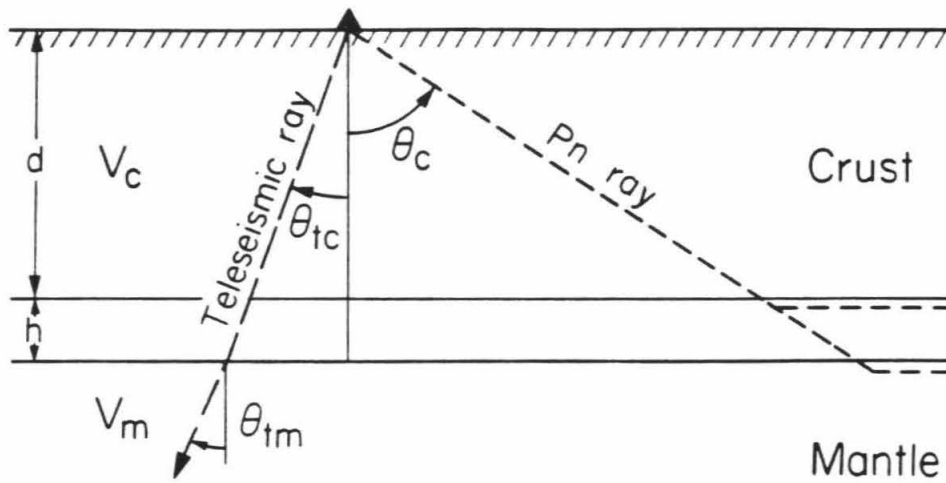
Figure 1.16 Schematic drawing of Pn and teleseismic rays incident at a station under which the Moho depth varies from d to $d + h$. Two Pn rays and one teleseismic ray are shown. See text for details of conversion from the Pn time term to the teleseismic equivalent.

We use v_c = 6.7 km/s and v_m = 8.0 km/s, so θ_c = 56.9°. Using (1.10), a teleseismic time term is calculated for each station and for each event. The incidence angles are computed with the whole-array ray parameter estimate and an assumed 30 km crust. The Pn time terms are also not corrected for elevation and the teleseismic times are, so the Pn elevation contribution, δt_{Pnel}, is removed:

$$\delta t_{Pnel} = \frac{e \, \cos \, \theta_c}{v_{uc}} \tag{1.11}$$

where v_{uc} is the upper crustal velocity of 5.5 km/s, and e is the station elevation in km.

We tested the effect of the teleseismic time terms on array diagrams for several subarrays; locations discussed below are indicated in Figure 1.17. Some subarrays, such as the one used by Vetter and Minster (1981) in their anisotropy study, show little change due to the crustal corrections (Figures 1.18a, b). This is not surprising, since this subarray is located above a postulated deep anomaly, the Transverse Ranges antiform. Additionally, the time terms have little effect on diagrams of Mojave Desert subarrays such as 116.06 (Figures 1.18c, d), consistent with the transparent crustal structure in that region.

Three subarrays located in sediment-dominated areas, however, are heavily affected by the removal of the time terms. Subarrays 33.05 and 115.03 (Figure 1.19) exhibit marked alterations in mislocation vector orientation, substantiating the claim that shallow structure is masking any deeper anomalies in the Imperial Valley. For the Ventura Basin, the time-term corrected vectors of subarray 119.01 look very similar to both 119.01 with the mean vector removed and the uncorrected nearby subarray 118.51 (Figure 1.20). This indicates that the Ventura Basin sediments,

Figure 1.17 Map of SCARLET with the five subarrays used as examples in the time term experiments. Subarrays 115.03 (#5) and 33.05 (#4) are in the Imperial Valley area, 119.01 (#1) covers the Ventura Basin, 116.06 (#3) is in the Mojave Desert, and the larger subnetwork (#2) was used by Vetter and Minster (1981) in a study of Pn anisotropy in southern California.
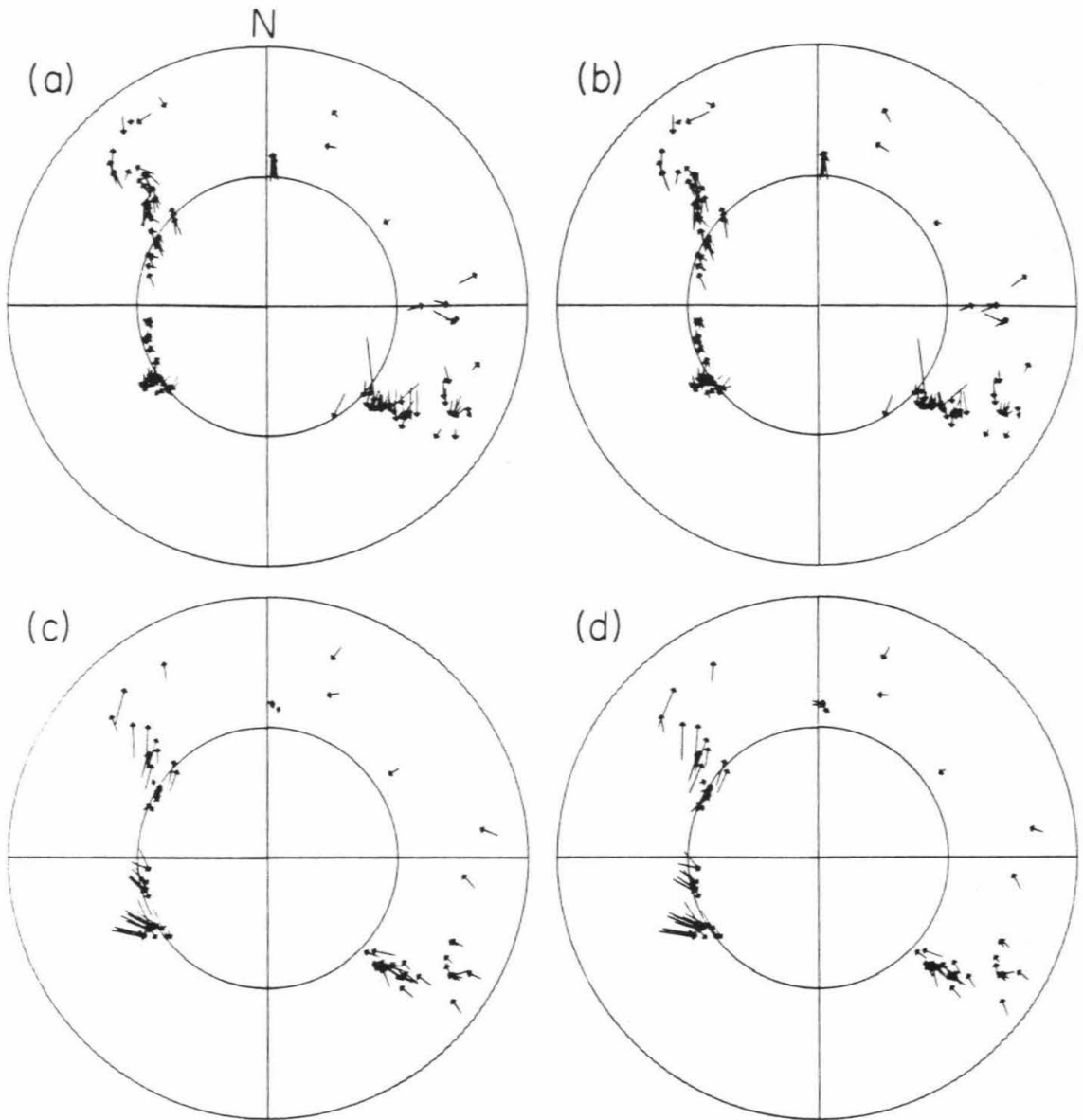
Figure 1.18 Array diagrams for subarrays unaffected by the addition of time terms (see Figure 1.17 for locations). a) The Vetter and Minster (1981) subarray with no corrections. b) With time term corrections. Note that the two diagrams are very similar, indicating that the structure causing the observed anomalies is deeper than the base of the crust. c) Subarray 116.06's diagram with no corrections. d) Same subarray with time term corrections.
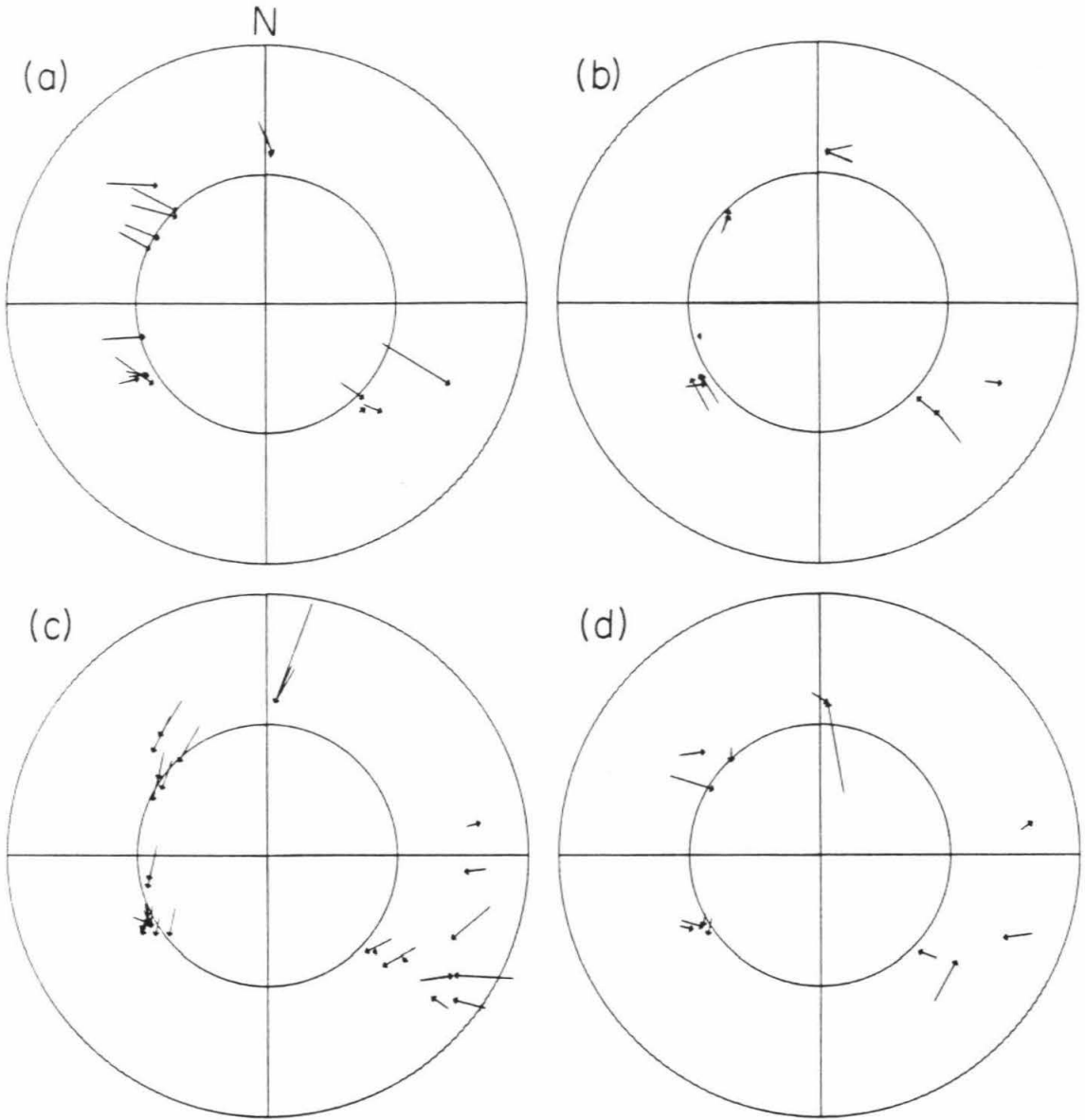
Figure 1.19 Diagrams for subarrays 33.05 and 115.03. a) 33.05 with no correc-
tions. These vectors show a shallow structure dipping to the southeast. b) 33.05
corrected with time terms. Now most of the vectors point to the north or northwest,
consistent with a deep slow anomaly beneath the Imperial Valley. c) 115.03 without
corrections. Most vectors point southwest. d) 115.03 after time terms. This
diagram has randomly oriented mislocation vectors.
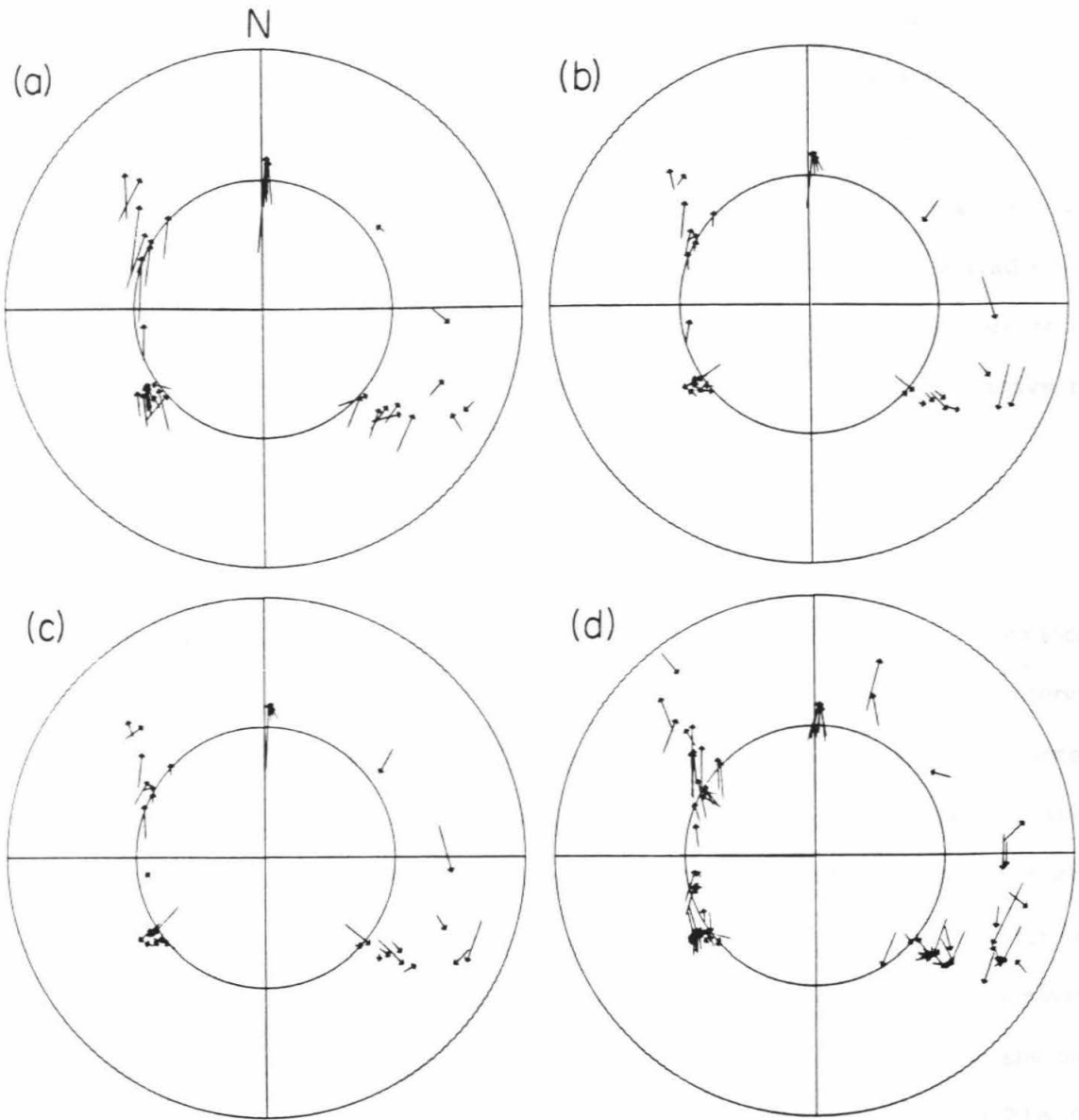
Figure 1.20 Array diagrams from the Ventura Basin area. a) Subarray 119.01 with no corrections. Note the indication of a north-dipping structure. b) 119.01 after time term corrections. Vectors in the southwest and southeast quadrants have changed orientation significantly. c) 119.01 without corrections, but with the mean vector removed. Note the similarity to (b). d) subarray 118.51 (center: 34°00',-118°30') with no corrections. It looks very much like (b) and (c).

which do not influence 118.51, are effectively removed by both the mean vector and by application of the time terms. The southeast quadrants of Figures 1.20b, 1.20c, and 1.20d now show the south-dipping limb of the Transverse Ranges anticline.

These results indicate that Hearn's (1983) time terms are representative crustal corrections and that such corrections are unimportant for subarays located away from large sedimentary basins. The addition of time terms into the relative array analysis does not change our view of the high-velocity body beneath the Transverse Ranges.

Net subarray delays

While relative array diagrams compare mean wave front orientations across local subarray and across the entire network, the net delay measures the time interval between the arrival of the local and whole array plane waves at the subarray center. It thus represents a net advance or delay integrated over the entire ray tube subtended by the subarray in the upper mantle and crust. Since sediment corrections are not applied, we cannot discriminate between shallow and deep sources for net delays, but might reasonably expect that if low-velocity shallow structures dominate a given subarray, the net delays would all be positive for the entire azimuth and distance range. The net delays plotted in Figures 1.21a, 1.21b, 1.21c, and 1.21e, for representative subnetworks in the Imperial Valley, Ventura Basin, San Bernardino Mountains, and Los Angeles Basin, respectively, demonstrate a distinct azimuthal variation in net delay sign and magnitude. For example, subarray 34.026 (Figure 1.21b) yields mainly negative net delays instead of the positive values expected if slow, shallow structure is dominant. For subarray 117.03 (Figure 1.21c), southeastern events arrive late relative to the array, while events from the north,
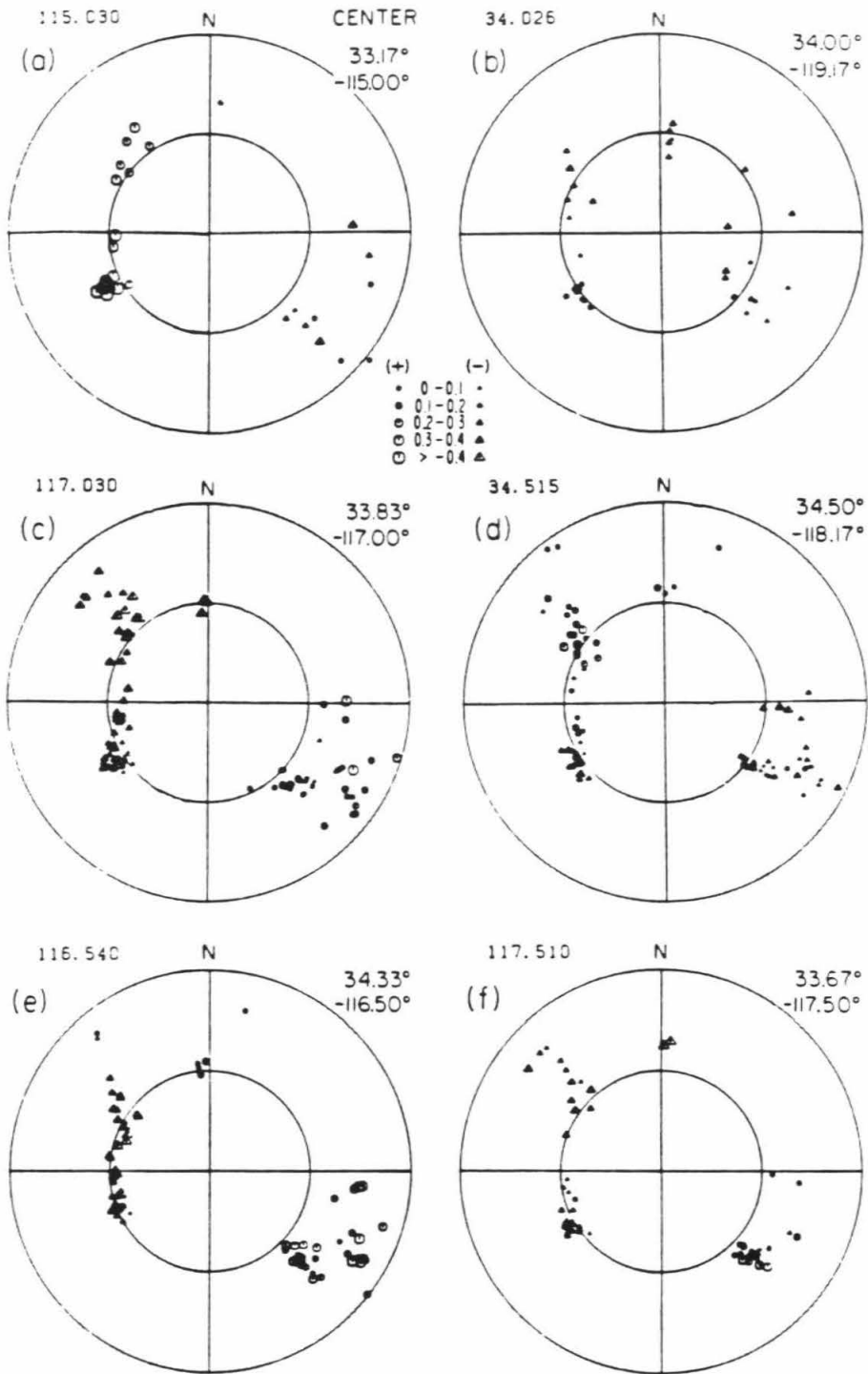
Figure 1.21 Plots of subarray net delays for six subarrays. Circles indicate positive delays (low velocity), triangles represent negative delays (high velocity). The symbols, which are plotted at the appropriate mislocation vector tails, are size coded according to delay magnitude. The coordinates of each subarray center are given to the right of each diagram.

northwest, and southwest sense faster velocities than the array mean. Such changes with azimuth indicate that in these cases the arrival time delay anomalies are representative of deep structure rather than shallow sediments. In the following, we assume that net delays primarily represent upper mantle rather than crustal velocity variations.

Net delays were originally plotted for a well-distributed set of 93 subarrays. The total observed range is nearly 1 s (-0.50 to 0.48 s). The data in Figure 1.21 demonstrate the typical consistency of these data within azimuth groups, both in sign and in magnitude. In general, the 'antiform' mislocation vectors coincide with large ($|\eta| > 0.2$ s) negative delays, as can be seen in the southeast quadrant of 34.515 (Figure 1.21d) and northwest and southwest quadrants of Figures 1.21c, 1.21e, and 1.21f. The Salton Trough deep low-velocity anomaly (Raikes, 1980) is evident in the positive delays observed in the southeast quadrants of Figures 1.21c and 1.21e.

A logical treatment of these data is to project the values onto a thin lens surface of time delays and to vary the lens depth until the best fit is achieved (Haddon and Husebye, 1978) (Figure 1.22). This method combines all the azimuthally and distance varying data into a best estimate of the location and depth of the velocity anomalies. The thin lens approximation makes the following assumptions (Haddon and Husebye, 1978):

1. The dominant heterogeneities are located in a single layer with some mean depth D.

2. The P waves entering the lens are plane waves.
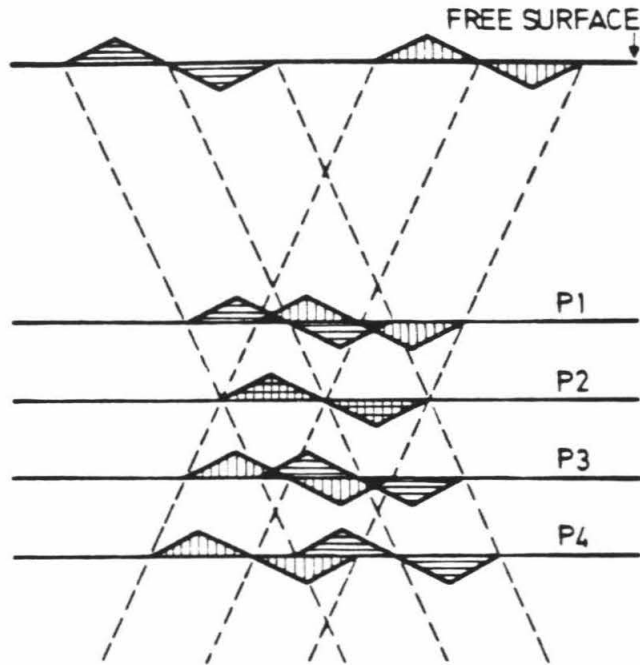
Figure 1.22 Schematic diagram of thin lens projection of time anomalies (from Haddon and Husebye, 1978). The two anomalies at the surface constructively interfere only at depth P2, the optimum projection depth. For other depths, there will be some destructive interference.

3. Phase conversions and anelastic effects can be ignored.

4. Ray theory is applicable.

5. The layer can be treated as a thin lens.

While a thin lens is perhaps not a very physical description of the structures, which almost certainly have some vertical thickness, Haddon and Husebye (1978) conclude that thin lens and associated 'thick lens' models yield virtually the same results in both travel time and amplitude patterns.

A total of 2798 net delays from a set of 48 subarrays (Figure 1.7) have been projected downward through a 30 km crust (V_p = 6.0 km/s) and mantle (V_p = 8.0 km/s) at depth intervals of 25 km to determine the optimal thin lens depth. Each net delay represents at least five arrival times at the appropriate subarray. Since the subarray data are averaged in space, the delays for a particular subarray are all assigned to the subarray center before projection. The strong azimuthal variation of these delays demands a thin lens depth greater than 100 km. The net delay data, which are unevenly distributed and concentrated in the central area of the lens, are interpolated at 0.1° intervals to a grid and are shown with contours at ±0.1 and ±0.25 seconds (Figure 1.23). These model grids were then tested against the projected data to find the optimal depth. For such a projection procedure the root-mean-square error will decrease with increasing depth because deeper projections have more degrees of freedom (see Haddon and Husebye, 1978). We attempted to remove this effect by finding the (assumed linear) rate of decrease of the error with depth for a randomized data set. That trend, -5.3 x 10^{-5} s/km, is removed from the error estimates presented in Figure 1.24. While no one depth has a strong error minimum, models at depths of more than 100 km clearly fit the data better than shallower lenses. The apparent local minimum at 50 km may be due to insufficient data

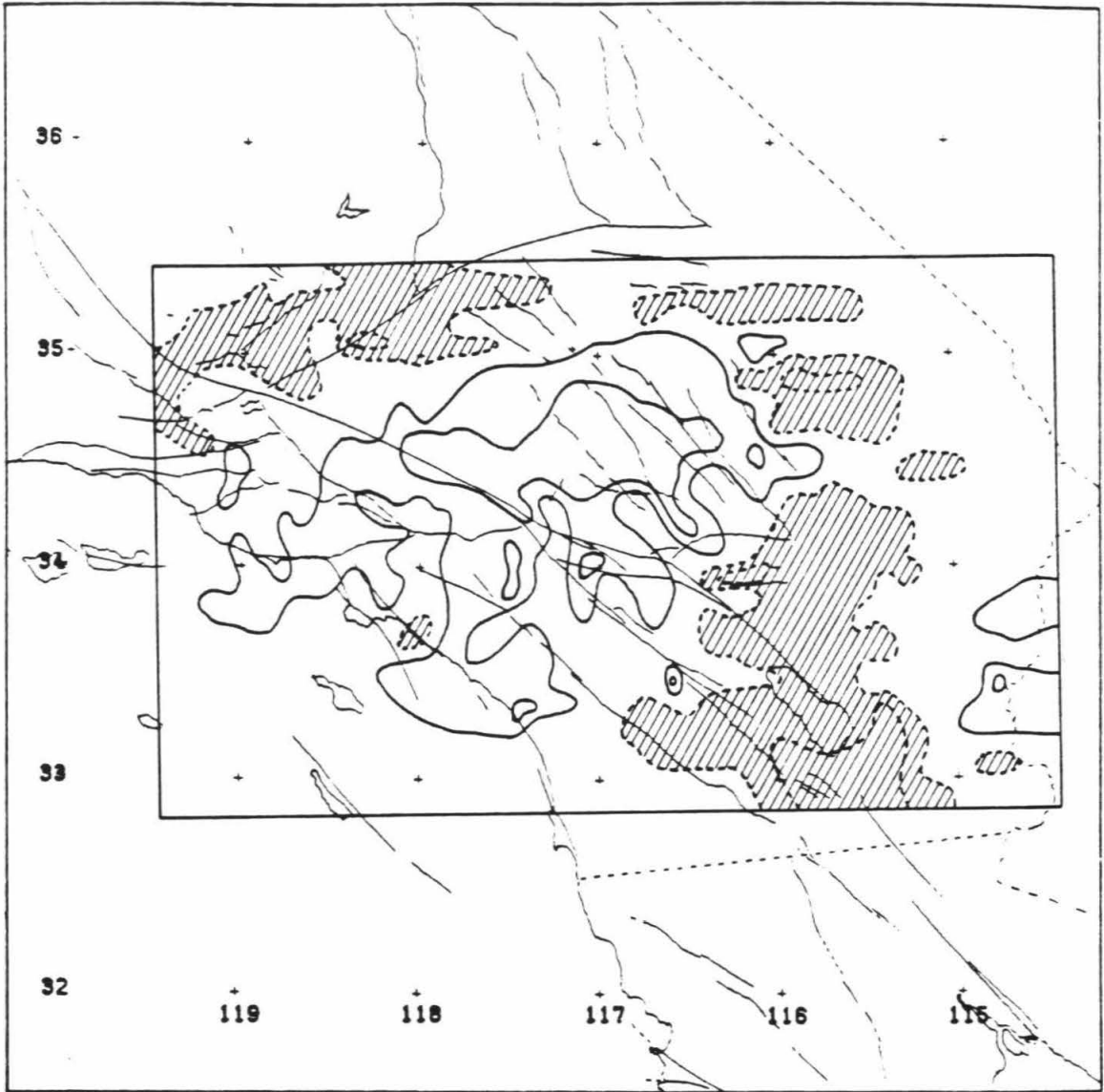THIN LENS CONTOURS - 150 KM DEPTH

Figure 1.23 Contour plot of the thin lens model obtained by projection of the net delay data to a depth of 150 km. Solid contours are for negative net delays, the dashed contours surrounding striped areas are for positive. The contour plotted are ± 0.1 and ± 0.25 seconds. Note the central concentrated area of negative delays which corresponds to the high-velocity antiform observed with relative array diagrams.
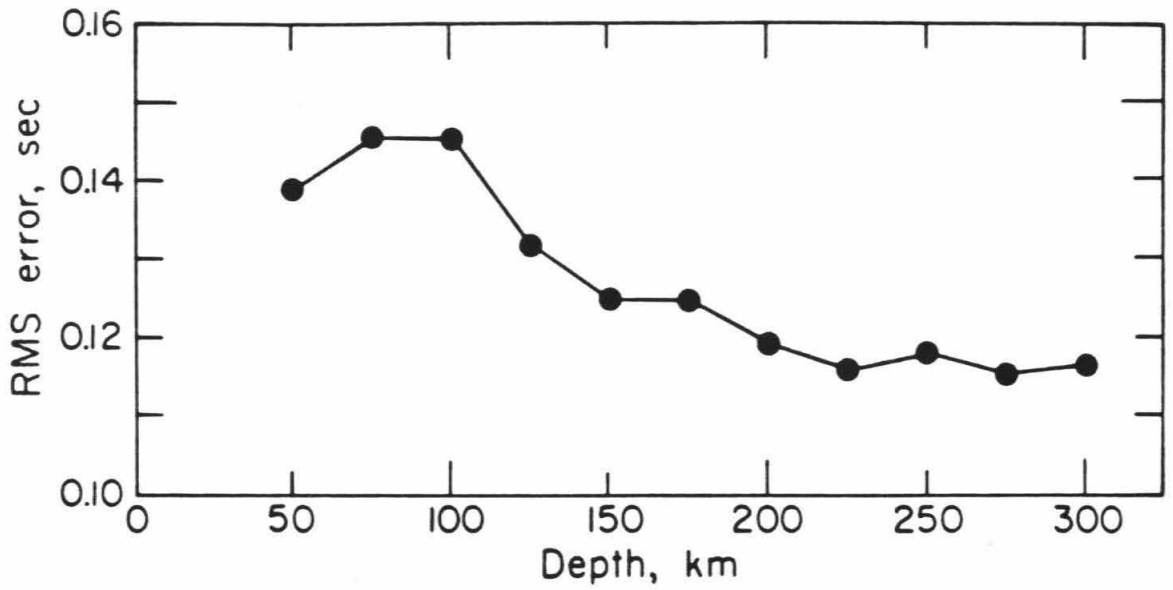
Figure 1.24 Root-mean square error versus depth for 11 thin lens models of the net delay data. Depths of more than 100 km satisfy the data best.

overlap at 50 km, or it may indicate that a single lens is inadequate to represent all the velocity variations: lenses at two or more depths may be more realistic. Other than at 50 km, the shape and magnitude range of our error curve (Figure 1.24) is very similar to that of Haddon and Husebye (1978). They also find a broad error minimum at depths of 100 km or more. We selected a representative lens at 150 km for Figure 1.23; the main features do not change significantly for deeper lenses. Compared to the fit of randomized data to the model, the 150 km lens yields a reduction in the RMS error of 49%. When compared to the raw data, the RMS reduction is 58%.

The contours of Figure 1.23 contain several interesting features. The dominant structure is the east-west trending zone of high velocity (negative lens values) at depth beneath the Transverse Ranges and southwest Mojave Desert, extending from 119°20' to 116°00'W and from 33°20' to 34°40'N. This anomaly, as might be expected, coincides well with the antiform mapped by relative array diagrams. The largest time advances, more than 0.25 s, occur along an east-west line at 34°30'N. Assuming a minimum velocity contrast of 3.75%, we calculate a vertical thickness of this structure of ≈100 km; a mean depth of 150 km then yields a high-velocity zone extending from 100 to 200 km depth in this area. Another concentrated region of high velocity occurs at the far eastern edge of the lens at 33°30'N latitude. A weaker high-velocity anomaly extends west from the central anomaly into the Santa Barbara Channel. It is interpreted to be a separate anomaly on the basis of misloca- tion vector patterns, which shift in orientation near (34°13'N, 118°30'W) (Figure 1.13d).

Velocities somewhat lower than the array mean are observed to the north of 34°40' at all longitudes. A stronger low velocity area occurs deep beneath much of

the Salton depression and southwestern Mojave Desert. Interestingly, the area of highest net delay gradient (> 0.5 s in about 30 km) occurs at (34° 00'N, 116° 25'W), directly beneath San Gorgonio Pass, the northwest terminus of the Salton Trough. The region below most of the southern California batholith is characterized by very small net delays.

Discussion

The many densely spaced stations of the Caltech-USGS Southern California Seismic Network, SCARLET, provide a unique opportunity to examine local variations in upper mantle velocities. By averaging the incoming teleseismic wave fronts over 100-km aperture subarrays, we obtained $dT/d\Delta$, azimuth, and average arrival time estimates for each event. These values are compared to whole array plane fit parameters with relative array diagrams and representations of net subarray delays. This technique eliminates the effects of near-source and lower mantle structure and reduces scatter due to random reading errors and isolated anomalies beneath individual stations. Examination of 171 overlapping subarrays has convinced us of the consistency of the data and the highly redundant averaging process yields good lateral resolution. Relative array diagram mislocation vectors are not very sensitive to structure depth, but projection of the net delay data to a thin lens supplies somewhat better depth constraints.

This study confirms the existence of a high-velocity body at depth beneath the Transverse Ranges and a low-velocity region under the Salton Trough. These two large features are prominent on both the suite of relative array diagrams and the thin lens model but somewhat easier to visualize from the latter. If we assume that the

high-velocity anomaly has a uniform velocity contrast with its surroundings, we can interpret the contour map (Figure 1.23) as a relief surface of the structure. The anomaly's greatest thickness lies in a grossly rectangular area from $118°30'$-$116°30'W$ and $34°15'$-$34°45'N$. Reasonable velocity contrasts imply a vertical thickness of 100 km or less, so a mean depth of 150 km or more places the entire body significantly deeper than the 40 km, 8.3 km/s refractor observed by Hadley and Kanamori (1977). The thin lens high-velocity contours almost directly overlie Hadley and Kanamori's PKP-delay contours (Figure 1.25), thus the lateral location of the 150 km anomaly agrees well with the position derived from the near-vertically incident core phase.

An uppermost mantle anomaly beneath the San Bernardino Mountains is well established both by this study and from local data: how is this body related to the deeper structure? One interpretation of the mislocation vector data presented in Figure 1.9 calls for an entirely separate shallow structure underlain by a high-velocity antiform. Alternatively, a predominantly deep feature with a narrow 'neck' reaching up to 40 km beneath the eastern Transverse Ranges is also possible within the data resolution. This explanation is more compatible with Raikes' (1980) ray tracing model. By assuming a velocity contrast of 7.8-8.3 km/s and fixing the anomaly's lower boundary at 150 km, she contoured the depth to the top of the 8.3 km/s layer. The resulting model featured an east-west trending zone of high velocity similar to the thin lens model, but which shallows to less than 50 km depth only near station CSP and becomes deeper away from the San Bernardino area.

Raikes (1980) also performed travel time residual inversions (e.g., Aki et al., 1977) on the southern California data. Each of four published models contains three layers; the differences are in the use of sediment corrections, changes of block size,
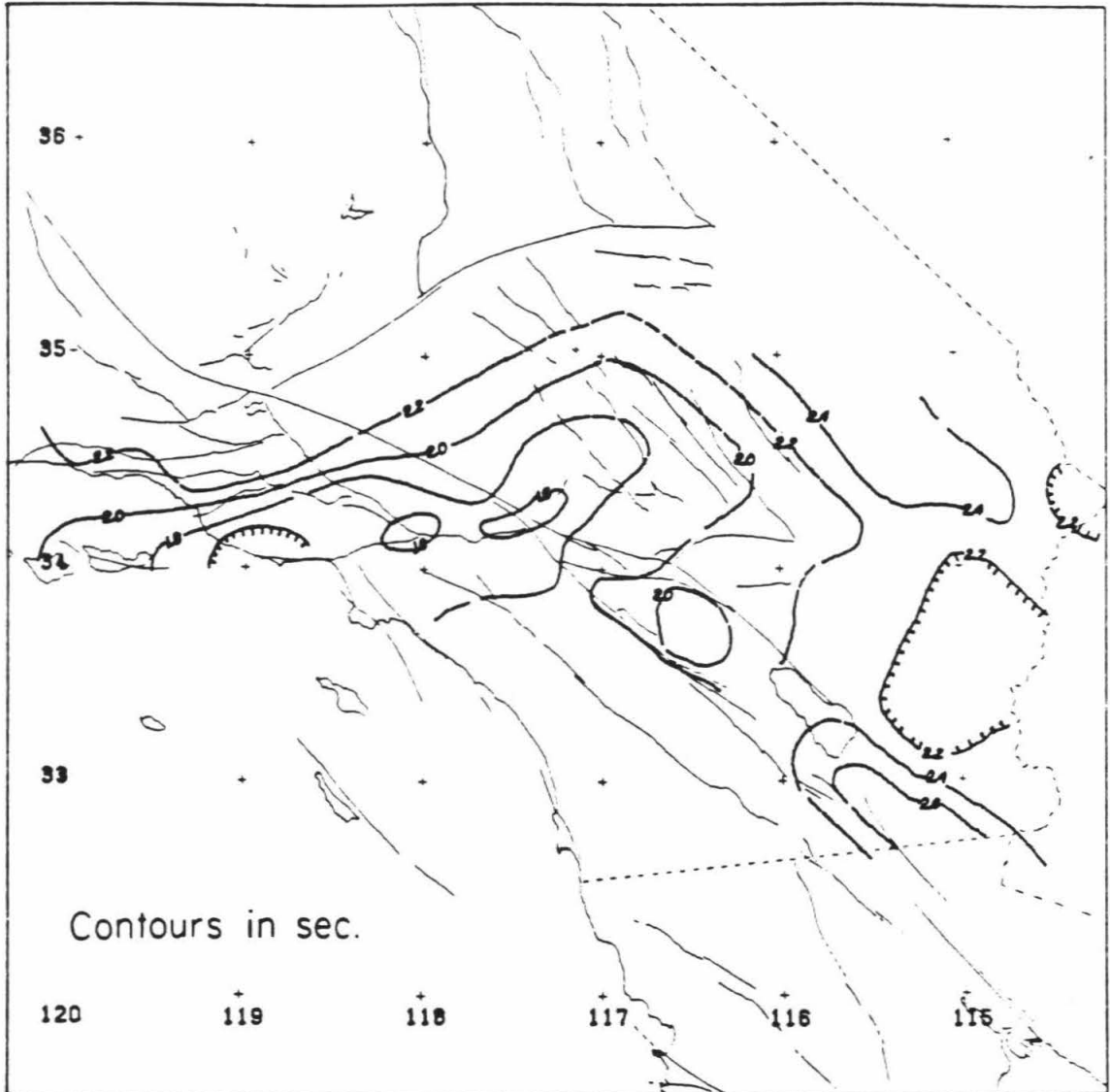
HADLEY – KANAMORI P-DELAY CONTOURS

Figure 1.25 PKP-delay contours from Hadley and Kanamori (1977). All stations are 1.5 to 2.9 seconds late compared to the JB tables. The contours are very similar in shape and extent to the negative contours of the 150 km lens model, Figure 1.23.

and rotation of block orientation. Despite some discrepancy in detail, all of the models contain high-velocity material beneath the Transverse Ranges in layer 3 (100-180 km), and none shows the locally intense velocity increases in layer 2 (40-100 km) expected from the ray tracing model and the Hadley and Kanamori (1977) study. The inversion results, then, support a deeper (100-200 km) high-velocity body. The adaptation of such an inversion scheme to relative event misloca- tion data is not simple and lies beyond the scope of this study. A more fruitful approach may be to modify the Jordan et al. (1981) joint travel time and gravity inversion method for use with the $(dT/d\Delta, \varphi)$ data set in order to incorporate the region's large number of gravity observations.

Humphreys (in preparation) takes a different approach to the teleseismic struc- ture determination problem: tomographic inversion. His results place the Transverse Ranges anomaly in essentially the same lateral position as previous studies. In the east, the maximum depth of the high velocity is 250 km; it shallows to the west. While Humphreys' results indicate fast material as shallow as 30 km, the strongest portion of this 3% velocity anomaly is at 150 km. This is very consistent with the results presented here. A separate, yet deeper still, high-velocity region lies to the southwest near Catalina Island. The work reported in this chapter has no resolution on the offshore feature, but its existence is consistent with observed mislocations for subarrays in the Channel Islands area.

We can examine the available gravity data for additional information. Hadley and Kanamori (1977) found that a buried cylinder at 40-100 km depth would produce a regional gravity high of 30-150 mGal for density contrasts of 0.03 and 0.15 g/cm^3. Since no such trend is observed (in fact Oliver (1982) notes a regional mass defi- ciency centered in the northwest Mojave Desert), they chose a partial melt model

which corresponds to the lower density contrast. But the absence of a large gravity anomaly could also be due to a deeper (150 km) emplacement of the high-velocity, high-density body. This would reduce the observed anomaly to 8-40 mGal for the same density and velocity contrasts. A deeper high-velocity zone is therefore compatible with the gravity data for a wider range of compositional models.

A notable feature of this anomaly is that it is not offset across the San Andreas Fault. Because of their relatively shallow (40 km) preferred depth of emplacement, Hadley and Kanamori (1977) argue that the subcrustal plate boundary must be displaced eastward beneath the Mojave block, to lie beyond the eastern terminus of the anomalous body. On the other hand, based on observations of Pn anisotropy in southern California, Vetter and Minster (1981) prefer a distributed subcrustal plate boundary in the form of a broad zone of simple shear, similar to models previously discussed by Lachenbruch and Sass (1980) and Prescott and Nur (1981). If the bulk of the anomalous body is in fact as deep as 150 km, then the lack of offset across the plate boundary does not constitute nearly as severe a constraint on the nature of relative plate motion at depth, since only the deepest part of the lithosphere could be involved, if at all.

The geographical relationship of the high-velocity block to the Murray fracture zone on the Pacific plate, the Transverse Ranges and Big Bend of the San Andreas, and the northern terminus of the Salton Trough clearly invites speculation about some evolutionary connection between these features. Hadley and Kanamori (1977) invoke a relic of subduction of the Farallon plate under North America. However, at the current rate of relative motion between the Pacific and North American plates, ≈ 6 cm/yr (Minster and Jordan, 1978), the observed alignment would be destroyed by as much as 300 km over the lifetime of the San Andreas system (≈ 5 m.y.), unless the

anomalous feature is in fact attached to the Pacific plate. The much greater depth of the anomaly suggested in the present study makes this explanation rather unsatisfactory. An attractive alternative has recently been proposed by Bird (1980): noting that the relative plate motion across the Big Bend of the San Andreas required that some kind of subduction take place in the Transverse Ranges Province, Bird suggests that the high-velocity anomaly is in fact associated with downwelling of cold, high-velocity material. This explanation is remarkably consistent with both the eastern and western terminus of the anomaly (Figure 1.23) which are, respectively, aligned with the northern extrapolation of the southern San Andreas and the southern extrapolation of the northern San Andreas trace. Assuming that the downwelling velocity is comparable to the plate velocity (say 5 cm/yr) a depth of 150 km can easily be reached over the lifetime of the San Andreas Fault.

An additional intriguing aspect of this model is raised by the interpretation of Pn anisotropy proposed by Vetter and Minster (1981). They find a fast Pn velocity along the direction of plate motion and a slower Pn velocity in the perpendicular direction; one of their interpretations calls for alignment of olivine a axes (fast axes) along the direction of shear in the subcrustal plate boundary zone. If downwelling beneath the Transverse Ranges is associated with rotation of the material such that the a axes of olivine are locally vertical, one should expect a locally high-velocity for P waves near vertical incidence, not unlike the anomaly described in this study. However, a more quantitative discussion would require actual mechanical modeling of the flow within the lithosphere, including possible phase changes, similar to the delamination calculations of Bird (1979) and lies beyond the scope of this study.

Another important element in the tectonics of southern California is the active spreading regime in the Gulf of California region. This area's positive net delays

predict low velocities deep beneath the Salton Trough which continue northward under much of the southeastern Mojave Desert. Directly below San Gorgonio Pass the thin lens model has a large net delay gradient: values change from $\eta < -0.25$ s (NW) to $\eta > 0.25$ s (SE) in 30 km. This correlates with the surface geology; San Gorgonio Pass marks the boundary between the Salton Trough to the southeast and the Transverse Ranges to the north. The large observed velocity gradient is consistent with a transition zone between downwelling associated with the compressive-transform environment of the Transverse Ranges and the tensional Salton Trough regime.

Chapter 2

Analysis techniques for dense data profiles

Introduction

In the preceding chapter, we developed a new method for determining lateral velocity variations beneath a seismic array using teleseismic data. In order to derive local anomalies, relative array analysis requires P arrivals free of distant structural complications; events which bottom in the smooth lower mantle ($30° < \Delta < 95°$) are ideal. The goal of the remainder of this thesis is to ascertain radial velocity structure in the upper mantle farther afield from SCARLET. Now we wish to examine seismograms at distances of $10°$ to $30°$. These records are representative of rays which have their turning points in the structurally complex upper mantle. Because the P waveforms are complicated, sophisticated techniques may be needed to sort out the generating structure.

We can analyze data collected from earthquakes at different ranges (a record section) and invert them for a velocity-depth model. This chapter examines several methods used in analysis and inversion of array data. Not all of the techniques are formulated strictly for arrays. The increased spatial sampling an array provides, however, should increase the model resolution. We review selected techniques based on travel times, ray parameter measurements, and synthetic seismograms.

A relatively new approach, wave field continuation (Clayton and McMechan, 1981), is adapted for teleseismic data and discussed in detail. While other methods may utilize only portions of the seismograms, such as travel times, wave field continuation retains all of the data at all times. Two linear transformations carry the seismograms from a (T, Δ) representation to the desired (p, τ) domain (where p is ray

parameter and r is radius), thus providing a direct estimate of the resolving power of the data in slowness-depth space.

Ray parameter estimation

Velocity structure estimation is dependent on reliable information about seismic phases: their travel times, apparent velocities, and amplitudes. The key in array analysis aimed at velocity structure is the array's ability to measure directly the ray parameter, $dT/d\Delta$, of an incident teleseismic wave. In study of the upper mantle, two or three phases which have interacted with one or more velocity discontinuities may arrive within a few seconds of each other on the record. Sophisticated methods have been developed to help identify these phases' $dT/d\Delta$ and thus their structural sources.

With ray parameter measurements for a range of distances, the function $p(\Delta)$ is constructed and inverted using the Herglotz-Wiechert integral for a velocity-depth profile (see the next section for a more detailed discussion). Since the $p(\Delta)$ data are typically quite scattered, partially due to receiver structure beneath the array, an alternative approach is to invert the dense absolute travel times using the tau method (Bessonova et al., 1974, 1976) and then constrain the model to fit the independent p-Δ data. An example of this technique is given in Chapter 3. The error bounds on the model allowed by the p-Δ and T-Δ (where T is travel time) data can be estimated using the method of Wiggins et al. (1973), although the required limits on p and Δ are somewhat subjectively chosen. Array determinations of p and azimuth (φ) are also useful in identification of very small phases, which often leads to structural interpretation. In the following, we discuss some array analysis techniques and their

applications in structural studies.

The most straightforward way to calculate the ray parameter of an incoming teleseismic body wave is by a simple least-squares plane fit to arrival times (Otsuka, 1966). The plane parameters also provide the array estimate of the wave front's azimuth of approach. This method has been used widely (e. g., Otsuka, 1966; Chinnery and Toksöz, 1967; Toksöz et al., 1967; Johnson, 1967, 1969; Fukao, 1977; Burdick and Powell, 1980) in mantle structural studies. For a very wide aperture network, the array cannot be treated in a Cartesian sense. The Appendix to this thesis contains a formulation for correcting the array plane for the Earth's curvature.

It is often difficult to pick the onset of seismic arrivals due to noise on the record, necessitating alternate methods of determining $dT/d\Delta$, or at least the relative arrival times at the array. Several techniques deal with this problem in different fashions, most of which involve the concept of an 'array beam'. A beam is nothing more than a sum of individual seismograms which have been relatively delayed in time so as to 'point' the array at a particular source region. The seismogram sum suppresses uncorrelated noise as $\sqrt{N}$, where N is the number of sensors (Davies, 1973). Manchee and Weichert (1968) use a cross-correlation technique for event detection and ray parameter estimation at the Yellowknife array (YKA) in Canada. This delay-sum-correlate (DSXC) method, as applied to event detection, forms many preset beams for each array leg and short time intervals, multiplies them together to form a correlogram, finds the maximum for each correlogram, and compares it to a preset threshold value. Buchbinder et al. (1973) utilize this method at YKA to search for the inner core reflection PKiKP. They select events at the proper distance and look for energy with the predicted PKiKP slowness at the right time, isolating 16 such records. Another application of DSXC is to calculate p and φ for precursors to PKP

(King et al., 1974), in order to determine their origin. King et al. conclude that these precursors are the result of scattering at heterogeneities in the lowermost mantle.

A correlogram, or TAP (time-averaged product) displays the variation of the square root of the correlation coefficient of the DSXC output with time (King et al., 1973). A TAP trace is helpful in secondary phase identification at small arrays, and is integral to the adaptive processing technique developed at WRA, the Warramunga seismic array in Australia. This iterative method determines accurate relative station delays for calculating least-squares plane fits and thus p and φ. Adaptive processing is repeatable along the trace, providing $dT/d\Delta$ and azimuth estimates for the entire wave train as a function of time. If there are two arrivals with differing phase velocities arriving closely in time, adaptive processing should reveal the change of $p(\Delta)$ in time along the record. Simpson et al. (1974) apply this method to WRA data to recover upper mantle structure, as do Ram and Mereu (1977) at the Gauribidanur array in India (GBA) and Ram et al. (1978) at YKA. Cleary et al. (1975) use adaptive processing to analyze P-wave codas in terms of scattering in the crust and upper mantle. A technique to detect very small velocity discontinuities, as might be expected in the lower mantle, is discussed by Wright and Lyons (1979); their method hinges upon slowness determinations with time, as does adaptive processing.

Kanasewich et al. (1973) describe a nonlinear noise-suppressing technique called the N-th root process; Muirhead and Ram Datt (1976) discuss its application to seismic arrays. By taking the N-th root of each sensor output before beamforming, where N is an integer, this system effectively damps non-Gaussian noise and is applicable to problems of spiky data, signal detection, signal enhancement and slowness determination, especially for noisy records. When the noise is Gaussian, N-th root processing performs nearly as well as linear processing. Muirhead and Ram Datt

(1976) use the N-th root process in conjunction with adaptive processing to make ray parameter measurements; other studies (Ram Datt and Muirhead, 1976, 1977; Ram Datt, 1981) utilize it in investigations of mantle structure with WRA data.

The Vespa process (Davies et al., 1971) examines beam power for various slowness values as a function of time for a constant beam azimuth. Vespa is useful for differentiating two signals with disparate phase velocities arriving from the same azimuth, and also aids in signal identification and $dT/d\Delta$ determination, when the azimuth is already known. Its limitation is in the constant azimuth assumption. Davies et al. (1971) investigate applications of Vespa for studies of the seismic coda and core structure. PKP precursor data are analyzed with Vespa by van den Berg et al. (1978) and King et al. (1974). Vespa could be applied to a teleseismic data profile to help separate triplicated mantle phases.

At NORSAR, analysis of complex signals is achieved with a beam power analysis method -- BEAMAN (King et al., 1976), which is similar to Vespa but with varying azimuth capability. Full array beams at points of a rectangular grid of slowness and azimuth record power as a function of T, p and φ. Every second of data has a corresponding beam power (energy/s) which is displayed in either of the (p, φ) or (p, T) planes. King et al. (1976) employ BEAMAN for analysis of PKIKP precursor data, while England et al. (1977, 1978) use it to assist in phase identification in their upper mantle studies.

Inversion techniques

Travel time inversions

Data gathered at arrays from earthquakes at 'mantle distances' ($10^\circ < \Delta <$ 90°) generally appear as points on a ray parameter versus distance plot. This is a very convenient form for inversion with the famous Herglotz-Wiechert integral (see e. g., Aki and Richards, 1980, p. 643). This inversion is exact for a perfectly known, complete travel time curve, $T(\Delta)$. Usually cast in terms of radius, ray parameter and distance, the Herglotz-Wiechert integral is simple to apply to array $dT/d\Delta$ estimates. Difficulties arise from regions in the Earth where there are negative velocity gradients with depth, such as low-velocity zones. With certain initial assumptions, Gerver and Markushevitch (1966) formulate an extension of the Herglotz-Wiechert formula which handles these troublesome areas of negative gradients.

The $p(\Delta)$ data are never exact or complete, resulting in a nonunique velocity model. The plane-wave approximation used in array estimation of $dT/d\Delta$ breaks down at regional distances, so some arbitrary velocity model must be assumed for close ranges (i.e. the topmost portion of the Earth). Scatter in ray parameter estimates, which is often considerable, is caused by event mislocations, timing errors and anomalous structure beneath the array itself. Receiver structure is an especially bothersome problem for medium aperture networks such as the UKAEA arrays, which are no larger than the subarrays of Chapter 1; near-surface structural irregularities often have wavelengths similar to the array aperture (England et al., 1977) and so cause significant biasing. When later arrival data are unavailable, the cusps and retrograde portions of the p-Δ curve (Figure 2.1) are unconstrained. In practice, many different p-Δ loci will satisfy the measured data points.
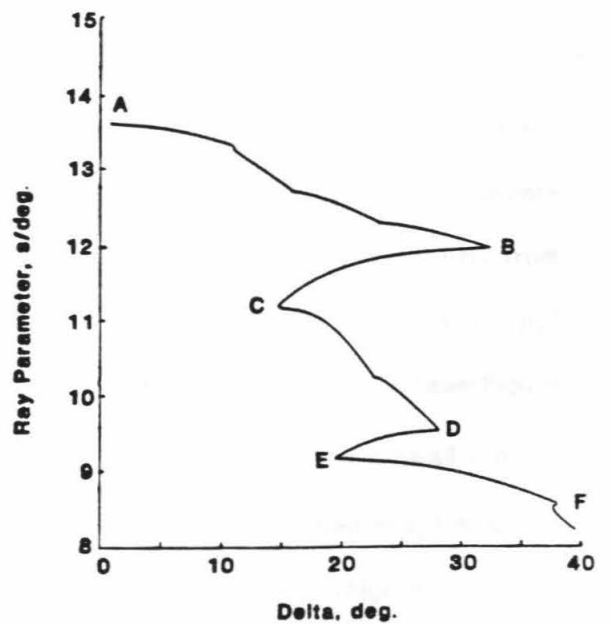
(a)
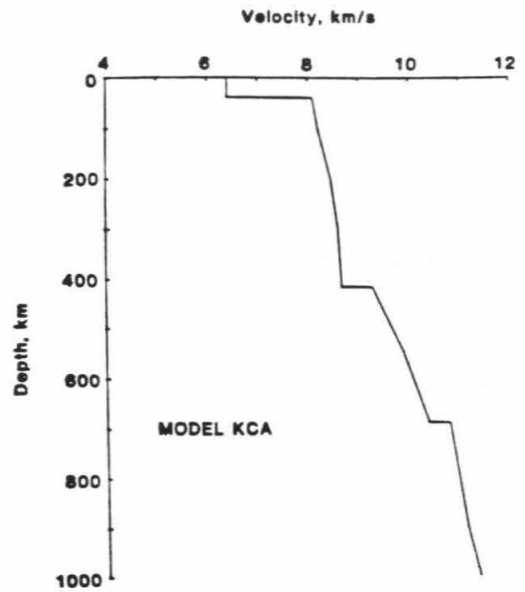
(b)
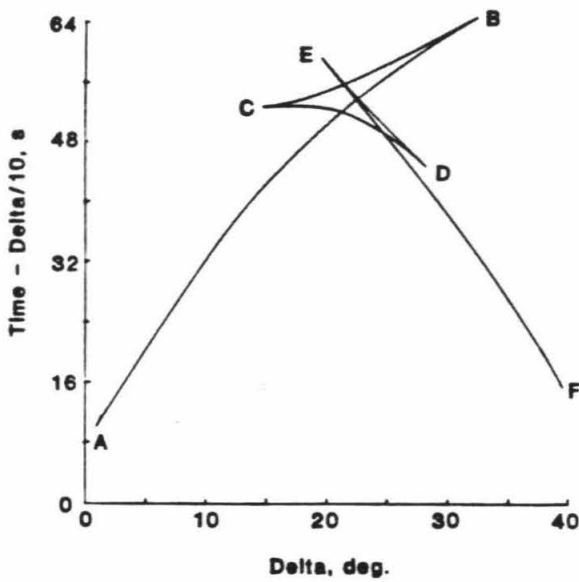
(c)

Figure 2.1 A simple upper mantle velocity model with its T-Δ and p-Δ curves. (a) Model KCA (King and Calcagnile, 1976) is derived for Fennoscandia. (b) Travel time curve for KCA. The letters refer to travel time branches, and will be used throughout this thesis. (c) p-Δ curve for KCA. Secondary arrival data are needed to constrain points B, C, D and E.

It is desirable to quantify the uncertainties in these nonunique models, and several distinct approaches have emerged. The Monte Carlo method (Wiggins, 1969) is simple in concept. A large number of random models are generated and tested for consistency against the data, mapping a region of acceptable models in the velocity-depth domain. Backus and Gilbert (1967) outline a generalized inverse technique for imperfect geophysical data; they discuss model resolution and uniqueness for gross earth data in their 1968 and 1970 papers. Given (1984) has developed an inversion formalism for body waves based on comparisons for data and synthetic seismograms. These methods may be difficult to apply to large bodies of array data due to prohibitive computation time.

Recently, techniques which employ the delay time,

$$\tau(p) = T(p) - p \, \Delta(p) \tag{2.1}$$

where T is travel time, p is ray parameter and Δ is epicentral distance have become popular. Wiggins et al. (1973) describe a method that locates extremal bounds on models such that travel times and ray parameter measurements are satisfied. Garmany et al. (1979) develop an extremal inversion, also based on $\tau(p)$, which uses linear programming. An important contribution utilizing only travel times cast in the τ domain is that of Bessonova et al. (1974, 1976). They formulate an extremal inversion based on error bounds on estimates of $\tau(p)$, which are calculated directly from the travel time data with a statistical approach. For a fixed ray parameter, p_0, $\tau(p_0)$ is the extremum of the function $\tau(\Delta)_{p=p_0}$ along a single travel time branch (see Figure 2.2a). To determine $\tau(p_0)$, we assume that $\tau(\Delta)_{p=p_0}$ is a constant for a small window in Δ centered on Δ_0, the distance at which $\tau(\Delta)$ is an extremum. Then $\tau(p_0)$ is a simple average of all the $\tau(\Delta)_{p=p_0}$ data points in that Δ interval (Figure 2.2b). A
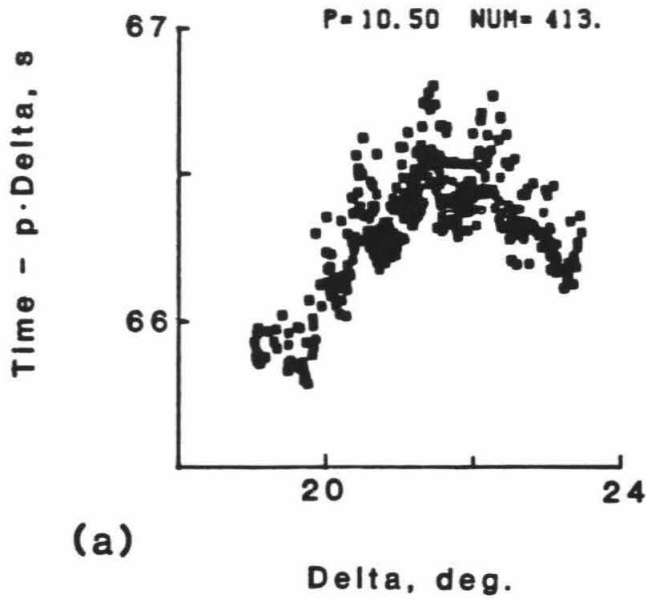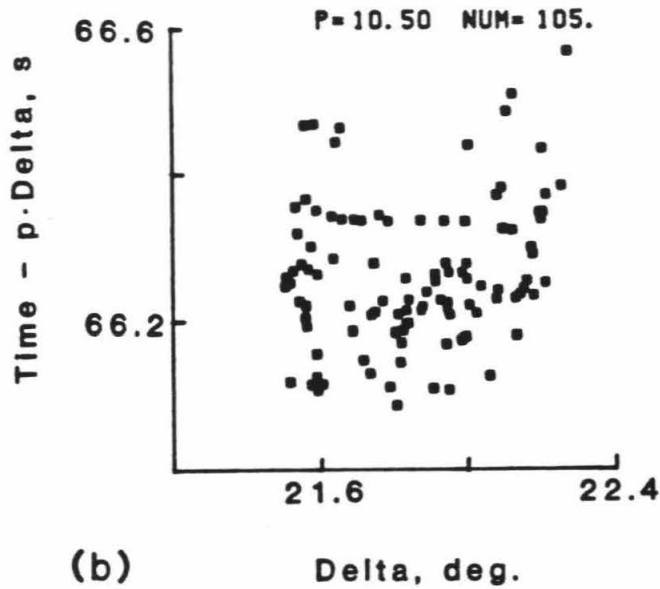
Figure 2.2 Statistical calculation of $\tau(p)$. This example uses data from the events described in Chapter 3. (a) The τ vs. Δ plot for the first-arrival portion of the CD travel time branch (see Figure 2.1), for a ray parameter of 10.5 s/deg.. Note the curvature defined by the data. (b) τ vs. Δ for the 'flat' portion of (a). We averaged these 105 points to obtain $\tau(10.5) = 66.46$ s, with $\delta_o = 0.18$ s.

confidence interval, δ_o, for the estimate is given by

$$\delta_o = n^{-1/2} s \ t_a (n-1) \tag{2.2}$$

Here n is the number of observations, s is the standard deviation of $\tau(p_o)$ and $t_a (n-1)$ are values for the Student's distribution with $n-1$ degrees of freedom (see Bessonova et al., 1976 for details). The statistical confidence limit is important in assessing the model uncertainty. This statistical calculation of τ is ideally suited for dense array data, where n is large enough to define a small confidence interval. The $\tau(p)$ curve may be inverted directly, in a similar fashion to the Herglotz-Wiechert integral, or the δ_o may be used to define limits on $\tau(p)$ which are transformed to uncertainty estimates in velocity-depth space. Many studies rely on the tau method to invert large data sets: England et al. (1977,1978) study upper mantle array data, Kennett (1976) analyzes a long range refraction profile, and Lee (1981) uses ISC (International Seismic Centre) travel times to investigate the structure of the entire mantle. An example of an extremal tau inversion applied to a high-quality set of array data appears in Figure 3.12 of this thesis.

Synthetic seismogram modeling

Helmberger and Wiggins (1971) and Wiggins and Helmberger (1973) initiated trial-and-error structural modeling of the upper mantle using short-period body waves. Requiring synthetic seismograms generated with a model to fit the observed records incorporates additional information into the modeling process. When two or more phases are present on a seismogram, the relative amplitudes of the signals are sensitive to the velocity gradients near the turning points of the waves (Figure 2.3). In addition, we gain improved relative timing between phases, since the synthetic
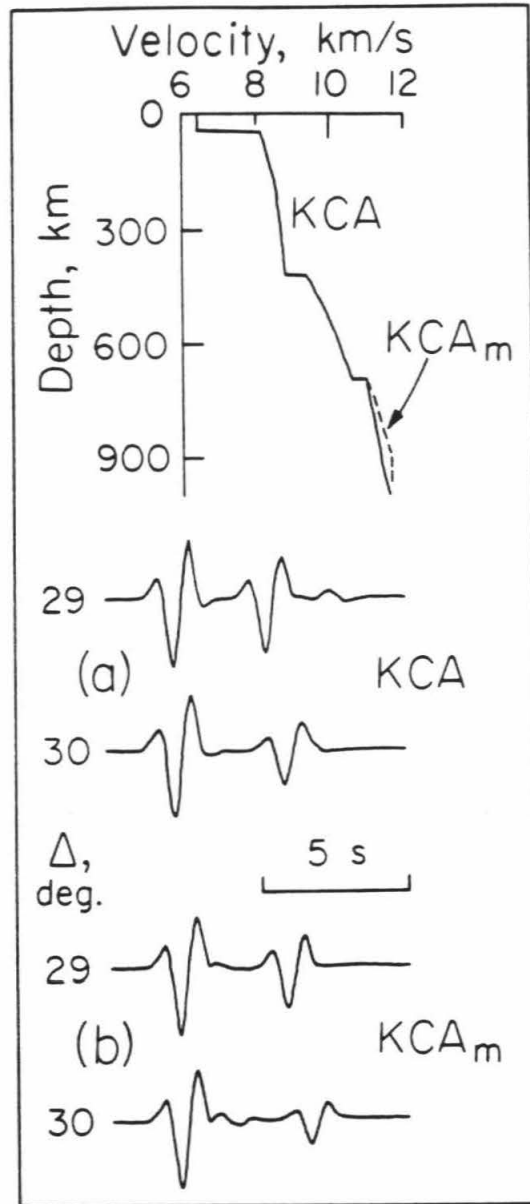
Figure 2.3 Model KCA (see Figure 2.1) and a slight perturbation of it, KCA$_m$, demonstrate the effect of velocity gradients on relative amplitudes. (a) WKBJ synthetic seismograms for distances of 29° and 30° for KCA. Figures 2.1 b and c show that at these distances the EF and BC branches are the first and second arrivals, respectively. (b) same for KCA$_m$, which has a steeper velocity gradient from 690 to 900 km depth. The first arrival is now larger relative to the second. The EF arrival is bottoming in the region of increased gradient, causing the larger wave.

seismograms properly include phase shifts of reflected waves. These innovations improve estimation of discontinuity sizes and velocity gradients between those discontinuities. By incorporating the relative amplitude and differential travel time data, the range of acceptable models should be reduced over the spread constrained by just travel time and ray parameter data. The achieved uncertainty reduction, however, is difficult to quantify for models derived in a forward, trial-and-error fashion. New efforts in formalized inversion of body waves for structure using criteria based on synthetic fits (Given, 1984) should yield models with well-developed error bounds.

A synthetic seismogram is constructed through a series of convolutions in the time domain:

$$y(t) = s(t) * m(t) * a(t) * i(t) \tag{2.3}$$

where y is the seismogram, s is the source-time function, a is the attenuation operator, i is the instrument response and m is the Green's function for the travel path, or the Earth response (Helmberger and Burdick, 1979). In structural modeling, the goal is to find an $m(t)$ which produces synthetic seismograms that match the data; we must make independent estimates of $s(t)$, $a(t)$ and $i(t)$.

Several algorithms are suitable for computing the mantle response, $m(t)$. The most popular method has been the Cagniard-deHoop generalized ray technique (Wiggins and Helmberger, 1974). Utilizing a layered representation of the Earth, this formalism is quite accurate but computationally intensive. Green's functions calculated with WKBJ theory (Chapman, 1976; Wiggins, 1976) take much less computer time, which is advantageous in trial-and-error modeling. Formulated for inhomogeneous media, WKBJ seismograms become inaccurate for grazing incidence or near very

steep velocity gradients, such as first-order discontinuities. Synthetics generated with these two methods for the same velocity-depth model are shown in Figure 2.4. At most ranges the two algorithms compare well, indicating that except in some special cases, WKBJ seismograms are sufficiently accurate for upper mantle modeling. Given (1984) develops a hybrid technique which uses the WKBJ approximation everywhere except near discontinuities and low-velocity zones, where generalized rays are computed. This method, while more time-consuming than simple WKBJ computation, produces accurate Green's functions much more quickly than the Cagniard-deHoop algorithm.

To estimate the source-time function, $s(t)$, we can either model the particular earthquake source independently (Burdick and Helmberger, 1978) or else use an empirical $s(t)$: obtain a record of the event for an uncomplicated propagation path (e. g., $\Delta > 30°$). For this case, the mantle response is an impulse, and the observed P wave is essentially $i(t) * s(t)$. In any situation, the instrument response is known. Causal attenuation cannot be easily included in either formalism. Effects of depth-varying attenuation on seismograms are not easily separable from those with structural causes; this imparts further nonuniqueness to the modeling problem.

Structural modeling with synthetic seismograms is useful for both short-period and long-period body wave data. Synthetic seismograms have been used extensively with upper mantle data sets gathered at widely separated sites (Helmberger and Wiggins, 1971; Wiggins and Helmberger, 1973; Dey-Sarkar and Wiggins, 1976; Burdick and Helmberger, 1978; McMechan, 1979; Given and Helmberger, 1980; Burdick, 1981; Grand and Helmberger, 1983); such modeling is also ideally suited for array data. Many of these studies use long-period data because short-period data, with its increased time resolution, is less stable. Closely spaced array data allows
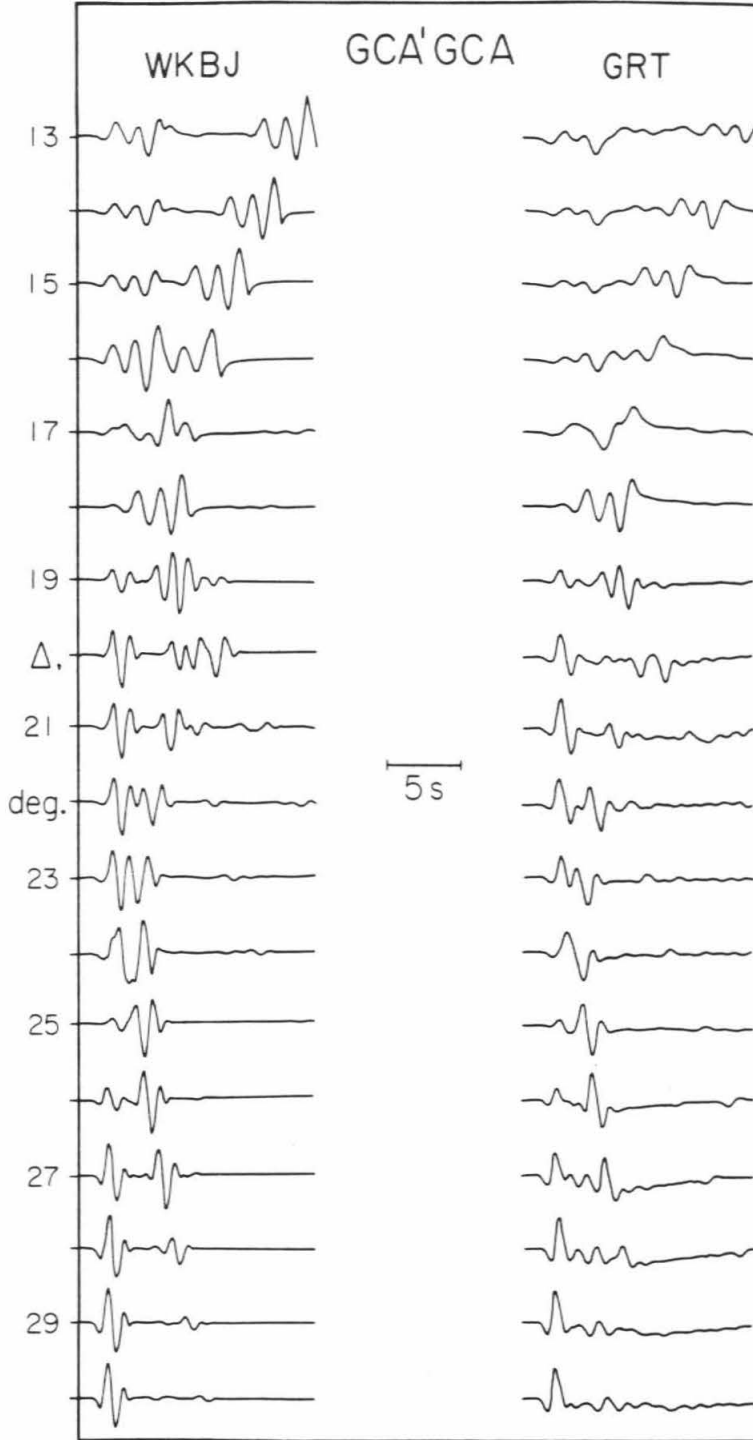
Figure 2.4 Comparison of synthetic seismograms computed with WKBJ theory and generalized ray theory (GRT) for the hybrid model GCA'GCA (see Chapter 3). Despite some differences in waveform, especially for distances closer than 17°, the two methods compare well enough to justify the use of the WKBJ method for upper mantle modeling.

visual checking of waveform stability across the array aperture, unobtainable for stations spaced many tens of kilometers apart. Better data coverage also results in superior constraints on travel-time triplication cusps and changes in relative amplitudes with distance, thus producing a better model. In the past few years, workers analyzing dense refraction lines (Clowes et al., 1981; Kempner and Gettrust, 1982; Lewis and Garmany, 1982) and upper mantle array data (Rademacher et al., 1983; this thesis) have increasingly depended on synthetic seismograms to ascertain resolvable details of the Earth's velocity structure.

Wave field continuation

The optimal inversion of seismological data for structure utilizes all possible information: the entire data wave field. From travel time inversions to those using p-Δ data to synthetic seismogram modeling, we have been adding new information to the inversion process which contributes additional resolving power. The quantification of the uncertainties present in the inverted model, however, is still a pervasive problem. The process of wave field continuation (Clayton and McMechan, 1981) optimizes the inversion process because the entire seismic data set is transformed, with no information loss, to the velocity-depth domain. The time resolution in the data converts to depth resolution for the model, eliminating the need to calculate an uncertainty envelope. Wave field continuation has been applied to reflection and refraction data (Schultz and Claerbout, 1978; Clayton and McMechan, 1981; McMechan et al., 1982) but not to teleseismic data. In this section, we present an adaptation of this method for teleseismic analysis, including synthetic examples. Chapters 3 and 4 contain examples of inverting actual upper mantle array data with the wave field continuation technique.

Clayton and McMechan (1981) outline the theory behind wave field continuation inversion. We follow their discussion and then extend it for data collected at ranges where the Earth's sphericity is important.

Wave equation continuation involves two linear transformations. Seismic data recorded in section form (T, x) where T is travel time and x is distance, are first slant stacked, producing a (τ, p) wave field. Here p and τ are the flat earth ray parameter and the delay time, respectively. Then this representation of the data is 'downward continued' to the final (p, z) (where z is depth) domain.

The slant stack (or inverse Radon transform) decomposes the wave field into its plane wave components (McMechan and Ottolini, 1980). The process is simple in concept. There is a point on each record which corresponds to a given p and τ. For each (τ, p) pair, these points are summed over all the records to give the stack amplitude at (τ, p). As long as p and τ are sampled densely enough, the slant stack contains all the data present in the original record section, but in a different format. The Radon transform is reversible; the complete seismic record section can be regenerated by applying a forward Radon transform to the stacked data. In the time domain, we write the slant stack as (McMechan and Ottolini, 1980)

$$S(\tau, p) = \int_{-\infty}^{\infty} p(\tau + px, x) \, dx \qquad (2.4)$$

where S is the slant stacked wave field. In practice, artifacts exist in the stack which are caused by the finite length of the data profile, gaps in the data section and insufficient spatial sampling (aliased data). If the source wavelets are not coherent, some unwanted destructive interference will occur where the waves should constructively interfere, degrading the image (Clayton and McMechan, 1981).

Once the data are stacked, the next step is to downward continue the (τ, p) wave field into the (p, z) domain. Assuming lateral homogeneity, $v = v(z)$, we continue the wave field observed at $z=0$, the surface, to any desired depth, z. For a two-dimensional Cartesian coordinate system, the wave equation written in terms of a wave field $P(z,\mathrm{x,t})$ transforms to

$$[\frac{\partial^2}{\partial z^2} - k_z{}^2 + 4 \, \frac{\omega^2}{v \, (z)^2}] \, P(z,k_z,\omega) = 0 \tag{2.5}$$

where k_z is the spatial wave number and ω is frequency. Then

$$P\,(z,k_z,\omega) \approx P\,(0,k_z,\omega) \, \exp \, [-i2 \int\limits_0^z [\, \frac{\omega^2}{v(z)^2} - \frac{k_z{}^2}{4}]^{\frac{1}{2}} \, dz\,] \tag{2.6}$$

(see Claerbout, 1976). If we substitute $-2\omega p$ for k_z in (2.6) and recognize that the slant stack in the frequency domain is

$$S(\omega,p) = P(\omega,-2\omega p) \tag{2.7}$$

then

$$S(\omega,p,z) = S(\omega,p,0) \, \exp \, [-i\omega \, \Psi(p,z)] \tag{2.8}$$

where

$$\Psi(p,z) = 2 \int\limits_0^z [\, \frac{1}{v(z)^2} - p^2]^{\frac{1}{2}} dz \tag{2.9}$$

Note that $\Psi(p,z)$ is just the delay time $\tau(p)$ for a flat earth. Next we use the inverse Fourier transform to obtain the downward continuation formula for slant stacked data.

$$S(\tau, p, z) = \int S(\omega, p, 0) \exp\left[-i\omega(\Psi(p,z) - \tau)\right]d\omega \qquad (2.10)$$

We seek to continue the data for each p to the depth where its ray bottoms; then $p = 1/v(z)$, so we choose $\tau = 0$. Equation (2.10) then becomes

$$S(0,p,z) = \int S(\omega,p,0) \exp\left[-i\omega\Psi(p,z)\right]d\omega \qquad (2.11)$$

$S(0,p,z)$ is the same as the slowness plane $s(p,z)$. We notice that the right-hand-side of the above equation is simply the Fourier transform of $S(\Psi(p,z),p,0)$ so in the time domain there is an alternate form:

$$s(p,z) = S(\Psi(p,z), p, 0) \qquad (2.12)$$

This means that to downward continue a slant stacked wave field with a velocity model $v(z)$ is easy. Looping over ray parameter, we calculate for each z the quantity $\Psi(p,z)$. Then the corresponding point from the slant stack is selected and placed in the position (p,z).

An adaptation of the above to spherical geometry is relatively simple. One approach is to transform the spherical earth data and model to the Cartesian equivalent using the earth flattening approximation (e. g., Müller, 1971)

$$x = R\,\Delta \qquad (2.13)$$

$$z = R\ln(R/r)$$

$$v(z) = \frac{u(r)\,R}{r}$$

$$p(z) = \frac{\sin i}{v(z)}$$

$$p(r) = \frac{r \sin i}{u(r)}$$

where the flat-earth coordinates x, z, v and p are as defined above. For a spherical earth, Δ is distance, R is the Earth's radius, r is the radius coordinate, $u(r)$ is the spherical velocity function, $p(r)$ is the ray parameter, and i is the angle between the ray and a radial line from the Earth's center. By transforming the teleseismic time-distance section appropriately and using the flat-earth version of the velocity model in equation (2.9), we can use the wave field continuation inversion as it stands. The slownesses and depths of the $(p(z), z)$ solution are then transformed back to the spherical counterparts $(p(r), r)$ through (2.13).

Using the earth-flattening approximation of $u(r)$, $p(r)$ and r to convert to $v(z)$, $p(z)$ and z in the function $\Psi(p,z)$ (equation (2.9)), is equivalent to retaining the spherical parameters in the spherical version of $\tau(p)$:

$$\Psi(p, r) = 2 \int_{r_0}^{r} [\frac{1}{u(r)^2} - \frac{p^2}{r^2}]^{\frac{1}{2}} dr \tag{2.14}$$

in the downward continuation equation. Therefore we can avoid the earth-flattening transformations by slant stacking the data in linear $p(r)$ to take (T, Δ) to $(\tau, p(r))$ and then performing downward continuation on the stacked wave field according to

$$s\ (p,r) = S\ (\Psi(p,r), p, 0) \tag{2.15}$$

where $\Psi(p,r)$ is defined in 2.14, to find the correct velocity model. Following Clayton and McMechan (1981), in order to avoid the branch cut in the definition of $\Psi(p,r)$, the absolute value of the integrand is taken in the actual computation:

$$\Psi\ (p,r) = 2 \int_{r_0}^{r} | \frac{1}{u(r)^2} - \frac{p^2}{r^2} |^{\frac{1}{2}} dr \tag{2.16}$$

Also, we apply a constant phase shift of $+5\pi/4$ to the entire wave field. This accounts for the far-field radiation condition ($\pi/2$), the two-dimensional approximation for three-dimensional propagation ($\pi/4$) and an average shift ($\pi/2$) associated with reflection coefficients of the various types of arrivals (see Clayton and McMechan, 1981 for details).

Given a sufficiently densely sampled teleseismic data profile representing an area that is not too laterally heterogeneous, this method will produce, directly, an image in the slowness-radius plane. There are several advantages in using wave field continuation over other inversions.

1. The raw data are the required input; no timing of arrivals is necessary.

2. All of the data are present at all times in the inversion process.

3. The data resolution in the time domain is transferred to velocity-depth

space, defining the resolution of the data precisely.

Several restrictions do apply to this powerful method.

1. Extremely dense spatial sampling is required. For inversions of

teleseismic waveforms, array data are essential.

2. Lateral homogeneity is assumed. Processing artifacts will appear for

areas with strong lateral variations.

3. If the source wavelets are not coherent, the image will be degraded.

4. Fine structural details ascertainable from synthetic seismogram modeling

of the very best data may be masked because of other, noisier data

included here.

The obtained (p,r) wave field is critically dependent on the input velocity model, $u(r)$, so the downward continuation process is iterative. We must guess at an initial model, use it for the first continuation, extract a $p-r$ curve from the wave field, and repeat the process until it converges: the input and output models are the same. The stable model should be the best estimate of the correct velocity structure given the available data. In practice, two alternating, quasi-stable states are often achieved; Clayton and McMechan (1981) find that a simple average of these two models corresponds to the best model. If the slant stack is continued with the correct model, the inversions' result will be that input model. Thus this type of inversion is also very useful in checking results obtained from other methods.

We illustrate the teleseismic adaptation of wave field continuation with a synthetic example. Figure 2.5 is a record section of 301 synthetic seismograms covering $9°$-$39°$ with an equal trace spacing of $0.1°$. The generating model is GCA' for $9°$-$13°$ and GCA for $13.1°$-$39°$; these models are presented in Chapter 3. The WKBJ algorithm was used to calculate these synthetics, and the same source wavelet is used throughout the section. Figure 2.6 is the actual stack of these synthetic seismograms; the pictured trace is actually the envelope of the slant stack for each p value in Figure 2.7. We downward continued this (τ, p) wave field using equation 2.15 to obtain Figure 2.8. Superimposed on the wave field is a (p,r) representation of the model. For this example, we used a depth spacing of 5 km and a Simpson's rule integration for $\tau(p)$ with an integration interval of 2.5 km. The observed coincidence of the initiation of the image and the input model demonstrates self-consistency: the wave field continuation of the synthetic data with the generating model reproduces the input function.
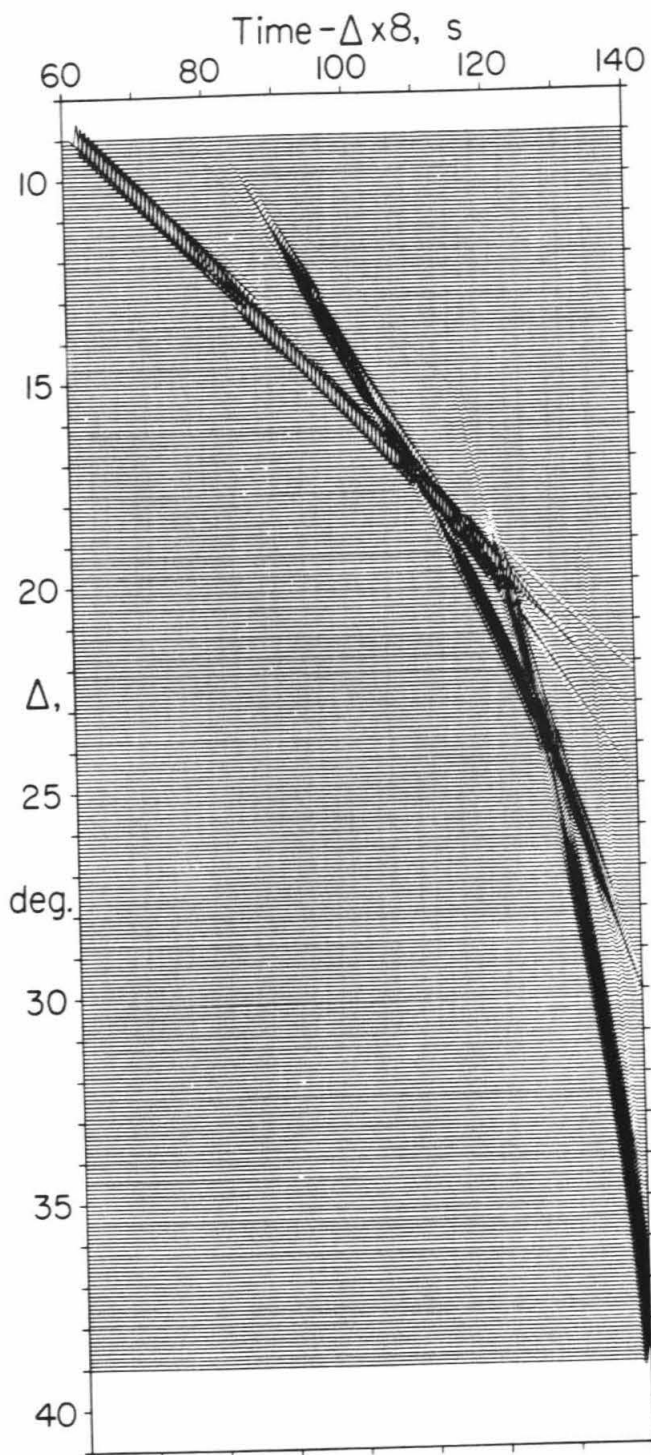
Figure 2.5 A synthetic seismogram profile for models GCA' and GCA, presented in Chapter 3. The two mantle triplications are very visible. The trace spacing is 0.1°, with 301 seismograms total. The same source wavelet is used for the entire record section.
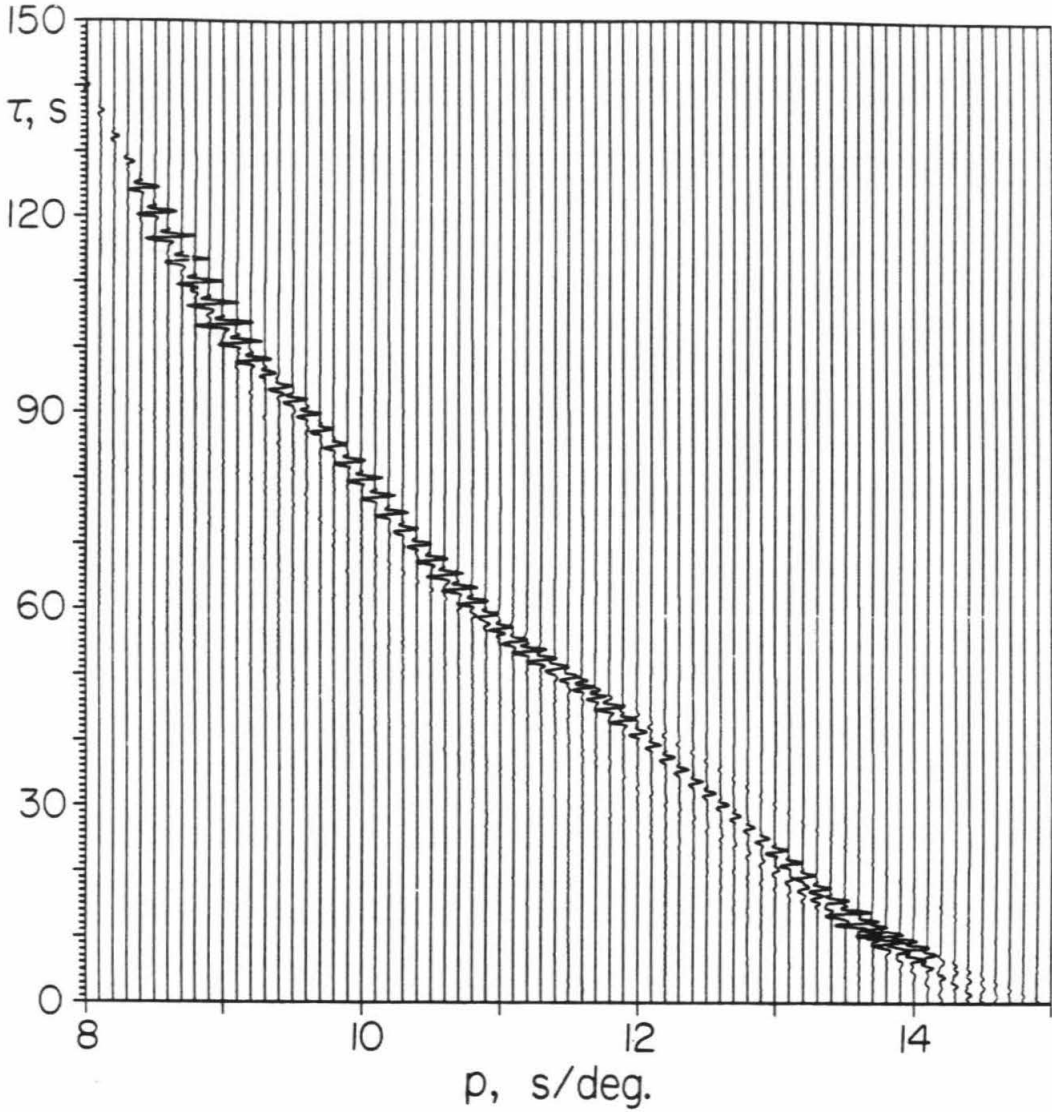
Figure 2.6 Slant stack of the synthetic data of Figure 2.5. The input source waveform is reconstructed for most p values. The overlapping models (see text) cause some complexity near p = 14.5 s/deg., and the synthetic data, which commence at 9°, do not contribute much energy for p > 14 s/deg.. There are 1575 τ points and 70 p values for each slant stack.
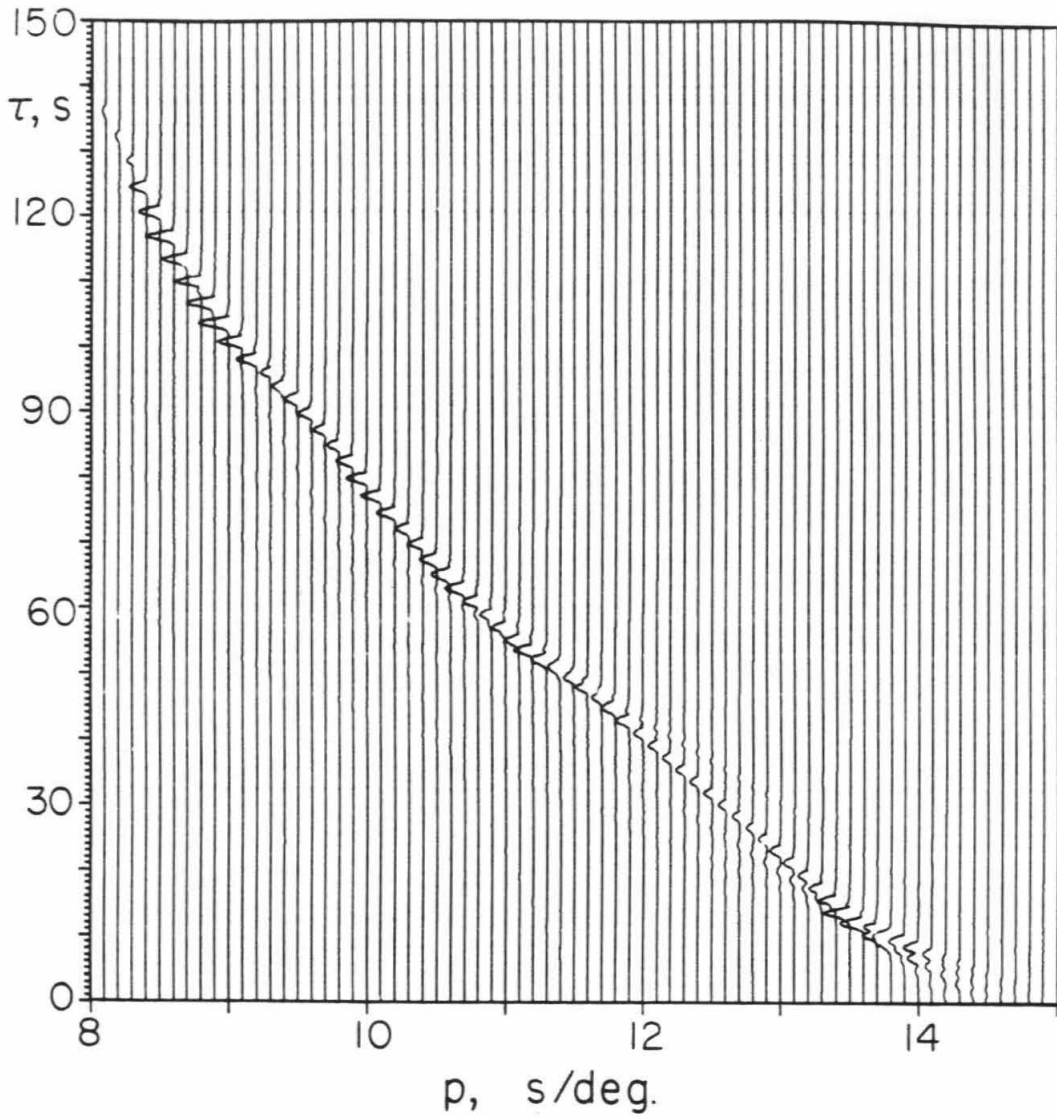
Figure 2.7 Same as Figure 2.6, except that for each p value, the envelope of the stack is presented. The image is even more simple than that of Figure 2.6.
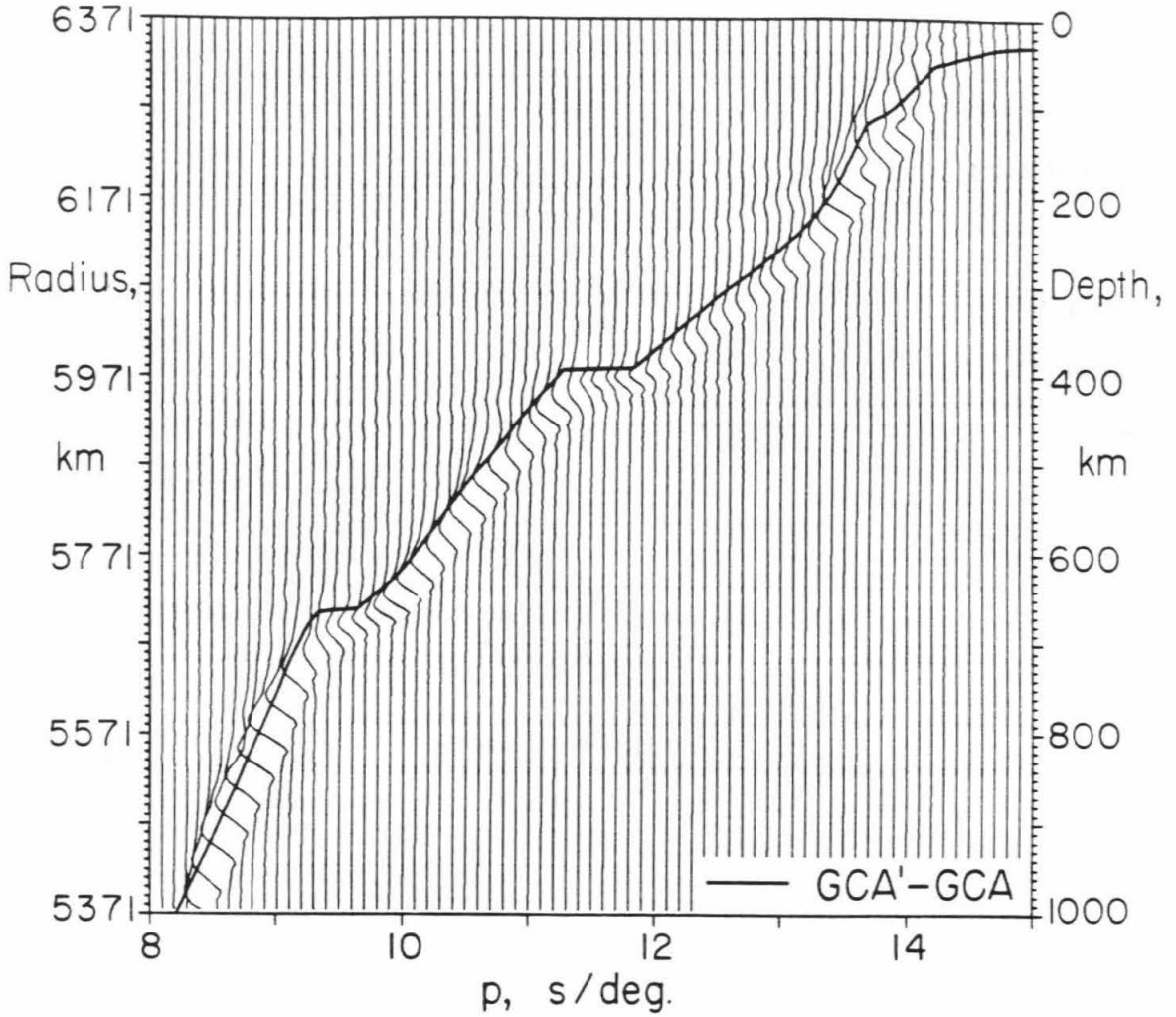
Figure 2.8 The downward continuation of the stack of Figure 2.7, using the generating model, which is plotted on top of the wave field. The coincidence of the initiation of the image and the model indicates that this method is successful. For the depth spacing of 5 km and seismogram spacing of ~11 km, with 1 s P waves we can achieve depth resolution of only tens of kilometers.

Figures 2.9, 2.10 and 2.11 are a similar series except that we used three dif-
ferent source-time functions, varying with distance, in generating the synthetic
record section. In both the slant stack (Figure 2.10) and the slowness-depth model
(Figure 2.11), the degradation of resolution due to the varying sources is easy to
see.

The slant stack representation of data has spawned still other inversion
methods. Brocher and Phinney (1981) suggest that, since amplitude information is
preserved in the stacked data, the integrated power of the stack should be used in
inversion schemes. A change in $v(z)$ results in a change in the integrated power for
a finite length record section. McMechan (1983a, b) develops an alternate complete
data transformation: (T, x) to (p, x) to (p,z) instead of (T, x) to (τ, p) to (p,z). The
intermediate image (p, x) is obtained with an overlapping sequence of local (in x)
slant stacks. Then a transformation analogous to equation (2.10) carries the (p, x)
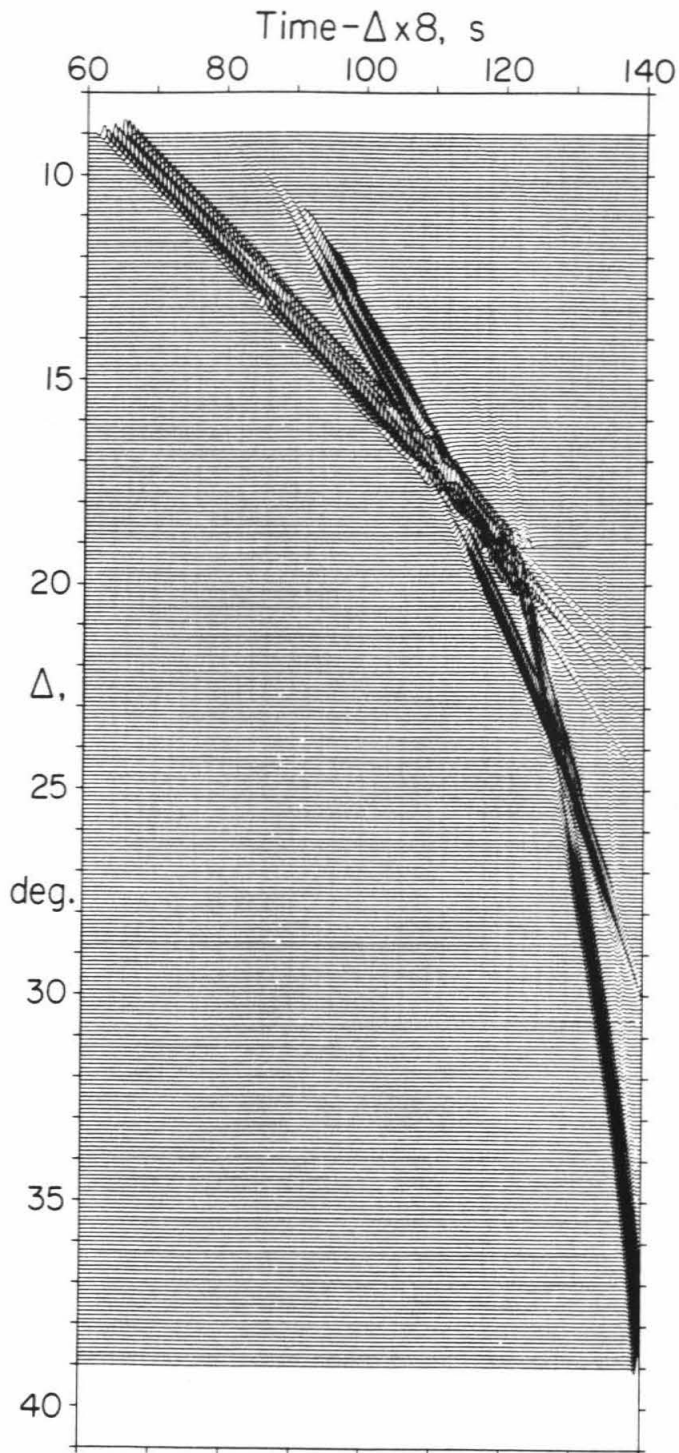image to the (p,z) plane.

Figure 2.9 Same as Figure 2.5 except that three different source wavelets are used along the profile. The changeover points are at 18° and 25°.
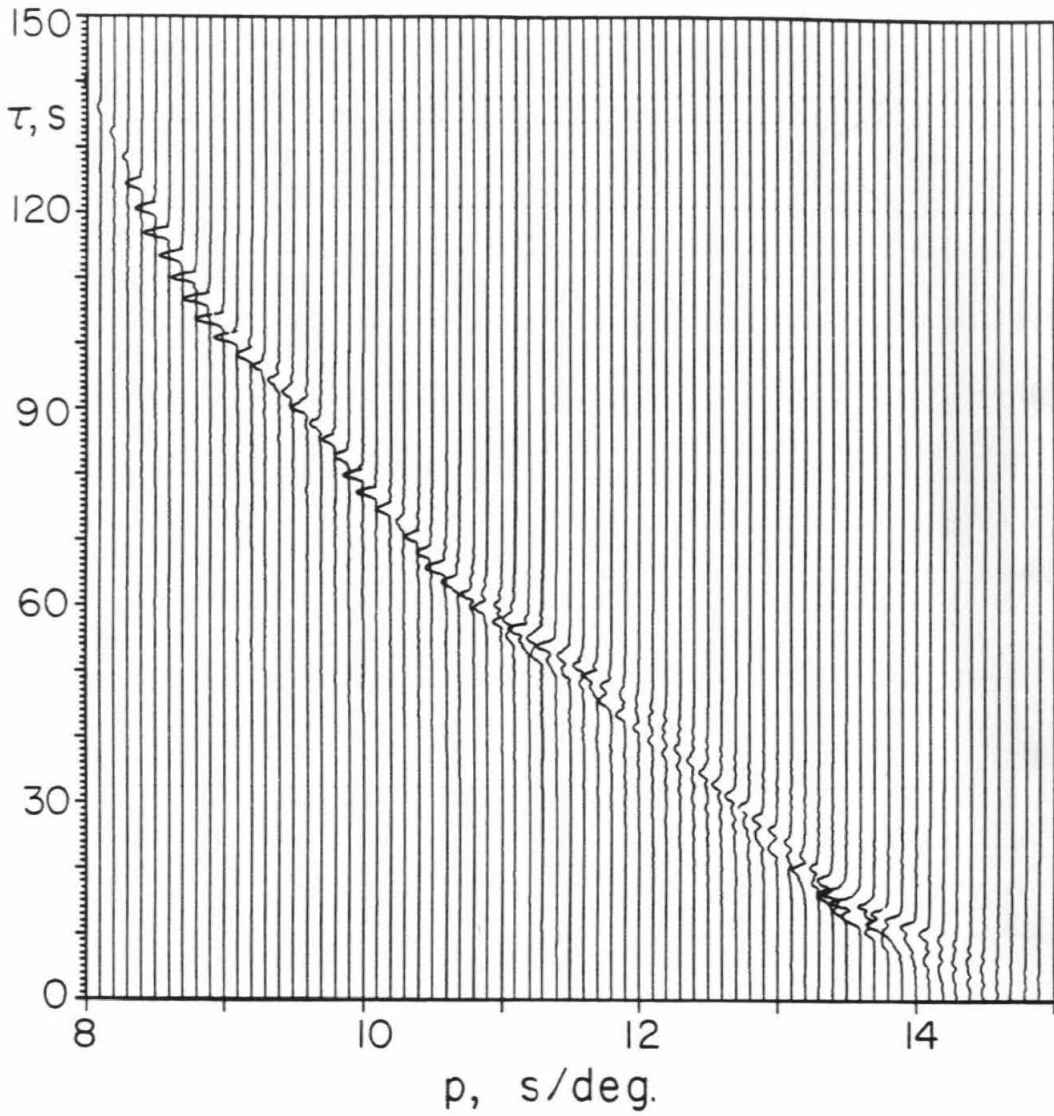
Figure 2.10 The envelope, for each p, of the slant stack of the varying source syn-
thetics presented in Figure 2.9. Compare the stack to that of Figure 2.7. The image
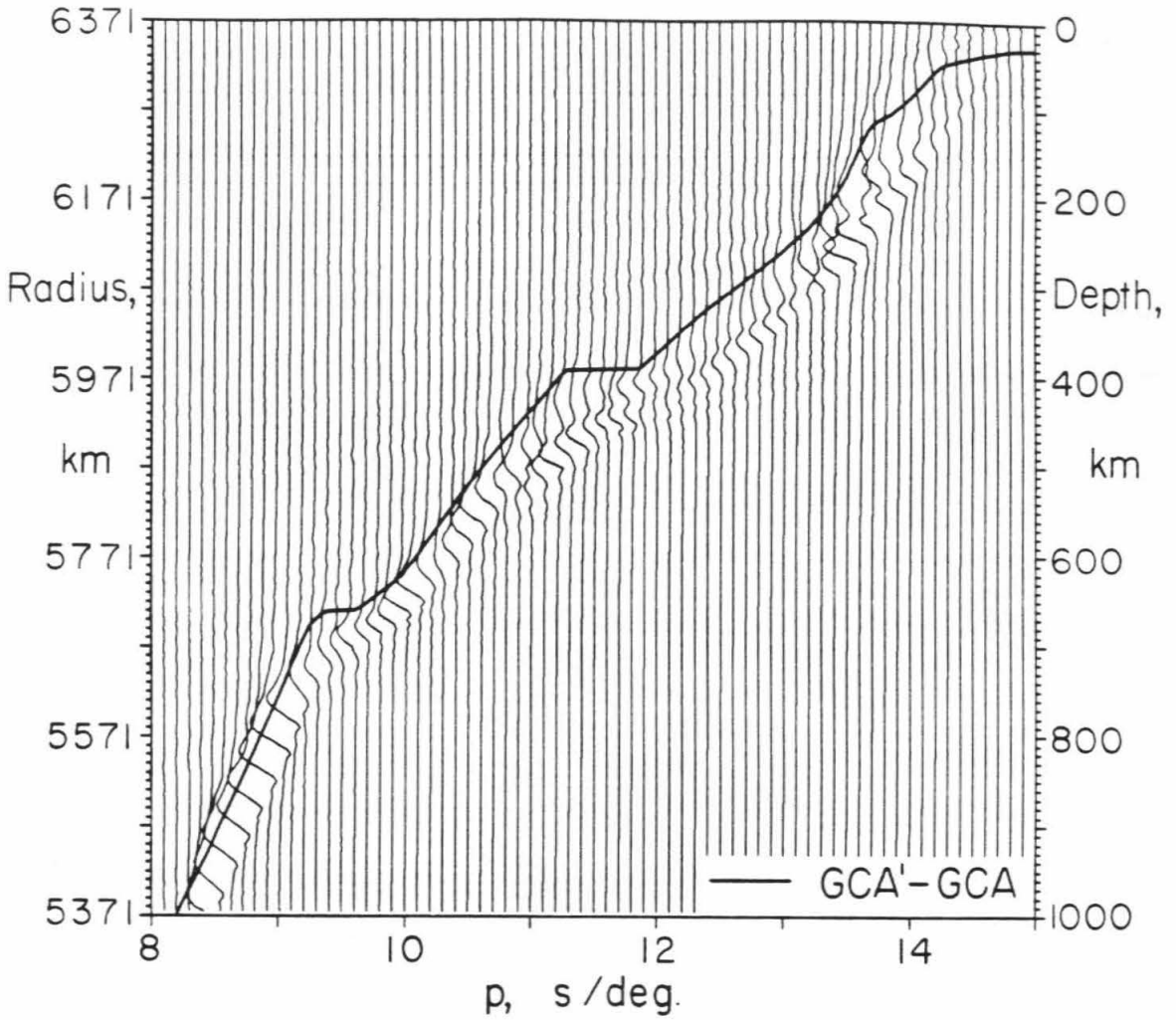is noticeably more complicated near the source changeover points.

Figure 2.11 Downward continuation with GCA'GCA (superimposed) of the stack shown in Figure 2.10. Compare this image to Figure 2.8. Here the complication of distance-varying sources has affected this method's ability to reconstruct the true slowness-depth field, even for synthetic data.

Chapter 3

The P-wave upper mantle structure beneath an active
spreading center: the Gulf of California

Introduction

The nature of lateral variations in upper mantle seismic velocities is a problem of broad geophysical interest. Velocity structure determinations for many regions can place constraints on both the scale of mantle convection and the depth extent of velocity differences between continents and ocean basins. Hager and Raefsky (1981) predict large depressions of a chemical '670 km' discontinuity beneath subducted slabs if convection is confined to the upper mantle. Sipkin and Jordan (1975, 1976) suggest that lateral differences between shields and old oceans extend to 400 km depth to satisfy multiple ScS travel times, while Okal and Anderson (1975) insist that most of the differences between shields and old oceanic ScS data are explained by heterogeneity shallower than 200 km. Recent upper mantle models for continental shields (e.g., King and Calcagnile, 1976; Given and Helmberger, 1980), 'young' continental regions (Johnson, 1967; England et al., 1977; Burdick and Helmberger, 1978; among others) and island arc regimes (Kanamori, 1967; Fukao, 1977) have been constructed using compressional body waves; these models tend to converge below 200 km.

A number of studies have measured Pn velocities for the uppermost mantle at spreading centers and continental rifts. Work in the Dead Sea Rift zone (Ginzburg et al., 1981), the Rio Grande Rift (Murdock and Jaksha, 1981) and the Salton Trough (Hearn, 1983) suggests normal Pn velocities of about 8 km/s for these features. Results from refraction lines at several oceanic ridges are more scattered. While

there is abundant evidence for very low velocities very close to the ridge axis (e. g., Tryggvason, 1962; LePichon et al., 1965; Bunch and Kennett, 1980; Hyndman and Rogers, 1981; Jackson et al., 1982), more normal speeds are also observed only a few kilometers off-axis, suggesting a very localized shallow magma chamber (Talwani et al., 1965; Keen and Tramontini, 1970; Reid et al., 1977; Bunch and Kennett, 1980). At the Mid-Atlantic Ridge, Keen and Tramontini (1970) and Jackson et al. (1982) discover evidence for significant P-wave anisotropy, as do Lewis and Garmany (1982) at the East Pacific Rise and Keen and Barrett (1971) in the northeast Pacific Ocean. Very slow teleseismic P residuals and PP residuals (Rowlett and Forsyth, 1979; Dorbath and Dorbath, 1981) prompt speculation about the deeper structure beneath ridges and rifts. For young ocean basins, several surface wave studies indicate low upper mantle velocities (Knopoff et al., 1970; Montagner and Jobert, 1981; Wielandt and Knopoff, 1982) to depths of at least 200 km. England et al. (1978) analyzed P-wave data from the North Atlantic Ocean, and Green (1978), Nolet and Mueller (1982) and Lenartowicz and Albert (1980) studied the African rift region, for which very slow teleseismic travel times have also been documented. The detailed characteristics of the upper mantle to 1000 km beneath spreading centers, however, are unknown.

We have investigated the upper mantle P-wave velocities under the Gulf of California spreading center. Mexican earthquakes recorded at the California Institute of Technology - U.S. Geological Survey Southern California Seismic Network (SCARLET) provide a unique, dense, high-quality data set. The narrow azimuthal range of the epicentral distribution results in a nearly ideal data profile. We exploit the large amount of travel time, apparent velocity ($dT/d\Delta$) and waveform data in the modeling process. While the travel times control the model's gross integral properties, the

$dT/d\Delta$ measurements provide information about the absolute velocities at the rays' turning points. The relative amplitudes of phases are most sensitive to the velocity gradients near the bottoming points. We combine these data by first inverting the travel times, perturbing that model to fit the p-Δ data, and then performing trial-and-error synthetic seismogram modeling to fit the short-period waveforms. The consistency between the model and data is checked using the wave field continuation technique (see Chapter 2). The final model satisfies all three data types for all observed ranges.

Many earlier upper mantle studies (e.g., Hales, 1972; Massé, 1973, 1974; Green, 1978) use only travel times to constrain the velocity structure. Other investigators (Johnson, 1967; Simpson et al., 1974; Ram and Mereu, 1977; King and Calcagnile, 1976; Ram et al., 1978; England et al., 1977, 1978; and others) utilize data from seismic arrays; the direct measurements of apparent phase velocities for different travel time branches place additional constraints on mantle structure. Wave field continuation (Clayton and McMechan, 1981) utilizes each entire seismogram in the inversion. The elegance and power of wave field continuation is demonstrated with synthetic data examples in Chapter 2. Ours is the first application of this method to teleseismic data; later in this chapter we test its structural resolving power on a suite of actual seismograms. Synthetic seismogram modeling, as used in this chapter, incorporates relative amplitudes into the inversion process while retaining the other information, providing, in conjunction with other techniques, a more complete data analysis. Helmberger and Wiggins(1971), Wiggins and Helmberger (1973), Dey-Sarkar and Wiggins (1976) and McMechan (1979) have demonstrated the usefulness of short-period synthetic seismogram modeling for upper mantle structure. Their studies employ explosions or earthquakes recorded at widely separated

receivers. The application of synthetic modeling to the array data is very successful because the dense station spacing makes phase identification less ambiguous. While short-period waveforms are not as stable as the equivalent long-period data, tele-seismic waveforms recorded across the 5° aperture of SCARLET are very reproducible, indicating good stability for simple events. Our final model represents a synthesis of differing constraints and results in a well-resolved, detailed view of the upper mantle under or near an active oceanic ridge.

The data set

The seismically active areas of the Gulf of California, Rivera Fracture Zone, East Pacific Rise, and Middle America Trench are the source regions for this study. Figure 3.1 illustrates the experimental geometry, including 2° arcs drawn at the travel path midpoints of the 22 events at distances of less than 30°. Clearly, the upper mantle sampled by these earthquakes is not influenced by the Middle America Trench, but represents the Gulf of California and adjacent extensional areas. Spreading initiated in the Gulf of California about 4 million years (m.y.) ago (Larson, 1972) but a proto-Gulf, probably a broad rift zone, may have appeared 10-15 m.y. before the present (Karig and Jensky, 1972). The dominant faults within the Gulf are en echelon fracture zones oriented in a northwest-southeast direction (Bischoff and Henyey, 1974); these are directly related to the sea-floor spreading process. The events occurring on the fracture zones have strike-slip mechanisms oriented unfavorably for P-wave radiation to SCARLET, and tend to have complicated source signatures. Most of these events are closer than 20°. The subduction zone earthquakes, on the other hand, at epicentral distances greater than 18°, are dip-slip events, which produce
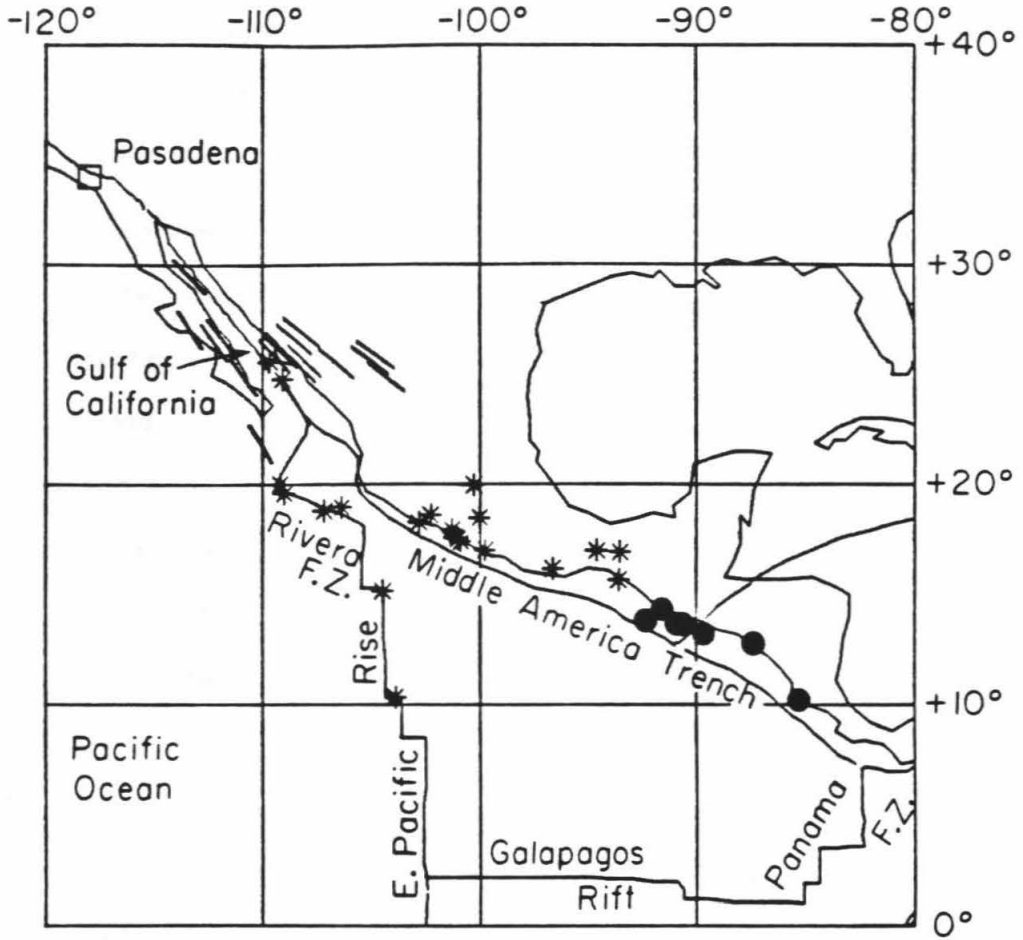
Figure 3.1 Location map for this study. Stars are epicenters of the 22 earthquakes closer than 30°. Small (2°) portions of the great circles between SCARLET and the events are also shown, indicating the area covered by model GCA. Note that all the arc segments fall within the region affected by the Gulf's spreading. Dots locate the calibration events which are farther than 30° from Pasadena.

ample P-wave energy and are often simple in character. The events range in distance from 9° to 40° and occur in the narrow event-station azimuth band of 310° to 345°. Varying in depth from 10 km to 150 km, they have body-wave magnitudes of 5.0 to 6.3. All events occurred between September, 1977 and December, 1979, and are listed with the PDE epicentral information in Table 3.1.

Each earthquake is recorded by the short-period vertical, digital, triggered CEDAR system (Johnson, 1979) at the California Institute of Technology. In its current configuration SCARLET has more than 200 stations; from 1977 to 1979 a well-recorded teleseism would trigger 120 stations, about 60 of which fit the criteria for inclusion in the data set (Figure 3.2). Elongate in the northwest-southeast direction, the array has an aperture of 5° and irregular station spacing averaging 25 km. Although the array stations have varying instrumentation, the responses are very similar at 1 Hz, the predominant frequency of the teleseismic signal.

Over 1400 digital seismograms were collected from the 29 events, yielding 1753 travel times including 438 which are secondary arrivals. In addition, we obtained 58 direct measurements of the ray parameter, $dT/d\Delta$, spanning the 31° distance range. Figures 3.3, 3.4, 3.5, and 3.6 show examples of record sections for several events at different distances. Because SCARLET is not well-calibrated, only relative amplitudes are used, and each trace is scaled to its maximum amplitude. Adjacent records are very similar, indicating excellent waveform stability across the array. The events in Figures 3.4, 3.5, and 3.6 are all simple and impulsive, allowing unambiguous selection of secondary phases. Each record section covers 4°-5° in distance and collapses about 10° of azimuthal variation onto a plane. Distances in Figures 3.3-3.6 are not corrected for event depth. Portions of interesting upper mantle triplication phases are visible for each event, but a more complete picture is

Table 3.1
Epicentral Information

Event		Date		Origin Time			Lat.	Long.	Depth	Mag.
No.	Day	Mo.	Year	Hr.	Min.	S.	deg.	deg.	km	m_b
1	28	Feb.	1979	20	10	20.2	17 35.40	-101 0.30	54.	5.1
2	21	Sep.	1977	13	15	57.3	20 01.98	-109 9.24	33.	5.7
3	10	Dec.	1978	06	39	55.3	25 36.42	-109 38.58	15.	5.3
4	26	Oct.	1978	11	35	27.1	17 58.38	-106 20.76	33.	5.2
5	26	Jan.	1979	10	04	32.0	17 24.78	-100 52.62	41.	5.8
6	29	Nov.	1978	20	49	48.8	16 11.10	-96 37.80	22.	5.7
7	25	Dec.	1978	23	57	55.0	10 21.96	-103 51.90	10.	5.8
8	19	Mar.	1978	01	39	14.0	17 01.56	-99 44.10	36.	5.8
9	22	Jun.	1979	06	30	54.3	17 0.00	-94 36.34	107.	6.3
10	30	May	1978	11	15	41.0	24 48.42	-109 03.36	10.	5.0
11	10	Sep.	1978	23	24	15.6	14 16.20	-91 29.82	94.	5.6
12	11	Jan.	1978	20	05	24.2	18 48.24	-107 08.40	33.	5.4
13	18	Dec.	1978	07	59	19.6	19 36.42	-108 58.56	33.	5.2
14	29	Sep.	1978	16	21	41.0	18 36.90	-102 15.72	96.	5.5
15	22	Feb.	1979	09	16	37.0	19 58.80	-100 16.08	56.	5.3
16	06	Jan.	1979	11	51	30.7	18 16.20	-102 47.10	38.	5.2
17	05	Jul.	1978	20	15	16.3	18 29.22	-100 0.42	62.	5.6
18	23	Aug.	1978	00	38	32.2	10 12.24	-85 13.32	56.	5.7
19	27	Oct.	1979	14	35	57.3	13 49.98	-90 52.86	58.	5.7
20	06	Dec.	1978	11	53	34.0	13 08.70	-89 38.10	33.	5.8
21	27	Oct.	1979	21	43	24.9	13 46.68	-90 43.80	65.	5.6
22	31	May	1978	01	07	22.4	12 46.02	-87 09.42	76.	5.4
23	06	Dec.	1978	14	26	52.6	13 42.78	-92 17.28	32.	5.7
24	14	Mar.	1979	12	01	24.8	17 57.12	-101 16.98	52.	5.5
25	18	Mar.	1979	20	12	31.7	17 32.76	-100 59.46	33.	5.4
26	22	Oct.	1978	14	07	0.2	15 10.56	-104 26.88	33.	5.2
27	4	Jun.	1979	06	26	42.7	15 41.04	-93 35.76	80.	5.7
28	10	Jan.	1979	13	24	14.3	16 56.64	-93 32.58	156.	5.6
29	26	Jan.	1979	17	10	44.1	17 33.24	-100 59.28	39.	5.4

The epicentral data are taken from the PDE Monthly Listings of
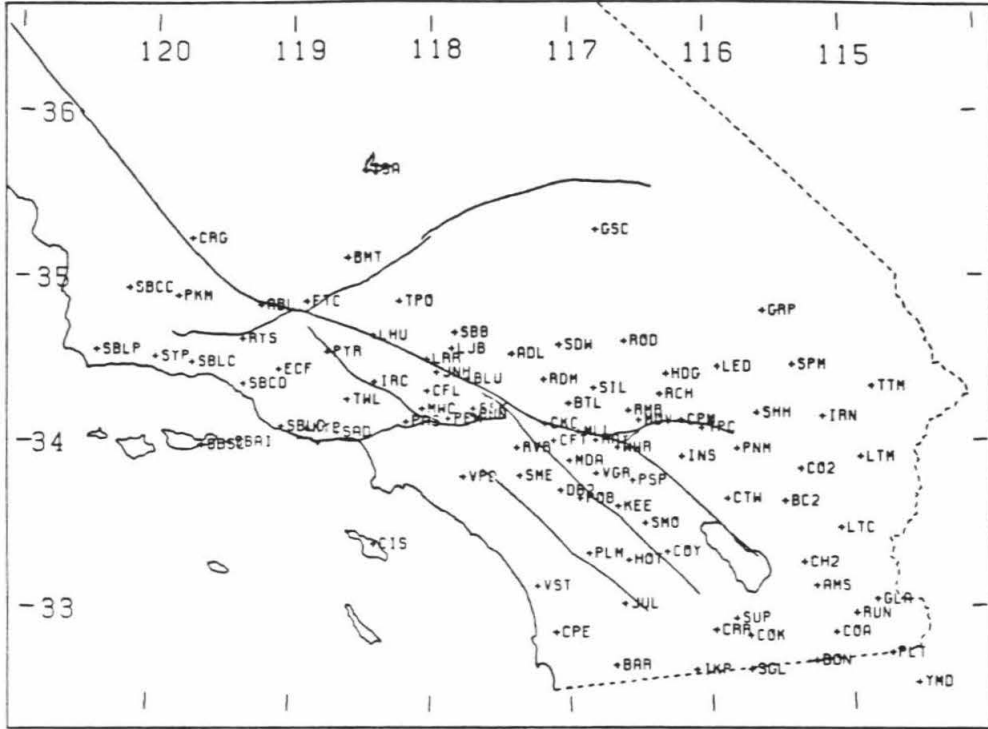the U. S. Geological Survey.

Figure 3.2 Stations of the southern Califonia array used in this chapter. Empirical corrections for these 96 stations are shown in Figure 3.9. Latitude is in degrees north, longitude in degrees west.
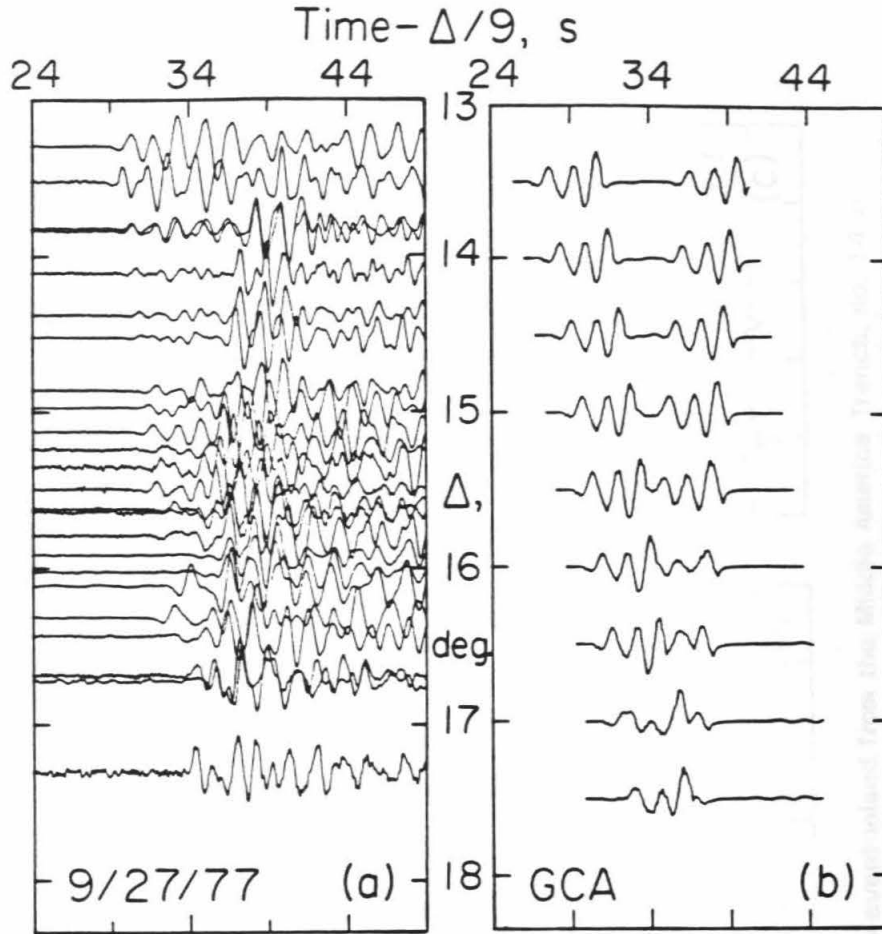
Figure 3.3 An example of an event record section recorded at SCARLET along with the synthetic section predicted by model GCA. Distances are not corrected for event depth. Amplitudes are scaled to the maximum of each trace. Empirical station corrections (Figure 3.9) have been applied, and the data have been filtered with a bandpass of .01 to 5 Hz. For clarity, only a few representative seismograms are shown. a) A shallow event on the Rivera Fracture Zone (no. 2 in Table 3.1) which shows a weak first arrival followed by the reflection from the 390 km discontinuity. b) Synthetic section for the same event.
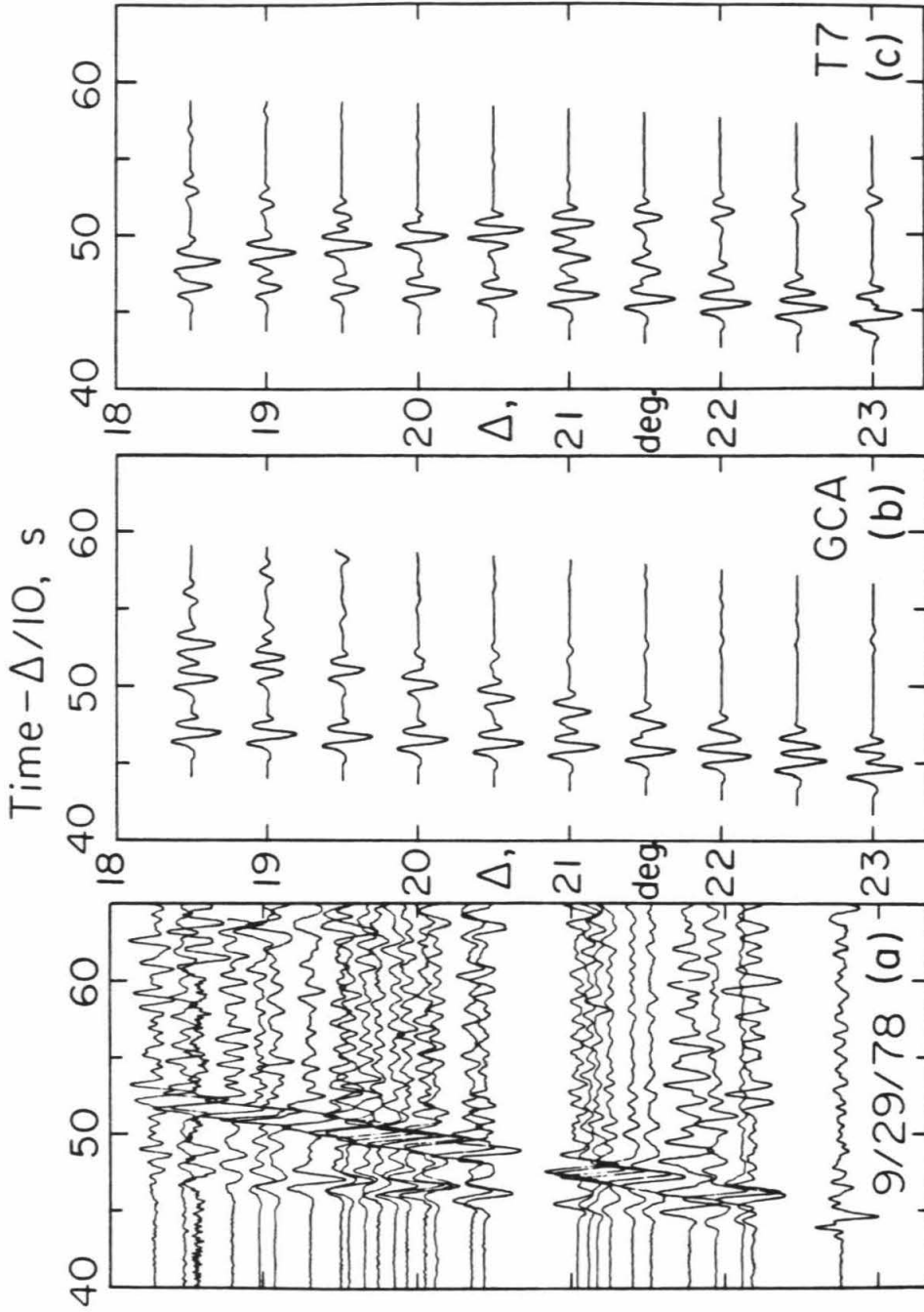
Figure 3.4 a) A 96 km deep event inland from the Middle America Trench, no. 14 in Table 3.1. Note the increasing strength of the first arrival near 20° and the strong arrival from the 660 km discontinuity. Also the 'back branch' of the 390 km triplication (see Figure 3.10b) is not in evidence. See Figure 3.3 for format explanation. b) Synthetic section for event 14 using GCA. c) Synthetic section for the same event for model T7 (Burdick and Helmberger, 1978). Note the strong AB branch extending to 22°, which is not visible in the data.
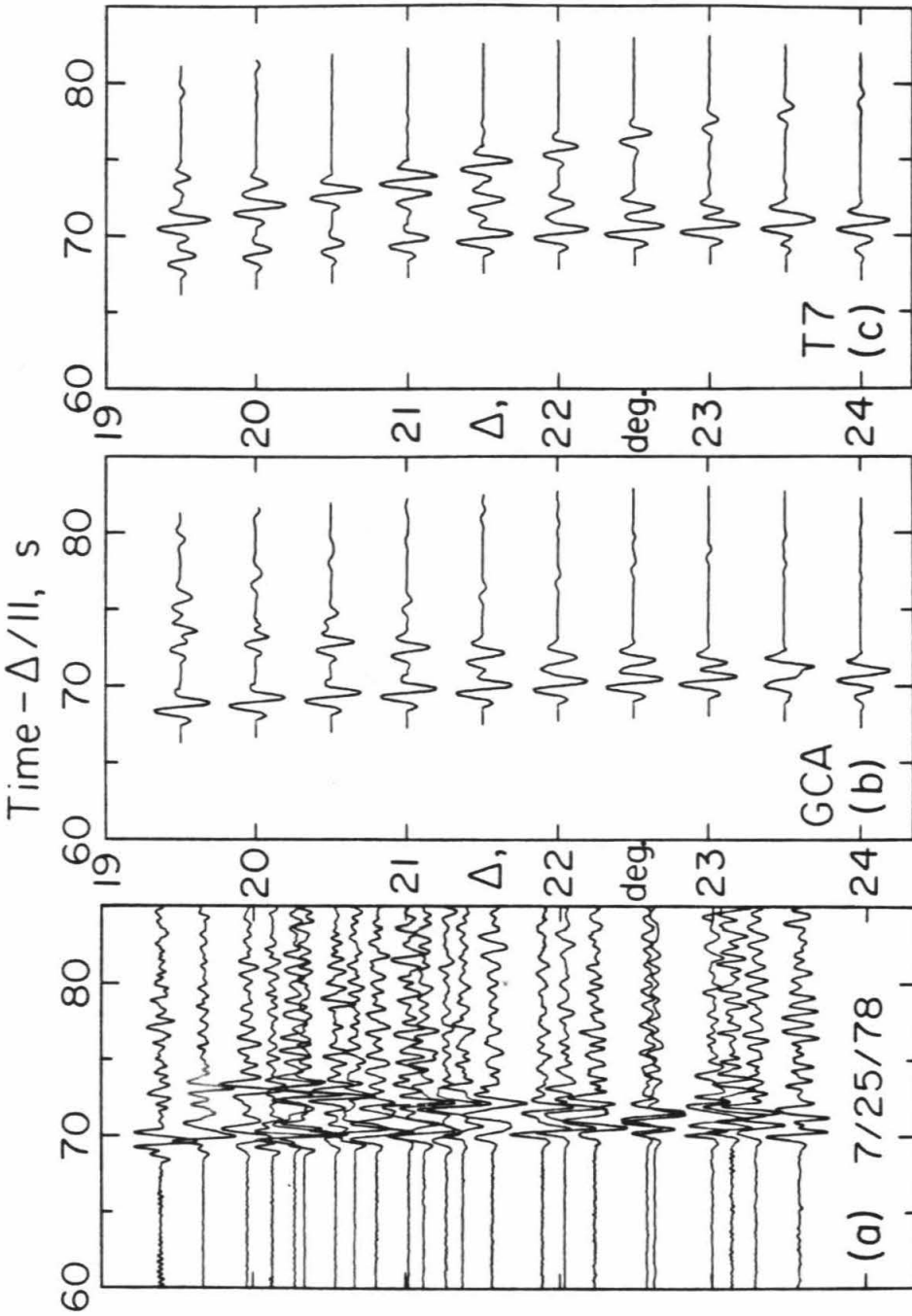
Figure 3.5 a) Format is the same as Figure 3.3. No. 17 of Table 3.1 is 56 km deep.
Again a strong first arrival and reflection from the 660 km velocity discontinuity are
visible with no sign of the AB travel time branch past 20°. b) GCA synthetic section
for event 17. c) T7 synthetic section for event 17. Again the AB branch is a very
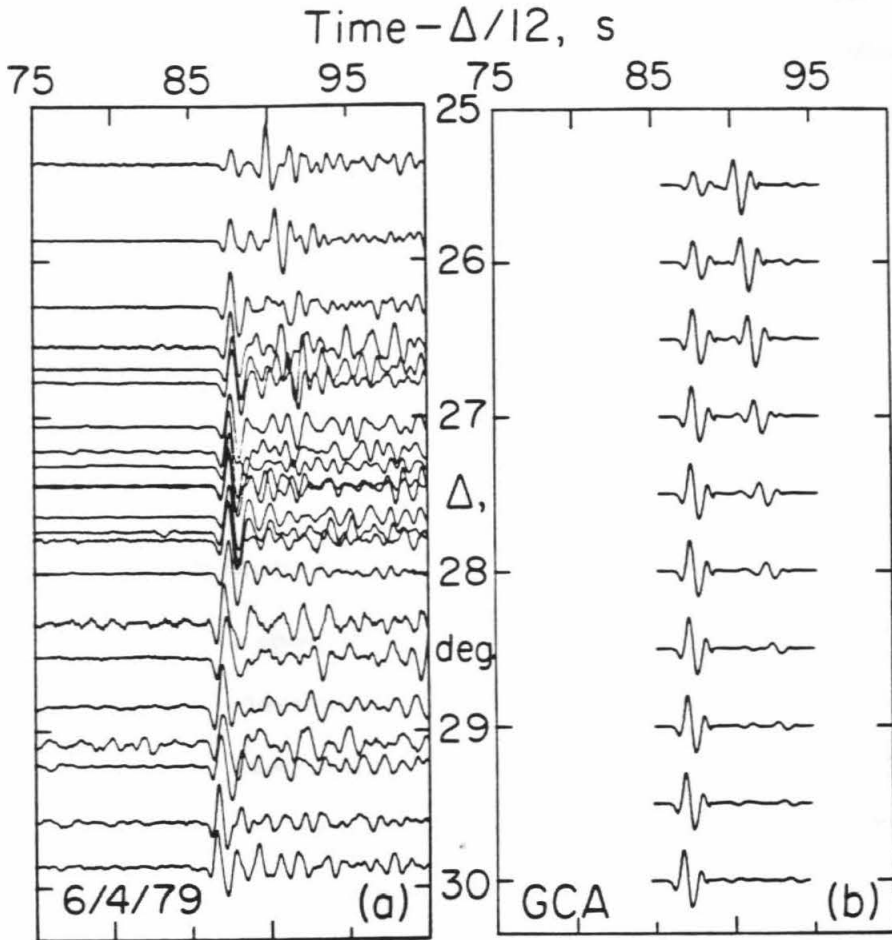strong phase in these synthetic seismograms, but not observed in the data.

Figure 3.6 a) No. 27 (Table 3.1), in the same format as Figure 3.3. Here the back branch of the 660 km triplication moves out with increasing distance, and the relative amplitudes change from a weak first arrival near 26° to a simple pulse near 28°. b) GCA synthetic section for event 27.

obtained by combining the 10 cleanest events covering the entire distance range into one record section (Figure 3.7). This representation contains 473 depth-corrected seismograms with an average data spacing of 8 km. Inclusion of all available data reduces the spacing to less than 5 km. Secondary arrivals from both the '400 km' and '670 km' discontinuities are seen clearly from $14°$ to $28°$. These high-quality data prompt careful and complete data analysis to insure a robust, detailed upper mantle model.

Data preparation and analysis

Receiver structure in southern California

An area of complex geology and present-day tectonic activity, southern California has a complicated, heterogeneous crust and uppermost mantle structure which affects incoming teleseismic signals (see Chapter 1 for a detailed discussion). The large amount of available data (both local and teleseismic events) has prompted several studies probing the nature of the receiver structure beneath SCARLET. Kanamori and Hadley (1975) report on the region's upper crustal velocities; Lamanuzzi (1981) and Hearn (1983) have investigated gross crustal and upper mantle properties using Pn travel times. Teleseismic P arrivals were used in upper mantle heterogeneity studies by Hadley and Kanamori (1977), Raikes and Hadley (1979), Raikes (1980) and in Chapter 1 of this thesis. The spatial pattern of the strong azimuthal variation of teleseismic P residuals (Raikes, 1980) is consistent with a high-velocity body in the upper mantle beneath the Transverse Ranges in southern California, first proposed by Hadley and Kanamori (1977) and verified in Chapter 1.
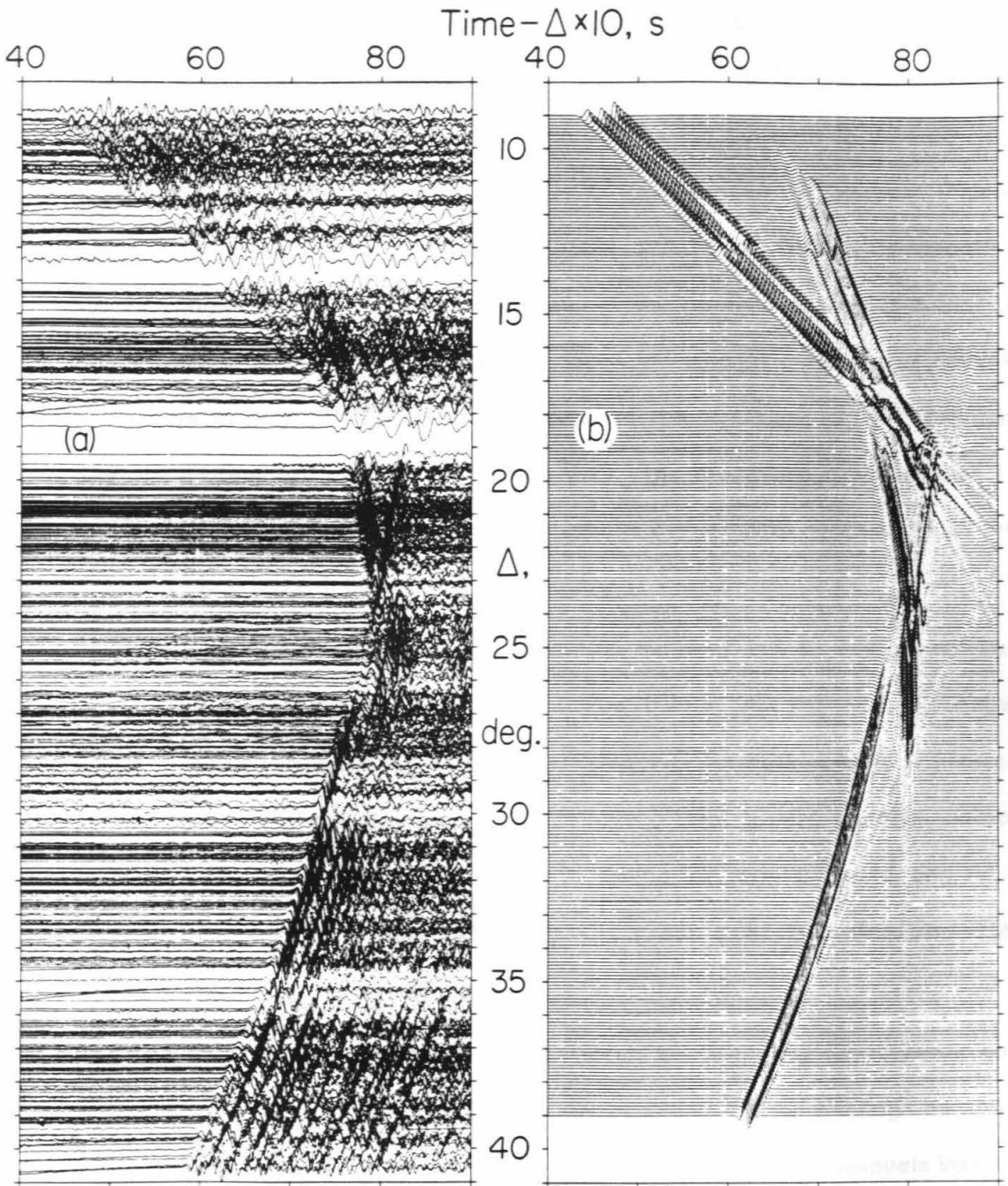
Figure 3.7 a) Data record section of 10 events spanning 9° to 40°. Amplitudes and filtering are as in Figure 3.3. Station and depth corrections have been applied. The mantle triplication phases are clearly visible. b) Synthetic record section for GCA on the same scale, computed for surface focus. Source wavelets vary with distance.

Correcting for near-receiver velocity variations in a multi-azimuth data set in this complex area could require detailed ray tracing, but for our 'single' azimuth data a simpler approach was adopted. We constructed station corrections derived from travel times of more distant ($30° < \Delta < 40°$) Central American earthquakes (Figure 3.1, Table 3.1) in the same azimuth band. These events are free of complicating upper mantle phases, yet the rays are incident at the receiver at angles similar to the closer events. Planes are fit to arrival times using least-squares for several large, impulsive events; the station corrections are the averaged station residuals from the plane-predicted arrival times (Table 3.2). The procedure assumes that 1) constant corrections are appropriate over the entire $30°$ azimuth spread and 2) the travel-time curve is smooth beyond $30°$ in distance.

The seven distant events have a total azimuth range of only $8°$ and are remarkably consistent: 96 stations have average residual values with standard deviations of less than 0.10 s (shown in Figure 3.2). Our empirical corrections include effects of both local structure and elevation, and thus are biased toward positive values; these adjustments are applied to all the data to reduce travel-time scatter and aid in identification of secondary phases. An example of a record section before and after application of the empirical corrections is shown in Figure 3.8.

We might expect a close correlation between the empirical adjustments and Raikes' (1980) teleseismic residuals for the same azimuth range. Although her data are from more distant ($\Delta \approx 55°$) earthquakes, and are single-station residuals instead of deviations to the array least-squares plane, the contour plots of the two residual sets (Figure 3.9) are similar in shape. The difference in absolute magnitude of the residuals occurs because Raikes' (1980) residuals are referenced to an individual station, GSC, instead of the plane average and have been corrected for elevation,

Table 3.2
Empirical Station Corrections
Gulf of California

Sta. Name	No. of Times	Standard Deviation, s	Empirical Corr., s	Sta. Name	No. of Times	Standard Deviation, s	Empirical Corr., s
SBB	5	0.06	-0.20	RVR	4	0.05	-0.02
VPD	4	0.07	0.33	MWC	6	0.06	0.15
PAS	7	0.08	0.11	TWL	3	0.05	0.53
IRC	3	0.01	0.10	PYR	2	0.06	-0.07
CKC	4	0.04	0.46	MDA	2	0.01	0.30
RAY	6	0.04	0.62	LRR	6	0.05	-0.01
BLU	7	0.03	0.38	ADL	3	0.07	0.38
PEM	6	0.02	0.08	BTL	6	0.03	1.08
SIL	6	0.03	0.70	SSK	5	0.07	0.14
SME	3	0.03	-0.05	RMR	7	0.04	0.63
ROD	4	0.04	0.50	ECF	5	0.07	0.67
KYP	6	0.06	0.16	SAD	4	0.05	0.27
LHU	7	0.03	-0.13	SBCD	4	0.09	0.36
SBLG	5	0.05	0.10	SBLP	3	0.06	-0.36
RYS	7	0.05	0.44	PLT	5	0.05	-0.38
PKM	4	0.04	0.25	FTC	3	0.04	0.00
BMT	6	0.05	0.03	ABL	3	0.06	0.07
RUN	6	0.05	-0.24	SGL	7	0.04	0.25
CRR	7	0.07	0.27	SUP	7	0.04	0.07
AMS	6	0.05	-0.65	LTC	6	0.05	0.00
BC2	7	0.05	0.22	CO2	6	0.03	-0.10
IRN	7	0.04	0.16	SPM	7	0.07	0.26
GRP	5	0.03	0.26	SHH	2	0.03	0.21
LED	5	0.01	0.19	INS	7	0.02	0.36
CPM	7	0.05	0.36	YMD	5	0.06	-0.09
LTM	6	0.03	0.24	TPO	6	0.05	-0.19
COY	5	0.03	0.12	HOT	7	0.03	0.44
SYP	3	0.02	0.00	KEE	7	0.02	0.29
PSP	2	0.01	0.01	CIS	5	0.07	-0.09
GLA	7	0.06	0.23	IKP	7	0.05	0.53
CPE	4	0.06	0.03	VST	7	0.04	-0.07
PLM	7	0.03	0.60	TPC	7	0.05	0.25
ISA	3	0.05	0.48	GSC	5	0.04	0.28
SBLC	3	0.04	-0.07	SBCC	7	0.09	0.17
SDW	6	0.02	0.17	LJB	7	0.03	-0.23
HDG	5	0.02	0.45	TTM	6	0.09	0.23
JNH	6	0.04	0.13	CTW	7	0.04	0.09
POB	4	0.03	0.28	SMO	6	0.03	0.39
CH2	6	0.05	-0.44	JUL	6	0.06	0.00
COA	4	0.05	-0.13	BAR	6	0.06	0.04
VG2	6	0.02	0.32	WWR	6	0.03	0.23

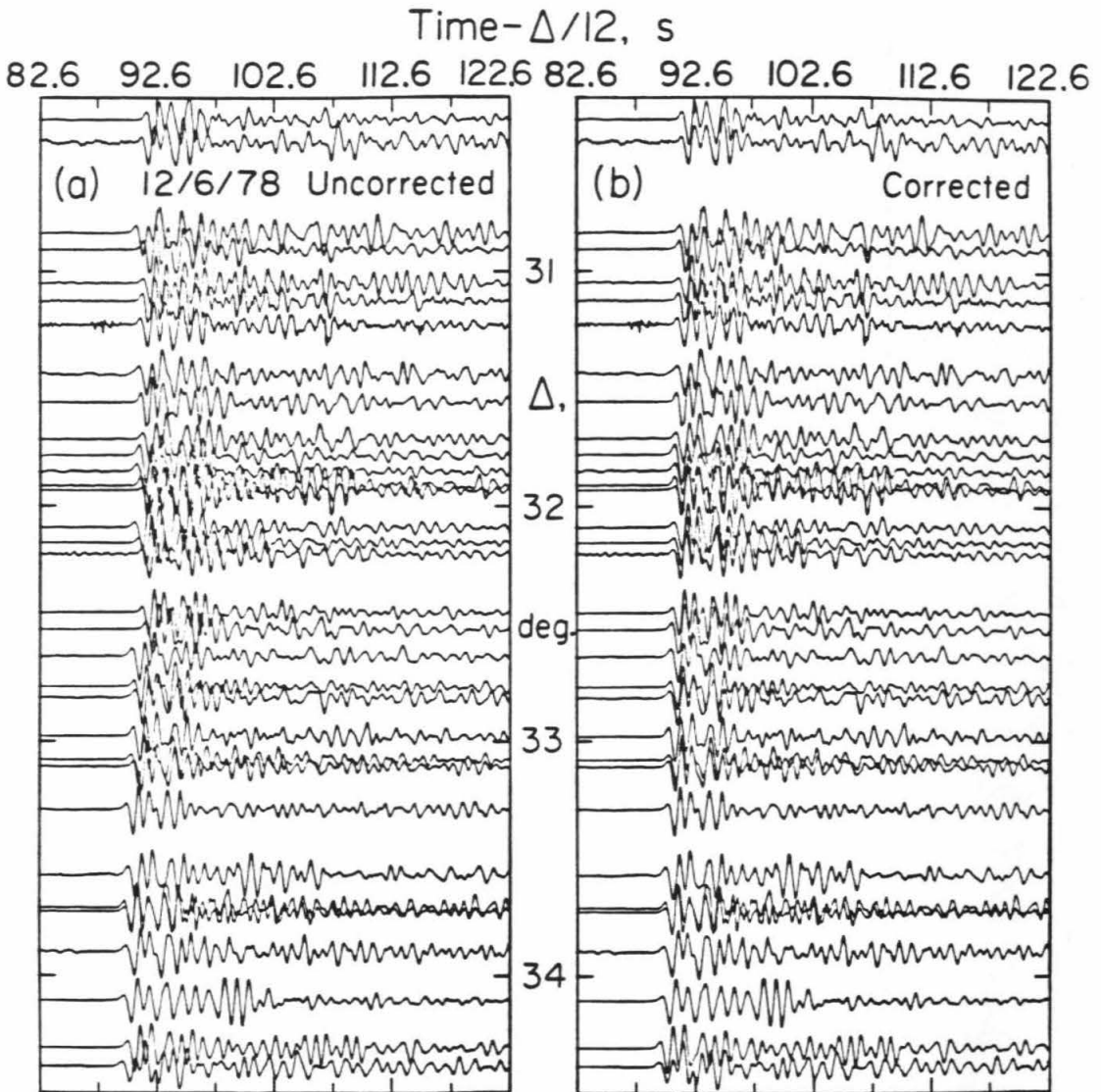| Sta. Name	No. of Times	Standard Deviation, s	Empirical Corr., s	Sta. Name	No. of Times	Standard Deviation, s	Empirical Corr., s
RDM	3	0.04	0.46	MLL	2	0.06	0.53
MOV	7	0.05	0.52	CRG	3	0.05	0.44
SBSC	4	0.06	-0.06	SBAI	2	0.00	-0.01
CFL	2	0.01	0.20	SUN	2	0.00	0.14
RCH	2	0.02	0.25	DB2	6	0.04	0.04
BON	2	0.07	0.40	COK	2	0.02	0.39
CFT	2	0.02	0.46	PNM	6	0.07	0.07

Table 3.2, continued

Figure 3.8 Comparison of event 20 (Table 3.1) before and after application of empirical station corrections. Record sections are set up as in Figure 3.3. a) uncorrected. b) corrected. Note the improved alignment of the traces near 30.3°, 31.9°, 33.1°, and 34.4°.

Figure 3.9 A comparison between the teleseismic P residuals of Raikes (1980) and the empirical station corrections used in this study. Raikes' values (b) are referenced to station GSC and include corrections for elevation, sediments and crustal thickness which are not included in (a). Still, many similarities exist, such as relatively negative values near (35°, -118°), positive residuals at (34.5°, -116.5°), negative (fast) corrections in the Santa Barbara Channel (34°, -120°) and negative values southeast of the Imperial Valley (33°, -115°). Differences occur due to elevation, sediment cover and crustal thickness in the Peninsular Ranges (33°, -116°) and the Ventura Basin (34.5°, -119°). The contour interval is 0.2 s.

basin sediments and large-scale Moho depth variations.

Travel times

The 29 events are retrieved from magnetic tape storage and the travel times hand picked with accuracy that approaches the digitization interval, .02 s. Both direct picking and cross-correlation techniques were tested with nearly identical results. The results displayed here are for hand-picked times. Many records are low-gain or noisy; about one-half of the original seismograms are ultimately rejected, leaving about 60 records for each event. Each travel time is corrected for ellipticity, for depth (using the Jeffreys upper mantle model) and with the empirical station correction. The 1753 travel times provide a continuous curve from $9°-40°$ (Figure 3.10). Errors in the earthquakes' hypocenters and origin times still cause considerable scatter in the travel time data. These uncertainties are removed by applying baseline shifts based on the average of JB residuals in completely overlapping $0.5°$ distance windows. These shifts preserve the shape of the observed travel time curve, yet reduce the data scatter to 0.4 s; the agreement in differential travel times for secondary phases is excellent (Figure 3.10b).

Apparent velocities

The numerous high-quality travel times allow calculation of many reliable $dT/d\Delta$, or ray parameter, estimates for both primary and later arrivals. The standard plane-fitting technique (e.g., Otsuka, 1966) for phase velocity determination is used on the empirically corrected but not baseline-shifted times. Because of the great size of the array, the Earth's sphericity is taken into account according to the procedure outlined in the Appendix. Before computation begins, each event record section is
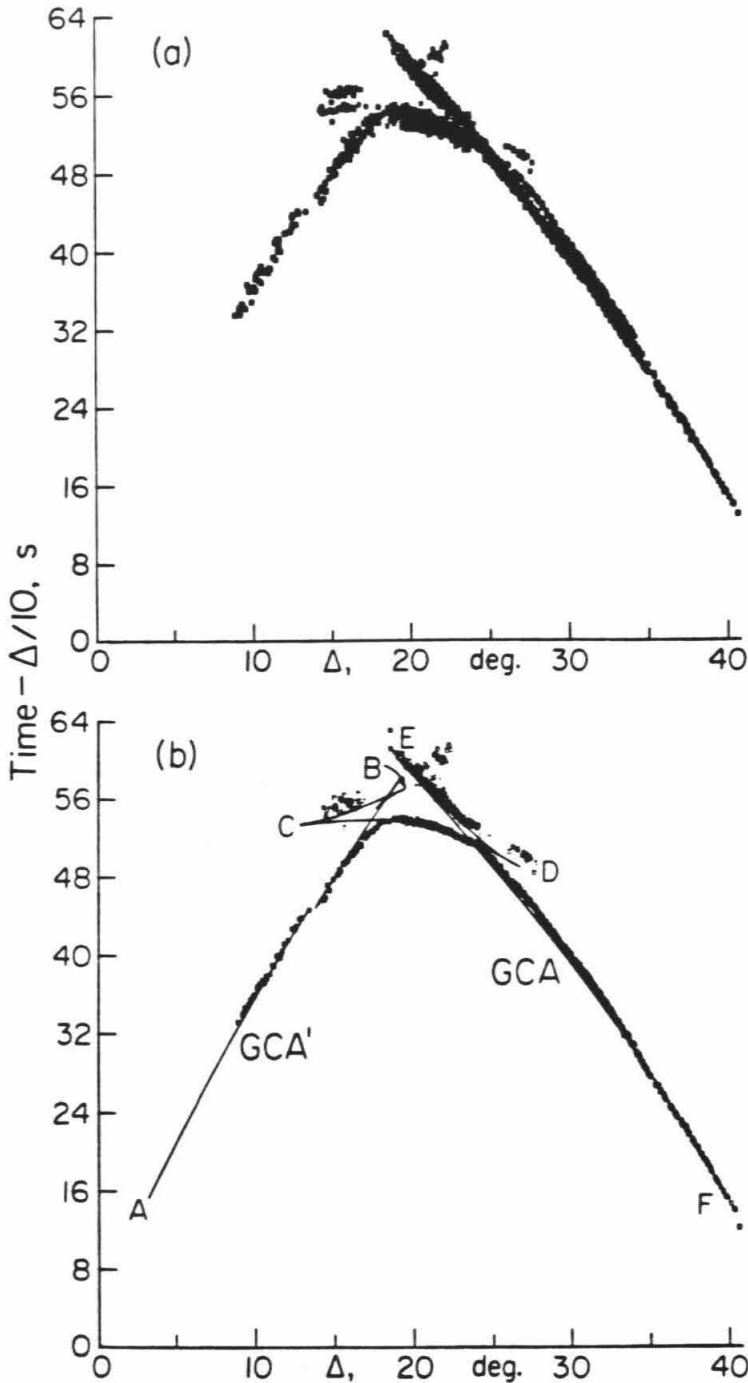
Figure 3.10 Travel time data for the 29 events. a) Travel times vs. distance, reduced by 10 km/s and corrected for elevation, depth and receiver structure. Data coverage is almost continuous from 9°-40°. There are 1753 data points; 438 are secondary arrivals. b) Models GCA and GCA' superimposed on the baseline-shifted travel times. GCA' is constructed for the axial region of the Gulf of California from only very close (9°-13°) data, while GCA represents adjacent continental areas; it has a thin lid and small low-velocity zone. The two models merge below 150 km. Data near (22°, 60 s) correspond to the anomalous p-Δ point of Figure 3.11. Letters refer to travel time branches discussed in the text.

visually inspected for changes in the travel-time slope with distance. When such a change exists, the array is divided into two sections and two ray parameter estimates are made. Measurements of dT/dΔ made with only part of the array are still stable and accurate because of the network's large number of stations.

We obtained 58 p-Δ points (Table 3.3) shown in Figure 3.11. Fourteen of the measurements are determined from later arrivals. The values have low error estimates, are stable and exhibit little scatter. Some smoothing of changes in apparent phase velocity could occur over SCARLET's 5° aperture. To test for this, the network is split in half by a northeast-southwest trending line and all p-Δ points redetermined and compared to the whole-array estimates. We found no significant differences between the 77-point split-array data set and the 58-point whole-array group. The excellent travel-time and dT/dΔ data permit standard inversions to find a reasonable starting model for synthetic seismogram modeling of the structure.

Inversions

Travel times

Instead of inverting the p-Δ curve with the classic Herglotz-Wiechert formula, we performed a direct travel time inversion using the tau method of Bessonova et al. (1974, 1976) which has advantageous statistical properties. Chapter 2 contains a detailed discussion of the scheme to estimate τ, the delay time, from travel time data.

The Mexico data set yields 36 values for τ in the p range 8.3 s/deg. to 14.0 s/deg., which roughly corresponds to distances of 10° to 40°. Typical values for n and δ_0 are 50 and .20 s, respectively, although some values are much better

Table 3.3

dT/dΔ Data

Event No.	Δ deg.	p s/deg.	RMS Error, s	Arrival Type	No. of Stations
1	21.22	10.76	.106	F	9
	22.66	10.33	.103	F	11
	21.93	9.53	.192	L	21
2	15.75	13.32	.350	F	35
	15.63	11.13	.191	L	28
3	9.79	14.44	.379	F	18
	11.65	13.56	.315	F	14
4	17.25	12.80	.240	F	22
	19.08	10.50	.157	F	11
5	21.35	10.68	.262	F	33
	23.13	10.28	.264	F	18
6	24.40	9.22	.092	F	23
	26.23	9.11	.084	F	26
	25.34	10.02	.170	L	49
7	26.83	9.00	.372	F	35
8	21.94	10.44	.160	F	22
	23.44	9.95	.293	F	28
	22.40	9.38	.277	L	32
9	25.35	9.12	.092	F	41
	27.23	9.03	.084	F	21
11	30.68	8.90	.031	F	55
12	16.77	12.81	.193	F	14
	18.75	11.88	.257	F	6
13	15.98	13.46	.220	F	20
	15.85	11.32	.285	L	30
14	20.56	10.75	.201	F	37
	22.34	10.54	.149	F	15
	20.79	9.46	.332	L	57
15	20.10	10.80	.168	F	31
	21.61	10.63	.107	F	11
16	19.62	10.97	.333	F	21
	21.73	10.24	.267	F	10
	20.35	9.43	.423	L	34
17	21.29	10.46	.129	F	34
	23.21	10.03	.173	F	14
	21.90	9.63	.214	L	45
18	37.91	8.42	.048	F	77
19	31.44	8.85	.039	F	76
20	32.59	8.79	.035	F	77
21	31.57	8.85	.039	F	74
22	34.59	8.68	.035	F	52
23	30.44	8.86	.040	F	71

dT/dΔ Data

Event No.	Δ deg.	p s/deg.	RMS Error, s	Arrival Type	No. of Stations
24	20.80	10.85	.183	F	34
	22.43	10.40	.157	F	22
	21.28	9.44	.332	L	50
25	20.89	10.72	.138	F	20
	22.45	10.42	.153	F	17
	21.63	9.49	.249	L	36
26	21.26	10.81	.244	F	25
	23.18	10.03	.268	F	10
	22.04	9.49	.810	L	34
	21.55	12.06	.332	L	25
27	28.23	9.00	.063	F	61
	27.02	9.91	.225	L	16
28	28.01	9.00	.054	F	45
29	20.96	10.71	.152	F	18
	22.67	10.46	.147	F	15
	21.79	9.55	.187	L	29

Table 3.3, continued.

For the dT/dΔ data, F denotes first arrivals, while L means later-arriving phases. The dT/dΔ determination for event 10 is unreliable and was discarded. The listed error estimate is that of the least-squares plane fit to the travel times. Arrival data are used only for the 96 stations which have empirical receiver corrections.
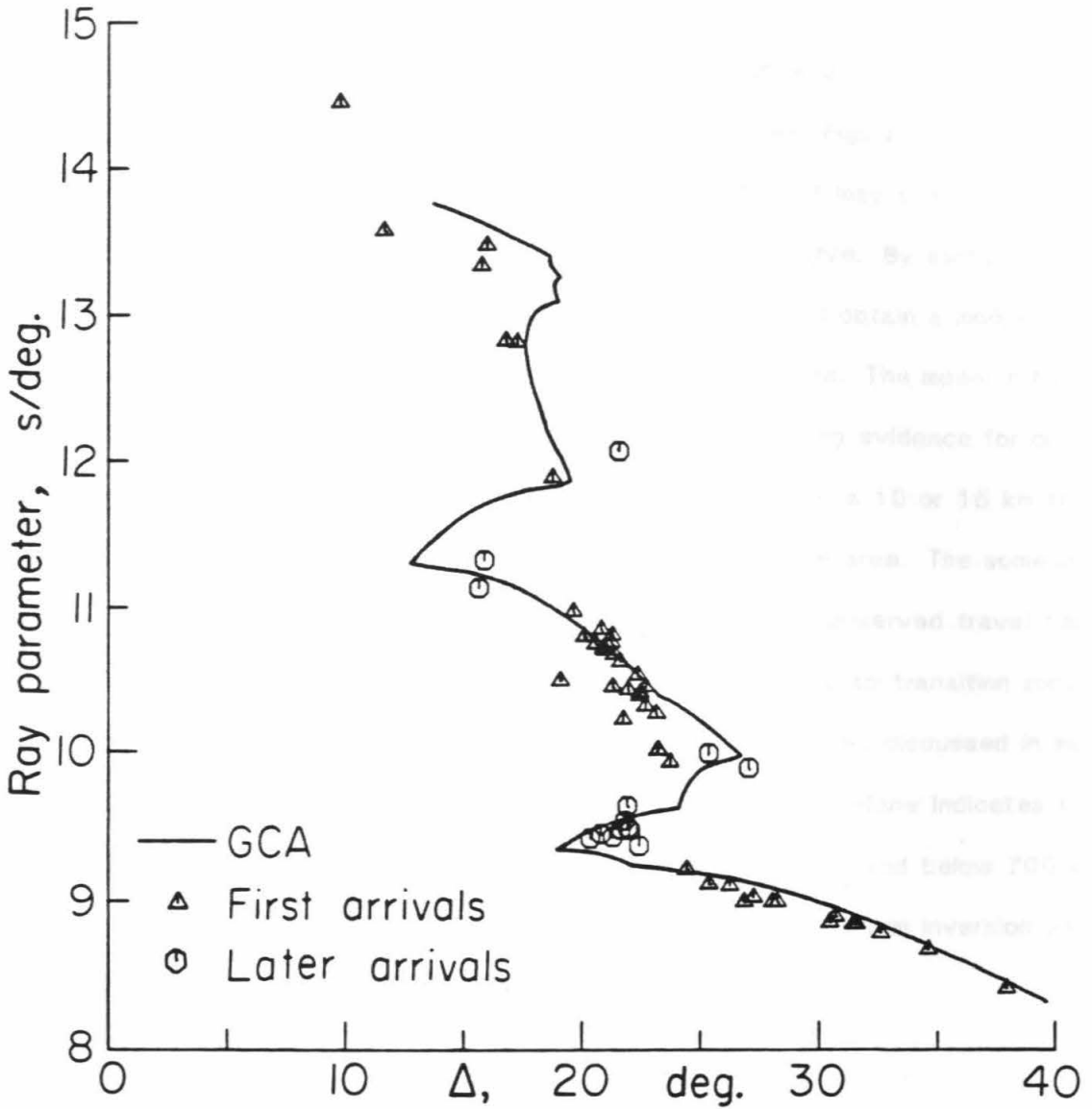
Figure 3.11 The 58 p-Δ points plotted with GCA. Triangles indicate measurements made with first arrivals; circles are secondary phases. The data point at (12.0s/deg., 23°) is from event 26 and is discussed in the text.

determined than others. After assuming a crustal model, the tau data were inverted first for the best single velocity model, and then, incorporating the uncertainty values, for the extremal bounds allowed by the travel times (Figure 3.12). The tau method does not utilize our independent p-Δ data and thus it may produce a model that fits the travel times but not the experimental $dT/d\Delta$ curve. By perturbing the individual $\tau(p)$ values within their statistical uncertainties, we obtain a model which matches both the travel time and apparent phase velocity data. The model in Figure 3.12 has no low-velocity zone because of a lack of compelling evidence for one in the waveform data. A 32 km thick crust was used arbitrarily; a 10 or 15 km thick oceanic crust may also be appropriate to represent the model area. The somewhat gradual crust-mantle transition is required by the very slow observed travel times from $9°$ to $13°$ (see Figure 3.10). The gradient above the 400 km transition zone is controlled by one group of lower-quality data points which will be discussed in more detail in a later section. The shape of the extremal bound envelope indicates that the best-determined model depth ranges are from 450-625 km and below 700 km. This tau model is the starting point for the trial-and-error waveform inversion using synthetic seismograms.

Waveforms

In order to model our short-period data with synthetic seismograms as described in Chapter 2, we need to make estimates of the source-time function, $s(t)$, the attenuation operator, $a(t)$ and the instrument response, $i(t)$. Then we generate a mantle response, $m(t)$, from the tau model (Figure 3.12) and compute synthetic seismograms, $y(t)$, for various distances to test against the data. This trial-and-error modeling proceeds in an iterative fashion until the synthetic waveforms match,
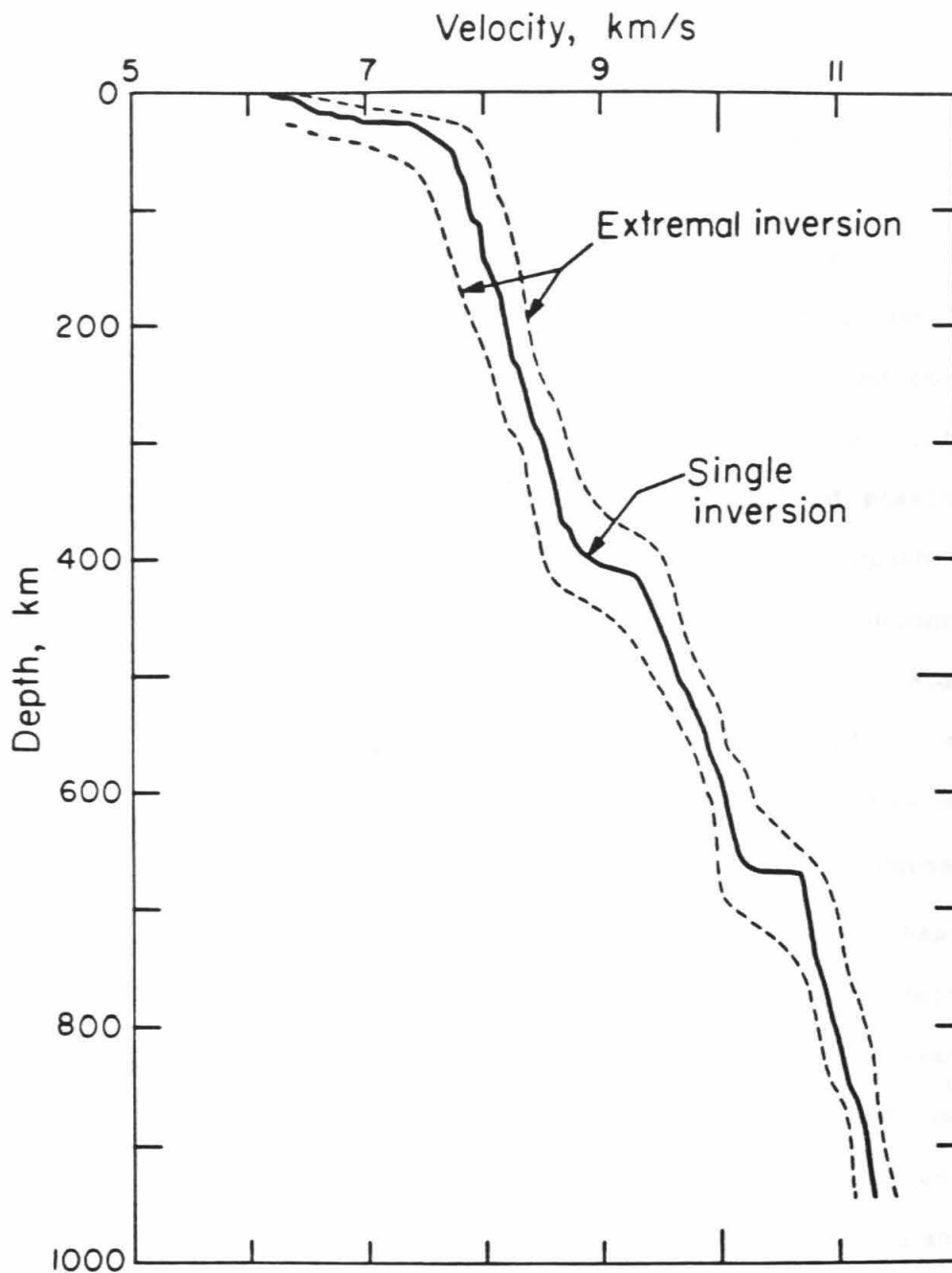
Figure 3.12 The results of tau inversion of the travel times shown in Figure 3.10. The solid line is the inversion of the best tau values, while the dotted lines represent error bounds implied by error estimates for each tau point. The single inversion model is used as the starting model for forward computations of synthetic seismograms.

in some subjective sense, the data at all distances.

The source-time functions $s(t)$ for events of $m_b \approx 5.5$ are often short (2-3 s) and impulsive, especially for subduction zone earthquakes. Thus for many of the events, a clear pulse which bottomed in a smooth portion of the mantle is the first arrival, separated from and followed by the reflected or refracted mantle-generated phase (see Figure 3.4 for an example). In this case the first arrival represents the source-time function $s(t)$ convolved with the instrument response $i(t)$; this is valid across the entire array. The attenuation operator is neglected; possible problems associated with this are discussed below. By extracting an high-quality first arrival from an actual digital seismogram to use as the source-instrument response, we eliminate source uncertainty from the modeling problem. Of course each event must be modeled with the appropriate source wavelet. Only one convolution is made in the synthetic calculation: mantle response with the source wavelet time series. Only events with simple source-time functions are used in the modeling process.

To compute the mantle Green's functions, the WKBJ method (Chapman, 1976; Wiggins, 1976) is utilized. Formulated for inhomogeneous media, this technique cannot readily accommodate causal attenuation and is not as accurate near first-order discontinuities and for grazing incidence as some other methods. It is, however, very rapid to compute WKBJ seismograms so that a wide suite of models can be tried at little expense. This modeling allows the inclusion of relative amplitude and waveform data which are sensitive to velocity gradients in the mantle. It is used to 'fine-tune' the models already derived from travel-time and $dT/d\Delta$ data.

We chose a subset of seven simple events to model, covering the distances $13°$ to $30°$. Starting from the tau model derived earlier, relative amplitude and timing problems were identified and corrected. Then the $T-\Delta$ and $p-\Delta$ plots are generated

for the revised model to insure that those parameters remain acceptable. This itera-
tive scheme is continued until all three data types are matched. The model is then
simplified as much as is possible while still matching the data. The final model, GCA, is
the result of more than 100 iterations using waveforms.

In the next section, we discuss the important features of GCA and how they
were determined. The model resolution and appropriateness are then addressed
using wave field continuation.

Relative amplitude patterns

Model GCA (Figure 3.13), which incorporates waveform data, differs consider-
ably in detail from the travel-time derived starting model (Figure 3.12). Relative
amplitudes provide constraints which eliminate many models allowed by the travel
times and imperfect ray parameter measurements. In our data set, many separate
events overlap in distance and are characterized by similar and stable relative ampli-
tude patterns, which we use in the synthetic seismogram modeling.

From $9°$ to $13°$, event signatures are generally complicated and exhibit less
consistency array-wide than do the more distant events. The two events in this dis-
tance range (nos. 3 and 10 in Table 3.1) are small, with m_bs of 5.0 and 5.3 respec-
tively. As they are located in the Gulf of California, their mechanisms are probably
strike-slip with a P-wave node facing the array; the source characteristics are com-
plex, vary with azimuth and so often result in poor records. While first arrivals are
small, no weakening trend with increasing distance or obvious secondary arrivals
argue conclusively for the presence of a well-defined low-velocity zone. Travel
times are very slow in this distance range, and apparent velocity measurements are
scattered and less reliable due to poor signal-to-noise ratios for many records.
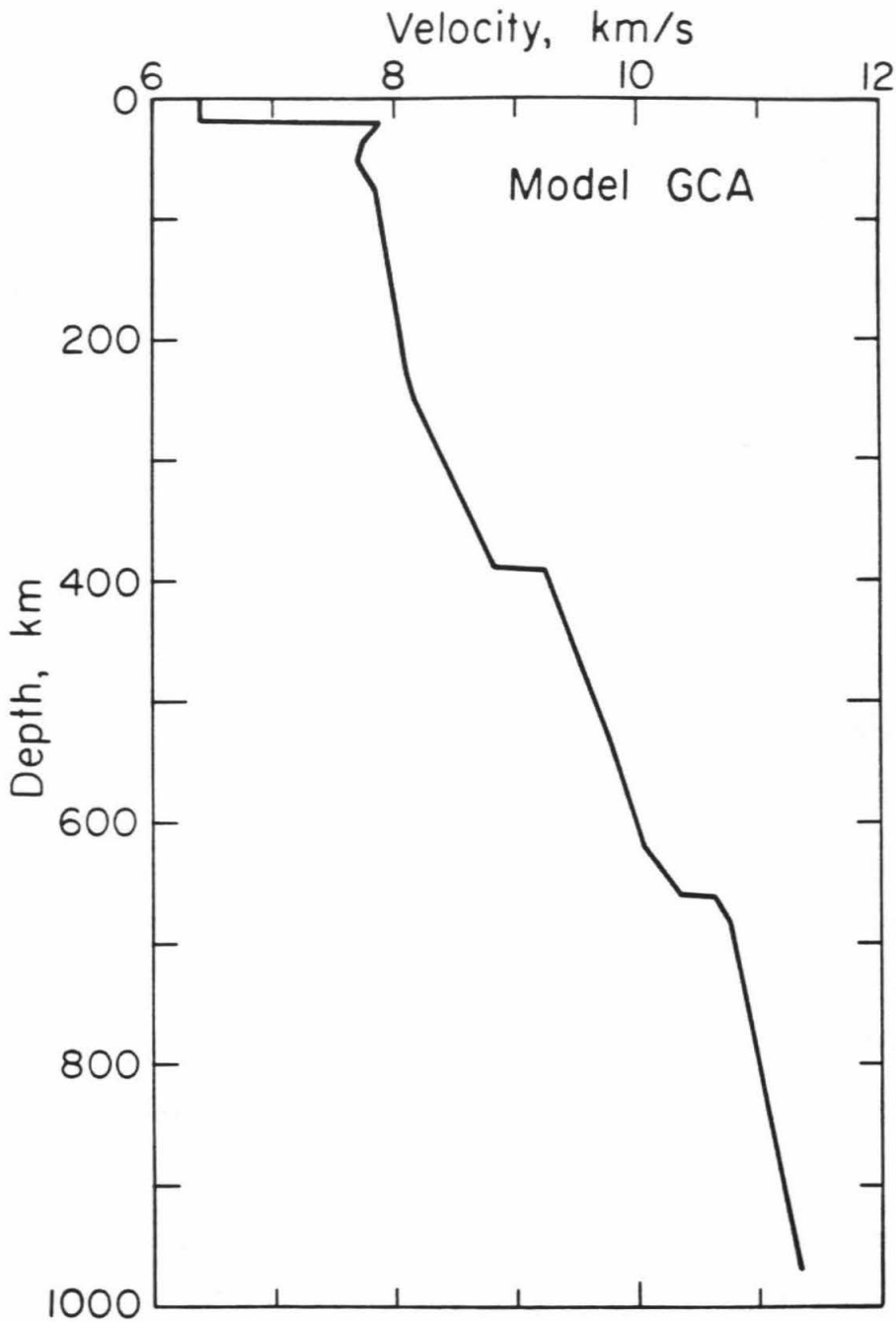
Figure 3.13 Model GCA. Valid for the Gulf of California spreading region, GCA features a 20 km crust and low velocities to 350 km depth, with an unusually large velocity gradient from 225 to 390 km. Velocity discontinuities are 4.9% at 390 km and 2.8% at 660 km.

Weak initial arrivals and energetic secondary phases characterize seismograms at distances of 14° to 18° (Figure 3.3). At 15°, the later arrival, which is the reflection from the 390 km discontinuity, is 5 s behind the first break. Near 18°, complex interference patterns develop as the later phase moves through and takes over as the first arrival. Earthquakes at these distances from Caltech occur on the Rivera Fracture Zone and many have complicated source signatures (Figure 3.3). The ray-paths for the first arrivals are entirely above 390 km depth; they are heavily affected by interactions with the seismic lid, low-velocity zone and lateral hetero-geneities. This makes accurate modeling of short-period records difficult for ranges of less than 20°.

Small near 19°, the first arriving energy increases in amplitude relative to a strong secondary phase until a distance of 21°. Now the initial-arriving energy is bottoming in the smooth portion of the mantle between 400 and 650 km. At this range both wavelets are equal in amplitude; the second wave group arrives 3 to 4 s behind the first (Figures 3.4, 3.5). The first arrival weakens near 23° and an interference pattern emerges at 24° between the two phases. This amplitude pattern is duplicated for several events in this distance range. The strong later arrival observed here is the part of the EF branch (Figure 3.10b) of the travel time curve which bottoms at the lower discontinuity. For many upper mantle models (e.g., those of King and Calcagnile, 1976; and Burdick and Helmberger, 1978), the AB branch would be moving out in this distance range with large amplitudes and would be highly visible. In Figures 3.4c and 3.5c, synthetic seismogram profiles of events 14 and 17 for model T7 (Burdick and Helmberger, 1978) are placed next to the data and GCA synthetics (Figures 3.4a, 3.4b, 3.5a, 3.5b). T7 predicts a large AB arrival where none is observed in the data. The null-observation of this travel time branch plays

an important role in the modeling process.

From 26° to 28° a secondary arrival moves out and weakens relative to the first arrival (see Figure 3.6). This is the 'back branch' of the second triplication and is part of the CD travel time branch. Seismograms become simple in character at distances beyond 28°.

Model description

The crust, uppermost mantle and low-velocity zone of GCA (Figure 3.13, Table 3.4), while subject to some bounding information, are non-unique. Above 125 km, the model parameters are adjusted mainly to agree with travel times, subject to several constraints: a single layer, 20 km crust is a compromise between the 30-km, two-layer southern California structure and a thin oceanic crust. The Pn velocity is set at 7.9 km/s, the best value for southern California (Hearn, 1983) and assumed to be appropriate for continental areas of northwest Mexico covered by GCA. Travel times beyond 13° control the integral of the size of the low-velocity zone and the absolute velocities above 125 km.

Arrivals closer than 13.5° are in the shadow zone of GCA (see Figure 3.10b). An offset in the travel time data is also observed at that distance. Figure 3.1 shows that the two closest events, in the Gulf of California, have midpoints beneath the Gulf itself, while the events from 13°-18° (nos. 2, 4, 12, 13 in Table 3.1) are located on the Rivera Fracture Zone, and their rays turn under the Baja California peninsula. The offset travel times could be due to strong lateral variations between the two regions for depths of less than 150 km. Larson (1972) observes severe lateral inhomogeneities in the Gulf of California crust for scale lengths of 100 km or less. Travel times from only events 3 and 10 (Table 3.1) and an arbitrary crustal

Table 3.4

Model GCA

Depth km	Velocity km/s	Depth km	Velocity km/s
0.	6.400	300.	8.403
19.	6.400	325.	8.520
20.	7.900	350.	8.638
35.	7.750	375.	8.750
50.	7.700	390.	8.819
75.	7.850	391.	9.250
100.	7.900	450.	9.476
125.	7.938	538.	9.800
150.	7.975	620.	10.060
175.	8.013	660.	10.360
200.	8.050	661.	10.650
225.	8.100	680.	10.760
250.	8.168	970.	11.340
275.	8.285		

structure were used in a separate tau inversion for shallow structure of the Gulf itself. Figure 3.14 shows that, in the absence of a low velocity zone that would put $9°$-$13°$ in a shadow zone, the transition from crust to mantle must be gradual for the spreading center (Figure 3.14, Table 3.5). A smooth, gradual crust-mantle transition is also documented for the Jordan-Dead Sea Rift (Ginzburg et al., 1979), the Rhine-graben (Perathoner et al., 1981) and the Reykjanes Ridge (Bunch and Kennett, 1980). The travel times of Figure 3.10b, then, can be satisfied by model GCA' (Table 3.5) for distances of less than $13°$ and GCA beyond $13.5°$. While two models are proposed based on the shift in travel times at $13°$, both GCA and GCA' satisfy the waveform data from $13°$ to $15°$ reasonably well. These two models are based on the differing crust-mantle transitions between the Gulf of California and adjacent con-tinental areas. While the Gulf itself may have no seismic lid, a gradual crust-mantle transition and no velocity reversal, the continental portion of the study area, with more usual Pn velocities, requires a region of negative velocity gradient to satisfy travel time data.

Tighter constraints on the model shape begin at depths of 125 km. The small amplitude first arrivals from $15°$ to $17°$ require a very slight positive velocity gra-dient between 125 and 225 km (see Figures 3.3, 3.15). A model for the western United States, T7 of Burdick and Helmberger (1978), has a more moderate gradient in this distance range and produces large first arrivals at $15°$ (Figure 3.15). The first arrivals of GCA are still large relative to the 390-km reflection at these distances, but Q may have an important effect here. The initial arrivals spend more time in the highly-attenuating asthenosphere than do the mantle reflections. The synthetic fits in this distance range are not as satisfying as at greater distances. As mentioned earlier, waveforms for this range are the result of complex interaction with shallow
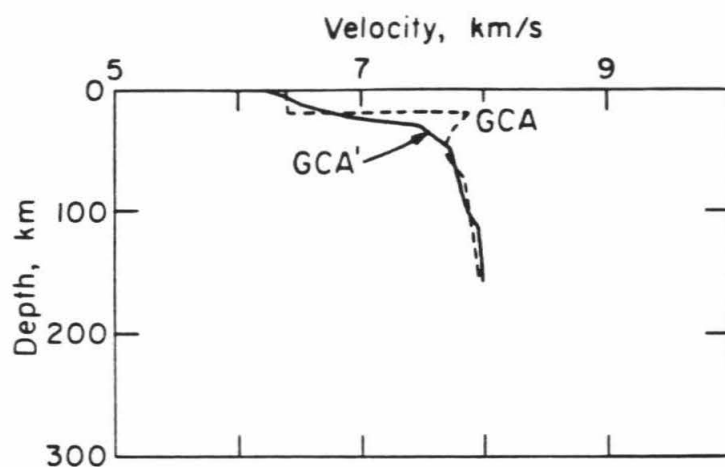
Figure 3.14 The top 150 km of GCA compared with GCA', the model constructed by tau inversion of arrival times from earthquakes closer than 13°. GCA' has no low velocity zone and a transition zone at the crust-mantle boundary. The difference between these models may represent lateral crustal variations between the Gulf of California itself (GCA') and the adjacent continental areas.

Table 3.5

Model GCA'

Depth km	Velocity km/s
0.0	6.200
5.0	6.400
12.0	6.700
25.5	7.000
31.0	7.500
51.0	7.750
100.0	7.870
115.0	7.970
150.0	8.000

This model, which merges with GCA below 150 km, is valid along the axis of the Gulf of California.
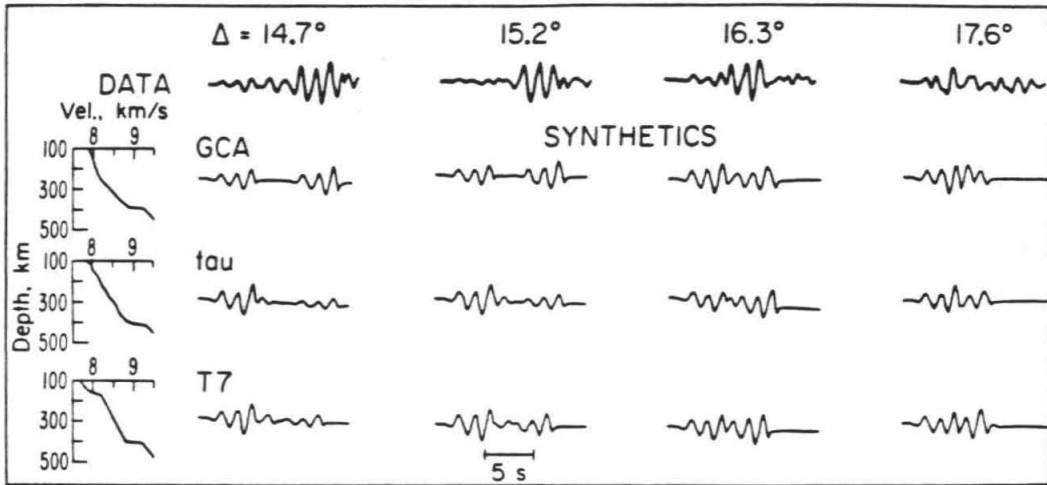
Figure 3.15 A comparison of waveform data for distances of 14°-18° with various models. The top row is the data, followed by GCA, the tau starting model and T7 (Burdick and Helmberger, 1978). Distances are corrected for depth. All seismograms are from event 2 (Table 3.1) and are scaled and filtered as in Figure 3.3. At Δ = 14.7° and 15.2°, the tau and T7 models predict a first arrival much stronger than the 390 km reflection, while GCA comes closer to the true relative amplitudes. The models are very similar at 16.3° and 17.6°.

structure, and are difficult to match precisely. Also, a lack of good data near $18°$ causes some uncertainty about the 390 km discontinuity's exact position. The uppermost mantle (30-200 km) is the most unconstrained portion of GCA because of the non-uniqueness caused by the velocity reversal and likely lateral variations.

A first-order discontinuity of 4.9% at 390 km produces large amplitude secondary arrivals at $14°$ which become first arrivals near $18°$ (see the CD branch of Figure 3.10b). All discontinuities in GCA are represented as steps in velocity because equivalent gradients over 10-20 km are not resolvable. In many regions, the back branch of the 390 km travel-time triplication (AB branch) is observed to distances of $24°$ (England et al., 1977; Burdick and Helmberger, 1978; and others) or even past $30°$ (King and Calcagnile, 1976). This is indicative of a small velocity gradient between 300 and 400 km which is inefficient at turning energy to the surface so that it is seen at larger ranges. The data used in this study show no evidence for the AB branch past $20°$ for 9 of 10 events in that distance interval. The anomalous event has a complicated source and a low signal-to-noise ratio, and occurred on a fracture zone rather than in the subduction regime (Figure 3.16). In the tau inversion, dubious secondary times from that event (no. 26 in Table 3.1) are used to help define the first discontinuity, so the resulting model has a more modest gradient above 400 km. Synthetic seismograms for this structure, however, fit observations from $20°$ to $23°$ very poorly (Figure 3.17). Synthetic seismograms for T7 (Figures 3.4c, 3.5c) show prominent AB arrivals which are not seen in the data. The absence of an observed AB branch past $20°$ thus requires the steep velocity gradient seen in GCA from 225 to 390 km (Figures 3.4a, 3.4b, 3.5a, 3.5b). This unusual gradient is well-supported by the data and is a feature significantly different from models proposed for shields, trenches or tectonic-continental areas.
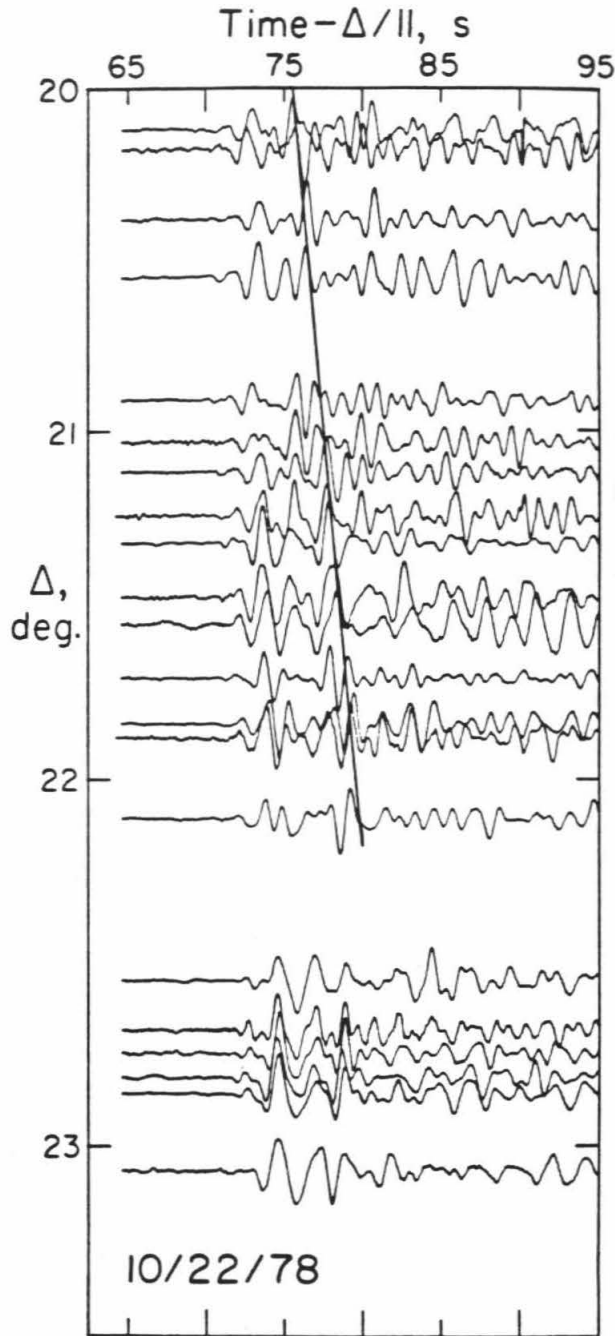
Figure 3.16 Record section for event 26 (Table 3.1), reduced by 11 km/s. The line indicates the arrivals picked as the AB branch in Figure 3.7 and used in the tau inversion. Notice the poor signal coherency and signal-to-noise ratio compared to the sections in Figures 3.3, 3.4, 3.5, and 3.6.
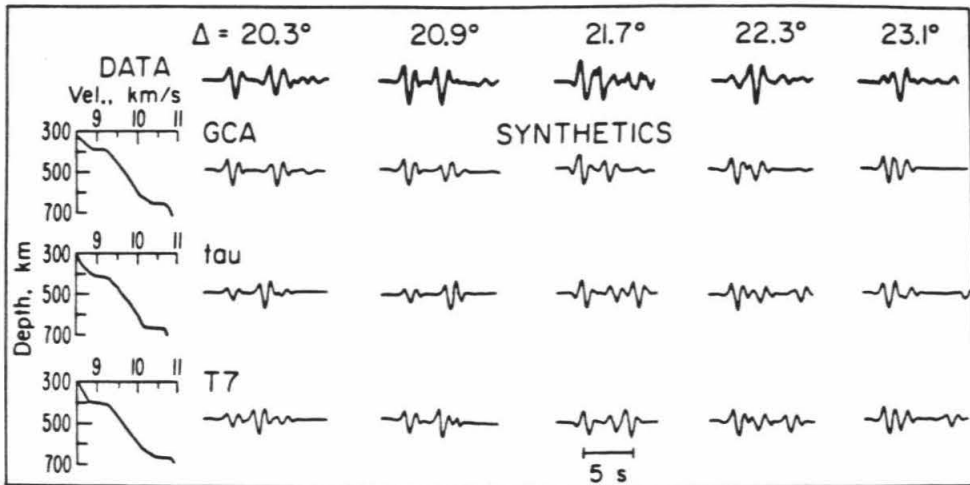
Figure 3.17 Same as Figure 3.15 for 20° to 23°. All data are from event 14 (Table 3.1) except for the trace at 21.7° which is from event 17. At 20.3°, GCA correctly predicts times and amplitudes of the two arrivals. The tau model and T7 both have large intermediate arrivals which are from rays turning just above the 390 km discontinuity. The three arrivals in the T7 synthetic are clearly not in the data. At 20.9°, the AB branch arrival is interfering with the reflection from the 660 km velocity jump in T7 and the tau model, causing the relative amplitudes and timing to be off. All three models predict the data at 21.7° rather poorly, but again for the tau and T7 models the large phase is that of the AB branch. At 22.3° and 23.1°, GCA provides the best fit in terms of subtle timing and amplitude comparisons. Here the AB arrivals would be more than 8 s behind the first break.

Large first arrivals are produced from 20° to 23° by the strong velocity gradient from 390 to 620 km depth; a small inflection near 540 km amplifies initial pulses near 21° (Figure 3.17). The shape of the velocity-depth curve from 620 to 700 km is particularly well-resolved by large amounts of data recorded in the appropriate distance interval, 22°-28° (Figures 3.4, 3.5, 3.6, 3.7). Figure 3.18 shows synthetic seismograms generated for different shapes of the 660 km discontinuity compared to the data. The very fast velocity increase from 620 to 660 km is necessary to generate the correct relative amplitudes between the EF branch (first arrival) and CD branch (second phase) on the seismograms at 25.9° and 27.1° (see also Figure 3.6 for a profile comparison of data and synthetics). Improved amplitude and timing relationships at 23° are gained by increasing the gradient just below the discontinuity. Thus a first order velocity jump of only 2.8%, coupled with large gradients immediately above and below, satisfies the waveform data best.

Observed seismograms are simple beyond 28° in distance (Figure 3.6). The gradient which fits the p-Δ data is adopted in GCA and is very similar to that for a JB earth.

The need for a sharp velocity gradient from 250 to 390 km and the increased resolution of the fine structure of the 660 km velocity break mark the improvements in detail of the waveform-constrained model GCA over the earlier tau-derived model for the same data set. Figure 3.7 demonstrates the overall fit of GCA to a large subset of the data. The addition of waveform techniques to traditional array analysis of short-period data are important in elucidating the fine structure of the upper mantle.
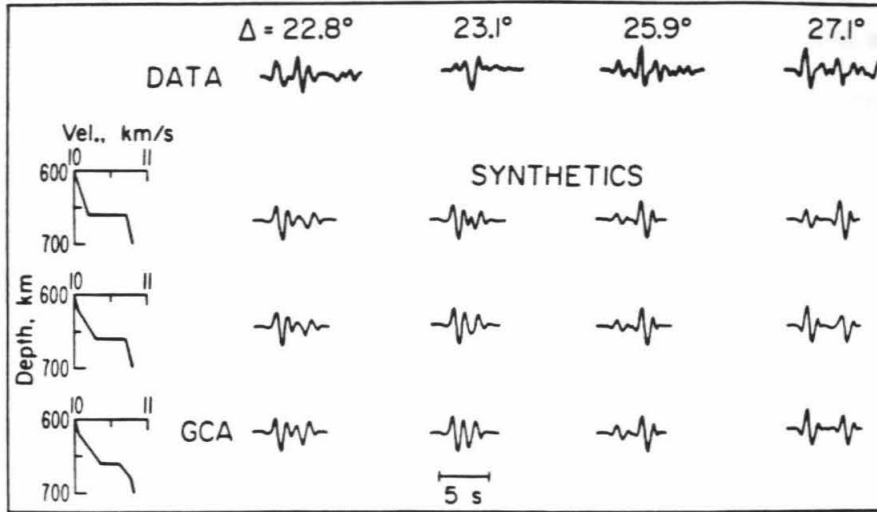
Figure 3.18 Detailed analysis of the 660 km discontinuity. The synthetics are calculated for model GCA with differing gradients above and below 660 km, from a simple step (top row) to large gradients both above and below (bottom row). The relative amplitudes and timing of arrivals are much better for the bottom model than for the other two attempts. Distances are corrected for surface focus.

Wave field continuation

Two linear transformations, the slant stack and downward continuation, change the teleseismic record section into a representation of the slowness-depth domain. As outlined in Chapter 2, wave field continuation is less biased than other inversion methods because it retains each entire seismogram at all times, includes all the data in the inversion, requires no timing, and it results in a direct measure of the resolution in the velocity-depth domain. The requirements and assumptions of this method are equally important. One necessity is dense data; for a 1-s P wave traveling at 10 km/s, we need a record every 5 km for sufficient sampling. For the 10-event data set (see Figure 3.7) the average station spacing is 8 km, so some spatial aliasing is expected. By using the entire 1355 record, 29-event data section, the aliasing problem is reduced substantially, although with uneven seismogram spacing some aliasing will still occur. It is doubtful that the upper mantle under the Gulf of California is laterally homogeneous, but we must assume it in order to employ this technique. Finally, the differing source wavelets for each event defocus the image in both the (τ, p) domain and (p, τ) space. With these caveats in mind, we apply the wave field continuation inversion to the Mexico data with the goal of determining both the resolving power of the data and the suitability of the proposed model GCA.

The first step is to slant stack the observed wave field. A simple slant stack of the 473 record data set with no polarity or empirical corrections is shown in Figure 3.19. It is difficult to extract any (τ, p) information from this representation. By taking the envelope of the stack for each p (Figure 3.20), the image is greatly simplified. The addition of polarity and empirical station adjustments sharpens the image still more (see Figure 3.21). While we attempted no deconvolution to unify the source wavelets, such a procedure should produce a more defined τ-p curve in the
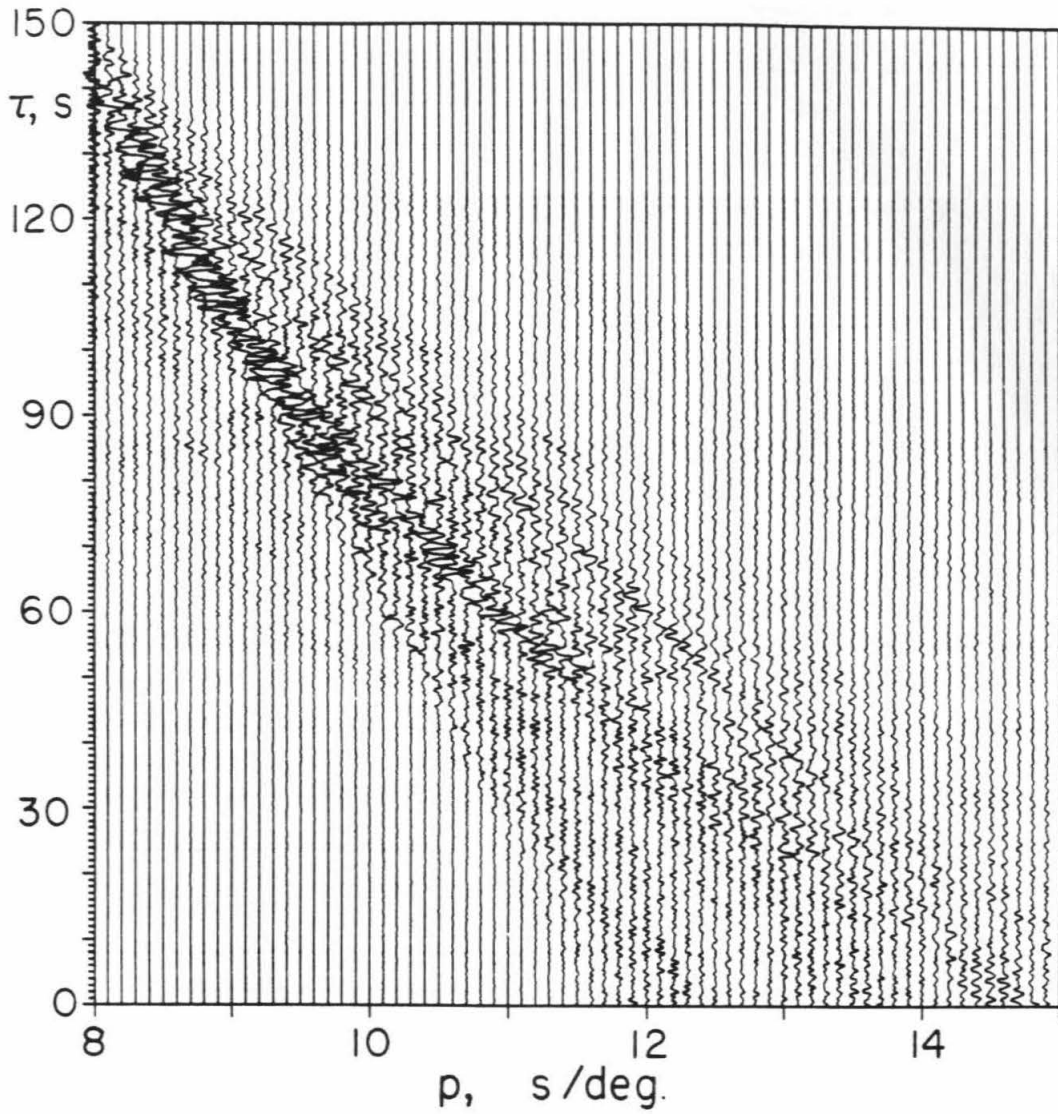
Figure 3.19 Slant stack of the 473 seismogram data subset of Figure 3.7. In this version the records are corrected only for event depth. The amplitude is scaled to the maximum for the entire stack.
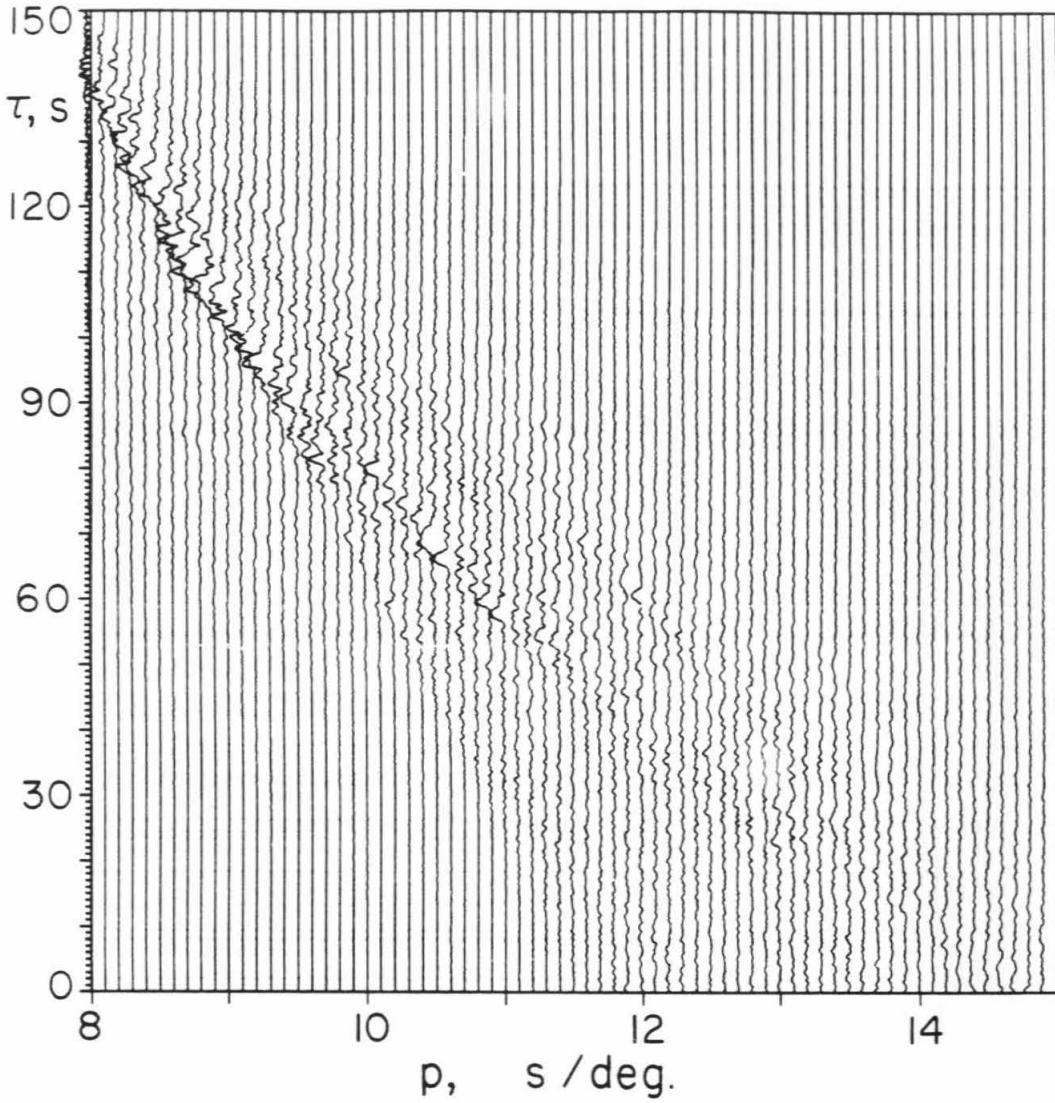
Figure 3.20 Same as Figure 3.19 except that, for each ray parameter value, the envelope of the stacked wave field is plotted. There are 70 p values and 1575 τ points.
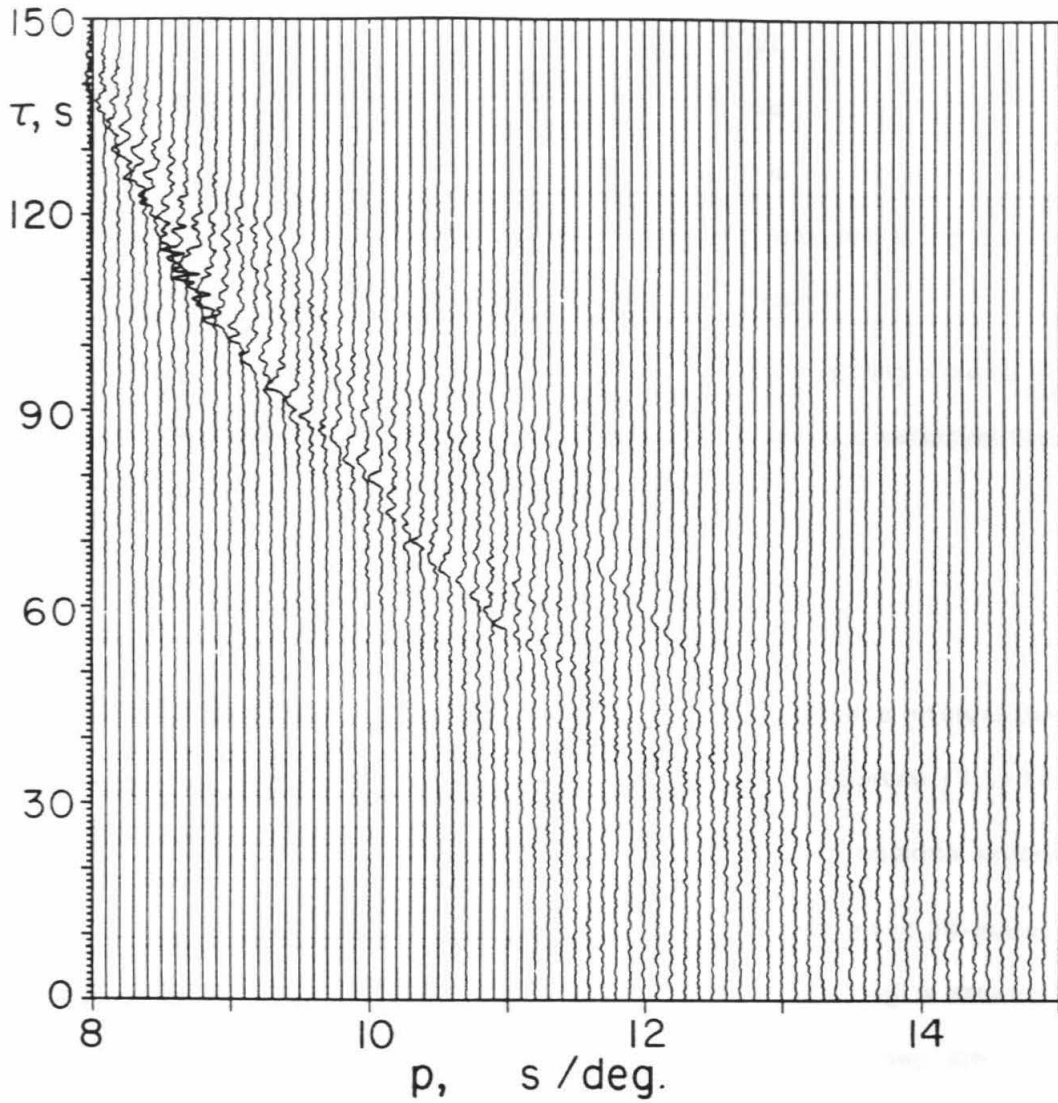
Figure 3.21 Same as Figure 3.20, except that the polarity and empirical station corrections have been applied. Notice the improved appearance of the τ-p image. There is little power in the stack for $p > 11.5$ s/deg..

slant-stacked wave field. Each of these stacks has 70 ray parameter values and 1875 τ points (a 0.08 s sampling interval for 150 s). Figure 3.22 is the fully corrected slant stack of the 1355 record data set. We have not shown a record section of the entire data set because the coverage is so dense for reasonable scales that most of the illustration is black. The main features of Figure 3.22 are essentially the same for both the large and small data groups.

Because the traces are not equally spaced, a trace weighting scheme dependent on the inter-record spacing may be desirable. We devised a weighting factor, f, of the form

$$f = \exp\left(x \ln \frac{1}{k} \right) \tag{3.1}$$

where k is the number of seismograms in each specified distance interval (we used $0.25°$) and x is an empirically chosen constant. For $x=1$, equation (3.1) becomes $f = 1/k$; if $x=2$, (3.1) is equivalent to $f = \frac{1}{\sqrt{k}}$. Through an empirical process, we chose $x=7/8$ as the best x value (Figure 3.23 shows the weighted 29-event (τ, p) wave field). While the image for p values greater than 11.5 s/deg. is enhanced with the weighting, the previously very sharp features for $p < 11.0$ s/deg. are now somewhat degraded, as the poorer-quality records from closer distances have more effect.

The next series of illustrations show the results of downward continuing these slant stacks with the combined model GCA'-GCA, which consists of GCA' replacing GCA to a depth of 150 km with GCA underneath. First the results for the 473 record subset, with and without weighting, are compared to the generating model (Figures 3.24 and 3.25). For p < 11.5 s/deg., it is clear that continuation of the data with
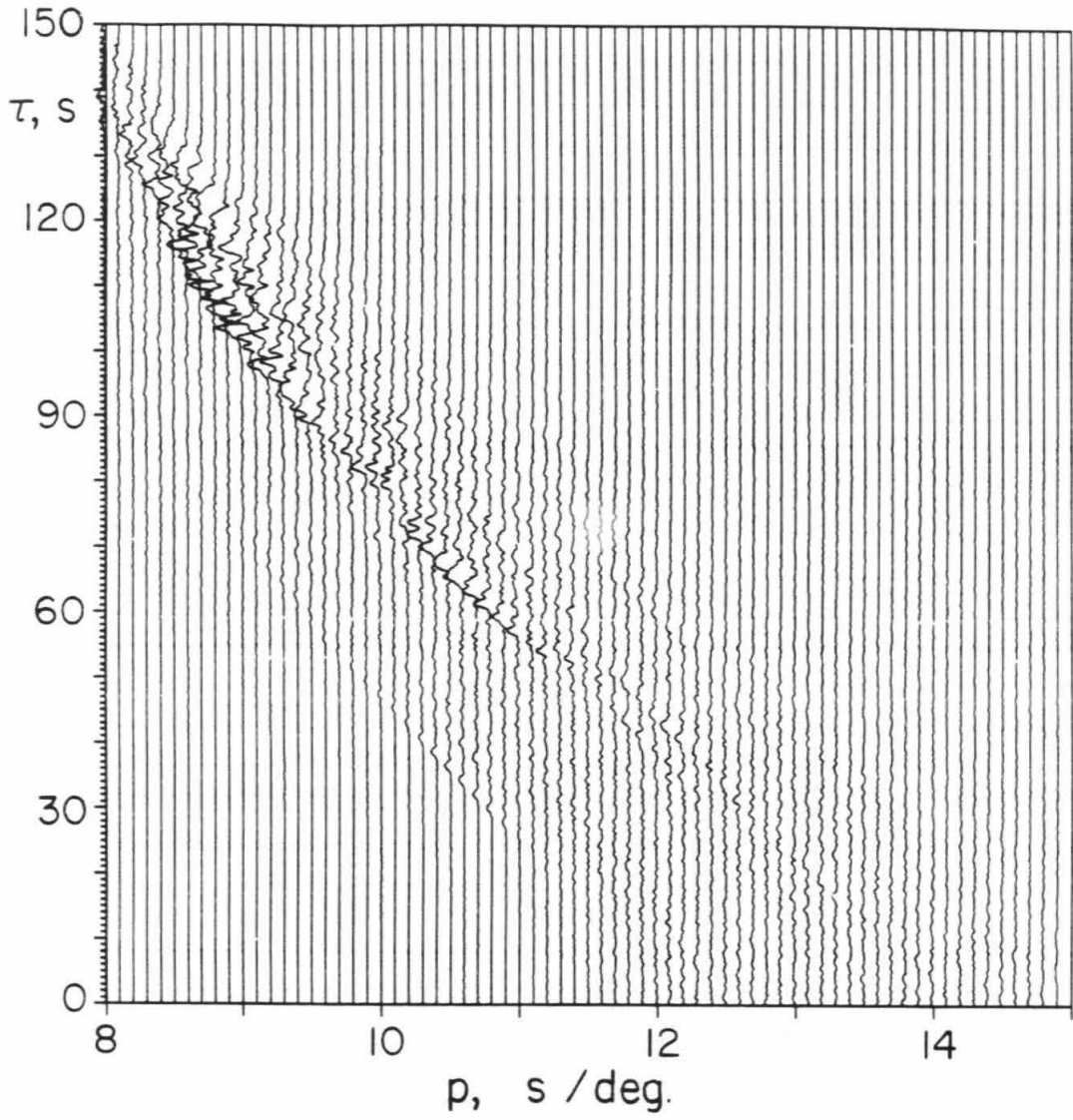
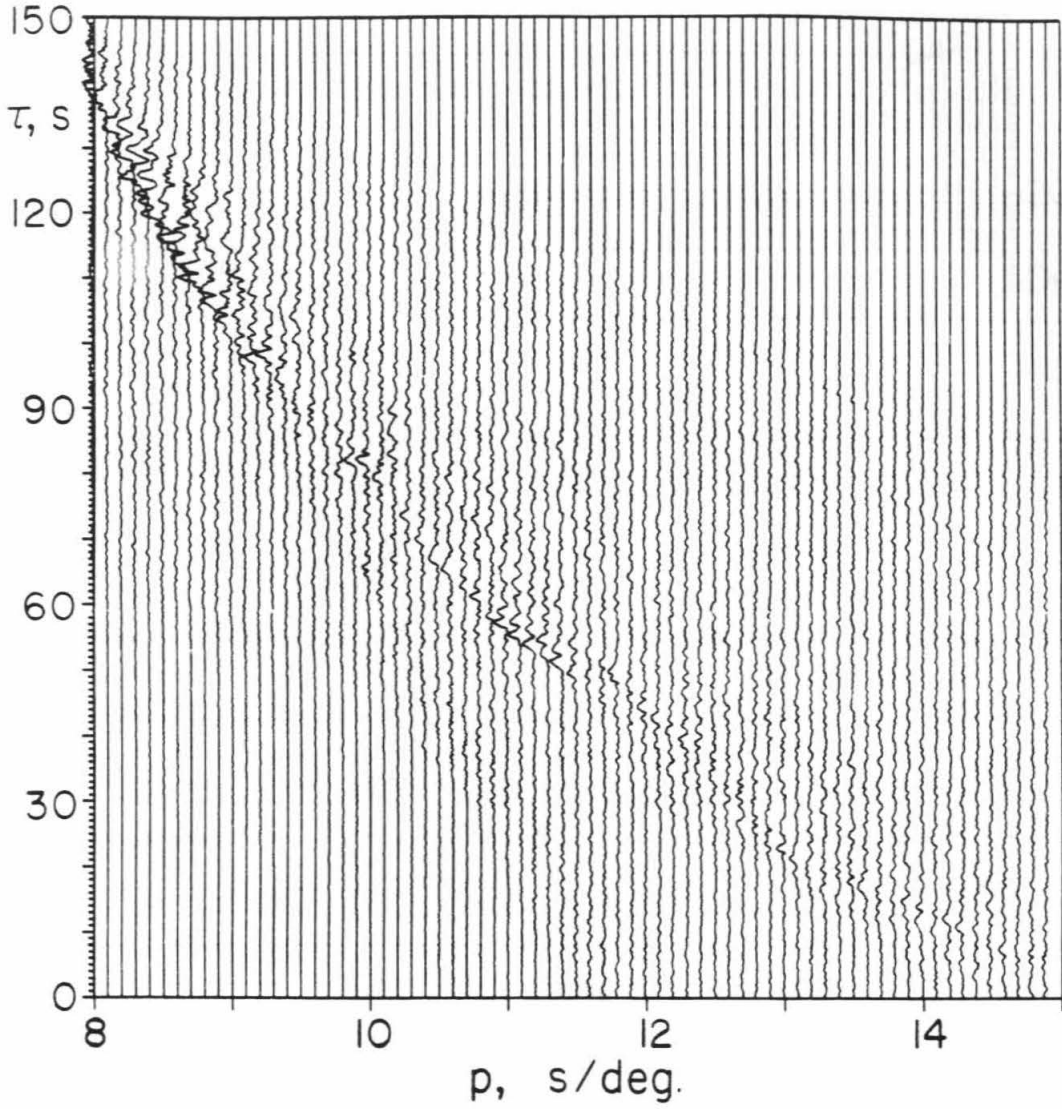Figure 3.22 The equivalent of Figure 3.21 with all 1355 seismograms included.

Figure 3.23 Stack of 1355 traces weighted with x = 7/8 (see text for complete discussion of weighting scheme). Compare to Figure 3.22. The signal for $p > 11.5$ s/deg. is stronger, but the overall noise level is also higher.
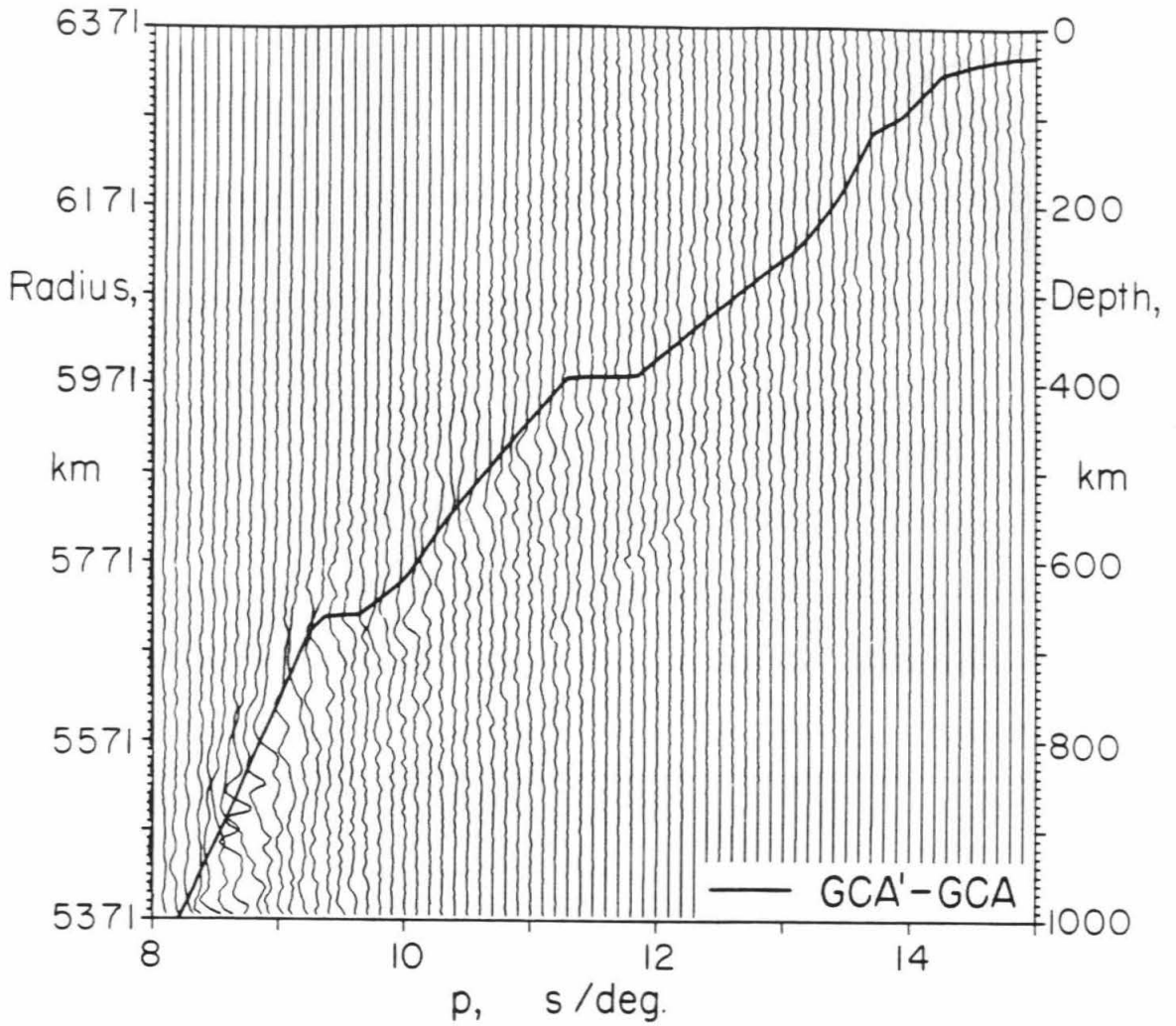
Figure 3.24 The 10 event subset after downward continuation with GCA'-GCA. The depth spacing in the continuation is 5 km. The model is superimposed on the section for comparison. GCA'-GCA fits very well for $p < 12.0$ s/deg.; the image is not clear for $p > 12$ s/deg..
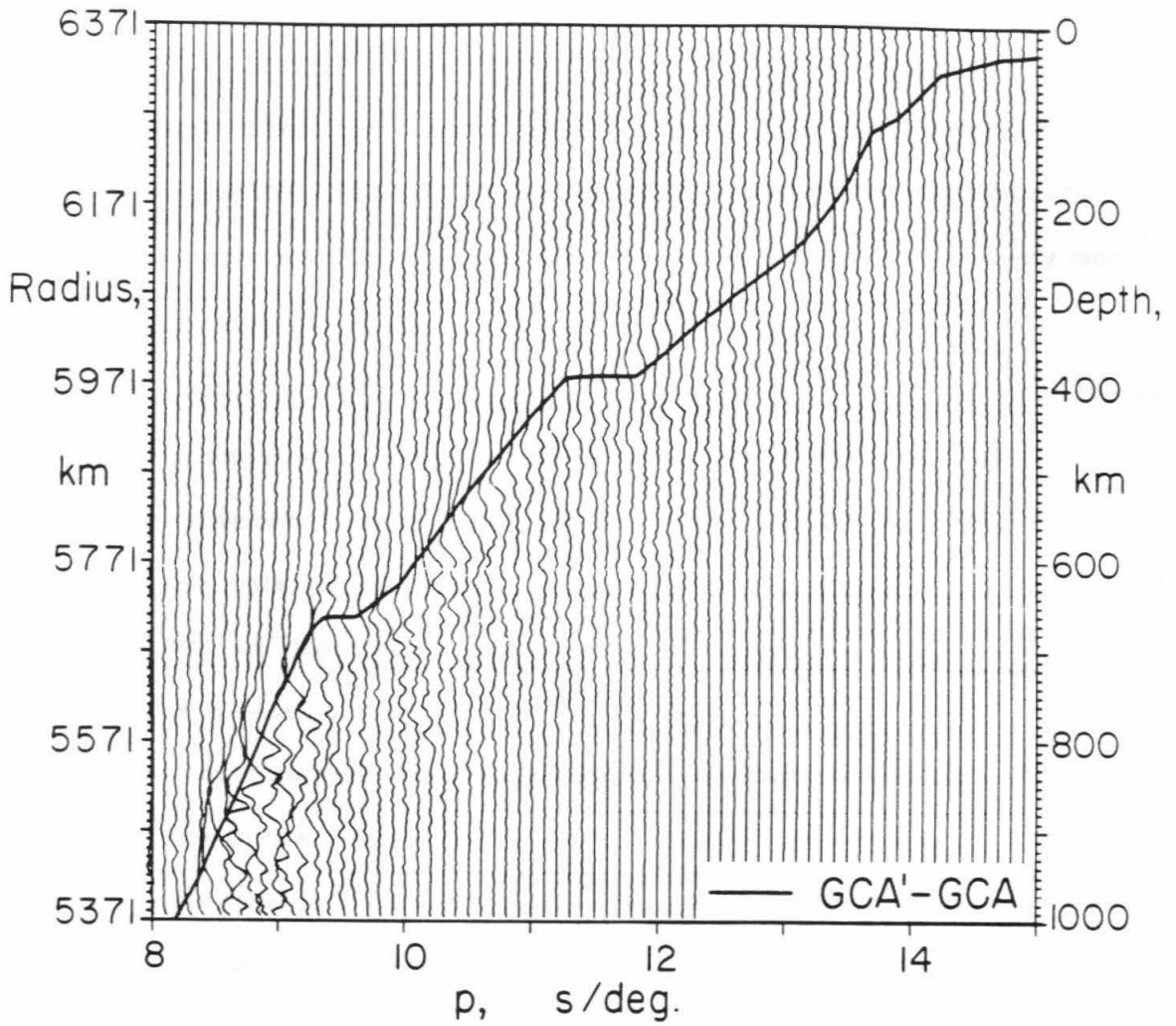
Figure 3.25 Weighted version of Figure 3.24, x = 7/8. The result is similar.

GCA'-GCA results in a return of the same model, thus these data are consistent with the proposed model. The image is poor, however, for $p > 11.5$ s/deg., although the weighting improves it somewhat. The continuations of the full data set are presented in Figures 3.26 and 3.27. The higher overall noise level of the weighted data (Figure 3.27) is apparent. Even the additional data do not help the image very much for higher ray parameter values.

The continued data dramatically demonstrate the range of p for which the data have resolving power. Certainly, GCA'-GCA is consistent with the data, but it is obvious that a meaningful wave field continuation inversion from scratch, even with this high-quality data set, would be difficult to accomplish. The steep velocity gradient above 390 km depth in GCA is not required by the downward continuation. Its existence is based on a repeated null-observation of the AB travel time branch in the excellent data gathered from ranges greater than $20°$. The image for the p values appropriate to this gradient must arise from secondary arrivals at distances of $18°$-$20°$, where there is a small gap in the data. It is understandable, therefore, that the wave field continuation does not contain a strong signal for those ray parameters.

We can read the slowness-depth resolution of the data directly off of the plot of the continued slant stack. With the depth spacing of 5 km, the maximum depth resolution is about 30 km.

Discussion

Wide-aperture arrays are extremely useful tools in earth structure determination. The large size and station density of SCARLET combine to produce several advantages in data analysis: stable $dT/d\Delta$ measurements can be made using the
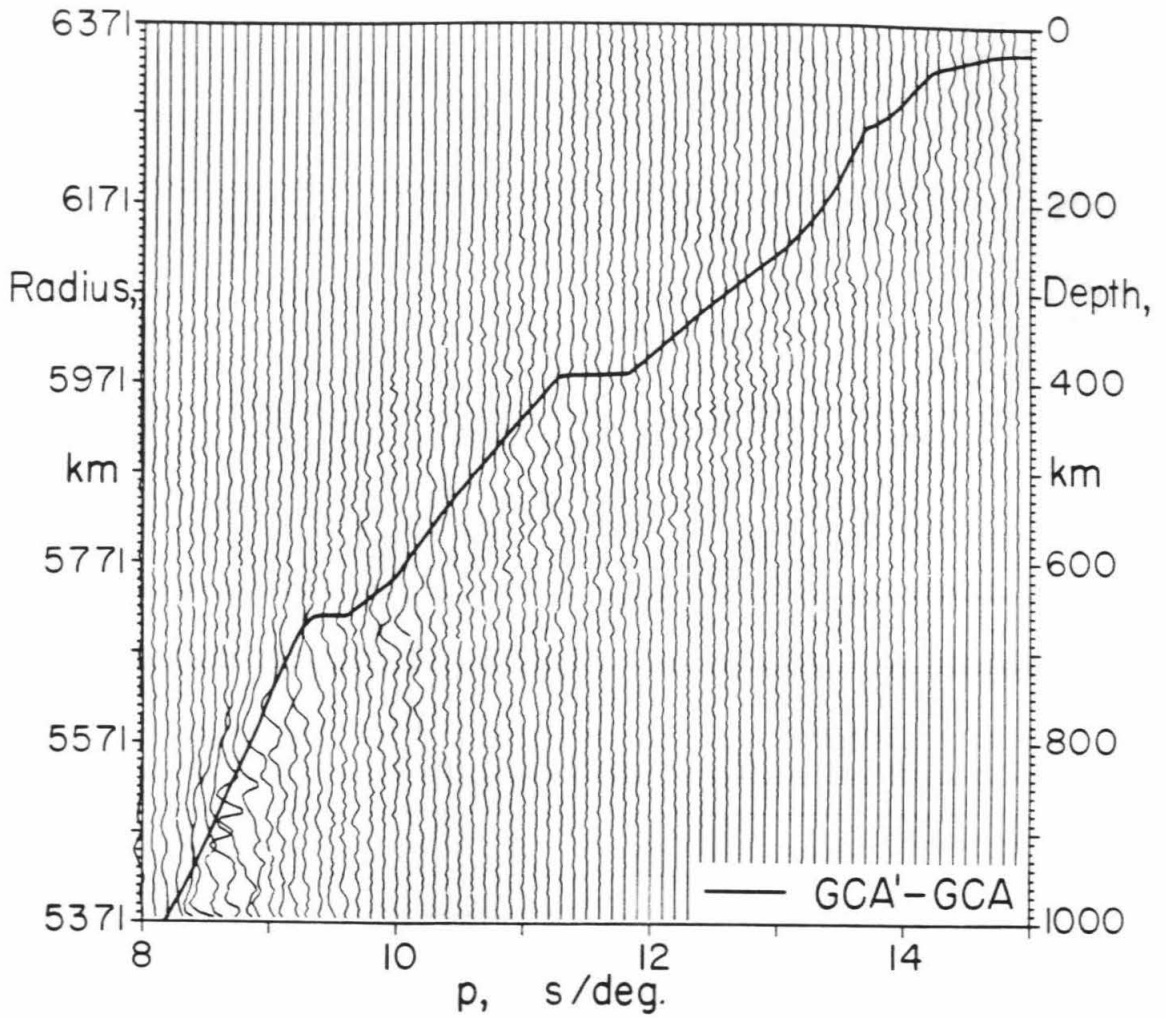
Figure 3.26 All of the Mexico data continued with GCA'-GCA. It looks very much like Figure 3.24.
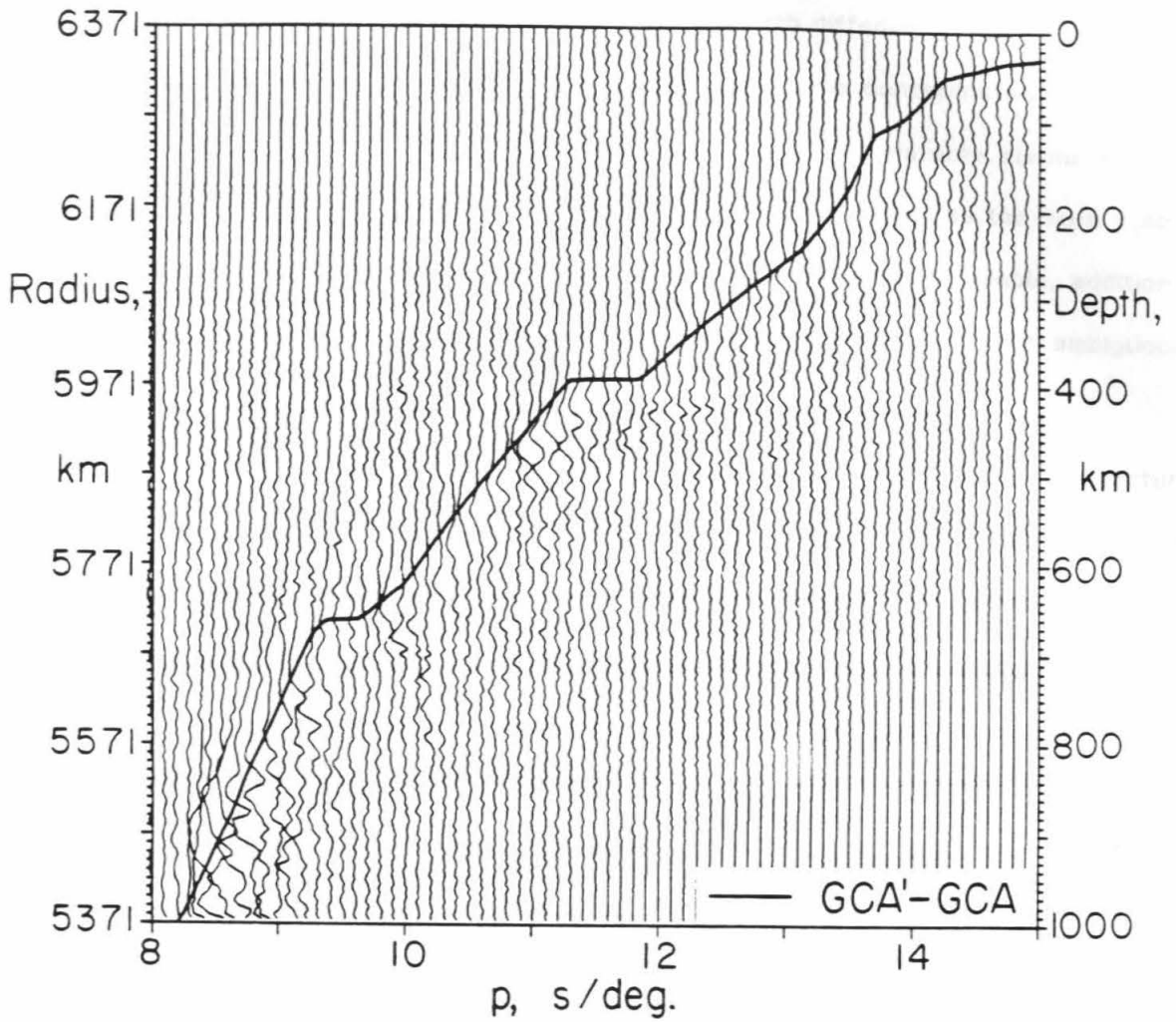
Figure 3.27 Same as Figure 3.26 except weighted with x = 7/8. More of an image is visible for $p > 12$ s/deg. than in Figure 3.26, but the overall noise level is again increased. In all cases, continuation with GCA'-GCA yields an image very similar to the model, proving that the model is consistent with the data.

whole network or subsets of it, secondary arrivals with differing phase velocities are easily identifiable, and anomalous traces, such as those contaminated by unusual receiver structure, can be identified and discarded. For suitably simple events, waveform modeling is a useful tool for short-period data as well as the more stable long-period energy. As more high-quality digital data becomes available, additional detailed investigations including many data types should result in less ambiguous, better resolved upper mantle models.

The effects of lateral heterogeneity, complicated source and receiver structure and depth-varying attenuation contaminate the data. We have attempted to deal with receiver structure and elimination of the source from the modeling problem in earlier sections of this paper. Because of the likelihood of strong lateral variations in at least the upper 100 km of the region, possible errors in the crustal model and ignorance of the Q structure, GCA is most uncertain above 200 km. At these depths it is constrained by travel times alone. More detailed analysis of regional phases are necessary to determine the velocities precisely at these depths. Excellent data recorded at distances of 19° and greater place closer bounds on the structure deeper than 200 km.

Without the wave field continuation technique, it would be difficult to quantify the error bars on model GCA. While the tau method computes errors due to travel time uncertainties in a straightforward manner, the addition of the p-Δ and waveform data through forward modeling reduces the uncertainty envelope, but not in a simple way. When sufficient spatial sampling is available, the wave field continuation method helps constrain a model's uncertainty. The slant stacked data present a (τ, p) image from which it becomes clear where the data have resolving power. With the downward continuation process, we first discover whether or not the model is suitable; we

can also state precisely where the model is best defined, and estimate error bounds for the well-determined portions of the model. The data are compatible with GCA; the slowness-depth image is fuzziest for $p > 12.0$ s/deg., and the image width (resolution) is on the order of 30 km. We used a 5 km depth spacing in the continuation process. A smaller depth interval may decrease the image width.

A comparison of the spreading center model GCA with well-constrained models for differing tectonic regimes is very revealing. We consider a continental shield model K8 (Given and Helmberger, 1980), tectonic-continental model T7 (Burdick and Helmberger, 1978), and trench-arc model ARC-TR (Fukao, 1977) (Figure 3.28). K8, which represents northwest Eurasia, was derived from synthetic seismogram modeling of both long- and short-period P waves and is constrained to fit the NORSAR-determined p-Δ curve of model KCA (King and Calcagnile, 1976). Similarly, Burdick and Helmberger's (1978) western United States model T7 relies on the Johnson (1967) apparent velocity measurements (made at TFSO in Arizona) as well as waveform modeling of earthquakes with known source mechanisms. An unusually complete travel time and dT/dΔ data set constrain the parameters of ARC-TR, a model for the Pacific Ocean trench near Japan. Figure 3.28 shows that all four velocity-depth curves are quite similar below 400 km depth, with some slight differences in velocity gradient at depths greater than 670 km. The small disparities in the depths to the '400 km' and '670 km' discontinuities are probably not resolvable within the data constraints and modeling error.

For depths shallower than 400 km, however, significant differences between the regions appear. In all the models, lid and low-velocity zone shapes are non-unique, with the arc and shield models predicting considerably faster arrival times for regional distances than do the young continent and ridge representations. At about
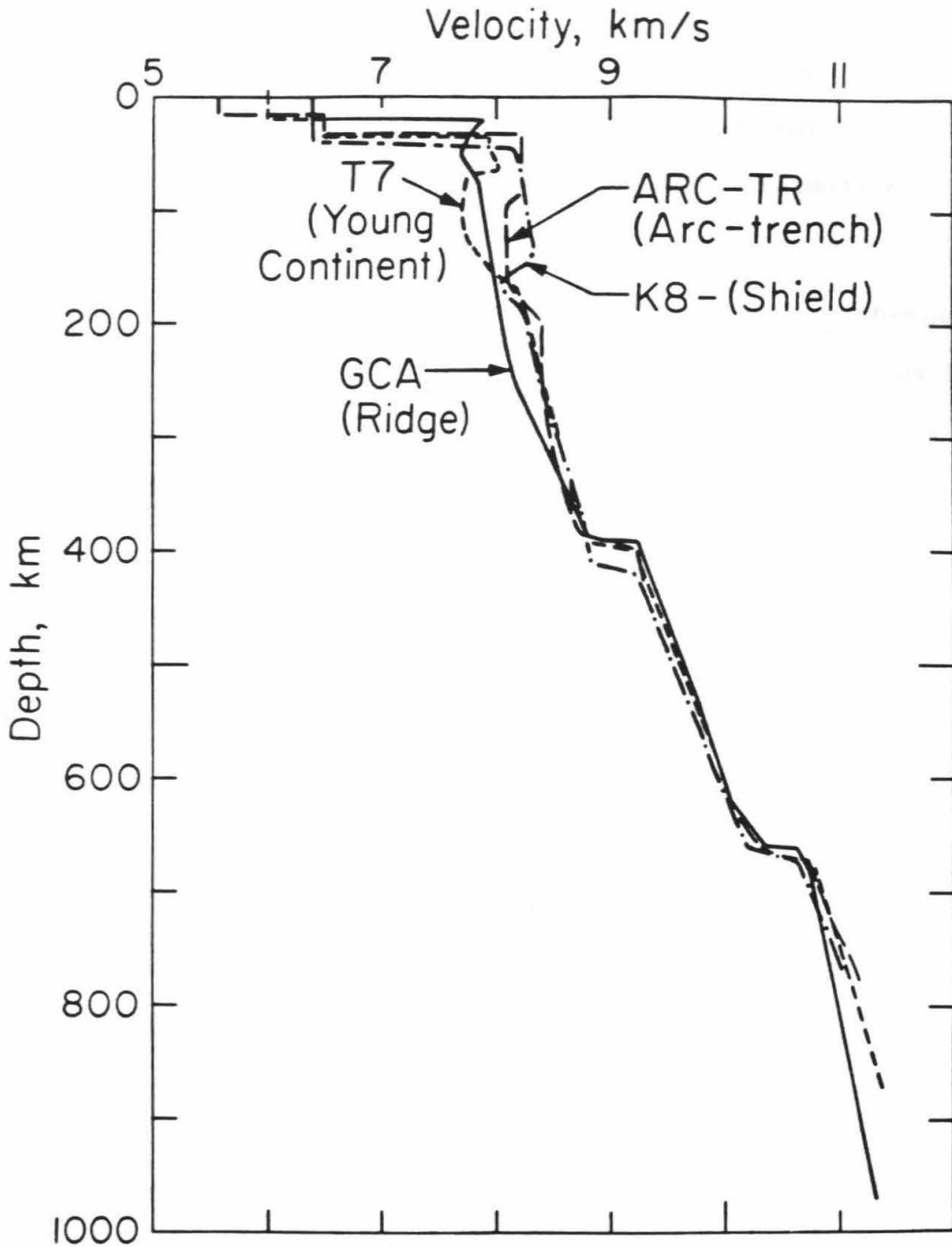
Figure 3.28 Four models for differing tectonic regimes. T7 (Burdick and Helmberger, 1978) is valid for a tectonically active continental region. Island arcs are represented by ARC-TR (Fukao, 1977) and shields by K8 (Given and Helmberger, 1980). GCA (this study) represents an oceanic spreading center. K8, T7 and ARC-TR are very similar below 200 km depth, but GCA is substantially slower than the other models to depth of 350 km.

200 km, K8, T7 and ARC-TR converge, while GCA features much lower velocities. Low (ARC-TR) to moderate (K8, T7) velocity gradients prevail between 200 km and 400 km except for GCA, in which velocity increases very rapidly with depth in that depth range; GCA velocities merge with the other models at 350 km.

Low velocities for both P and S waves are well-documented for oceanic ridges and continental rifts. Surface wave dispersion studies require very low S-wave speeds beneath young ocean (e.g., Knopoff et al., 1970; Montagner and Jobert, 1981; Wielandt and Knopoff, 1982). Some refraction work performed on rifts (Ginzburg et al., 1979; Maguire and Long, 1976; Puzyrev et al., 1973) supports low values for Pn velocities, although others (e. g., Murdock and Jaksha, 1981) have measured normal Pn velocities in rift areas. Oceanic ridge refraction studies (e.g., Gettrust et al., 1982; Lewis and Garmany, 1982) find compressional speeds of 8.0 km/s at shallow (8 km) levels, but this 'lid' may be very thin (see Bulin, 1979) and underlain by extremely slow material, or the material directly beneath the ridge crest may be anisotropic (e.g., Keen and Tramontini, 1970).

There are few data pertinent to the deep structure of rifts and ridges. Available P residuals (Rowlett and Forsyth, 1979) and PP residuals (Dorbath and Dorbath, 1981) for the Mid-Atlantic Ridge are large and positive, indicating very low velocities, possibly to great depth. Very late P-wave arrivals at Addis-Ababa (Dziewonski and Anderson, 1983) are also observed for the East African Rift. Thus the velocity value of only slightly over 8 km/s at 200 km in GCA is consistent with the available data.

Small observed first arrival amplitudes from $14°-16°$ require a very slowly increasing velocity from 100 to 200 km. The gradient, however, trades off with a possible low Q zone just below the lid which could reduce the amplitudes of the first

arrivals near 14°. While such an attenuating zone will probably have a greater effect on wave amplitudes than on periods, the synthetic seismograms indicate that there is no noticeable frequency depletion of the first arrival relative to the second at 14°.

The main reason for GCA's steep gradient from 225-390 km is that no arrivals corresponding to the AB travel time branch (Figure 3.10b) are observed beyond a (surface focus) distance of 20° (see Figures 3.4a, 3.4b, 3.5a, 3.5b, 3.7). In some shield regions (King and Calcagnile, 1976), this branch is noted past 30°. Typical observational limits for tectonic continental areas are 24° to 26° (Wiggins and Helmberger, 1973; Ram et al., 1978; Burdick and Helmberger, 1978). England et al. (1978) used oceanic events recorded at NORSAR for their model NAT and see the AB branch to 24°, but for that range the rays' bottoming points are no longer beneath young ocean, so a different structure might be expected. In Australia, Simpson et al. (1974) do not observe an AB branch beyond 21°. Model SMAK I has a small velocity gradient above 400 km which predicts AB arrivals well past 30°; Simpson et al. appeal to a properly placed low Q zone to suppress amplitudes of the AB phase. For Indian Ocean earthquakes recorded at the Gauribidanur array in southern India, Ram and Mereu (1977) cannot identify the AB branch past 19°. Their model RM-3 also has a shallow gradient above 400 km but terminates the AB branch with a very deep (175-332 km) low velocity zone.

Other studies with oceanic sources, therefore, document the absence of the AB branch beyond 20° but resort to non-deterministic methods to diminish that phase's amplitudes. Since low upper mantle velocities are consistent for ridges, the very slow uppermost mantle of GCA underlain by a region of unusually fast velocity increase with depth is very appropriate and a less artificial way of effectively shortening the predicted AB travel time branch.

Shear wave data from the East Pacific Rise support the idea of a large velocity gradient between the depths of 200 and 400 km. Grand and Helmberger's (1983) model TNA (Figure 3.29), derived from long-period SS phases recorded at North American stations, is very similar to GCA in general character, and includes a high gradient from 250-400 km in depth.

The discontinuities near 400 km in the four models of Figure 3.28 are all quite consistent in size and shape. The absolute depth to the velocity transition is dependent on the assumed shallow structure, so the slightly deeper discontinuity of K8 is probably not significant. The Fukao (1977) model ARC-TR has a pronounced 'bump' in the velocity-depth profile at 500 km because of a rapid decrease in $p(\Delta)$ at 20°. GCA also has a very slight inflection near 540 km to match strengthened first arrival amplitudes near 21°. While all the models are very similar in the 650 km depth range, GCA is derived from the most complete data set in the 20°-30° interval. The seismograms shown in Figures 3.4, 3.5, and 3.6 are very sensitive to the fine structure of the 660 km discontinuity as is demonstrated in Figure 3.18. The T7 model contains the strong gradient just above 670 km but a lack of convincing data near 27° precludes delineation of the transition shape just below the break. Grand and Helmberger (1983) include increased gradients from 660 km to 750 km for both shield and tectonic S-wave models, while a P-wave model for a shield has a similar form (Given and Helmberger, 1980). Dziewonski and Anderson's (1981) model PREM also features an increased gradient near 700 km on a global scale.

The differences between the four models with depth are further illustrated by comparison of cumulative one-way vertical travel times. In Figure 3.30, vertical travel times are computed for each model starting at 620 km in 20 km steps and are compared to the Herrin (1968) velocity model. It is evident that the curves for T7 and
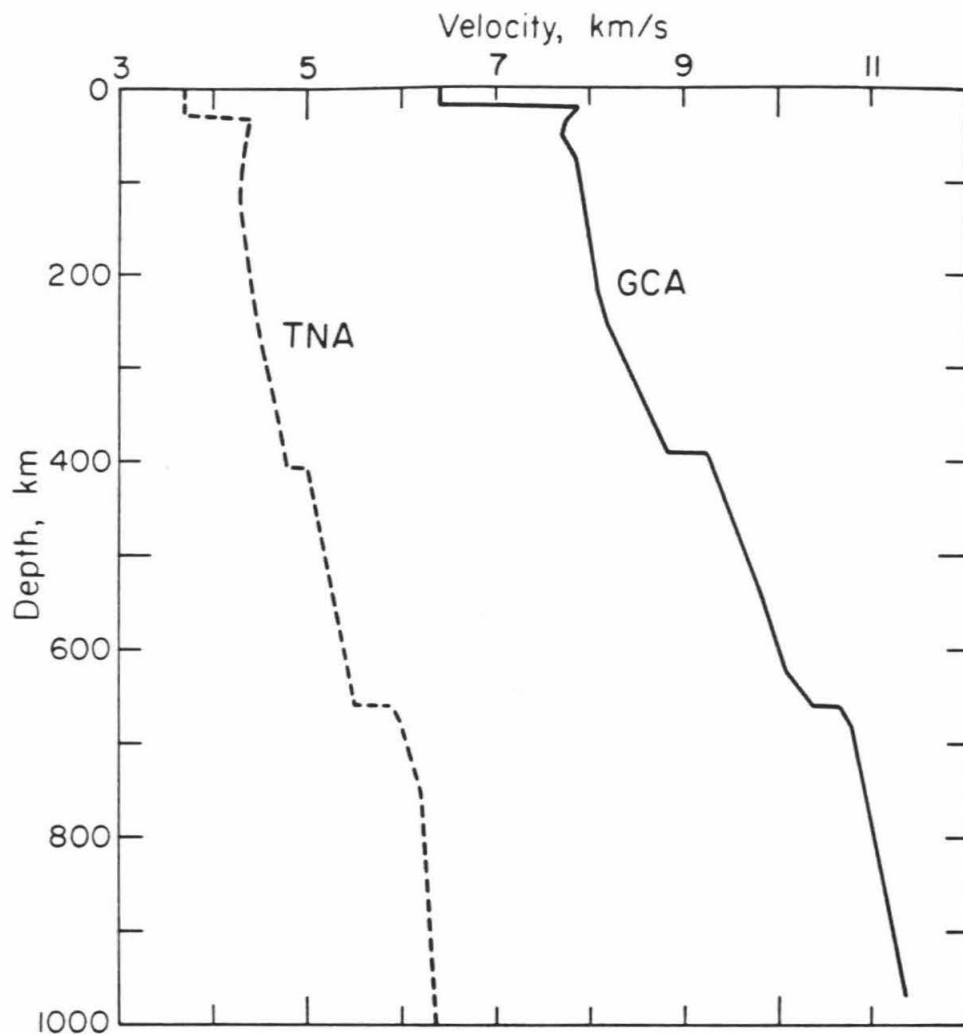
Figure 3.29 A comparison of TNA, Grand and Helmberger's (1983) shear-wave model for Mexico and the western United States, and GCA. Note the great similarity in general character between the models. TNA has a 4.7% velocity jump at 405 km and a 7.8% change at 660 km.
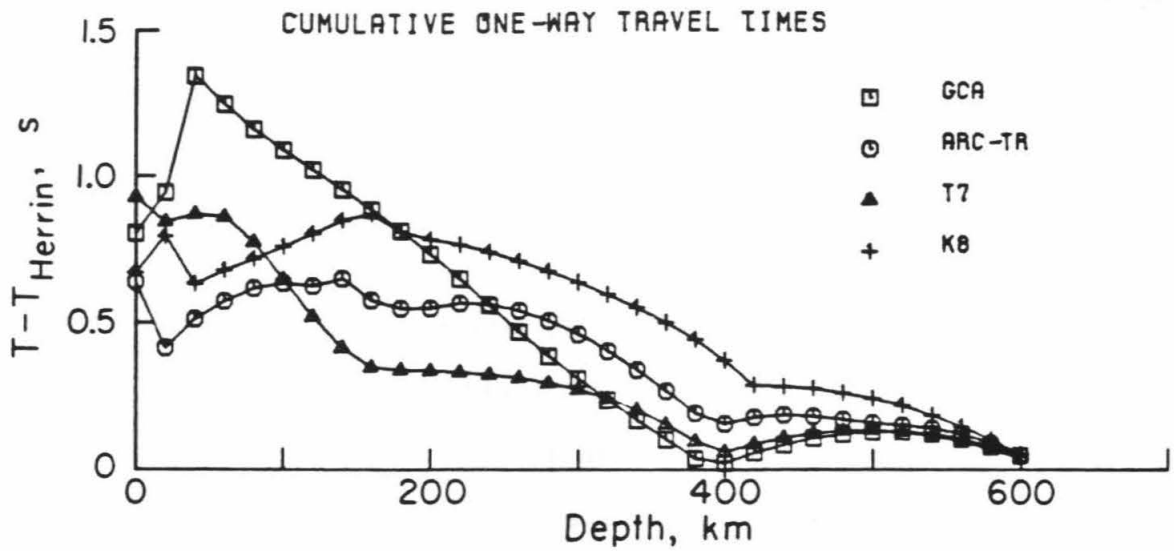
Figure 3.30 For a starting depth of 620 km, cumulative vertical one-way travel times are computed for four models and compared to the 1968 Herrin mantle velocities. Symbols are plotted at 20 km intervals. T7 and GCA are very close from 600 km to 320 km, then T7's residuals flatten out but GCA's become increasingly positive. This illustrates the very slow GCA velocities above 350 km.

GCA are very similar from 620 km to 300 km, then T7 flattens out with respect to the Herrin times while GCA continues to be very slow relative to the 1968 model. ARC-TR and K8 also have nearly constant values for $T - T_{Herrin}$ for 100-200 km depth. The arc and shield models' residuals decrease above 150 km as expected from their faster uppermost mantle velocities, while T7 and GCA become more positive for that depth range. The various crustal thicknesses have large effects on the overall vertical travel times.

Conclusions

Earthquakes in Mexico recorded at SCARLET form a unique, high-density digital short-period P-wave data set for upper mantle study. We have analyzed about 1400 seismograms and utilized travel time, apparent phase velocity and relative amplitude information to produce a tightly constrained, detailed model for depths to 1000 km beneath an active oceanic ridge region, the Gulf of California. Unusually low velocities to depths of 350 km characterize the spreading center model, consistent with teleseismic P and PP residuals of Rowlett and Forsyth (1979) and Dorbath and Dorbath (1981), respectively. The abrupt cutoff in distance of observations of the travel time branch (AB) for which rays bottom just above 400 km leads to an interpretation of an anomalously high velocity gradient from 225 to 390 km, rather than a large velocity step at the base of the low velocity zone. Grand and Helmberger (1983) make a similar observation for shear waves from East Pacific Rise earthquakes. Thus the ridge model, GCA, differs significantly from models observed for shield, young continental, and arc regimes to 350 km depth.

Abundant data from 19° to 28° constrain the detailed shape of the 660 km discontinuity. A small, 2.8% jump in compressional velocity is accompanied by increased gradients both above and below the break.

Present available data are not sufficient to confirm or reject the idea of undulations of the major velocity discontinuities in the upper mantle. Lateral velocity variations between shields, arcs, and tectonic-continental regions seem well established to depths of 200 km. This study demonstrates that oceanic spreading centers have velocities slower than the other regions to the even greater depth of 350 km.

Chapter 4

The upper mantle under the Cascade Ranges:
a comparison with the Gulf of California

Introduction

An accurate global assessment of the upper mantle velocity distribution would be helpful in solving many pressing geophysical problems. Assembling such a world-wide map is not straightforward because the widely varying methods and types of data used in regional studies are difficult to compare directly. The ideal upper mantle experiment might involve multiple identical three-component, broad-band seismic arrays cleverly situated within $30°$ distance of every major seismic zone. The lack of such instrumentation forces us to consider an alternate method: identical analysis of multiple data sets, facilitating structural comparison between regions. Burdick (1981) and Grand and Helmberger (1983) model long-period P and SS waves, respectively, with synthetic seismograms and establish gross structural differences between continental shields and tectonically active continental areas. Burdick (1981) presents two models which separate only in the uppermost 250 km. The shear wave models of Grand and Helmberger (1983), however, are disparate to 400 km depth. Their tectonic model, TNA, is in excellent agreement with the P-wave spreading center model, GCA, developed in Chapter 3 of this thesis.

Wiggins and Helmberger (1973) and Dey-Sarkar and Wiggins (1976) compare smaller regions within midwestern and western North America using synthetic seismo-gram modeling of short-period P waves recorded from several source regions at widely separated receivers. The two models for the United States, HWA and HWB (Wiggins and Helmberger, 1973) disagree to depths of over 400 km. Dey-Sarkar and

Wiggins (1976) propose three varying models for areas of northwest Canada; their model discrepancies are mostly in lithospheric thickness and in the shapes of low-velocity zones. Because the data types and analysis are identical, these models are directly comparable and document lateral variations within the North American continent.

For a conveniently located seismic array, comparative studies of the upper mantle are simple. We can record events in the proper distance ranges from several azimuths and process the data uniformly to obtain good estimates of the model changes required by the data. Niazi and Anderson (1965) utilize earthquakes from two azimuths in their data collected at the Tonto Forest Seismological Observatory (TFSO) in Arizona. While they have insufficient data to conduct separate analyses, the $dT/d\Delta$ measurements from both source areas are consistent. Johnson (1967), also using TFSO, similarly combines multi-azimuth data sets into one upper mantle model.

Several investigators have directly compared data collected from similar distances but differing azimuths at a single array. England et al. (1978) contrast P waves sensitive to the North Atlantic and Arctic oceans to those bottoming under Russia and central Europe. Ram and Mereu (1977) probe the upper mantle in four different regions using the Gauribidanur array in southern India. While neither study employs waveform modeling, the travel time and p-Δ data from the different areas are dissimilar enough to document significant structural variations between the oceanic and continental source regions. At YKA, Ram et al. (1978) study the lateral variations in the upper mantle to the west and south of that northern Canadian array. Their extreme data scatter precludes strong statements about absolute velocities, yet once again the two data groups are quantitatively different, indicating lateral

velocity gradients within the mantle.

The addition of waveform modeling techniques to the dense array data should aid in identification and documentation of even subtle structural variations between regions. SCARLET is conveniently located between two seismically active zones on the Pacific Ocean rim. The results of modeling upper mantle velocities beneath the Gulf of California spreading center, derived from data recorded from Mexican events, are presented in Chapter 3. Significant seismic activity also occurs to the northwest of southern California at appropriate distances for upper mantle study, from northern California to Alaska. Energy from these events arriving at SCARLET is especially sensitive to velocities under the Cascade Ranges of Oregon and Washington and the Juan de Fuca plate (Figure 4.1). The Cascade Ranges represent Quaternary volcanism related to subduction, and the Juan de Fuca plate is very young oceanic crust. The disparities between this tectonically active region and the Gulf of California, therefore, may not be as dramatic as those between continental shields and ocean basins.

We utilize the wide aperture and digital recording capability of SCARLET to collect the large amounts of data required to constrain discrepancies in velocities for these two areas. The data from the northeast Pacific are processed exactly as those from Mexico. We construct T-Δ and p-Δ curves and then model the waveforms with GCA, the spreading center model, as a starting point; the only differences between the final Cascades model and GCA are demanded by the travel time and waveform data. The resolvability of variations between the data sets is tested with wave field continuation. The high-quality, dense array data are essential to definitively establish the existence of lateral variations in upper mantle structure between the Gulf of California and the Cascade Ranges.
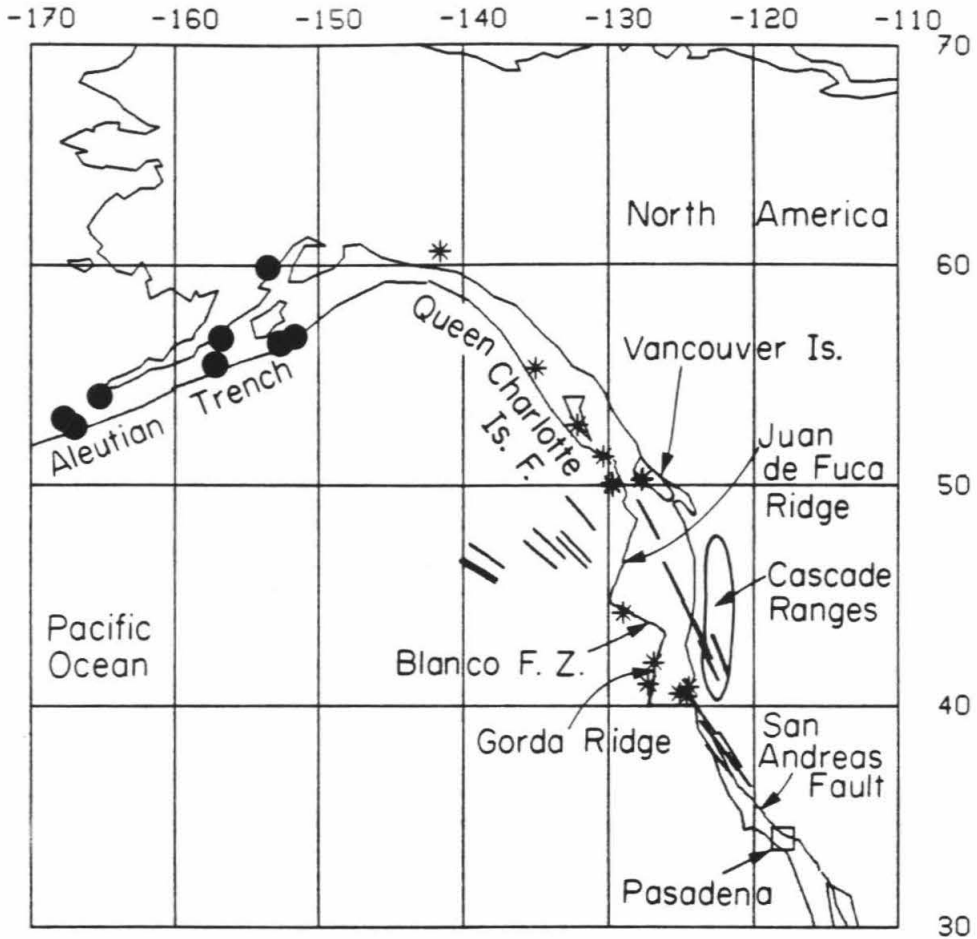
Figure 4.1 Locations of the 22 earthquakes used in this chapter. Dots show the epicenters of the eight calibration events; stars denote the 14 events closer than 30°. The short lines are 2° arcs drawn around the midpoints of the great circle paths to Pasadena for all events. Notice that the calibration events bottom beneath the Pacific Ocean, while for the other events, rays turn near the continental margin.

Tectonic setting

The study area is one of complex, recent tectonism. We utilize seismic events from northern California around the northeast Pacific Ocean margin to Alaska and the Aleutian trench (see Figure 4.1). The earthquakes at distances of more than 30°, as in Chapter 3, are used for calibrating the array for receiver corrections. These events have rays which bottom under the Pacific plate; their mechanisms are probably thrusts, and they range in depth from shallow to intermediate (the deepest is 123 km, see Table 4.1). Moving clockwise around the Pacific rim, the next source area is the Queen Charlotte Island fault zone, which moves in a right-lateral sense at 5.5 cm/yr and is the most active fault system in western Canada (Milne et al., 1978; Keen and Hyndman, 1979). Tobin and Sykes (1968), Chandra (1974) and Milne et al. (1978) present fault-plane solutions for earthquakes in this locale which support dextral movement on the Queen Charlotte Island system. The complex Juan de Fuca Ridge system, which separates the Pacific and Juan de Fuca plates, intersects the Queen Charlotte Island fault zone west of Vancouver Island (e. g., Chandra, 1974). Focal mechanisms in this region are indicative of north-south compression with dominantly shallow, strike-slip movement (Rogers, 1979). The actual Juan de Fuca Ridge has few earthquakes, but to the south, the Blanco Fracture Zone and Gorda ridge are very active, with right-lateral strike slip and normal events, respectively. In the Puget Sound region, most seismicity is shallow, but some events are as deep as 50-60 km (Chandra, 1974); mechanisms are consistent with north-south compression (Crosson, 1972).

Rays from earthquakes closer than 30° turn below the very young oceanic Juan de Fuca plate and also the Cascade Ranges of Oregon and Washington (Figure 4.1).

Table 4.1
Epicentral Information

Event No.	Day	Date Mo.	Year	Origin Time Hr.	Min.	S.	Lat. deg.	Long. deg.	Depth km	Mag. m_b
1	19	Jul.	1978	09	32	08.6	56 46.14	-151 38.82	33.	5.7
2	25	May	1979	16	45	27.3	52 36.66	-167 01.14	23.	6.0
3	12	Apr.	1978	03	42	03.5	56 25.38	-152 41.46	14.	6.0
4	01	Sep.	1979	05	27	17.6	53 58.68	-165 12.24	69.	5.8
5	24	Mar.	1980	03	59	51.3	52 58.14	-167 40.20	33.	6.2
6	20	May	1979	08	14	00.1	56 38.82	-156 43.50	71.	6.4
7	17	Aug.	1978	18	52	28.4	59 53.10	-153 31.92	123.	5.7
8	02	Jun.	1978	20	41	43.7	50 15.54	-127 41.28	21.	5.1
9	11	Jul.	1978	02	55	01.6	52 45.90	-132 06.24	10.	5.4
10	13	Mar.	1979	12	00	17.2	49 59.22	-129 41.28	10.	5.4
11	21	Jun.	1979	17	03	17.5	51 19.38	-130 18.90	10.	5.0
12	11	Jul.	1979	12	28	02.9	55 19.38	-134 57.90	10.	5.1
13	14	Mar.	1979	15	13	32.4	50 06.48	-129 42.96	10.	5.3
14	28	Feb.	1979	21	27	06.1	60 38.52	-141 35.58	10.	6.4
15	03	Feb.	1979	09	58	16.1	40 53.40	-124 24.78	28.	5.2
16	07	Apr.	1979	06	18	33.0	41 59.22	-126 48.96	15.	5.5
17	01	Aug.	1979	10	50	26.6	41 01.86	-127 13.26	15.	5.3
18	03	Mar.	1980	14	17	04.6	40 36.00	-125 01.98	5.	5.0
19	25	Jul.	1978	23	30	50.9	50 18.18	-127 34.62	11	5.3
20	28	Jul.	1977	15	22	18.5	44 14.64	-128 57.72	15.	5.1
21	06	Oct.	1978	21	26	31.8	40 27.12	-124 35.22	32.	4.8
22*	13	Feb.	1979	05	34	25.9	55 27.18	-157 09.72	33.	5.9

* This event is used only for the corrections in Table 4.2.

Located along the western coast of the United States, the silicic volcanoes of the Cascades are the result of recent, slow subduction of young oceanic material. Whether or not subduction is continuing at present is the subject of active debate (Crosson, 1972; Riddihough, 1978; Keen and Hyndman, 1979; Heaton and Kanamori, 1983).

Low Pn velocities are typical at the Juan de Fuca Ridge (Shor et al., 1968; Hyndman and Rogers, 1981; Cheung and Clowes, 1981). Davis et al. (1976) observe normal, 8.3 km/s, Pn speeds across the ridge, while Keen and Barrett (1971) present evidence for P-wave anisotropy in this region.

A number of workers have investigated the crustal and uppermost mantle structure of the Pacific Northwest-Vancouver Island region; a complex, laterally varying picture as emerged. Tatel and Tuve (1955) were the first to document the thin (< 20 km) crust in the Oregon Coast Ranges. Their results are substantiated and refined by Dehlinger et al. (1965), Berg et al. (1966) and Johnson and Couch (1970). Dehlinger et al. (1965) and McCollom and Crosson (1975) measure laterally varying Pn velocities for the Cascade region: low values for the western Cascades and higher velocities to the east.

Near Puget Sound, the uppermost mantle structure includes a high velocity anomaly dipping eastward at about 50° (McKenzie and Julian, 1971; Crosson, 1972). Pn velocities are also low here; 7.8 km/s is a typical value (Crosson, 1972; McCollom and Crosson, 1975; Crosson, 1976).

The crustal structure beneath Vancouver island is problematic: White and Savage's (1965) refraction study proposes an anomalous 50 km thick crust for the island. A Pn velocity of 7.8 km/s is observed from body waves (Berry and Forsyth, 1975); this value is consistent with surface wave data as well (Wickens, 1977).

Riddihough (1979) points out that the observed gravity data are incongruous with such a great crustal thickness. More recent work by Langston and an associate (Langston, 1977, 1981; Langston and Blum, 1977) and McMechan and Spence (1983) proposes a zone of negative velocity gradient at 40-50 km depth for the entire region. Such a low-velocity zone filled with rocks of lithospheric density (Riddihough, 1979) would explain both the seismic and gravity data.

The complicated, laterally varying shallow structure of the northeast Pacific margin raises questions concerning the nature of the deeper structure under the subducted plate. In this chapter we present data pertinent to this problem and attempt to characterize the upper mantle structure in terms of a comparison to the Gulf of California.

The data set

Records of 22 events at distances of 6° to 42° from southern California comprise the data for study of the upper mantle in the Pacific Northwest (Table 4.1). In Figure 4.1, the epicenters of these events are shown, along with 2° arcs drawn about the midpoints of the appropriate great circle paths. The Mexican data presented in Chapter 3 have a narrow azimuthal range; the experimental geometry for these northern events is not as favorable. The eight calibration earthquakes from Alaska and the Aleutian trench are at a slightly different azimuth from the 14 events closer than 30°, and their rays turn under the Pacific plate rather than below the Juan de Fuca plate or the continent. The total azimuthal range for the data is 70°. The nearer earthquakes are shallow, with depths ranging from 10-32 km. Body wave magnitudes vary from 4.8 to 6.4. These events occurred between September, 1977

and March, 1980 and were recorded by an average of 117 stations at SCARLET with the digital, triggered CEDAR system. Approximately 40 records from each earthquake are included in the final data analysis.

The 22 events yield 853 seismograms covering a $36°$ range in a rather uneven fashion. While there is an abundance of data from $6.5°$ to $13°$, we have few records from $13°$ to $16°$, and those data are relatively poor in quality. The active seismic zone west of Vancouver Island generates large amounts of high-quality data recorded at distances of $16°$ to $22°$. Figure 4.2 contains two examples of waveforms from events in this distance range. The relative quiescence of the Queen Charlotte-Fairweather fault system for $M \geq 5$ events during the experimental time period results in poor coverage from $23°-29°$, with a large data gap from $26.5°$ to $29°$.

The distribution of seismograms with distance for the northeast Pacific data is quite dissimilar to the Gulf of California data set of Chapter 3. A record section of 290 seismograms from eight northeast Pacific events (Figure 4.3) provides an overall view of the northern data. For the Mexican events, we have sparse data near $18°$, which is the most densely sampled range for the northern azimuth. For the Cascade data the poor coverage is farther out at $23°-29°$; at those ranges the spreading center has excellent data (compare Figure 3.7, the southern record section, with Figure 4.3).

The disparities in seismogram distribution between the two data sets have important implications for the attainable structural resolution for each region. For the Gulf of California, the ample data beyond $20°$ place tight bounds on structure below 400 km depth and also on the velocity gradient above the 400 km discontinuity, but not on the size and shape of the discontinuity itself. The discontinuous data
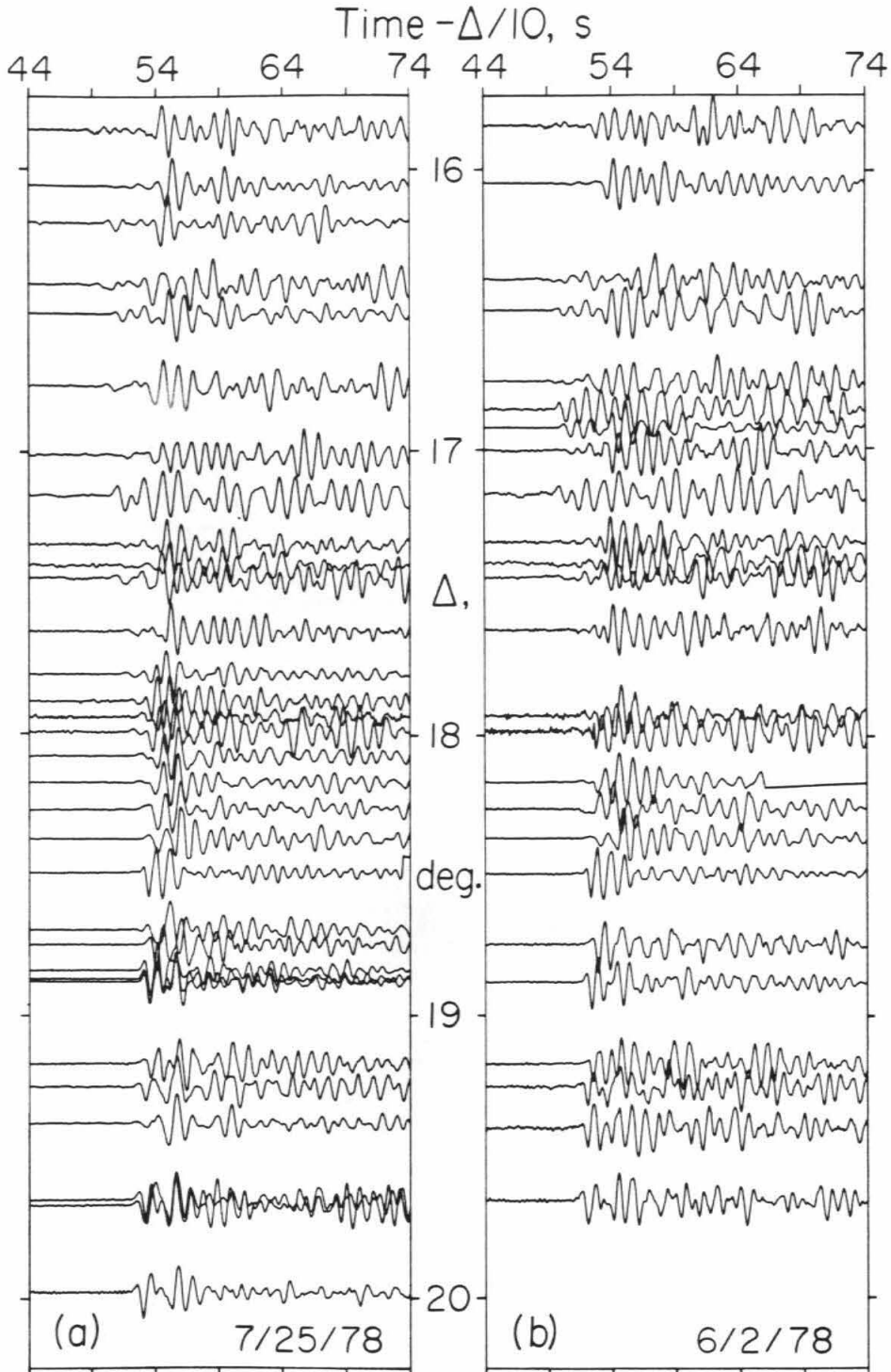
Figure 4.2 Record sections for two events near Vancouver Island. a) Event 19 in Table 4.1. A weak first phase is followed by the strong reflection from the 400 km discontinuity from 16°-18°. Past 19°, the AB branch is now a secondary arrival moving out with distance. It is still very strong at 20°. b) Event 8 in Table 4.1. The same general patterns are visible.
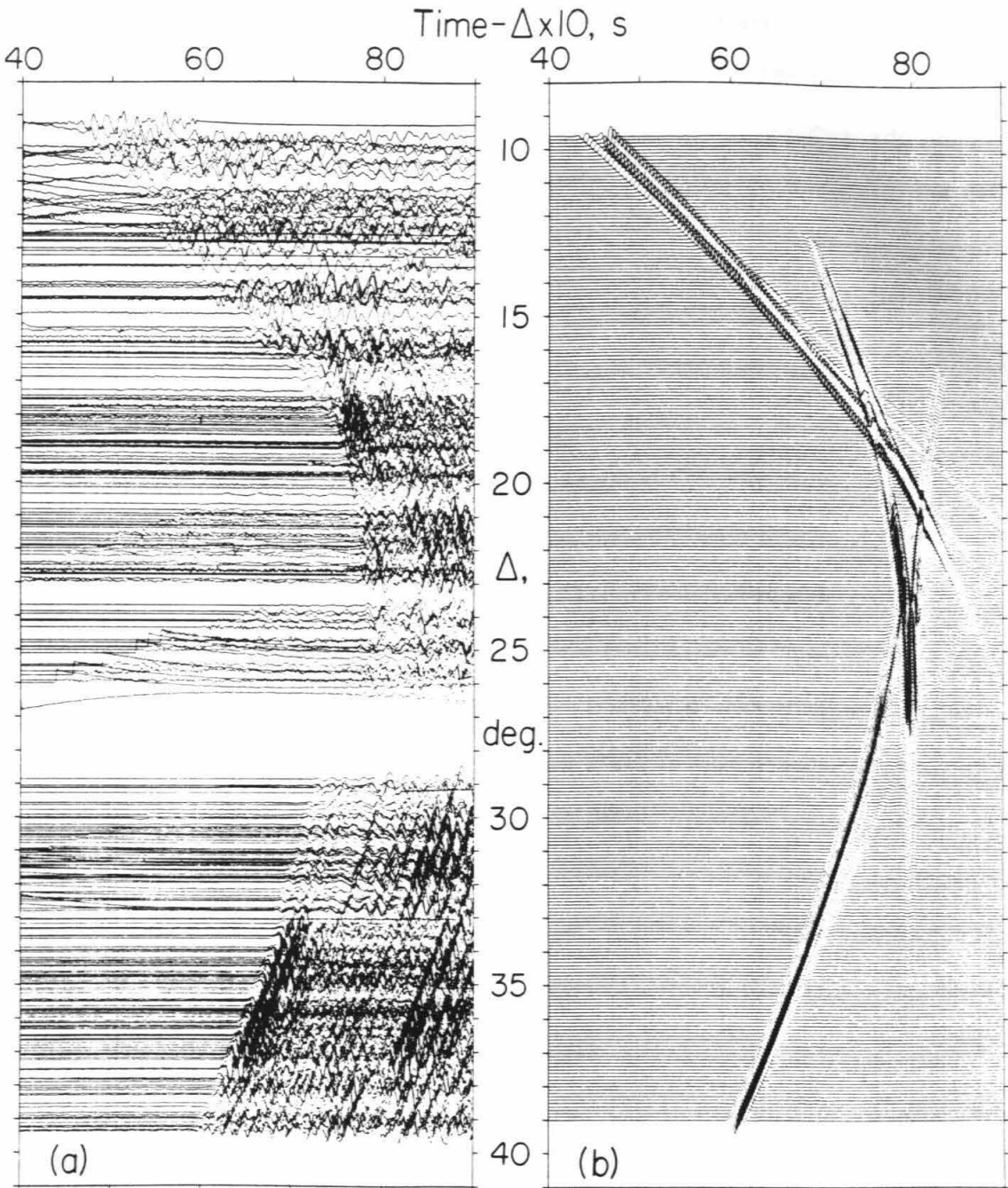
Time-Δx10, s

Figure 4.3 a) Composite record section of 290 seismograms from eight events span-ning 9°-39.5°. Inclusion of all available records does not eliminate the gaps in the data seen here. Records are corrected for event depth and receiver structure. b) Synthetic record section made with model CJF (Table 4.4); 301 seismograms are shown.

available beyond 23° from Canadian events do little to constrain the structure of the 660 km discontinuity for that azimuth. Abundant records from 16° to 22°, however, assist in detailed modeling of the 400 km discontinuity below the Cascade Ranges. Even though these two data sets have their strengths at different ranges, the data overlap sufficiently to compare and contrast the travel times, $dT/d\Delta$ measurements and waveforms and hence the velocity structures of the two regions.

Receiver corrections

To construct station corrections for the northeast Pacific data, we utilize the empirical method outlined in Chapter 3. Least-squares planes are fit to travel times from eight Alaskan earthquakes ($30° < \Delta < 42°$) (Figure 4.1, Table 4.1) and the residuals averaged to compute corrections. These calibration events define a larger azimuthal swath ($30°$) than the corresponding Mexican events ($8°$) and the results are not as consistent. We choose to retain 86 stations with standard deviations of less than 0.15 s (Table 4.2) as compared to 96 stations and 0.10 s for the southern data. Our assumption of constant corrections for the entire azimuth band is less certain considering the fanlike ($70°$ azimuthal range) epicenter distribution shown in Figure 4.1. As a result, the record alignment obtained after application of the corrections is less satisfying than for the other data set.

We can again compare the empirical corrections to Raikes' (1980) teleseismic P-residuals from the same source area (Figure 4.4). Despite the lack of adjustments for station elevation and crustal structure in our receiver corrections, the qualitative agreement between the two sets of residuals is striking. Both exhibit early arrivals in a broad east-west zone near 34°N latitude as well as late arrivals in the Imperial Valley, northern Mojave Desert and near the intersection of the Garlock and San

Table 4.2
Empirical Station Corrections
Cascade Ranges

Sta. Name	No. of Times	Standard Deviation, s	Empirical Corr., s	Sta. Name	No. of Times	Standard Deviation, s	Empirical Corr., s
SBB	7	0.12	0.05	RVR	2	0.01	-0.41
MWC	4	0.09	0.24	PAS	4	0.10	-0.23
CKC	2	0.01	0.47	RAY	5	0.06	0.24
LRR	7	0.12	0.29	BLU	7	0.09	0.58
PEM	3	0.10	-0.12	SIL	4	0.09	0.37
SSK	3	0.11	0.34	SME	5	0.07	-0.53
RMR	7	0.05	0.38	ECF	8	0.14	0.41
CAM	2	0.03	0.59	SIP	7	0.07	0.10
KYP	8	0.10	-0.38	SAD	3	0.11	-0.35
LHU	6	0.14	0.03	SBCD	3	0.14	0.41
SBLG	5	0.06	-0.27	SBLP	3	0.10	0.12
RYS	4	0.07	0.74	PLT	5	0.05	0.14
PKM	6	0.14	0.58	FTC	3	0.04	-0.28
BMT	8	0.08	-0.19	YEG	7	0.13	0.42
TMB	4	0.13	0.49	ABL	4	0.05	0.17
BCH	7	0.13	0.51	RUN	3	0.14	0.22
SGL	5	0.05	-0.17	CRR	7	0.07	0.12
SUP	6	0.08	-0.12	AMS	5	0.07	-0.04
LTC	6	0.05	-0.41	BC2	3	0.07	-0.19
CO2	8	0.12	-0.26	SPM	6	0.08	0.47
GRP	7	0.11	0.31	LED	5	0.06	0.39
PNM	4	0.09	-0.05	INS	7	0.05	-0.08
CPM	7	0.14	0.17	LTM	5	0.13	0.29
RVS	2	0.05	0.31	TPO	7	0.13	-0.17
KEE	5	0.13	0.05	SWM	3	0.08	0.31
CIS	3	0.03	-0.39	GLA	8	0.04	0.31
IKP	6	0.04	0.38	CPE	7	0.08	0.27
VST	5	0.09	0.03	PLM	7	0.11	0.47
TPC	6	0.10	0.04	CLC	4	0.14	0.32
ISA	6	0.06	-0.22	GSC	7	0.09	0.36
SBSM	2	0.12	-0.01	SBCC	7	0.12	0.36
SDW	5	0.06	0.06	LJB	8	0.13	0.13
HDG	3	0.09	0.44	TTM	7	0.09	0.53
JNH	7	0.11	0.43	RVM	5	0.09	0.17
CTW	7	0.12	-0.21	POB	5	0.07	-0.06
SMO	6	0.11	0.32	CH2	7	0.09	-0.07
JUL	7	0.10	0.35	COA	3	0.09	0.54
BAR	8	0.08	0.30	SS2	4	0.11	0.45
VG2	4	0.11	-0.03	WWR	3	0.06	-0.12
MLL	4	0.09	0.44	MOV	4	0.07	0.28
CRG	5	0.13	0.53	SBSC	2	0.05	-0.08
SBAI	3	0.07	-0.21	CFL	3	0.02	0.19
RCH	4	0.05	0.08	DB2	5	0.08	-0.36

Figure 4.4 a) Empirical station corrections (Table 4.2) in contour format. These values include the effects of station elevation and shallow structure. Note the wide, east-west band of negative values near 34° latitude becoming more positive to the north and south. b) P residuals of the same source area relative to station GSC (Raikes, 1978). Adjustments for elevation, sediments and Moho variation have been made. The same pattern is observed; much more negative residuals are found just north of the Salton Sea with more positive delays both south and north. The contour interval is 0.25 s.

Andreas faults.

Travel times

After corrections for ellipticity, earthquake depth and receiver structure, the 22 events generate 1068 usable travel times; 152 of these are secondary arrivals. Figure 4.5 displays the travel time data, both with and without distance dependent baseline shifts devised to to eliminate the effects on source location and origin time. Superimposed on Figure 4.5b are two models: GCA, the spreading center model of Chapter 3, and CJF, the Cascades-Juan de Fuca model described below.

Close inspection of the two sets of travel time data reveals systematic regional disparities in $T(\Delta)$. Waves from earthquakes offshore northern California and Oregon arrive earlier than the corresponding events in the Gulf of California for distances up to $12°$. This discrepancy is not surprising, since the northern travel path is beneath the western margin of the continent instead of an actively spreading ridge. First arrival times in the range $15°-23°$ are similar for both groups within the data scatter, but the time separation of the AB and CD branches at $16°$ is significantly greater for the Vancouver Island events.

The nature of the observable secondary arrivals in the $18°-23°$ distance range (Figure 4.5), however, is quite different from the Mexico data. The data described in Chapter 3 do not contain identifiable arrivals from the AB travel time branch past $20°$ and exhibit strong phases representing the EF branch (reflection from the 660 km discontinuity) from $20°$ to $24°$ (see Figure 3.10b). Only a few times from one event north of Vancouver Island can be identified as part of the EF branch, in contrast, a number of observations of the AB, or back branch of the 400 km discontinuity, are seen to at least $21°$ with dubious arrivals extending to $23°$. The predominance in
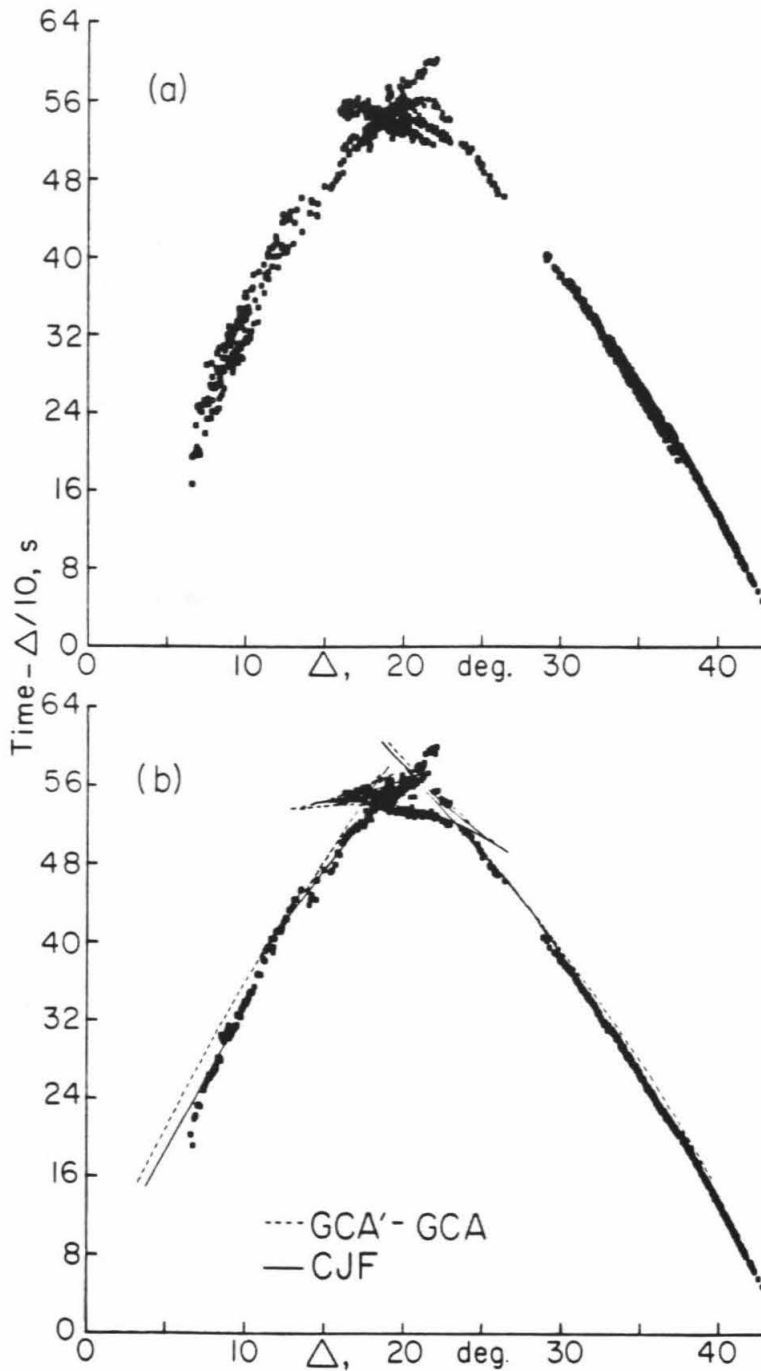
Figure 4.5 Reduced travel time data. a) The 1068 times (152 secondary arrivals) are plotted with only depth and receiver corrections applied. Note the large scatter for $\Delta < 15°$. b) The same data after distance-varying baseline shifts are applied. The model derived from these data, CJF, is superimposed along with the Gulf of California model (see Figure 3.10 for comparison). Notice that GCA'-GCA is too slow for $\Delta < 12°$, $14° < \Delta < 18°$ and $\Delta > 30°$.

the northeast Pacific records of the AB branch over the EF arrivals at these distances signifies a real, quantifiable change in structure between the spreading center and the Cascade Ranges at depth.

Due to relatively poor data from $23°$-$26°$ and none at all from $26°$-$29°$, we cannot make observations of the forward branch (CD) of the 660 km discontinuity for the northern model area. First arrivals beyond $25°$ are clearly earlier from Alaska than from Central America.

Ray parameter measurements

We obtain 40 estimates of $p(\Delta)$ for the northeast Pacific utilizing the processing scheme discussed in Chapter 3 (Table 4.3); nine of these measurements are for secondary phases. A number of events are too close to SCARLET for the plane wave assumption to be valid, and the least-squares routine yields unreliable results. For these earthquakes, graphical estimates of $dT/d\Delta$ are made (Table 4.3). The ray parameter values for these events are only approximate and are more uncertain than the plane-fit estimates for the more distant events.

The data and corresponding curves for CJF and GCA are presented in Figure 4.6. The above-discussed data distribution with distance is also reflected in the p-Δ measurements. While we can calculate only a single $dT/d\Delta$ value for the forward (EF) branch of the 660 km discontinuity, several estimates are available for the back (AB) branch of the 400 km velocity break. Unfortunately, these measurements are quite scattered, probably due to complex source functions for several events which make accurate picking of secondary phases problematic.

In general, the $p(\Delta)$ data for the northern azimuth are more scattered than the equivalent spreading center values, precluding unambiguous interpretations of lateral

Table 4.3

dT/dΔ Data

Event No.	Δ deg.	p s/deg.	RMS Error, s	Arrival Type	No. of Stations
1	33.096	8.71	.088	F	48
2	39.909	8.22	.096	F	52
3	33.024	8.71	.073	F	30
4	39.175	8.24	.061	F	68
5	40.318	8.15	.081	F	59
6	35.461	8.53	.060	F	78
7	35.703	8.52	.096	F	50
8	17.450	12.57	.422	F	20
	19.084	10.51	.099	F	9
	17.485	10.92	.480	L	19
9	21.406	10.40	.266	F	30
	20.922	12.51	.427	L	26
	22.449	9.56	.266	L	11
10	17.424	11.99	.346	F	20
	19.317	10.49	.256	F	21
	17.381	10.90	.388	L	19
	19.569	11.52	.370	L	12
11	19.812	10.97	.386	F	45
	20.127	12.16	.303	L	36
12	24.685	9.16	.265	F	23
13	19.412	10.98	.323	F	19
	19.468	11.48	.283	L	19
14	30.094	8.98	.180	F	25
	31.852	8.72	.164	F	30
15	8.007	12.68	**	F	8
	10.152	13.42	**	F	12
16	10.563	13.94	**	F	13
	12.690	13.63	**	F	7
17	9.226	14.23	**	F	12
	11.438	13.28	**	F	9
18	7.203	14.68	**	F	9
	9.435	13.95	**	F	13
19	17.422	12.48	.500	F	23
	19.125	10.54	.240	F	19
	17.392	11.10	.420	L	22
	19.283	11.91	.365	L	12
20	13.308	12.95	**	F	10
	15.512	12.74	.189	F	9
21	9.693	13.42	**	F	10
22	35.062	8.57	.077	F	57

** For these events, dT/dΔ is calculated graphically.
F denotes first arrivals, L later phases.
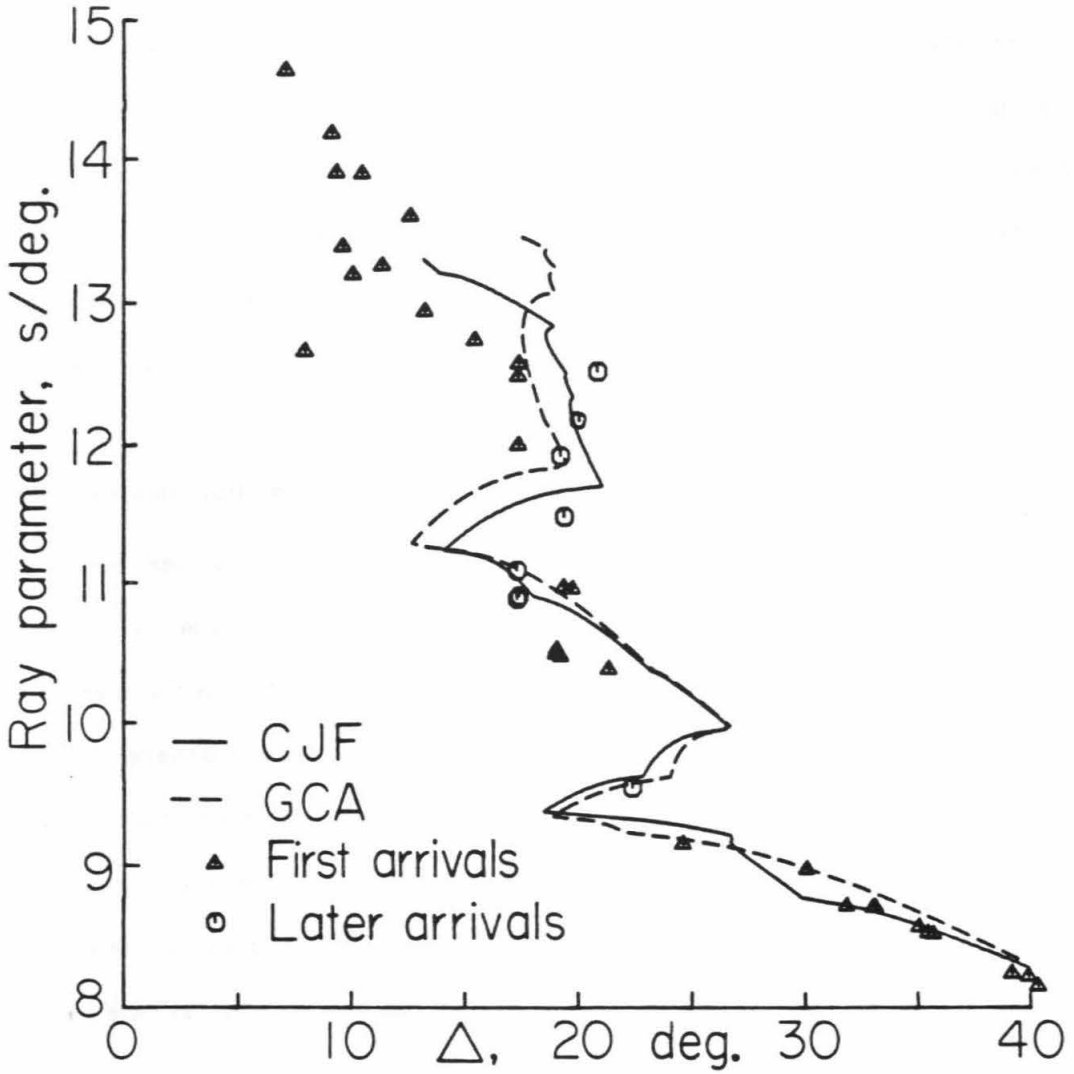
Figure 4.6 Ray parameter measurements for the northeast Pacific data, displayed with both CJF and GCA. These data are not very useful in distinguishing between the two models but are generally more consistent with CJF.

variations based on dT/dΔ data alone. Clear distinctions between the two data groups exist only for first arrivals closer than $17°$ and the AB secondary phases near $21°$. The p-Δ curve for CJF fits these two subsets of the data better than GCA, but in an overall sense $p(\Delta)$ for GCA and CJF (Figure 4.6) are quite similar. We do not rely heavily on the ray parameter data to make distinctions between the two, but will instead explore relative amplitude differences with waveform modeling, and attempt to compare each entire data set at once using wave field continuation.

Relative amplitude patterns

The seismograms from $6°$ to $13°$ are extremely complicated, often high-frequency (relative to 1 Hz) and contain no identifiable, consistent later phases in the P-wave train. While we do not observe reflections from the 400 km discontinuity in this distance range, the one event located $13°$-$15°$ from SCARLET is particularly poor and we cannot definitely state that CD arrivals from the 400 km discontinuity do not appear at these distances because of the messy records. In contrast, excellent secondary arrival data exist at $13°$-$15°$ for the southern data from an earthquake on the Rivera Fracture Zone (see Figure 3.3).

Beginning at $16°$, larger events from the Vancouver Island region provide more useful waveform data. Although the source signatures are often complex, the relative amplitude observations are stable for $16°$-$22°$. At $16°$, the first arrival is extremely weak and is followed by a strong reflection from the 400 km discontinuity about 5 s later (Figures 4.2, 4.7a). The time separation decreases with increasing waveform complexity (Figure 4.7b) until the AB-CD crossover occurs at $18.4°$. By a distance of $20°$, the AB branch arrives 3 s after the first wave (Figure 4.7c), and is at least as large as the refracted arrival. It is difficult to determine the exact cutoff
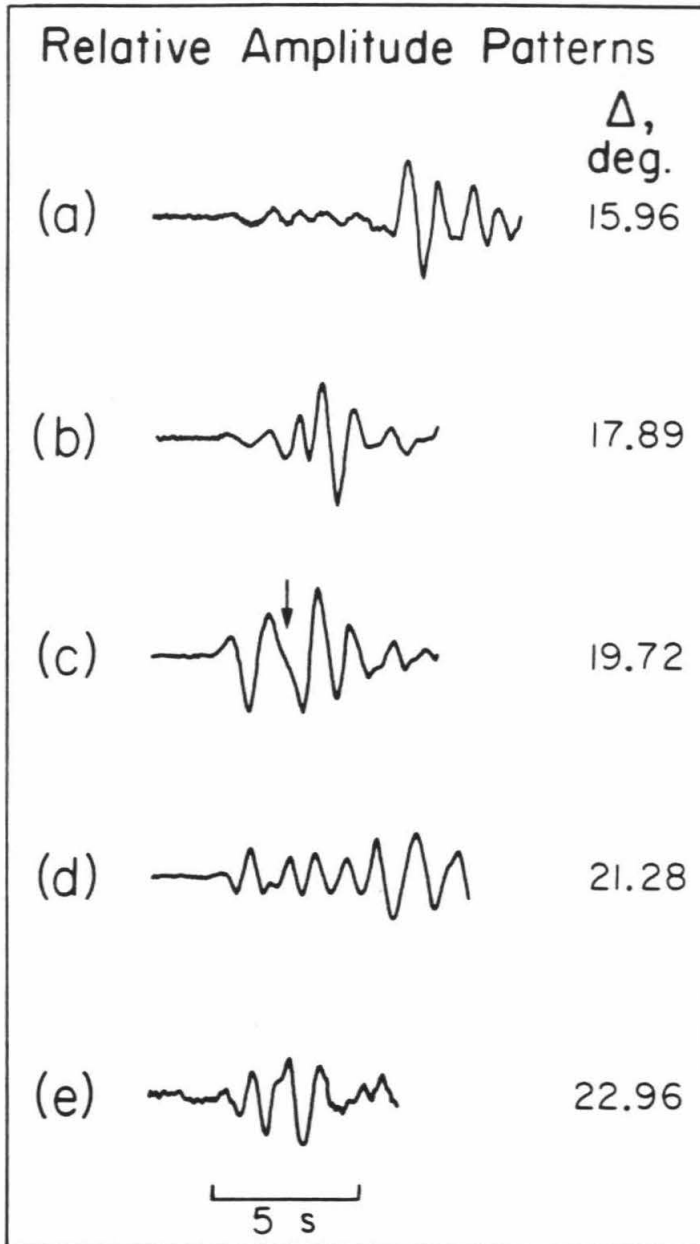
Figure 4.7 Relative amplitude patterns for the northern data. a) Near 16°, the first arrival (AB branch) is very weak, while the reflection from the 400 km discontinuity is quite strong. b) At 18° the CD branch has moved in closer to the first arrival but not yet crossed it. c) At 20°, the arrow indicates the approximate onset of the AB branch, now a large secondary phase. d) The larger phase 5 s behind the first break on this noisy record may be the AB arrival, still comparable in size to the CD branch at 21°. e) The record at 23° shows the reflection from the 650 km discontinuity 2 s behind the first-arriving CD branch. This relatively poor-quality record is typical of observations in this distance range from Queen Charlotte Island Fault events.

distance for the AB branch due to the complicated P-wave codas; a good estimate is 22°-23° (Figure 4.7d). We see no evidence for a reflection from the 660 km discontinuity at 20° in any of five available record sections. This pattern is in contrast to the southern data for this distance range. At 16°, the ridge data have a weak first arrival, but the strong second phase is only 3 s behind the first, and the crossover point occurs closer to 18°, although there is a gap in the data precisely at that point. Middle America Trench events at distances of 20° or more feature no AB arrival at all and a strong EF reflection from the 660 km discontinuity starting at 19°.

First arrivals from the northern azimuth are reasonably strong from 20° to 21.5°, then start to weaken relative to the arrival from the 650 km discontinuity (Figure 4.7e) which is observed for only one event (No. 9 in Table 4.1) at distances of 21.8° to 23°. Beyond 23°, we cannot identify any obvious secondary arrivals in the northern data, primarily due to poor data quality (23°-26°) or a total absence of records (26°-29°).

These relative amplitude patterns are similar to GCA except in the critical distance range of 18°-23°, where the northeast Pacific records are dominated by the back branch arrival from the 400 km discontinuity and the Mexico data shows mainly the forward branch of the 660 km discontinuity. In the next section, we model the Cascade Ranges data set using synthetic seismograms and compare the result to GCA and the spreading center data.

Model description

Model CJF (Figure 4.8, Table 4.4) satisfies the data described above: travel times, apparent velocities and waveforms. Because we used GCA as the starting
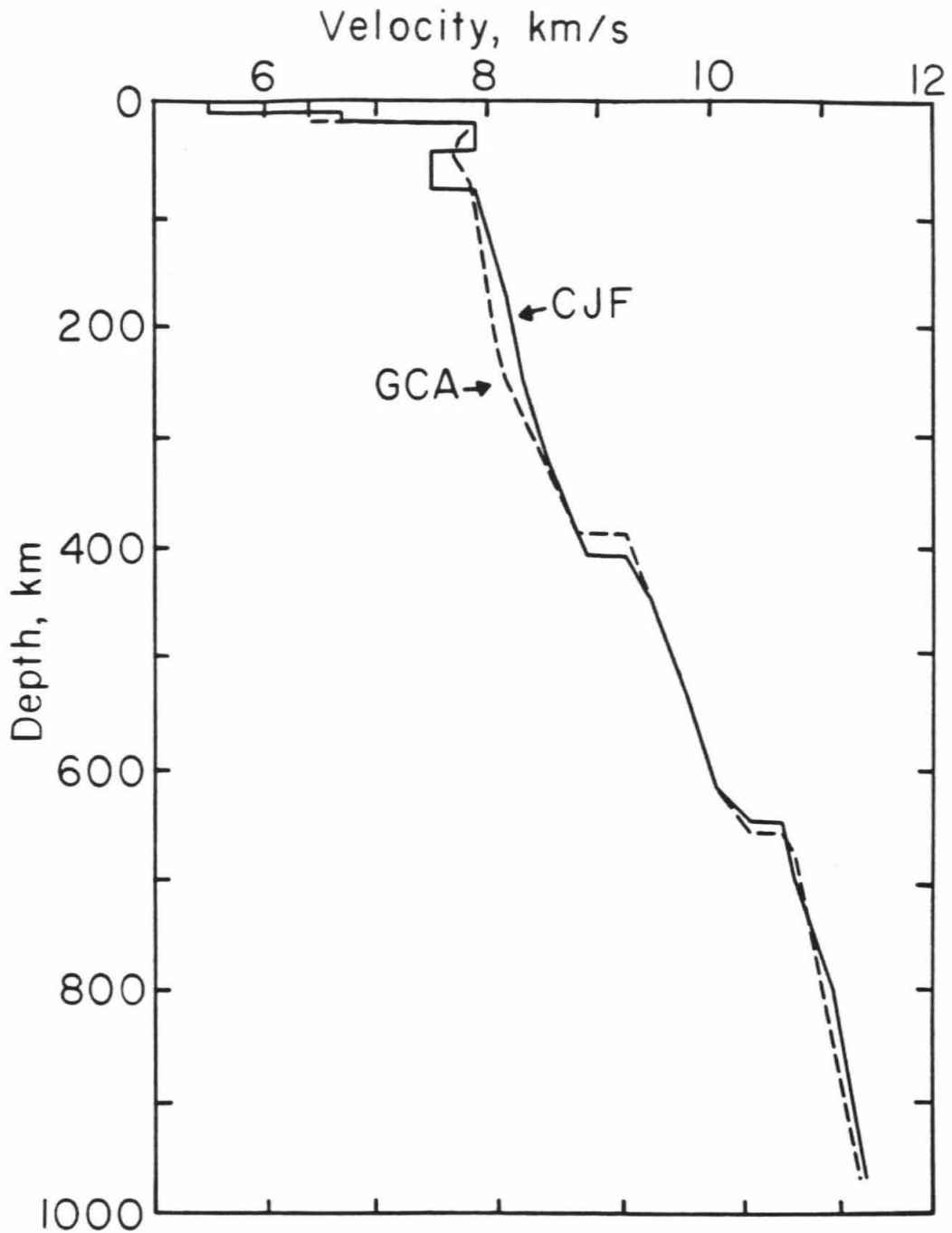
Figure 4.8 Models CJF and GCA. CJF is derived for the Cascade Ranges data set using GCA (Chapter 3) as a starting model. The important differences between the two are in the absolute velocities and gradients above 400 km; also, CJF's velocities are higher below 800 km.

Table 4.4

Model CJF

Depth km	Velocity km/s	Depth km	Velocity km/s
0.	5.500	275.	8.400
10.	5.500	300.	8.475
11.	6.700	325.	8.560
19.	6.700	350.	8.660
20.	7.900	375.	8.760
45.	7.900	400.	8.860
46.	7.500	410.	8.900
80.	7.500	411.	9.250
81.	7.900	450.	9.476
100.	7.952	538.	9.800
125.	8.025	620.	10.060
150.	8.100	650.	10.360
175.	8.175	651.	10.650
200.	8.225	700.	10.750
225.	8.275	800.	11.100
250.	8.325	970.	11.400

point in the modeling process, it is shown along with CJF for comparison. The differences between the two are not drastic but they are significant and resolvable. In essence, CJF is more similar to previously published models for tectonically active continental regions such as Burdick and Helmberger's (1978) T7 or Burdick's (1981) T9; it features higher velocities with a less severe gradient near 200 km and does not coincide with GCA until a depth of 350 km. These results have important implications for the depth extent of lateral heterogeneities in the mantle.

Travel times are dominant in constructing the topmost portion of CJF. The crust and uppermost mantle in the study area is extremely complicated and has large lateral variations in Moho depth and Pn velocity. Figure 4.9 shows several of the proposed models for shallow structure in the Cascades-Vancouver Island region. There is obviously no consensus on the area's crust and uppermost mantle velocity structure.

Several refraction studies have established a crust of less than 20 km thickness in the Oregon Coast Ranges (Tatel and Tuve, 1955; Berg et al., 1966; Shor et al., 1968), but thickening to the east in the Cascades (Dehlinger et al., 1965; Johnson and Couch, 1970). The observed Pn velocities correlate with the crustal thickness. Dehlinger et al. (1965) and McCollom and Crosson (1975) document very low values of ≈ 7.7 km/s west of the Cascades, increasing to about 8 km/s to the east. To further complicate matters, Langston (1977) decides on the basis of converted teleseismic phases that a shallow low velocity zone (to 45 km depth) lies below a 20 km thick upper crust at Corvallis, Oregon.

The anomalous structure at Vancouver Island adds still more complexity to the problem of selecting an appropriate topmost structure for CJF. The absence of Pn first arrivals on a 360 km north-south refraction line led White and Savage (1965) to
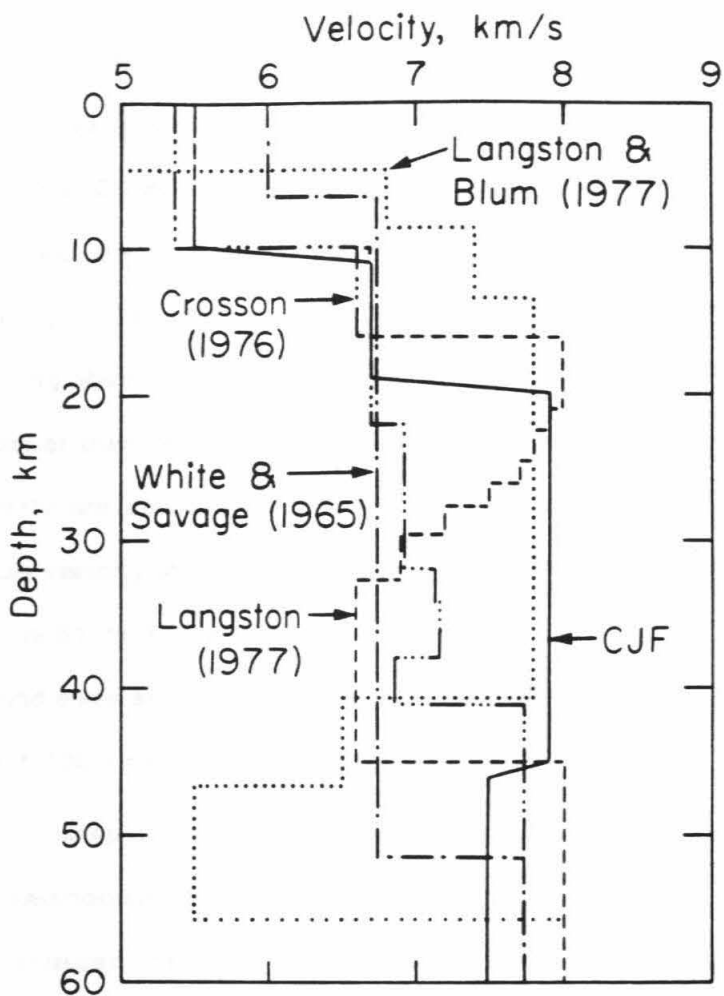
Figure 4.9 Comparison of five crustal models for the northwest United States-Vancouver Island region. There is little agreement between the studies.

propose a 50 km, two layer crust for the island. McMechan and Spence (1983) also find a layer of intermediate velocity ($\approx$7.0 km/s) at 15.5 km depth, but agree with Langston (1981) that there might be a shallow low-velocity zone as well, with a total crustal thickness of less than 40 km. Riddihough (1979) infers crustal sections of 10 km offshore, 20 km beneath the Coast Ranges and 30-40 km farther inland. As an average, we use the Coast Ranges crust of 20 km with the crustal velocity values of Langston (1977). Our Pn velocity of 7.9 km/s is a reasonable average of the widely varying observations for the region. We construct a low-velocity zone that is slightly deeper than Langston's (1981) feature; its 45-80 km depth extent and 7.5 km/s velocity are constrained only by travel times from 8°-15°. The lid thickness and minimum velocity in the low-velocity zone trade off; we choose a lid thickness of 25 km. From 81 to 175 km, CJF's gradient is adjusted to fit first arrival times near 15°. Beyond some simple averaging of available data on local crustal structure, then, the topmost 200 km of CJF are determined from travel time data alone.

The first step in the comparative waveform modeling process is to generate GCA synthetic seismograms for selected data profiles from the northern azimuth. We have already discussed the topmost portion of the final northern model which clearly differs from GCA. Because at least the uppermost 100 km of GCA is not appropriate for the northeast Pacific, waveforms predicted from the southern model are not expected to match the northern data well at short distances. At distances greater than 16°, though, comparisons are useful in determining the changes necessary to fit the Cascade Ranges data.

In Figure 4.10, records from an event near Vancouver Island (No. 19 in Table 4.1) are compared to synthetic profiles for GCA and CJF. The amplitudes, timing and waveshapes for GCA do not match the data throughout the profile. Near 16°, GCA's
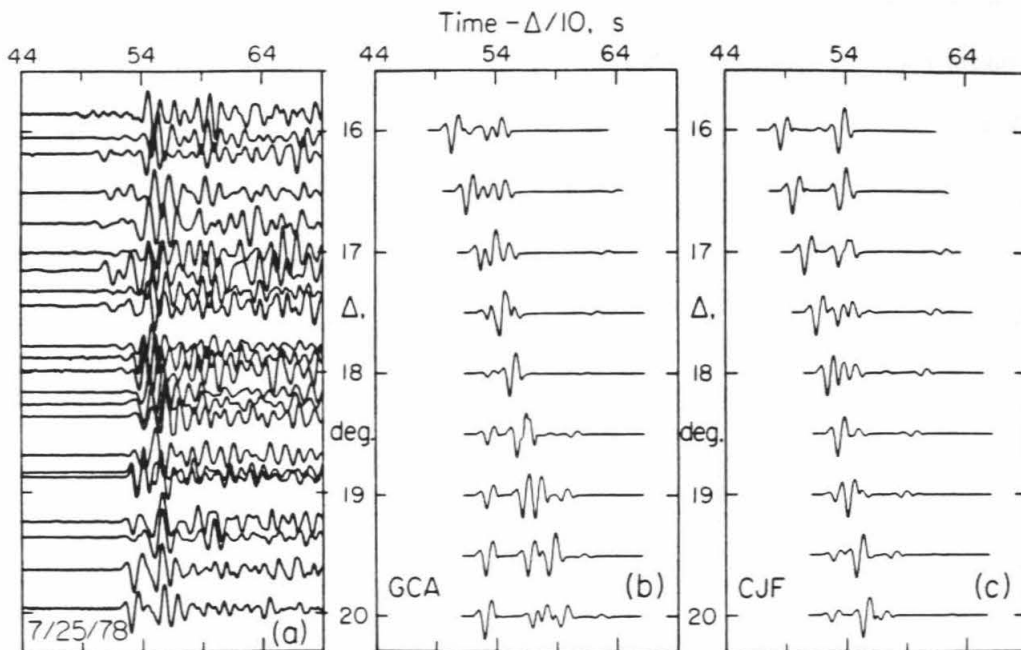
Time – Δ/10, s

Figure 4.10 Observed and synthetic record sections for event 19 of Table 4.1. a) Data. b) GCA synthetics. From 16°-18° the first arrival is too large and the second phase too early. Past 19°, the second arrival (AB branch) is too late and decays in amplitude too quickly, indicating that GCA's large gradient above 390 km is too severe for the northern data. c) CJF synthetics. Relative amplitudes and timing are better than GCA at all distances.

first arrival (AB branch) is too large and the secondary phase (CD branch) is too small and arrives much too early. Some problems in the relative timing between these two branches could be due to the disparate uppermost mantle velocities, but close inspection of Figure 4.10 demonstrates that the entire 400 km discontinuity triplication for GCA occurs too close in distance. The GCA first arrival crossover occurs near 18° instead of the observed 18.4° and at 20°, the AB arrival of GCA (second phase) is both too small and too late. These basic features are confirmed with data from several other events in the same vicinity.

Figure 4.11 displays the only northern data section which contains any reliable arrivals from the 660 km discontinuity. This event unfortunately exhibits large-amplitude coda arrivals which are problematic to interpret, and the AB branch is difficult to identify near 21°. Even though this record section is not of the same high quality as corresponding data from Mexico, comparisons to GCA are still revealing. Event 9 (Figure 4.11, Table 4.1) has very weak first arrivals until about 21°, in contrast to GCA. The EF arrival from the lower discontinuity emerges from the noise at about 21.8°, but it is very clear in GCA synthetics as early as 20°. Furthermore, GCA's 660 km reflection is late relative to the first arrivals from 21.8°-23°.

The lack of good waveform data from northeast Pacific events at distances of 23°-28° prevents further assessment of the suitability of GCA's velocities near 660 km depth for the Juan de Fuca region. The differences in first arrival travel times beyond 25° between the two data sets, however, requires slightly faster velocities in the north below 700 km.

Some relatively small adjustments to GCA alter the predicted waveforms so they are much more consistent with the Cascade Ranges data. After restructuring the top 100 km of CJF as outlined above, we need to increase the absolute velocities from
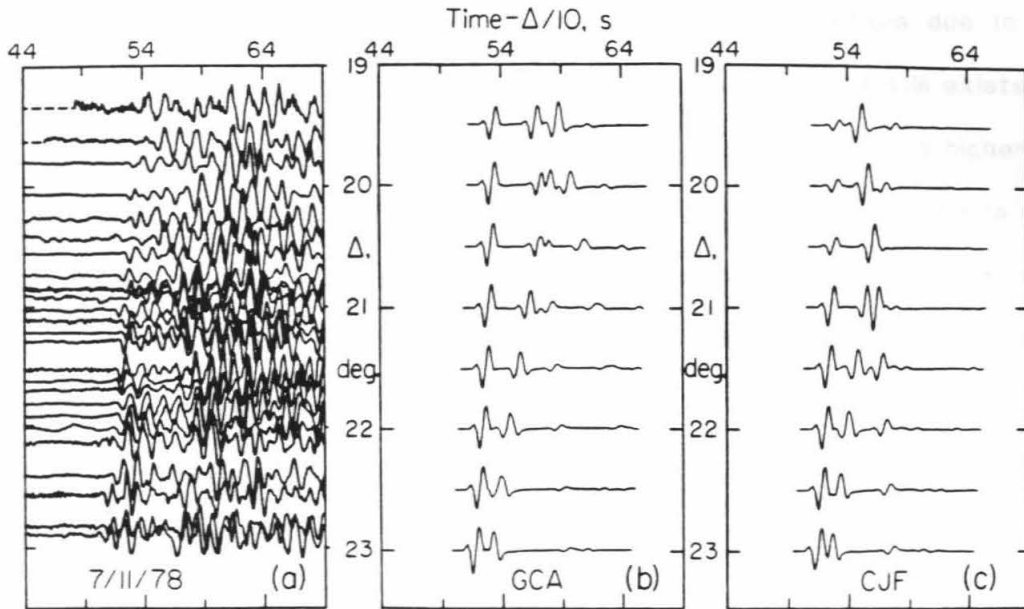
Time-Δ/10, s

Figure 4.11 Data and synthetic sections for event 9 (Table 4.1). a) Data. This earthquake has large-amplitude arrivals 8-9 s after the first arrival; the first 5-7 s are important for the modeling. First arrivals are weak from 19°-20°; the AB branch is not obvious in this distance range. Initial phases are stronger past 21°. Near 22°, the reflection from the 650 km discontinuity (EF branch) is visible as a second arrival. b) GCA synthetic section. Before 22°, the first arrival and the EF branch are both too strong. The 650 km reflection is a little late at all observed distances. c) CJF synthetic section. The first-arrival relative amplitudes are correct. CJF's slightly shallower 650 km discontinuity matches the data better from 22°-23°.

100-300 km depth to agree with first arrival travel time data from $8°$-$13°$. As in GCA, we have incorporated a region of very slight positive velocity gradient from 175-250 km to try to reduce the size of the first arriving waves near $16°$. This effort is again not totally successful (Figures 4.10a, c), perhaps due to depth-varying attenuation. The sharp gradient from 225-390 km in GCA still exists in CJF, but only deeper than 350 km; this change is in accordance with CJF's higher velocities from 100-300 km and the observation of the AB travel time branch to at least $22°$. In order to increase the time separation between the first arrival and the reflected phase from $16°$ to $18°$, and to shift the crossover point from $18°$ to $18.4°$, the 390 km discontinuity of GCA was placed at 410 km and decreased in size to a 3.8% velocity jump. The effects of these structural changes above 450 km are visible in the CJF synthetic record section computed for a sample event covering $16°$-$20°$ (Figure 4.10c).

An improved fit to the EF branch data near $22°$ (Figure 4.11) is achieved by raising the lower discontinuity to 650 km and decreasing the gradient immediately below that velocity jump to make later arrivals less prominent from $20°$-$21°$. A slightly stronger velocity gradient below 700 km matches the faster travel times from Alaskan events from $25°$-$42°$. Figure 4.3 compares the overall character of the northern data to the CJF synthetics.

While GCA obviously does not satisfy data from Vancouver Island events recorded at Caltech, to establish the validity of the model changes it is vital to demonstrate that CJF is not representative of Gulf of California structure. To do this, we compare synthetic seismogram sections computed with CJF for some of the Mexican events modeled in Chapter 3. Figure 4.12 presents the same data as in Figure 3.3 with both GCA and CJF synthetics plotted below the appropriate traces. CJF
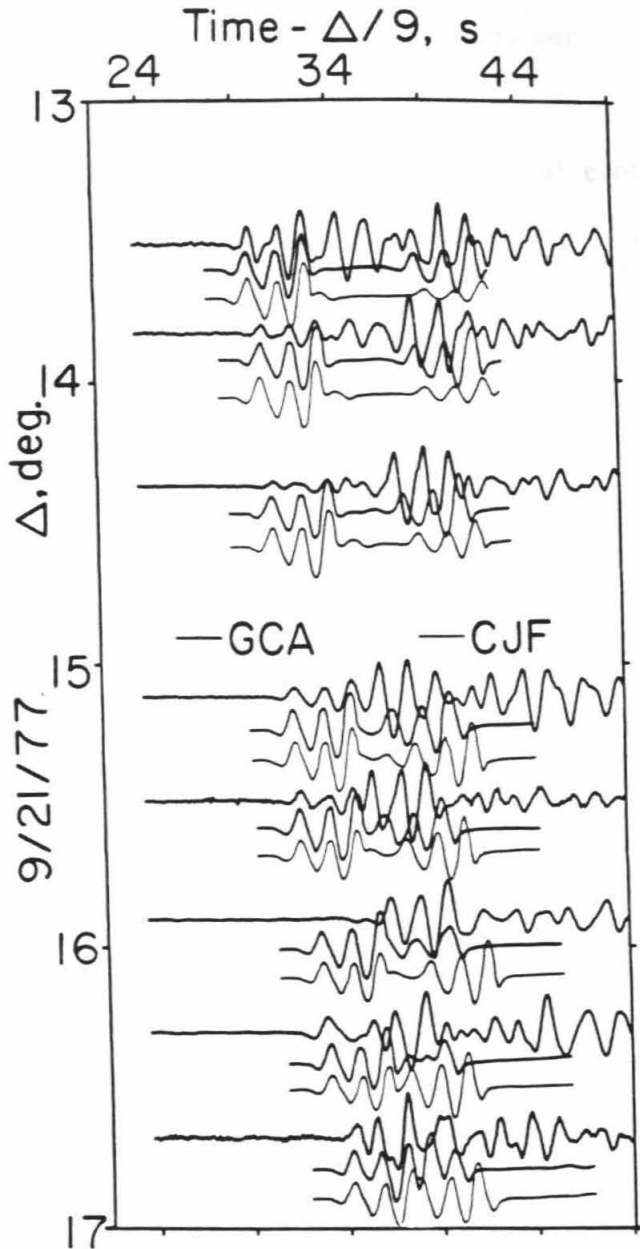
Figure 4.12 Comparison of GCA and CJF for Gulf of California data from 13°-17°
(event 2, Table 3.1). For each set of three traces, the data is topmost, GCA is in the
middle and CJF is plotted lowest. The reflection from CJF's 410 km discontinuity
arrives much too late at all distances. CJF's first-arrival amplitude is also much too
large. GCA's relative amplitudes and timing match the data better.

does not match these data well. The first arrival amplitudes are too large for $13°$-$15°$ and the reflections from the 410 km discontinuity occur too late for the entire section.

Two southern events in the distance range $18°$-$23°$ confirm that CJF is inappropriate in the corresponding 300-700 km depth range. Figure 4.13 displays the data of Figure 3.4 as well as the corresponding synthetic records. For this deeper (96 km) earthquake, the extended AB branch CJF predicts is not compatible with observed seismograms from $18°$-$20°$. CJF's slightly shallower 650 km produces secondary arrivals which are too early in the $21°$-$22°$ range. The record section and synthetic seismograms for a shallower Mexican event (No. 24 in Table 3.1) (Figure 4.14) exhibit the same basic patterns at slightly shifted distances.

The more subtle structural changes near 660 km are reflected in correspondingly smaller changes in CJF synthetic records for $26°$-$30°$ (Figure 4.15). Here the reduced gradient below 650 km in CJF results in a relatively larger first arrival from $26°$-$28°$ (these are uncorrected distances for an 80 km deep event) and also small changes in timing. These synthetic waveforms are not as satisfactory as GCA's predictions. The above examples demonstrate that while GCA does not satisfy the data from the north, neither does CJF fit the southern records. The structural differences between the two regions are resolvable and real. The disparities are subtle, however, and may not be noticeable at longer periods. Grand and Helmberger (1983) derive a single model for the entire west coast of North America for long-period shear waves. Both of the study areas discussed here lie within the region of their single model TNA and are presently tectonically active. The greater resolving power of the short-period data assist in defining significant structural variations between the Gulf of California and the Cascade Ranges to depths of 350 km.
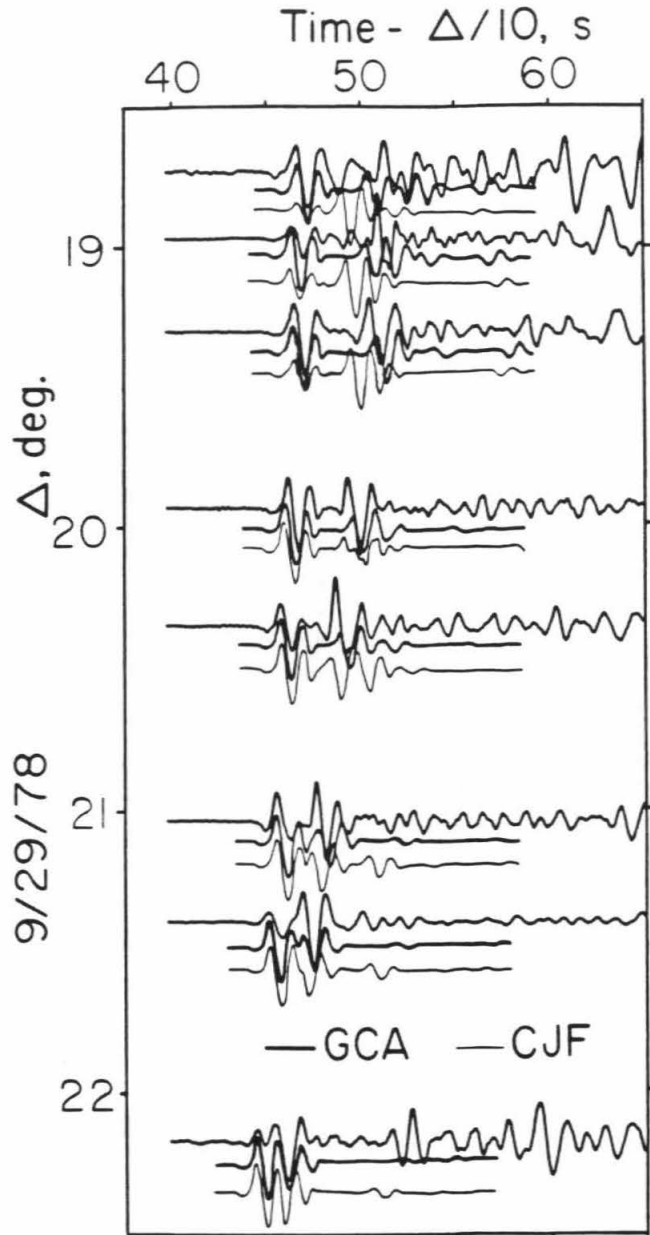
Figure 4.13 GCA and CJF compared to Mexican event 14 (Table 3.1). The distances shown here are not corrected for the event depth of 96 km. See Figure 4.12 for format explanation. From 18.5°-19.5°, CJF predicts a very large AB arrival that is not in the data, while GCA's sharp gradient above 390 km cuts off that branch before 19° for this event depth. Beyond 20°, CJF's slightly shallower 650 km discontinuity results in small timing errors.
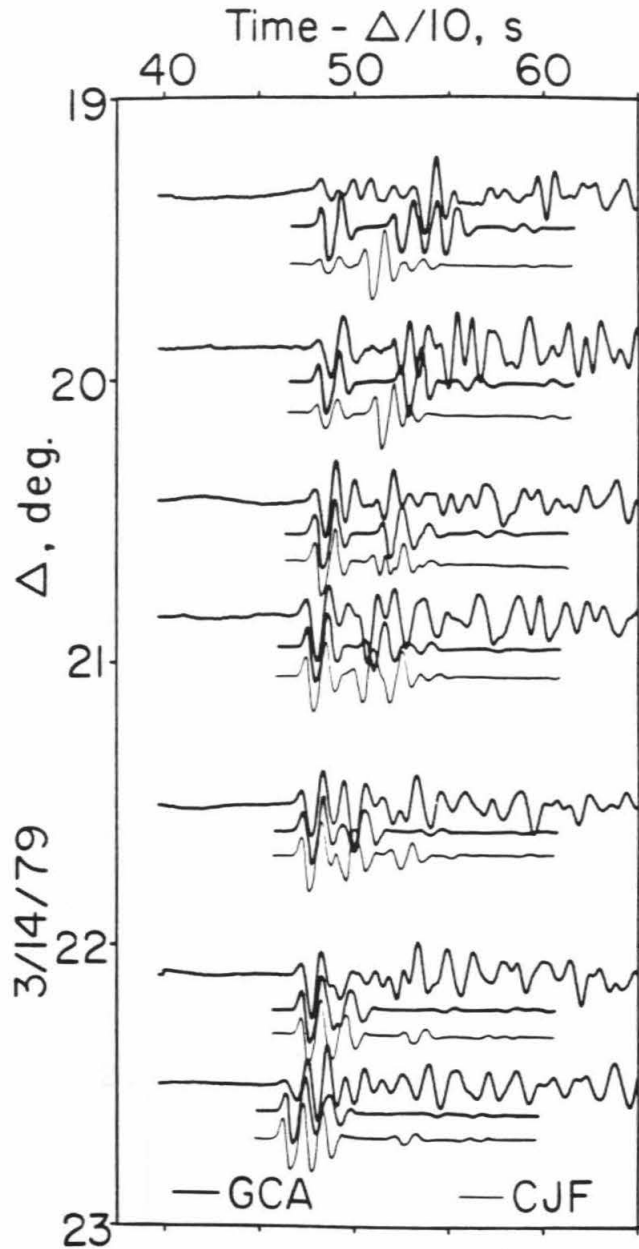
Figure 4.14 GCA and CJF compared to Mexican event 24 (Table 3.1). This earth-quakes' depth is 52 km; distances are not corrected. See Figure 4.12 for format. As in Figure 4.13, we see that the large AB branch produced by CJF up to 20.5° is not present in the data. CJF's more moderate gradient above 350 km is not sufficient for the southern data set.
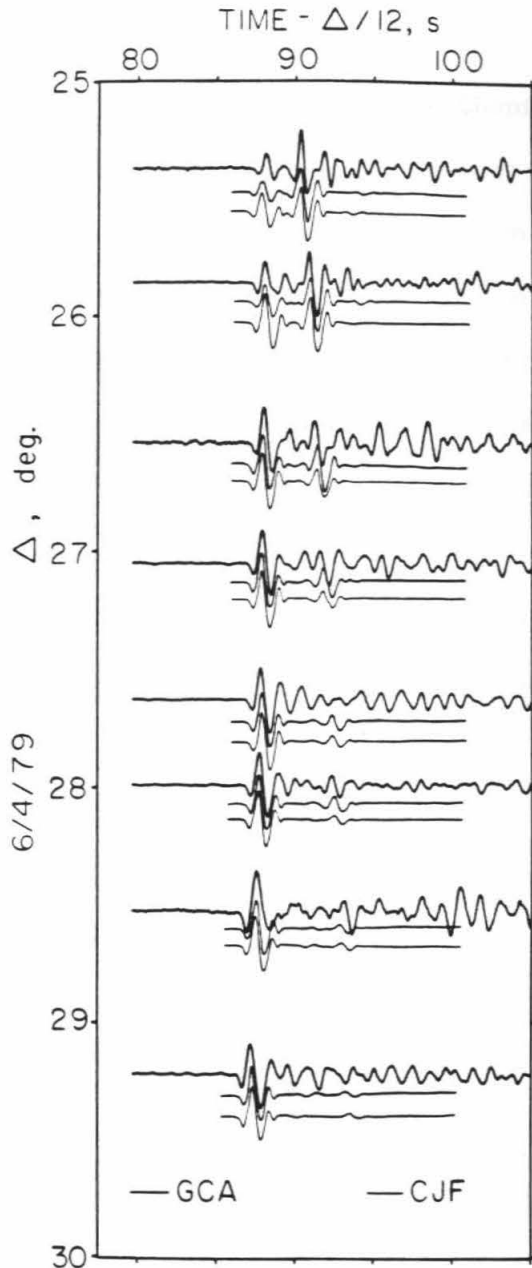
Figure 4.15 GCA and CJF compared to the 80 km deep event 27 of Table 3.1. As before, distances are uncorrected for source depth; see Figure 4.12 for format. Due to the smaller differences between GCA and CJF below 450 km, the synthetics for the two models are similar from 25°-30°. GCA's amplitude ratios from 25°-27° do fit this record section better.

Wave field continuation comparison

Following the same procedure developed in Chapters 2 and 3, we slant stack and downward continue the northeast Pacific data set to check its consistency with the waveform-derived model CJF. Fewer seismograms spread out over a slightly longer distance range will result in more spatial aliasing than for the Mexico data. In addition, the waveforms from the northern azimuth are generally less coherent array-wide than their southern counterparts: we expect the τ-p image to be less sharp. More data in the $16°$-$22°$ range from events near Vancouver Island, however, should provide superior resolution for ray parameters greater than 11.5 s/deg..

A 301-record synthetic data set (see Figure 4.3b) is slant stacked using the same technique and parameters as in Chapter 3 (Figure 4.16). The data equivalent (Figure 4.17) contains 853 seismograms over the $36°$ distance range. Because the slant stack is merely the entire data set in another format, the (τ, p) domain, by looking at Figure 4.17 we can see the strengths and weaknesses of the Cascade Ranges data set. A linear artifact departing from the maximum (τ, p) locus at about (80 s, 9.5 s/deg.) is caused by the data gap from $26°$-$29°$. The image is fuzzy for all p values from 9.2-10.2 s/deg. due to the poor data coverage at the corresponding distances (compare to Figure 3.22). More abundant data at closer ranges, though, provides a more convincing image for $p \geq 11.5$ s/deg. than the southern data of Figure 3.22, indicating more resolving power for the depths near the 410 km discontinuity.

As expected, downward continuation of the synthetic data with CJF as the input velocity model returns a slowness-depth image that is equivalent to CJF (Figure 4.18). While the signal-to-noise ratio is poorer than for the Mexican events, continuation of the data with CJF yields a satisfying result; the Cascade Ranges data
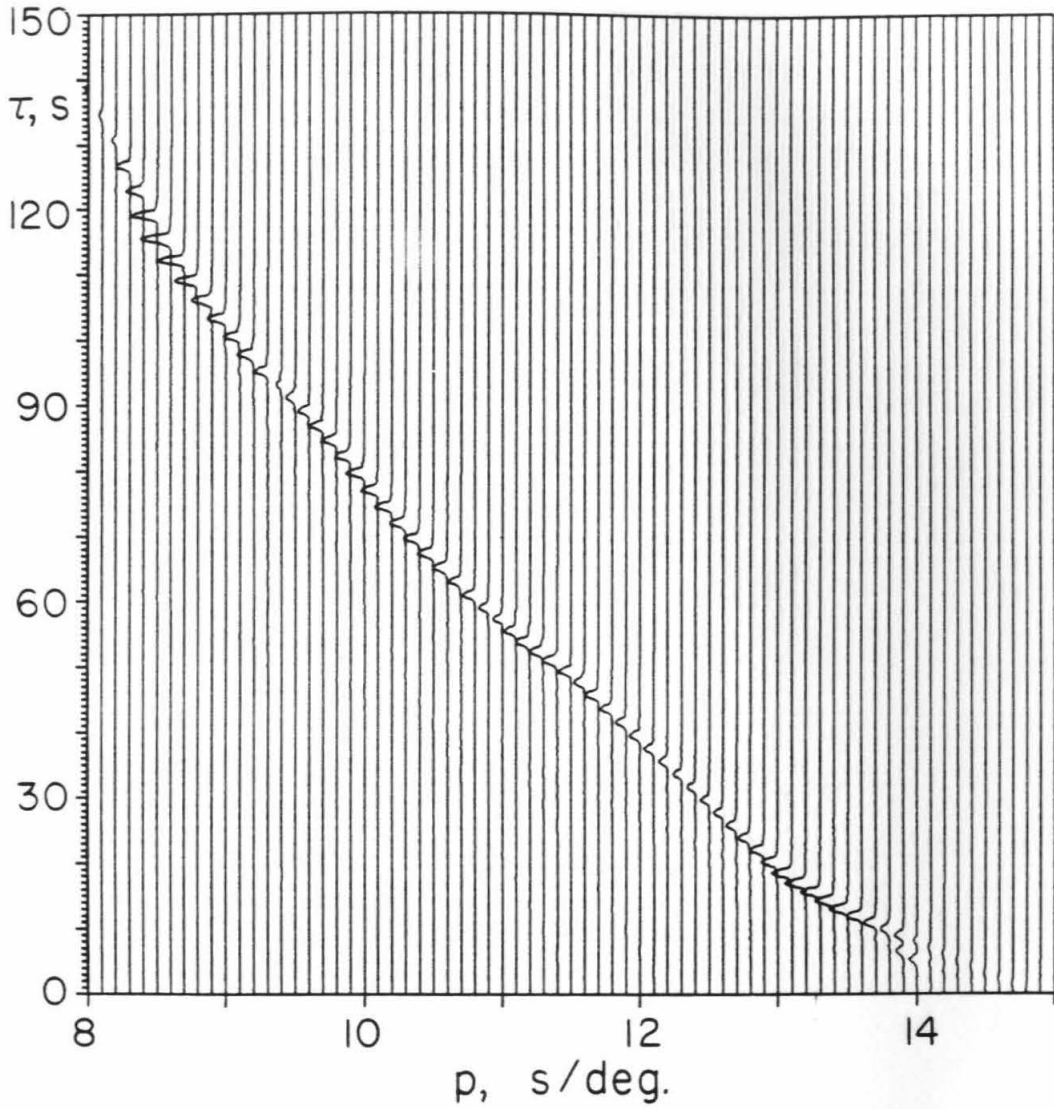
Figure 4.16 The slant-stacked wave field for CJF. For each p value, the envelope of the wave field is shown. Parameters used in the stacking process are the same as in Chapter 3.
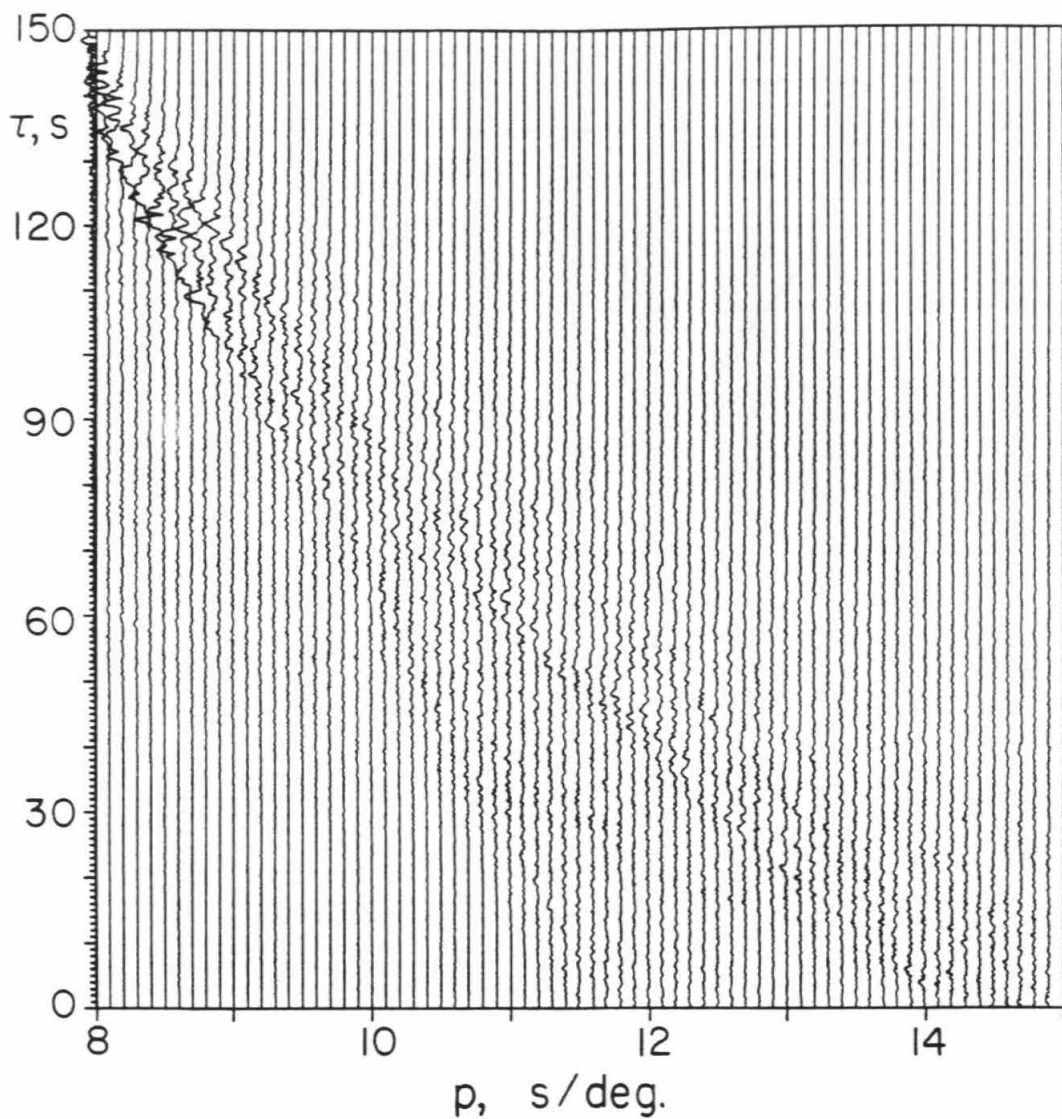
Figure 4.17 Seismograms from 21 northern events in the (τ, p) domain. Note that the stack is generally noisier that the equivalent for the southern data, Figure 3.22. More data from $16°-22°$ for the Cascade Ranges data, however, provides a better signal for $p > 12$ s/deg. than appears for the Mexican data set.
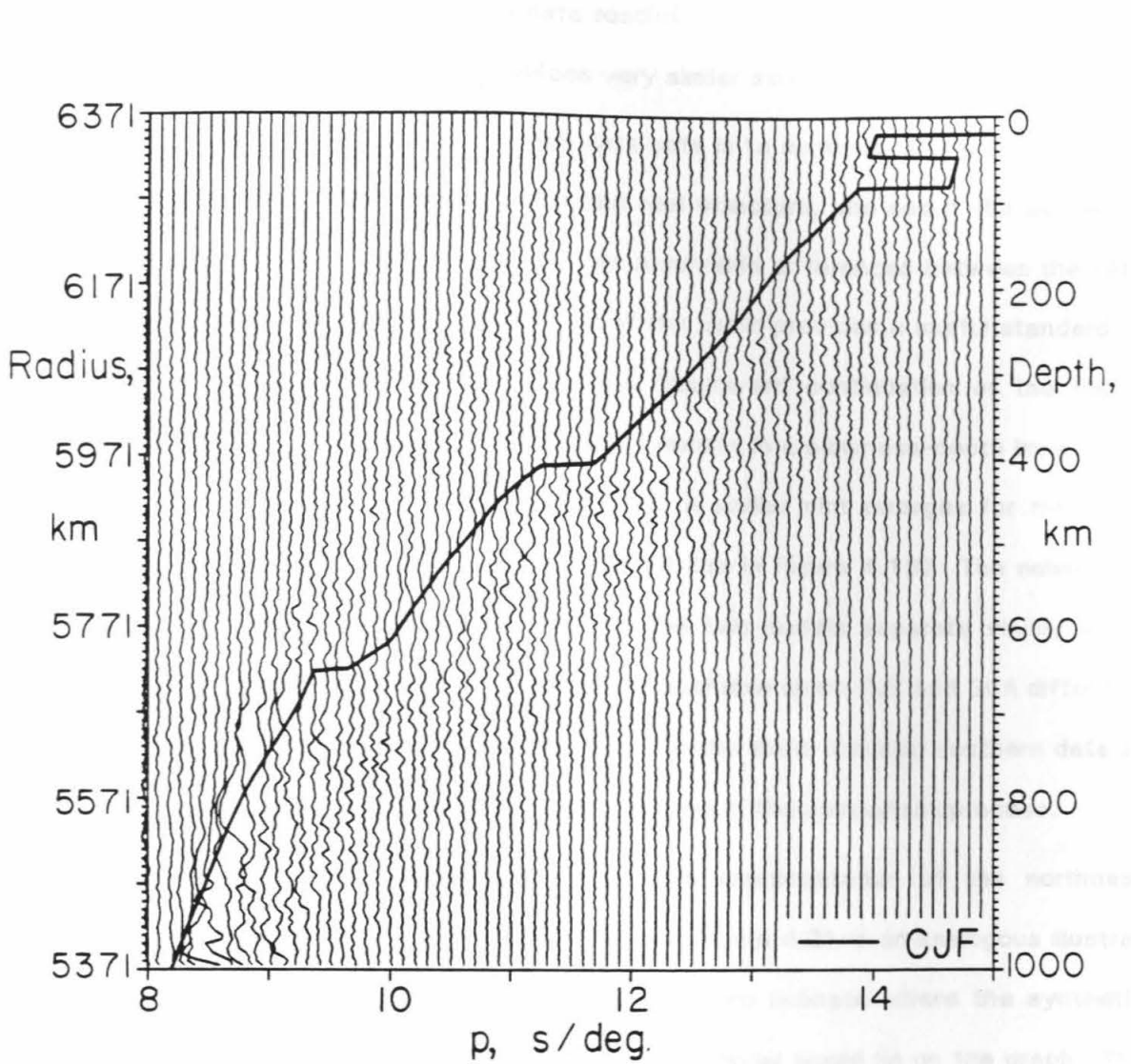
Figure 4.18 The northeast Pacific data downward continued with CJF, which is superimposed. The results are consistent; CJF is generally appropriate for these data.

are consistent with CJF within the data resolution. Implementation of the weighting scheme introduced in Chapter 3 produces very similar slowness-depth pictures.

One way of directly comparing two data sets is to continue both groups of data with a single model, quite distinct from the real structure, and see if the outcomes coincide. Visually disparate results indicate resolvable differences between the sets of seismograms. The Herrin (1968) model of the Earth provides a useful standard of comparison for our two suites of records. Downward continuation of the slant-stacked CJF synthetics with the Herrin model results in a slowness-depth image that matches neither Herrin nor CJF (Figure 4.19). A similar plot emerges for the same process applied to GCA'-GCA (see the dashed line in Figure 4.19). The noise-free continuations of the synthetic sections for the two models separate visibly for p values of 11.5 s/deg. and greater, which is reasonable since CJF and GCA differ the most above 350 km depth. The weaker signal in the slant-stacked southern data at high ray parameters may, therefore, be troublesome in the comparison process.

Figure 4.20 presents the slowness-depth representation of the northeast Pacific data continued with the Herrin model, and Figure 4.21 is an analogous illustration for the Gulf of California data. Both plots also indicate where the synthetic GCA'-GCA and CJF data continued with the Herrin model would lie on the graph. The images for large ray parameters are not particularly distinct for either data group. Still, careful inspection of the two figures shows that, for a given $p \geq 12.0$ s/deg., the northern data continuation yields shallower depths, similar to CJF. The image for the Mexico data at the same p value, while not as distinct, is deeper, in accordance with GCA'-GCA. The differences are slight, but visible. Thus the wave field continuation analysis supports our assertion that these two data sets, and the velocity structures associated with them, are distinct.
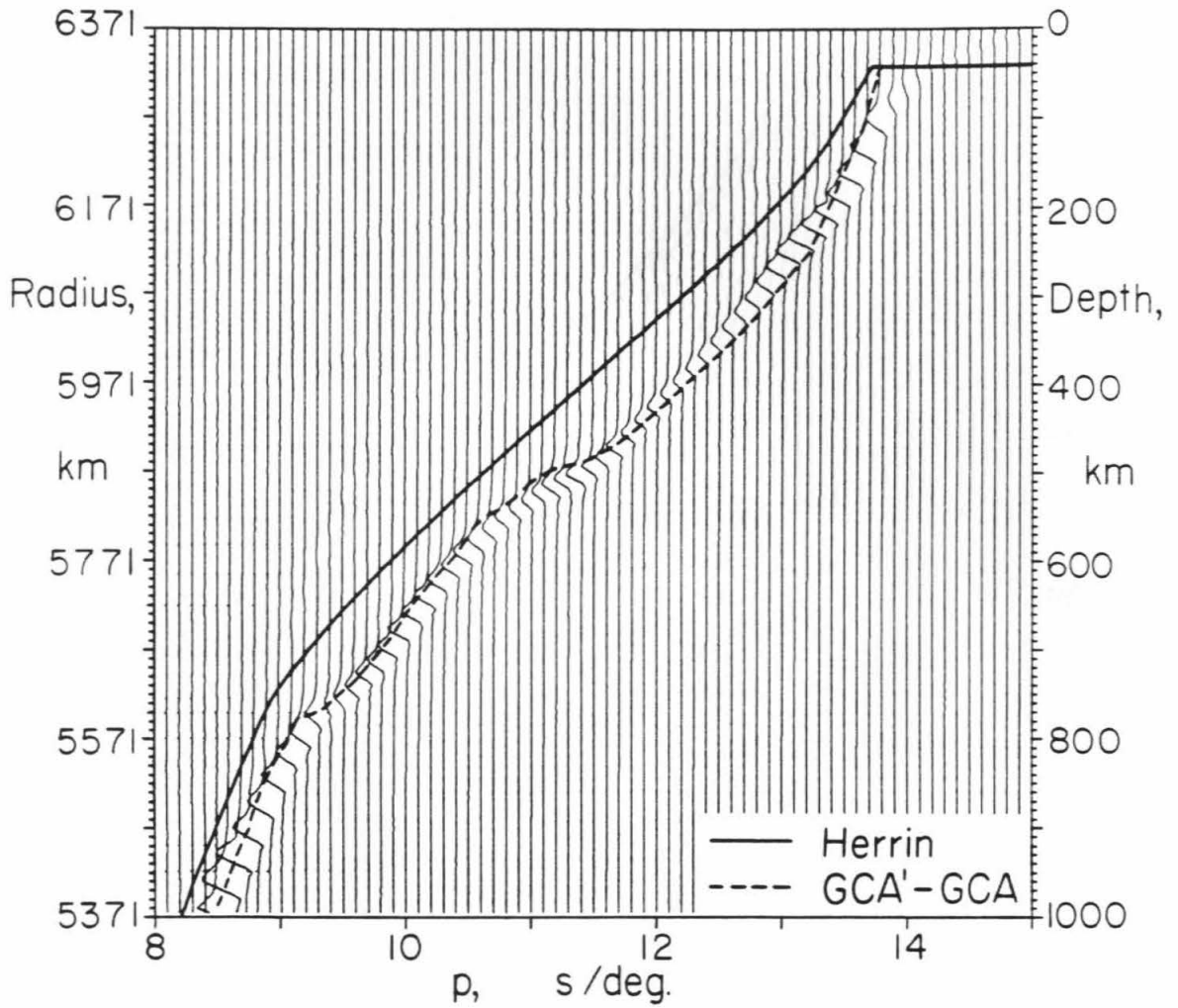
Figure 4.19 The CJF synthetic data continued with the Herrin (1968) velocity model. The Herrin model is shown and does not coincide with the image, indicating that is it not a good representation of the synthetic data. The dotted line marks the top of the image obtained by continuation of GCA'-GCA synthetic data with the Herrin velocities. CJF and GCA'-GCA diverge significantly only for $p > 11.5$ s/deg..
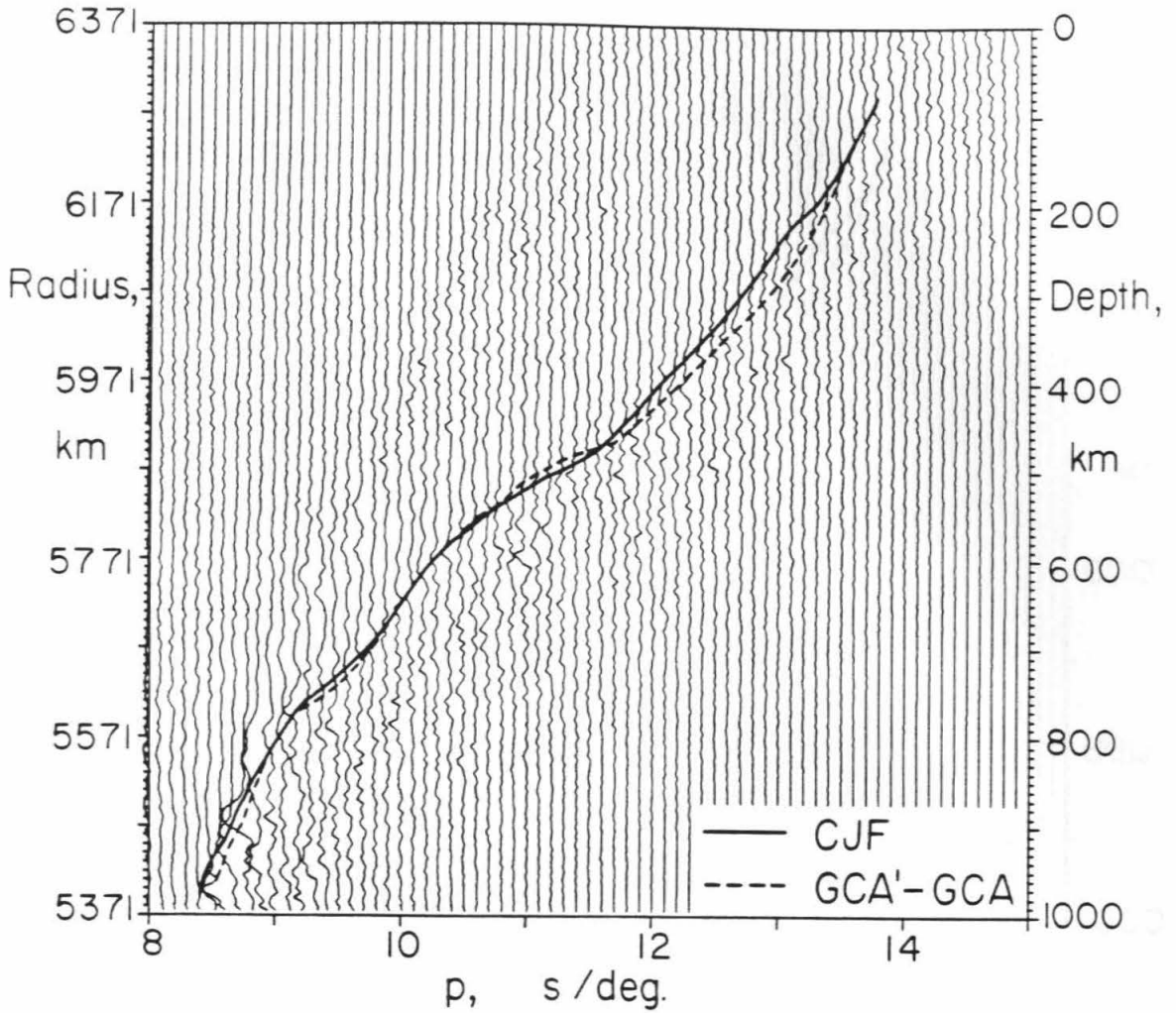
Figure 4.20 The Cascade Ranges-Juan de Fuca data continued with the Herrin model, along with lines representing CJF and GCA'-GCA continued with the same velocities. The data are noisy, but careful inspection for $p > 11.5$ s/deg. shows that these data are more consistent with CJF than GCA'-GCA. This is easier to see by looking from an angle along the plotted CJF and GCA'-GCA lines.
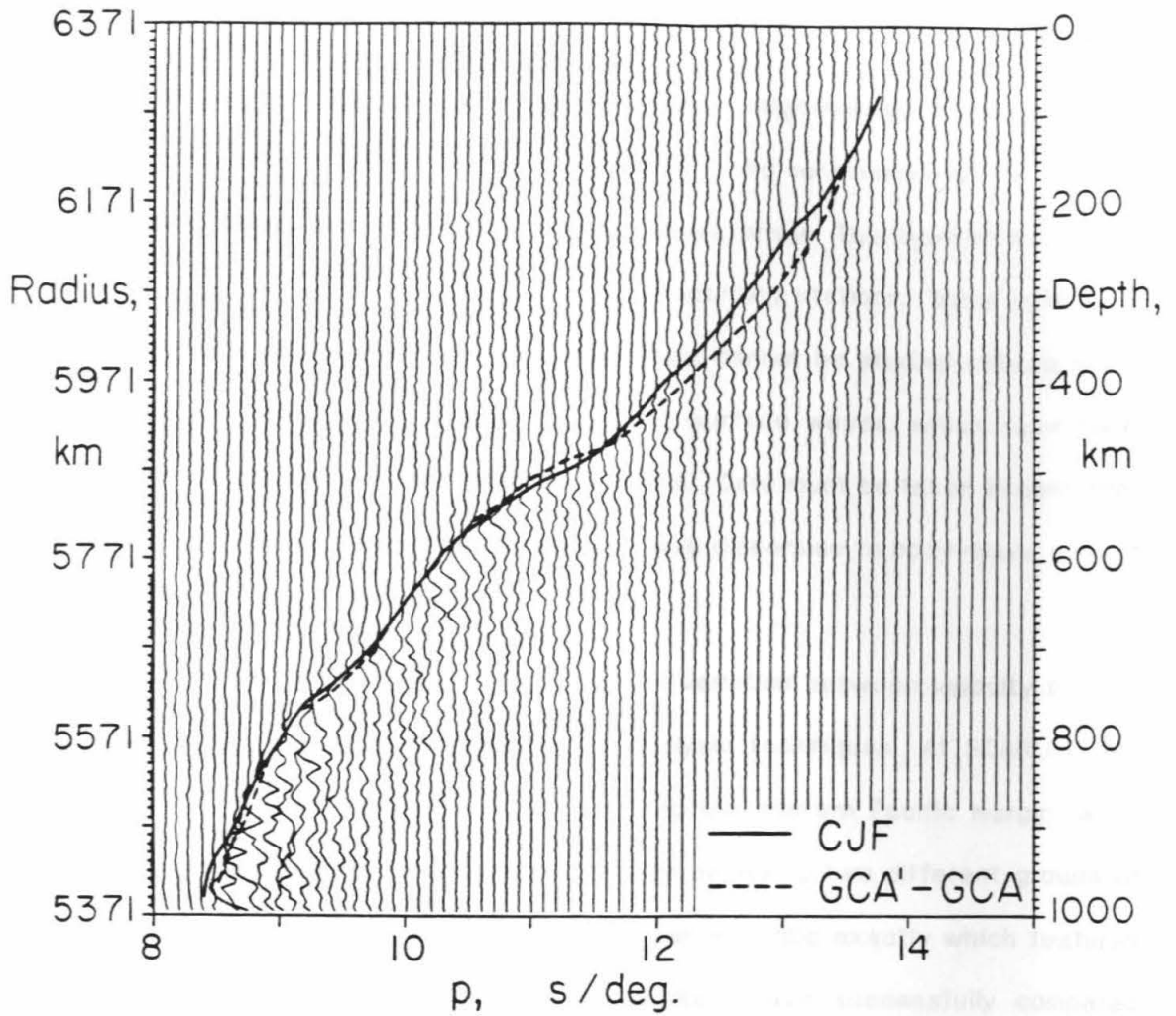
Figure 4.21 The Gulf of California data in the same format as Figure 4.20. Due to limited data near 18°, the image is not obvious for higher ray parameters. For $p >$ 12.5 s/deg., however, GCA'-GCA matches the continued data better than CJF. As in Figure 4.20, looking along the diagonal of the plot aids in observing the image.

Discussion

At present, the most complete way to obtain a high-resolution view of upper mantle velocity structure is through body-wave modeling constrained with $dT/d\Delta$ and travel time measurements, preferably from a seismic array. This type of analysis is limited to data from regions within 30° of the recording stations. Many potentially interesting portions of the upper mantle, therefore, cannot be studied utilizing body-wave modeling, and must be investigated using surface waves, which have lower resolution because of their very long wavelengths. Care must be taken in comparing shear velocity profiles obtained from surface wave dispersion to body-wave derived compressional structure.

It is much easier to identify true structural variation between velocity profiles constructed with the same data types and analysis techniques. At SCARLET, the close proximity of two major seismic zones along the eastern Pacific margin facilitates comparative study of the two regions. By analyzing two different groups of seismograms in precisely the same manner, we can describe exactly which features of each data set do not coincide. Earlier workers have successfully compared short-period structure between areas using waveform modeling at regional stations (e.g., Wiggins and Helmberger, 1973; Dey-Sarkar and Wiggins, 1976). Others utilized array-derived travel time and ray parameter estimates but used no relative amplitude constraints (e.g., Ram and Mereu, 1977; Ram et al., 1978; England et al., 1978). With the exception of Rademacher et al. (1983) who employ waveform modeling in study of Greek earthquake data gathered at the 13-station German broadband array GRF, the work presented here is the first to combine the waveform techniques of wave field continuation and synthetic seismogram modeling with traditional array

methods in determination of upper mantle structure.

The two data sets representing the Gulf of California and the Cascade Ranges underwent identical data processing. Still, several factors contribute to uncertainties in each model. We have attempted to minimize the effects of source mislocations with baseline shifts to the travel time data. These location errors can still have significant effect, however, if a poorly located event is important in the waveform modeling process. Another problem is the assumption of lateral homogeneity along our data 'profiles'. Tectonic regimes change with distance in both directions from SCARLET. With its wider azimuthal range, the northeast Pacific data are probably more contaminated by lateral heterogeneity effects than the ridge data. We have also ignored the possibility of attenuation variations with depth in the modeling process. Since we cannot uniquely distinguish between effects caused by attenuation and structure, the relationship of the velocities to the Q structure is ambiguous for both data sets. Further, if the attenuation structure varies laterally between the two regions, erroneous interpretations about lateral velocity variations could be made. Finally, SCARLET's teleseismic receiver structure varies with azimuth. The separate sets of empirical station corrections are to designed to eliminate receiver structure bias. Since there is a $40°$ azimuthal difference between the Alaskan calibration events and the Vancouver Island earthquakes, however, the northern corrections (Table 4.2) may not be totally appropriate.

When comparing our two data sets and the resultant models, it is important to remember the differences in data quantity, quality and distance distribution between the two record groups. Below the 660 km discontinuity, for example, the gradients of the two models diverge. Many travel time and $dT/d\Delta$ measurements for distances up to $40°$ as well as waveform modeling from $23°-28°$ constrain GCA's structure in this

depth range. In contrast, CJF's velocities are not well known near the lower discontinuity because of a lack of data from 26°-29°. Waves from northern earthquakes beyond 29°, though, arrive earlier than their southern counterparts, necessitating the steeper velocity gradient for CJF below 700 km.

Closer to the surface, GCA's upper discontinuity is at 390 km and the lower at 660 km, while the range between the two velocity breaks is only 240 km in CJF, 30 km less (see Figure 4.8). The disparity in EF branch data near 22° is slight but convincing, requiring the 10 km upward adjustment in the 650 km discontinuity for CJF. An unfortunate data gap near 18° for the southern data adds to the uncertainty of the exact depth of GCA's upper discontinuity because the first-arrival crossover point is not observed directly. Relative timing of arrivals from 13°-15° do not pin down the absolute depth to the discontinuity beneath the spreading center; the first arrivals at those distances are very dependent on poorly known shallow structure. CJF's 410 km discontinuity, on the other hand, is very well constrained by data recorded continuously from 16°-22°. Thus the change in absolute discontinuity depth near 400 km from GCA to CJF is not particularly well resolved.

Both data sets have many records from 20°-23°; the character of the AB branch arrival in this distance range controls the velocity gradient from about 300-400 km, and the first arrivals (CD branch) prescribe the structure in the transition zone. We do not require any changes from 400-650 km depth: both sets of data have amazingly similar first-arrival travel times. The data do demand a different gradient above 400 km for the Cascade Ranges. Clear observations of the AB branch to 21° from Vancouver Island events are in direct contrast to null-observations for the south past 19° for nine events. Perhaps because the AB branch cuts off so early, the forward branch (EF) reflection of the 660 km discontinuity is very prominent in

the Mexico data as early as 19° (see Figures 3.4, 3.5), while it is not seen from the north until nearly 22° (Figure 4.11). This repeatable contrast between the two groups of data supports GCA's steep gradient from 225-390 km and CJF's less severe rate of increase to 350 km.

Changes between the models above 200 km are largely dictated by the regional uppermost mantle structure and also by the travel times for $\Delta < 15°$. For GCA, velocities must be low to 200 km depth to accommodate the large gradient above the upper discontinuity. Since the gradient in CJF is more moderate, the low-velocity zone and speeds below 100 km are constructed to fit the travel times at close distances. These structures are by no means unique. Better control on velocities at asthenospheric depths would improve the entire velocity profile for each region.

The wave field continuation experiments emphasize the resolution capabilities of each data set as a function of ray parameter. By continuing both record sections with the Herrin velocities, subtle differences corresponding to the small structural changes are apparent. The work in this thesis with the wave field continuation technique is only a beginning; given sufficiently dense, high-quality data, this method is very powerful and has great potential in both providing less biased velocity models and in quantifying data resolution.

Now that we have documented the changes between CJF and GCA in detail, it is instructive to compare them to a model designed for the entire western United States, T7 (Burdick and Helmberger, 1978). Figure 4.22a displays all three velocity profiles, and Figure 4.22b displays the cumulative one-way vertical travel times of T7, GCA and CJF. The velocity-depth plot reveals that CJF is more similar to T7 than GCA, especially below 200 km. Above that depth, the relatively unconstrained structure varies widely from model to model. CJF is actually intermediate between T7 and
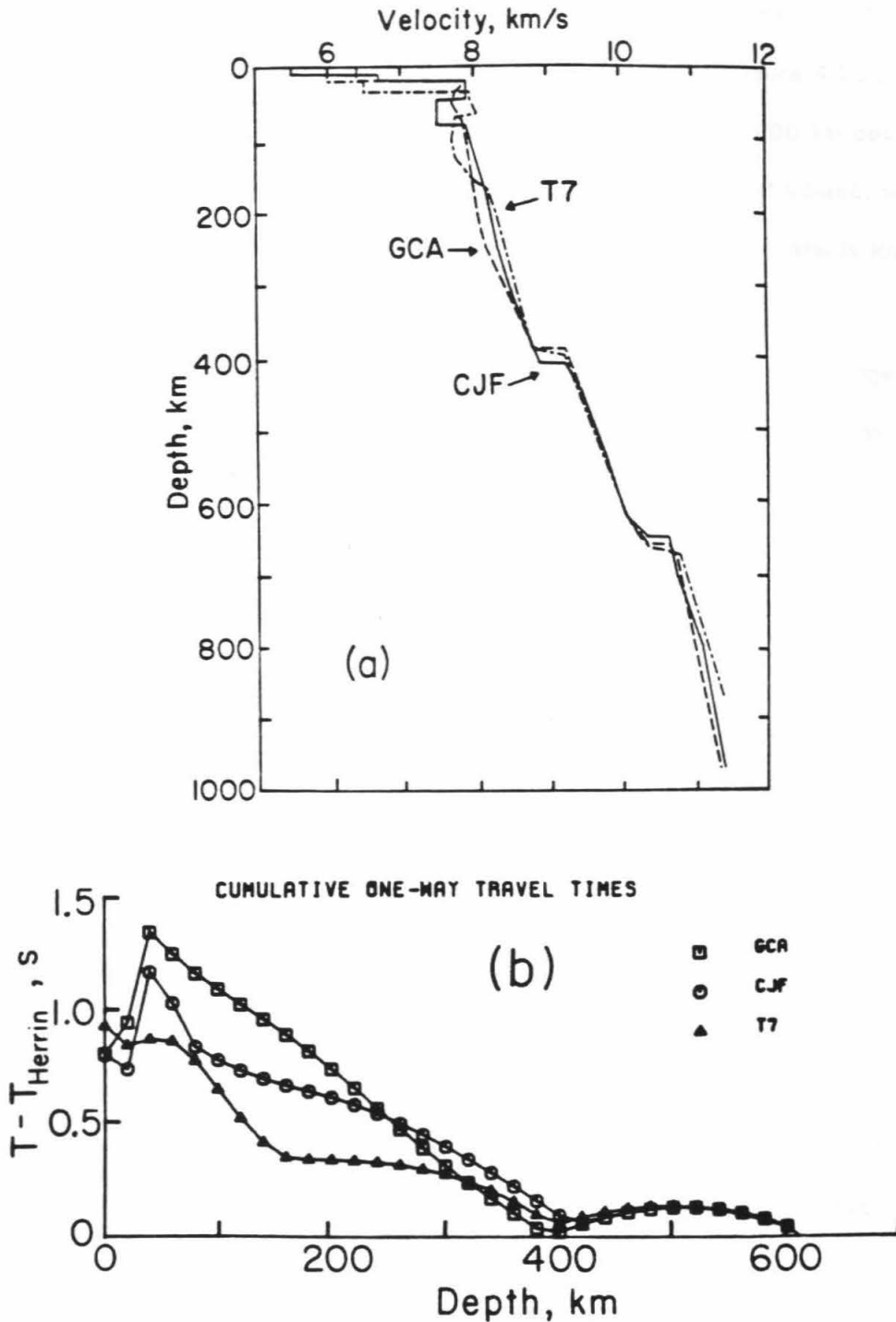
Figure 4.22 a) Comparison of CJF, GCA and T7 (Burdick and Helmberger, 1978). Between 200 and 350 km depth, CJF's velocity gradient is similar to T7's but the absolute velocities are lower. b) Cumulative one-way vertical travel times for these three models.

GCA between 200 and 350 km, having slightly lower velocities than T7. The one-way travel times illustrates CJF's median character very nicely (Figure 4.23b). Relative to the Herrin model, all three regional models are similar below 400 km depth. Above 240 km, GCA's slower velocities result in very positive residual values, while CJF's times flatten with respect to Herrin, as do T7's residuals. The various low-velocity zone shapes affect the near-surface cumulative times.

That CJF is intermediate in character between continental and ridge models is not surprising because it represents a transition region between tectonically active continent and very young oceanic material. Dey-Sarkar and Wiggins (1976) model western Canada upper mantle structure, including some data near the continental margin for $\Delta < 22°$. The AB travel time branch for their model WCA extends to $24°$, but is constrained only by data sensitive to structure inland, beneath the main continent. Their observations for $\Delta < 20°$ are in good agreement with our records for the Cascade region. Similarly, Burdick and Helmberger (1978) observe the AB branch in the western United States to $24°$, but their data are gathered much farther inland than our records.

In the oceanic regime, Ram and Mereu's (1977) work with Indian Ocean data recorded at the Gauribidanur seismic array confirm the analysis of Chapter 3: they do not observe the AB branch past a distance of $19°$. England et al.'s (1978) oceanic model NAT predicts an AB branch that extends beyond $20°$, but the travel paths used for the model vary widely in azimuth and sample regions under much older oceanic lithosphere.

Significant evidence exists for the variation of velocity gradient between 200 and 400 km as a function of tectonic regime. For some shield areas (e.g., King and Calcagnile, 1976; see Figure 2.1) the gradient is very shallow; it is more moderate

beneath tectonically active continental areas and older oceanic material (Fukao, 1977; Burdick and Helmberger, 1978; England et al., 1978) and very steep beneath at least one oceanic ridge (Chapter 3, this thesis). The transition from a young oceanic plate to a continent, represented by CJF, has structure intermediate to the young ocean and young continent regimes. From 200-350 km the gradient is moderate and from 350-400 km the velocities increase very quickly. On a global scale, results from the assimilation of many different upper models for differing tectonic settings support lateral heterogeneities in the mantle to depths close to the 400 km discontinuity; these heterogeneities are functions of surface tectonic regimes.

References

Aki, K.,1982. Three-dimensional seismic inhomogeneities in the lithosphere and asthenosphere: evidence for decoupling in the lithosphere and flow in the asthenosphere, *Rev. Geophys. Space Phys.*, **20** , 161-170.

Aki, K. and P. G. Richards, 1980. Quantitative seismology: theory and methods, San Francisco, W. H. Freeman Co.

Aki, K., A. Christoffersson and E. S. Husebye, 1976. Three-dimensional seismic structure of the lithosphere under Montana LASA, *Bull. Seism. Soc. Am.*, **66** , 501-524.

Aki, K., A. Christoffersson and E. S. Husebye, 1977. Determination of the three-dimensional seismic structure of the lithosphere, *J. Geophys. Res.*, **82** , 277-296.

Anderson, D. L., 1979. The deep structure of continents, *J. Geophys. Res.*, **84** , 7555-7560.

Backus, G. E. and J. F. Gilbert, 1967. Numerical application of a formalism for geophysical inverse problems, *Geophys. J. R. astr. Soc.*, **13** , 247-276.

Backus, G. E. and J. F. Gilbert, 1968. The resolving power of gross earth data, *Geophys. J. R. astr. Soc.*, **16** , 169-205.

Backus, G. E. and J. F. Gilbert, 1970. Uniqueness in the inversion of inaccurate gross earth data, *Phil. Trans. Roy. Soc. London Ser. A*, **216** , 123-192.

Bailey, T. L. and R. H. Jahns, 1954. Geology of the Transverse Range province, southern California, *Calif. Div. Mines Bull.*, **170** , 83-106.

Berg, J. W., L. Trembly, D. A. Emilia, J. R. Hutt, J. M. King, L. T. Long, W. R. McKnight, S. K. Sarmah, R. Souders, J. V. Thiruvathukal and D. A. Vossler, 1966. Crustal refraction profile, Oregon Coast Range, *Bull. Seism. Soc. Am.*, **56** , 1357-1362.

Berry, M. J. and D. A. Forsyth, 1975. Structure of the Canadian Cordillera from seismic refraction and other data, *Can. J. Earth Sci.*, **12**, 182-208.

Berteussen, K. A., 1975. Crustal structure and P-wave travel time anomalies at NORSAR, *J. Geophys.*, **41**, 71-84.

Berteussen, K. A., 1976. The origin of slowness and azimuth anomalies at large arrays, *Bull. Seism. Soc. Am.*, **66**, 719-741.

Bertrand, A. E. S. and R. M. Clowes, 1974. Seismic array evidence for a two-layer core transition zone, *Phys. Earth Planet. Int.*, **8**, 251-268.

Bessonova, E. N., V. M. Fishman, V. Z. Ryaboyi and G. A. Sitnikova, 1974. The tau method for inversion of travel times -- I. Deep seismic sounding data, *Geophys. J. R. astr. Soc.*, **36**, 377-398.

Bessonova, E. N., V. M. Fishman, M. G. Shnirman, G. A. Sitnikova and L. R. Johnson, 1976. The tau method for inversion of travel times -- II. Earthquake data, *Geophys. J. R. astr. Soc.*, **46**, 87-108.

Biehler, S., R. L. Kovach and C. R. Allen, 1964. Geophysical framework of the northern end of the Gulf of California structural province, *Am. Assoc. Pet. Geol. Mem.*, **3**, 126-143.

Bird, P., 1979. Continental delamination and the Colorado Plateau, *J. Geophys. Res.*, **84**, 7561-7571.

Bird, P., 1980. Fault slip rates, microplate velocities and mantle flow in southern California (abstract), *EOS Trans. AGU*, **61**, 1125.

Bischoff, J. L. and T. L. Henyey, 1974. Tectonic elements of the central part of the Gulf of California, *Bull. Geol. Soc. Am.*, **85**, 1893-1904.

Bolt, B. A., 1980. The detection of PKIIKP and damping of the inner core, *Annali. Geofis.*, **30**, 507-520.

Brocher, T. M. and R. A. Phinney, 1981. Inversion of slant stacks using finite-length record sections, *J. Geophys. Res.*, **86**, 7065-7072.

Buchbinder, G. G. R., C. Wright and G. Poupinet, 1973. Observation of PKiKP at distances less than 110°, *Bull. Seism. Soc. Am.*, **63**, 1699-1707.

Bulin, N. K., 1979. Upper mantle velocities on the northern Cocos plate -- a discussion, *Earth Planet. Sci. Lett.*, **43**, 168-171.

Bunch, A. and B. Kennett, 1980. The crustal structure of the Reykjanes Ridge at 59° 30'N, *Geophys. J. R. astr. Soc.*, **61**, 141-166.

Burdick, L. J., 1981. A comparison of the upper mantle structure beneath North America and Europe, *J. Geophys. Res.*, **86**, 5926-5936.

Burdick, L. J. and D. V. Helmberger, 1978. The upper mantle P velocity structure of the western United States, *J. Geophys. Res.*, **83**, 1699-1712.

Burdick, L. J. and C. A. Powell, 1980. Apparent velocity measurements for the lower mantle from a wide-aperture array, *J. Geophys. Res.*, **85**, 3845-3856.

Cara, M., J. B. Minster and R. LeBras, 1981. Multimode analysis of Rayleigh-type Lg, II, Application to southern California and the northwestern Sierra Nevada, *Bull. Seism. Soc. Am.*, **71**, 985-1002.

Chandra, U., 1974. Seismicity, earthquake mechanisms and tectonics along the western coast of North America, from 42°N to 61°N, *Bull. Seism. Soc. Am.*, **64**, 1529-1549.

Chapman, C. H., 1976. A first-motion alternative to geometrical ray theory, *Geophys. Res. Lett.*, **3**, 153-156.

Cheung, H. P. Y. and R. M. Clowes, 1981. Crustal structure from P- and S-wave analyses: ocean bottom seismometer results in the north-east Pacific, *Geophys. J. R. astr. Soc.*, **65**, 47-73.

Chinnery, M. A., 1969. Velocity anomalies in the lower mantle, *Phys. Earth Planet. Int.*, **2**, 1-10.

Chinnery, M. A. and M. N. Toksöz, 1967. P wave velocities in the mantle below 700 km, *Bull. Seism. Soc. Am.*, **57**, 199-226.

Christoffersson, A. and E. S. Husebye, 1979. On three-dimensional inversion of P-wave time residuals: option for geological modeling, *J. Geophys. Res.*, **84**, 6168-6176.

Claerbout, J. F., 1976. Fundamentals of geophysical data processing, New York, McGraw-Hill Book Co., Inc.

Clayton, R. W. and G. A. McMechan, 1981. Inversion of refraction data by wave field continuation, *Geophysics*, **46**, 860-868.

Cleary, J. R. and R. A. W. Haddon, 1972. Seismic wave scattering near the core-mantle boundary: a new interpretation of precursors to PKP, *Nature*, **240**, 549-551.

Cleary, J. R., D. W. King and R. A. W. Haddon, 1975. P-wave scattering in the Earth's crust and upper mantle, *Geophys. J. R. astr. Soc.*, **43**, 861-872.

Clowes, R. M., A. J. Thorleifson and S. Lynch, 1981. Winona basin, west coast Canada: crustal structure from marine seismic studies, *J. Geophys. Res.*, **86**, 225-242.

Corbishley, D. J., 1969. Multiple array measurements of the P-wave travel time derivative, *Geophys. J. R. astr. Soc.*, **19**, 1-14.

Crosson, R. S., 1972. Small earthquakes, structure, and tectonics of the Puget Sound region, *Bull. Seism. Soc. Am.*, **62**, 1133-1171.

Crosson, R. S., 1976. Crustal structure modeling of earthquake data 2. Velocity structure of the Puget Sound region, Washington, *J. Geophys. Res.*, **81**, 3047-

3054.

Davies, D., 1973. Seismology with large arrays, *Rep. Progr. Phys.*, **36** , 1233-1283.

Davies, D. and R. M. Sheppard, 1972. Lateral heterogeneities in the Earth's mantle, *Nature*, **239** , 318-323.

Davies, D., E. J. Kelly and J. R. Filson, 1971. Vespa process for analysis of seismic signals, *Nature Phys. Sci.*, **232** , 8-13.

Davis, E. E., C. R. B. Lister and B. T. R. Lewis, 1976. Seismic structure of the Juan de Fuca Ridge: ocean bottom seismometer results from the median valley, *J. Geophys. Res.*, **81** , 3541-3555.

Dehlinger, P., E. F. Chiburis and M. M. Collver, 1965. Local travel-time curves and their geologic implications for the Pacific Northwest states, *Bull. Seism. Soc. Am.*, **55** , 587-607.

Dey-Sarkar, S. K. and R. A. Wiggins, 1976. Upper mantle structure in western Canada, *J. Geophys. Res.*, **81** , 3619-3632.

Dorbath, C. and L. Dorbath, 1981. Travel time residuals of PP waves reflected under the central Atlantic Ocean, *Phys. Earth Planet. Int.*, **25** , 121-128.

Dziewonski, A. M. and D. L. Anderson, 1981. Preliminary reference earth model, *Phys. Earth Planet. Int.*, **25** , 297-356.

Dziewonski, A. M. and D. L. Anderson, 1983. Travel times and station corrections for P-waves at teleseismic distances, *J. Geophys. Res.*, **88** , 3295-3314.

Engdahl, E. R., E. A. Flinn and C. F. Romney, 1970. Seismic waves reflected from the Earth's inner core, *Nature*, **228** , 852-853.

England, P. C., B. L. N. Kennett and M. H. Worthington, 1978. A comparison of upper-mantle structure beneath Eurasia and the north Atlantic and Arctic Oceans,

Geophys. J. R. astr. Soc., **54**, 575-585.

England, P. C., M. H. Worthington and D. W. King, 1977. Lateral variation in the structure of the upper mantle beneath Eurasia, *Geophys. J. R. astr. Soc.*, **48**, 71-79.

Filson, J., 1975. Array seismology, *Ann. Rev. Earth Planet. Sci.*, **3**, 157-181.

Fuis, G. S., W. D. Mooney, J. H. Healy, G. A. McMechan and W. J. Lutter, 1982. Crustal structure of the Imperial Valley region, *in U.S. Geol. Surv. Prof. Pap.* **1254**, U. S. Government Printing Office, Washington, D. C., 25-50.

Fukao, Y., 1977. Upper mantle P structure on the ocean side of the Japan-Kurile arc, *Geophys. J. R. astr. Soc.*, **50**, 621-642.

Garmany, J., J. A. Orcutt and R. L. Parker, 1979. Travel time inversion: a geometrical approach, *J. Geophys. Res.*, **84**, 3615-3622.

Gerver, M. L. and V. Markushevitch, 1966. Determination of a seismic wave velocity from the travel time curve, *Geophys. J. R. astr. Soc.*, **21**, 337-357.

Gettrust, J. F., K. Furukawa and W. B. Kempner, 1982. Variation in young oceanic crust and upper mantle structure, *J. Geophys. Res.*, **87**, 8435-8446.

Ginzburg, A., J. Makris, K. Fuchs, B. Perathoner and C. Prodehl, 1979. Detailed structure of the crust and upper mantle along the Jordan-Dead Sea Rift, *J. Geophys. Res.*, **84**, 5605-5612.

Ginzburg, A., J. Makris, K. Fuchs and C. Prodehl, 1981. The structure of the crust and upper mantle in the Dead Sea Rift, *Tectonophysics*, **80**, 109-119.

Given, J. W., 1984. Inversion of body-wave seismograms for upper mantle structure, Ph.D. thesis, Calif. Inst. of Technol., Pasadena, 154 pp.

Given, J. W. and D. V. Helmberger, 1980. Upper mantle structure of northwestern Eurasia, *J. Geophys. Res.*, **85**, 7183-7194.

Grand, S. and D. Helmberger, 1983. Upper mantle shear velocity structure of North America, *Geophys. J. R. astr. Soc.*, in press, 1983.

Green, A. G., 1978. An upper mantle P-wave velocity model for eastern and southern Africa, *Pageoph.*, **116**, 1262-1273.

Haddon, R. A. W., and J. R. Cleary, 1974. Evidence for scattering of seismic PKP waves near the mantle-core boundary, *Phys. Earth Planet. Int.*, **8**, 211-234.

Haddon, R. A. W. and E. S. Husebye, 1978. Joint interpretation of P-wave time and amplitude anomalies in terms of lithospheric heterogeneities, *Geophys. J. R. astr. Soc.*, **55**, 19-43.

Hadley, D. M. and H. Kanamori, 1977. Seismic structure of the Transverse Ranges, California, *Geol. Soc. Am. Bull.*, **88**, 1469-1478.

Hager, B. H. and A. Raefsky, 1981. Deformation of seismic discontinuities and the scale of mantle convection (abstract), *EOS Trans. AGU*, **62**, 1074.

Hales, A. L., 1972. The travel times of P seismic waves and their relevance to the upper mantle velocity distribution, *Tectonophysics*, **13**, 447-482.

Hearn, T. M., 1983. Pn travel times in southern California, in press, *J. Geophys. Res.*

Heaton, T. H. and H. Kanamori, 1983. Seismic potential associated with subduction in the northwestern United States, submitted to Bulletin of the Seismological Society of America.

Helmberger, D. V. and L. J. Burdick, 1979. Synthetic seismograms, *Ann. Rev. Earth Planet. Sci.*, **7**, 417-442.

Helmberger, D. V. and R. A. Wiggins, 1971. Upper mantle structure of the midwestern United States, *J. Geophys. Res.*, **76**, 3229-3245.

Herrin, E., 1968. 1968 seismological tables for P phases, *Bull. Seism. Soc. Am.*, **58**, 1193-1241.

Humphreys, E., 1983. A tomographic inversion of teleseismic P travel times to southern California, manuscript in preparation.

Husebye, E. S., A. Christoffersson, K. Aki and C. Powell, 1976. Preliminary results on the 3-dimensional seismic structure of the lithosphere under the USGS central California seismic array, *Geophys. J. R. astr. Soc.*, **46**, 319-340.

Hyndman, R. D. and G. C. Rogers, 1981. Seismicity surveys with ocean bottom seismographs off western Canada, *J. Geophys. Res.*, **86**, 3867-3880.

Jackson, H. R., I. Reid and R. K. H. Falconer, 1982. Crustal structure near the Arctic mid-ocean ridge, *J. Geophys. Res.*, **87**, 1773-1783.

Johnson, C. E., 1979. Part I: CEDAR - An approach to the computer automation of short-period local seismic networks, Part II, Seismotectonics of the Imperial Valley of southern California, Ph.D. thesis, Calif. Inst. of Technol., Pasadena, 332 pp.

Johnson, L. R., 1967. Array measurements of P velocities in the upper mantle, *J. Geophys. Res.*, **72**, 6309-6325.

Johnson, L. R., 1969. Array measurements of P velocities in the lower mantle, *Bull. Seism. Soc. Am.*, **59**, 973-1008.

Johnson, S. H. and R. W. Couch, 1970. Crustal structure in the north Cascade mountains of Washington and British Columbia from seismic refraction measurements, *Bull. Seism. Soc. Am.*, **60**, 1259-1269.

Jordan, T. H., W. L. Rodi and J. M. Savino, 1981. Crustal and upper-mantle structure beneath the Columbia Basin from the joint inversion of travel-time and gravity data, paper presented at the 21st General Assembly, International Assembly for Seismology and Physics of the Earth's Interior, London, Canada.

Julian, B. R., D. Davies and R. M. Sheppard, 1972. PKJKP, *Nature*, **235**, 317-318.

Kanamori, H., 1967. Upper mantle structure from apparent velocities of P waves recorded at Wakayama Micro-earthquake Observatory, *Bull. Earthq. Res. Inst.*, **45**, 657-678.

Kanamori, H. and D. M. Hadley, 1975. Crustal structure and temporal velocity change in southern California, *Pageoph.*, **113**, 257-280.

Kanasewich, E. R., C. D. Hemmings and T. Alpuslan, 1973. Nth-root stack non-linear multichannel filter, *Geophysics*, **38**, 327-338.

Karig, D. E. and W. Jensky, 1972. The proto-gulf of California, *Earth Planet. Sci. Lett.*, **17**, 169-174.

Keen, C. E. and D. L. Barrett, 1971. A measurement of seismic anisotropy in the northeast Pacific, *Can. J. Earth Sci.*, **8**, 1056-1064.

Keen, C. E. and R. D. Hyndman, 1979. Geophysical review of the continental margins of eastern and western Canada, *Can. J. Earth Sci.*, **16**, 712-747.

Keen, C. and C. Tramontini, 1970. A seismic refraction survey on the Mid-Atlantic Ridge, *Geophys. J. R. astr. Soc.*, **20**, 473-491.

Kempner, W. C. and J. F. Gettrust, 1982. Ophiolites, synthetic seismograms and ocean crustal structure I. Comparison of ocean bottom seismometer data and synthetic seismograms for the Bay of Islands ophiolite, *J. Geophys. Res.*, **87**, 8447-8462.

Kennett, B. L. N., 1976. A comparison of travel-time inversions, *Geophys. J. R. astr. Soc.*, **44**, 517-536.

King, D. W. and G. Calcagnile, 1976. P-wave velocities in the upper mantle beneath Fennoscandia and western Russia, *Geophys. J. R astr. Soc.*, **46**, 407-432.

King, D. W., R. A. W. Haddon and J. R. Cleary, 1974. Array analysis of precursors to PKIKP in the distance range 128° to 142°, *Geophys. J. R. astr. Soc.*, **37**, 157-173.

King, D. W., E. S. Husebye and R. A. W. Haddon, 1976. Processing of seismic precursor data, *Phys. Earth Planet. Int.*, **12**, 128-134.

King, D. W., R. F. Mereu and K. J. Muirhead, 1973. The measurement of apparent velocity and azimuth using adaptive processing techniques on data from the Warramunga seismic array, *Geophys. J. R. astr. Soc.*, **35**, 137-167.

Knopoff, L., J. W. Schlue and F. A. Schwab, 1970. Phase velocities of Rayleigh waves across the East Pacific Rise, *Tectonophysics*, **10**, 321-334.

Lachenbruch, A. H. and J. H. Sass, 1980. Heat flow and energetics of the San Andreas fault zone, *J. Geophys. Res.*, **85**, 6185-6222.

Lacoss, R. T., E. J. Kelly and M. N. Toksöz, 1969. Estimation of seismic noise structure using arrays, *Geophysics*, **34**, 21-38.

Lamanuzzi, V. D., 1981. Relative Pn travel-time residuals for stations in southern California, M.S. thesis, Univ. of S. Calif., Los Angeles, 117 pp.

Langston C. A., 1977. Corvallis, Oregon, crustal and upper mantle receiver structure from teleseismic P and S waves, *Bull. Seism. Soc. Am.*, **67**, 713-724.

Langston, C. A., 1981. Evidence for subducting lithosphere under southern Vancouver Island and western Oregon from teleseismic P wave conversions, *J. Geophys. Res.*, **86**, 3857-3866.

Langston, C. A. and D. E. Blum, 1977. The April 29, 1965 Puget Sound earthquake and the crustal and upper mantle structure of western Washington, *Bull. Seism. Soc. Am.*, **67**, 693-711.

Larson, R. L., 1972. Bathymetry, magnetic anomalies and plate tectonic history of the mouth of the Gulf of California, *Bull. Geol. Soc. Am.*, **83**, 3345-3360.

Lee, R. C., 1981. Constraints on seismic velocity in the Earth's mantle, Ph.D. thesis, University of California, Berkeley, 73 pp.

Lenartowicz, E. and R. N. H. Albert, 1980. P-wave travel-time residuals and the crust and upper mantle lateral inhomogeneities in Africa, *Tectonophysics*, **67**, 123-137.

LePichon, X., R. E. Houtz, C. L. Drake and J. E. Nafe, 1965. Crustal structure of the mid-ocean ridges 1. Seismic refraction measurements, *J. Geophys. Res.*, **70**, 319-339.

Lewis, B. T. R. and J. D. Garmany, 1982. Constraints on the structure of the East Pacific Rise from seismic refraction data, *J. Geophys. Res.*, **87**, 8417-8425.

McCollom, R. L. and R. S. Crosson, 1975. An array study of upper mantle velocity in Washington state, *Bull. Seism. Soc. Am.*, **65**, 467-482.

McKenzie, D. and B. Julian, 1971. Puget Sound, Washington earthquake and the mantle structure beneath the northwestern United States, *Bull. Geol. Soc. Am.*, **82**, 3519-3524.

McMechan, G., 1979. An amplitude constrained P-wave velocity profile for the upper mantle beneath the eastern United States, *Bull. Seism. Soc. Am.*, **69**, 1733-1744.

McMechan, G. A., 1983a. p-x imaging by localized slant stacks of T-x data, *Geophys. J. R. astr. Soc.*, **72**, 213-221.

McMechan, G. A., 1983b. Wavefield inversion of seismic refraction data via the p-x plane, *Geophys. J. R. astr. Soc.*, **72**, 809-810.

McMechan, G. A. and R. Ottolini, 1980. Direct observation of a p-τ curve in a slant stacked wave field, *Bull. Seism. Soc. Am.*, **70** , 775-789.

McMechan, G. A. and G. D. Spence, 1983. P-wave velocity structure of the Earth's crust beneath Vancouver Island, *Can. J. Earth Sci.*, **20** , 742-752.

McMechan, G. A., R. W. Clayton and W. D. Mooney, 1982. Application of wave field continuation to the inversion of refraction data, *J. Geophys. Res.*, **87** , 927-935.

Maguire, P. K. H. and R. E. Long, 1976. The structure on the western flank of the Gregory Rift (Kenya) Part I. The crust, *Geophys. J. R. astr. Soc.*, **44** , 661-675.

Manchee, E. B. and D. H. Weichert, 1968. Epicentral uncertainties and detection probabilities from the Yellowknife seismic array data, *Bull. Seism. Soc. Am.*, **58**, 1359-1377.

Massé, R. P., 1973. Compressional velocity distribution beneath central and eastern North America, *Bull. Seism. Soc. Am.*, **63** , 911-935.

Massé, R. P., 1974. Compressional velocity distribution beneath central and eastern North America in the depth range 450-800 km, *Geophys. J. R. astr. Soc.*, **36** , 705-716.

Massé, R. P., E. A. Flinn, R. M. Seggelke and E. R. Engdahl, 1974. PKIIKP and the average velocity of the inner core, *Geophys. Res. Lett.*, **1** , 39-42.

Menke, W. H., 1977. Lateral inhomogeneities in P-velocity under the Tarbela array of the lesser Himalayas of Pakistan, *Bull. Seism. Soc. Am.*, **67** , 725-734.

Milne, W. G., G. C. Rogers, R. P. Riddihough, G. A. McMechan and R. D. Hyndman, 1978. Seismicity of western Canada, *Can. J. Earth Sci.*, **15** , 1170-1193.

Minster, J. B. and T. H. Jordan, 1978. Present-day plate motions, *J. Geophys. Res.*, **83**, 5331-5354.

Montagner, J. P. and N. Jobert, 1981. Investigation of upper mantle structure under young regions of the southeast Pacific using long-period Rayleigh waves, *Phys. Earth Planet. Int.*, **27**, 206-222.

Muirhead, K. J. and Ram Datt, 1976. The N-th root process applied to seismic array data, *Geophys. J. R. astr. Soc.*, **47**, 197-210.

Müller, G., 1971. Approximate treatment of elastic body waves in media with spherical symmetry, *Geophys. J. R. astr. Soc.*, **23**, 435-449.

Murdock, J. N. and L. H. Jaksha, 1981. The P wave velocity of the uppermost mantle of the Rio Grande Rift region of north central New Mexico, *J. Geophys. Res.*, **86**, 7055-7063.

Niazi, M. and D. L. Anderson, 1965. Upper mantle structure of western North America from apparent velocities of P waves, *J. Geophys. Res.*, **70**, 4633-4640.

Nolet, G. and S. Mueller, 1982. A model for the deep structure of the east African rift system from simultaneous inversion of teleseismic data, *Tectonophysics*, **84**, 151-178.

Okal, E. A. and D. L. Anderson, 1975. A study of lateral heterogeneities in the upper mantle by multiple ScS travel-time residuals, *Geophys. Res. Lett.*, **2**, 313-316.

Okal, E. A. and G. Kuster, 1975. A teleseismic array study in French Polynesia: implications for distant and local structure, *Geophys. Res. Lett.*, **2**, 5-8.

Oliver, H. W., ed., 1982. Transverse Ranges, interpretation of the gravity map of California and its continental Margin, *Calif. Div. Mines. Geol. Bull.* **205**.

Otsuka, M., 1966. Azimuth and slowness anomalies of seismic waves measured on the central California seismographic array Part I. Observations,

Bull. Seism. Soc. Am., **56** , 223-239.

Perathoner, B., K. Fuchs, C. Prodehl and A. Ginzburg, 1981. Seismic investigation of crust-mantle transition in continental rift systems -- Jordan-Dead Sea Rift and Rhinegraben, *Tectonophysics*, **80** , 121-133.

Powell, C. A., 1976. Mantle heterogeneity: evidence from large seismic arrays, Ph.D. thesis, Princeton Univ., Princeton, N.J., 326 pp.

Powell, C. A., M. C. Walck, and J. B. Minster, 1979. The relative array diagram: a novel approach to the determination of crust and upper mantle structure beneath an array (abstract), *EOS Trans. AGU*, **60** , 876.

Prescott, W. H., and A. Nur, 1981. The accommodation of relative motion at depth on the San Andreas fault system in California, *J. Geophys. Res.*, **86** , 999-1004.

Prodehl, C., 1981. Structure of the crust and upper mantle beneath the central European rift system, *Tectonophysics*, **80** , 255-269.

Puzyrev, N. N., M. M. Mandelbaum, S. V. Krylov, B. P. Mishenkin, G. V. Krupskaya and G. V. Petrich, 1973. Deep seismic investigations in the Baikal rift zone, *Tectonophysics*, **20** , 85-95.

Rademacher, H., R. I. Odom and R. Kind, 1983. The upper mantle structure under south-east Europe derived from GRF broadband records of Greek earthquakes, *J. Geophys.*, **52** , 7-13.

Raikes, S. A., 1976. The azimuthal variation of teleseismic P-wave residuals for stations in southern California, *Earth Planet. Sci. Lett.*, **29** , 367-372.

Raikes, S. A., 1978. Part I: Regional variations in upper mantle compressional velocities beneath southern California, Part II, Post shock temperatures: their experimental determination, calculation, and implications, Ph. D. thesis, Calif. Inst. of Technol., Pasadena, 307 pp.

Raikes, S. A., 1980. Regional variations in upper mantle structure beneath southern California, *Geophys. J. R. astr. Soc.*, **63**, 187-216.

Raikes, S. A. and D. M. Hadley, 1979. The azimuthal variation of teleseismic P-residuals in southern California: implications for upper mantle structure, *Tectonophysics*, **56**, 89-96.

Ram, A. and R. F. Mereu, 1977. Lateral variations in upper mantle structure around India as obtained from Gauribidanur seismic array data, *Geophys. J. R. astr. Soc.*, **49**, 87-113.

Ram, A., R. F. Mereu and D. H. Weichert, 1978. The identification and interpretation of upper mantle travel-time branches from measurements of dT/dΔ made on data recorded at the Yellowknife seismic array, *Can. J. Earth Sci*, **15**, 227-236.

Ram Datt, 1981. Seismic velocity structure using array data, *Phys. Earth Planet. Int.*, **24**, 33-52.

Ram Datt and K. J. Muirhead, 1976. Evidence for a sharp increase in P-wave velocity at about 770 km depth, *Phys. Earth Planet. Int.*, **13**, 37-46.

Ram Datt and K. J. Muirhead, 1977. Evidence of multiplicity in the P travel time curve beyond 30°, *Phys. Earth Planet. Int.*, **15**, 28-38.

Reid, I., J. Orcutt and W. A. Prothero, 1977. Seismic evidence for a narrow zone of partial melt underlying the East Pacific Rise at 21°N, *Bull. Geol. Soc. Am.*, **88**, 678-682.

Riddihough, R. P., 1978. The Juan de Fuca plate, *EOS Trans. AGU*, **59**, 836-842.

Riddihough, R. P., 1979. Gravity and structure of an active margin -- British Columbia and Washington, *Can J. Earth Sci.*, **16**, 350-363.

Rogers, G. C., 1979. Earthquake fault plane solutions near Vancouver Island, *Can. J. Earth Sci.*, **16**, 523-531.

Rowlett, H. and D. Forsyth, 1979. Teleseismic P-wave delay times in a major oceanic fracture zone, *Geophys. Res. Lett.*, **6**, 273-276.

Sacks, I. S. and G. Saa, 1971. The structure of the transition zone between the inner core and the outer core, *Carn. Inst. Ann. Rept. Dir. Dept. Terr. Mag.* 1969-70, 419-426.

Scheidegger, A. E. and P. L. Willmore, 1957. The use of a least squares method for the interpretation of data from seismic surveys, *Geophysics*, **22**, 9-22.

Schultz, P. S. and J. F. Claerbout, 1978. Velocity estimation and downward continuation by wavefront synthesis, *Geophysics*, **43**, 691-714.

Shor, G. G., P. Dehlinger, H. K. Kirk and W. S. French, 1968. Seismic refraction studies off Oregon and northern California, *J. Geophys. Res.*, **73**, 2175-2194.

Simpson, D. W., R. F. Mereu and D. W. King, 1974. An array study of P-wave velocities in the upper mantle transition zone beneath northeastern Australia, *Bull. Seism. Soc. Am.*, **64**, 1757-1788.

Sipkin, S. A. and T. H. Jordan, 1975. Lateral heterogeneity of the upper mantle determined from the travel times of ScS, *J. Geophys. Res.*, **80**, 1474-1484.

Sipkin, S. A. and T. H. Jordan, 1976. Multiple ScS travel times in the western Pacific: implications for mantle heterogeneity, *J. Geophys. Res.*, **81**, 853-861.

Talwani, M., X. LePichon and M. Ewing, 1965. Crustal structure of the mid-ocean ridges 2. Computed model from gravity and seismic refraction data, *J. Geophys. Res.*, **70**, 341-352.

Tatel, H. E. and M. A. Tuve, 1955. Seismic exploration of a continental crust, *Geol. Soc. Am. Sp. Pap.* **62**, 35-50.

Tobin, D. G. and L. R. Sykes, 1968. Seismicity and tectonics of the northeast Pacific Ocean, *J. Geophys. Res.*, **73**, 3821-3845.

Toksöz, M. N., M. A. Chinnery and D. L. Anderson, 1967. Inhomogeneities in the Earth's mantle, *Geophys. J. R. astr. Soc.*, **13**, 31-59.

Tryggvason, E., 1962. Crustal structure of the Iceland region from dispersion of surface waves, *Bull. Seism. Soc. Am.*, **52**, 359-388.

van den Berg, A. P., S. A. P. L. Cloetingh and D. J. Doornbos, 1978. A comparison of PKP precursor data from several seismic arrays, *J. Geophys.*, **44**, 499-510.

Vermeulen, J. M. and D. J. Doornbos, 1977. Mantle heterogeneity and mislocation patterns for seismic networks, *J. Geophys.*, **43**, 545-559.

Vetter, U. and J. B. Minster, 1981. Pn velocity anisotropy in southern California, *Bull. Seism. Soc. Am.*, **71**, 1511-1530.

Vinnik, L. P., and A. V. Nikolayev, 1970. The velocity profile of the lower mantle from direct measurements of $dT/d\Delta$, *Isv. Acad. Sci. USSR Phys. Sol. Earth Engl. Tr.*, **11**, 699-708.

White, W. R. H. and J. C. Savage, 1965. A seismic refraction and gravity study of the Earth's crust in British Columbia, *Bull. Seism. Soc. Am.*, **55**, 463-486.

Wickens, A. J., 1977. The upper mantle of southern British Colombia, *Can. J. Earth Sci.*, **14**, 1100-1115.

Wielandt, E. and L. Knopoff, 1982. Dispersion of very long-period Rayleigh waves along the East Pacific Rise: evidence for S wave velocity anomalies to 450 km depth, *J. Geophys. Res.*, **87**, 8631-8641.

Wiggins, R. A., 1969. Monte Carlo inversion of body wave observations, *J. Geophys. Res.*, **74**, 3171-3181.

Wiggins, R. A., 1976. Body-wave amplitude calculations -- 2., *Geophys. J. R. astr. Soc.*, **46**, 1-10.

Wiggins, R. A. and D. V. Helmberger, 1973. Upper mantle structure of the western United States, *J. Geophys. Res.*, **78** , 1870-1880.

Wiggins, R. A. and D. V. Helmberger, 1974. Synthetic seismogram computation by expansion in generalized rays, *Geophys. J. R. astr. Soc.*, **37** , 73-90.

Wiggins, R. A., G. A. McMechan and M. N. Toksöz, 1973. Range of earth structure nonuniqueness implied by body wave observations, *Rev. Geophys. Space Phys.*, **11** , 87-113.

Willmore, P.L. and A.M. Bancroft, 1960. The time-term approach to refraction seismology, *Geophys. J. R. astr. Soc.*, **3** , 419-432.

Wright, C. and J. R. Cleary, 1972. P-wave travel-time gradient measurements for the Warramunga seismic array and lower mantle structure, *Phys. Earth Planet. Int.*, **5** , 213-230.

Wright, C. and J. A. Lyons, 1979. The identification of radial velocity anomalies in the lower mantle using an interference method, *Phys. Earth Planet. Int.*, **18** , 27-33.

Yerkes, R. F., T. H. McCulloh, J. E. Schoellhamer and J. G. Vedder, 1965. Geology of the Los Angeles Basin, California - An Introduction, *in U S. Geol. Surv. Prof. Pap.* **420A,** U. S. Government Printing Office, Washington, D. C., 1-15.

Appendix

Determination of dT/dΔ and φ from teleseismic arrival times

Consider the seismic array in Figure A.1 with center (x_0, y_0) and a teleseism incident at azimuth φ_0. The travel time $T(x,y)$ at any station (x,y) may be written where $T_{JB}(x,y)$ is the JB travel time and $\Delta T(x,y)$ is the JB residual as

$$T(x,y) = T_{JB}(x,y) + \Delta T(x,y). \tag{A.1}$$

The set of JB residuals across the array are fit with a plane:

$$\Delta T(x,y) = a(x - x_0) + b(y - y_0) + \Delta t(x_0, y_0) \tag{A.2}$$

Here a and b are coefficients and Δt is the predicted JB residual at the array mid-point. Substituting (A2) into (A1) we obtain

$$T(x,y) = T_{JB}(x,y) + a(x - x_0) + b(y - y_0) + \Delta t(x_0, y_0). \tag{A.3}$$

Next expand $T_{JB}(x,y)$ in a Taylor series about the array center and keep only the first two terms:

$$T_{JB}(x,y) \approx T_{JB}(x_0, y_0) + (dT/d\gamma)\, d\gamma. \tag{A.4}$$

Here γ is the direction of approach (Figure A.1) and is measured on the Earth's spherical surface so as to incorporate the curvature of the earth over the array aperture.

Transforming to the (γ, ζ) coordinate system, we represent the vector $\hat{v}$ from the array center to a station as

$$\hat{v} = (x - x_0)\hat{x} + (y - y_0)\hat{y} = \gamma\hat{\gamma} + \zeta\hat{\zeta}. \tag{A.5}$$

Rotation yields

$$\hat{v} = \hat{\gamma}[-(x - x_0)\sin\varphi_0 - (y - y_0)\cos\varphi_0] + \hat{\zeta}[(x - x_0)\cos\varphi_0 + (y - y_0)\sin\varphi_0]. \quad (A.6)$$

Substituting into (A4) for $d\gamma$ we obtain

$$T_{JB}(x,y) = T_{JB}(x_0,y_0) + dT/d\gamma\,[-(x - x_0)\sin\varphi_0 - (y - y_0)\cos\varphi_0] \quad (A.7)$$

where

$$dT/d\gamma = dT/d\Delta_{JB}(x_0,y_0).$$

Substituting (A7) into (A3) we find a plane equation for the data in terms of the theoretical (JB) estimates and the plane fit to the JB residuals.

$$T(x,y) = T\,'(x_0,y_0) + \alpha\,(x - x_0) + \beta\,(y - y_0) \quad (A.8)$$

where

$$T\,'(x_0,y_0) = T_{JB}(x_0,y_0) + \Delta t(x_0,y_0),$$

$$\alpha = a - \sin\varphi_0\; dT/d\Delta_{JB}(x_0,y_0),$$

and

$$\beta = b - \cos\varphi_0\; dT/d\Delta_{JB}(x_0,y_0).$$

Then

$$dT/d\Delta_{JBobs} = (\alpha^2 + \beta^2)^{\frac{1}{2}} \quad (A.9)$$

$$= [a^2 + b^2 + (dT/d\Delta_{JB})^2 - 2\,(dT/d\Delta_{JB})\,(a\,\sin\varphi_0 + b\,\cos\varphi_0)]^{\frac{1}{2}}$$

$$\tan(\varphi_{obs}) = (\alpha/\beta) = \frac{a - dT/d\Delta_{JB}\sin\varphi_0}{b - dT/d\Delta_{JB}\cos\varphi_0}$$
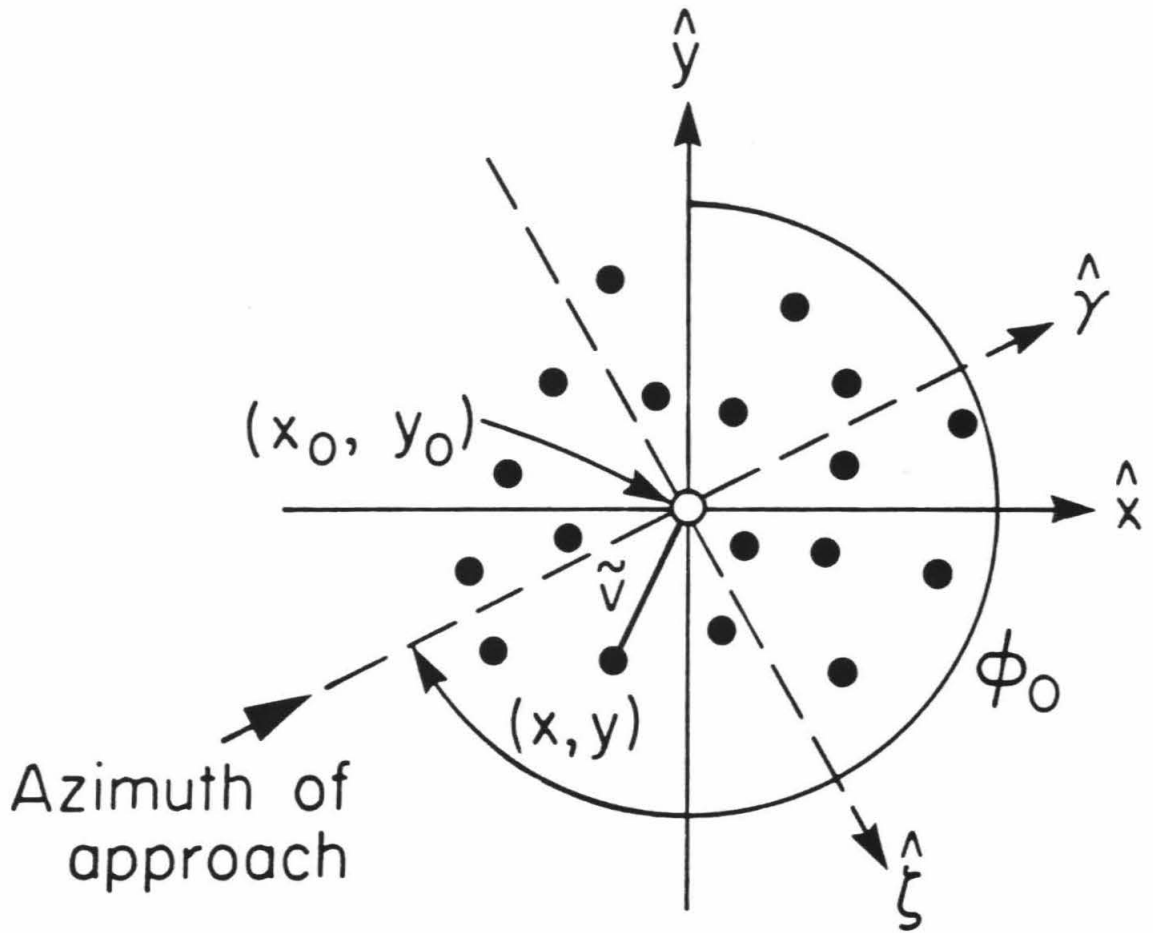
Figure A.1 Schematic map view of an array of stations with a plane wave incident at azimuth φ_0.